UNIVERSIDAD
DE GRANADA

Motional frequency spectroscopy in a Penning trap via a single laser-cooled ion

TESIS DOCTORAL

Joaquín Berrocal Sánchez

PROGRAMA DE DOCTORADO EN
FÍSICA Y CIENCIAS DEL ESPACIO

Granada, Diciembre de 2023

Motional frequency spectroscopy in a Penning trap via a single laser-cooled ion

REALIZADO POR:
Joaquín Berrocal Sánchez

DIRIGIDO POR:
Daniel Rodríguez Rubiales

DEPARTAMENTO:
Departamento de Física Atómica, Molecular y Nuclear

UNIVERSIDAD DE GRANADA

PROGRAMA DE DOCTORADO EN FÍSICA Y CIENCIAS DEL ESPACIO

Granada, Diciembre de 2023

Editor: Universidad de Granada. Tesis Doctorales
Autor: Joaquín Berrocal Sánchez
ISBN: 978-84-1195-219-4
URI: https://hdl.handle.net/10481/89887

Resumen

Esta tesis doctoral trata sobre el uso técnicas de enfriamiento y manipulación láser para la determinación de las frecuencias de movimiento en una trampa Penning. La detección óptica del estado de movimiento del sistema tiene las ventajas de ser universal, necesitar de un solo ion de interés, y ser altamente robusta frente a imperfecciones en los campos de atrapamiento. En este trabajo se presentan los primeros resultados experimentales al respecto, así como diversas mejoras técnicas llevadas a cabo: un nuevo sistema óptico de diseño propio, una bomba criogénica a medida y dos fuentes de iones. El ion $^{40}Ca^{+}$ ha sido caracterizado como detector de radiofrecuencia en el límite Doppler, desarrollando un protocolo de medida en el que se pulsa el enfriamiento láser para leer la amplitud de oscilación del ion a partir de una cámara EMCCD y un PMT. La determinación alterna de la frecuencia de ciclotrón de dos iones individuales de isótopos de calcio ($^{40}Ca^{+}$ vs $^{A}Ca^{+}$ con $A = 42, 44, 48$) ha arrojado las primeras medidas de cocientes de masas usando el método óptico. Por su parte, los experimentos con cristales de Coulomb de dos iones de la misma especie ($^{40}Ca^{+}$ - $^{40}Ca^{+}$) y de especies diferentes ($^{42}Ca^{+}$ - $^{40}Ca^{+}$) se han utilizado para estudiar la validez del teorema de invariancia generalizado. Esta últimas medidas constituyen la primera implementación del método en una plataforma universal. Se concluye necesario enfriar el cristal hasta el estado fundamental de movimiento para elevar la precisión de la técnica a un nivel competitivo.

Abstract

This thesis reports on the use of laser cooling and manipulation techniques for the determination of the motional frequencies in a Penning trap. The optical detection of the motional state of the system has the advantages of being universal, demanding only one ion of interest, and being robust against imperfections of the trapping fields. In this work, the first experimental results, as well as several technical improvements are presented: a novel optical system, a customized cryogenic pump, and two ion sources. $^{40}Ca^{+}$ has been characterized as a radiofrequency detector at the Doppler limit, developing a laser-pulsed measurement protocol to read out the ion's oscillation amplitude from an EMCCD and a PMT. The alternating determination of the cyclotron frequency of two individual calcium isotope ions ($^{40}Ca^{+}$ vs $^{A}Ca^{+}$ with $A = 42, 44, 48$) has yielded the first mass ratio measurements of the optical method. Experiments on balanced ($^{40}Ca^{+}$ - $^{40}Ca^{+}$) and unbalanced ($^{42}Ca^{+}$ - $^{40}Ca^{+}$) Coulomb crystals have been used to study the validity of the generalized invariance theorem. These measurements constitute the first implementation of the method on a universal platform. To bring the accuracy of the technique to a competitive level, it will be necessary to cool the crystal down to its ground state of motion.

A mis padres.
A mi abuelo.

Acknowledgements

First of all, I would like to thank my supervisor, Daniel, for his guidance and support throughout my doctoral thesis. I appreciate the time and effort he has always dedicated to the work in the laboratory.

I am deeply grateful to Fran and Manu, with whom I have shared most of this journey (especially with Fran). Working with them has always been very easy, and they have offered me their support and help whenever I have needed it. I am also grateful to Alex for helping me run the Penning trap during my last months in the lab. Special thanks to Javier for his assistance with everything related to the control system and Ana for her readiness to discuss anything about optics. I am grateful to all the other former (David, Emilio, Jaime, Javi, Jesús, Raúl, Víctor) and current (David and Jesús) members of the group, and to the bachelor and master students I have met in the lab throughout these years. Gracias también a Pablo, que siempre ha estado dispuesto a mecanizar cualquier pieza por muy pequeña que fuese.

I would like to thank Michael Block for giving me the opportunity of doing my stays at GSI. I must say I have always felt very welcomed, for which I especially thank Francesca, Sebastian, Oliver, and Manu, among all the people I was lucky to meet.

I would like to thank Christian Ospelkaus for providing us access to Zemax, which was utilized for the simulations of the new optical system.

I also want to mention here Alejandro, Álvaro, Ana María, Antònia, Aurora, Dani, David, Elena, Garví, Irene, Juan, Matilde, Nishal, Pablo, Pablo, Pedro, and Reza. I have enjoyed the friendly working environment they have created in the department and all the moments we have spent together.

Por último, quiero dar las gracias a mi familia, en especial a mis padres, por haberme apoyado siempre de forma incondicional.

This Thesis has been carried out under the FPU fellowship FPU2017/02596 from the Spanish Ministry of Education.

Contents

List of Figures

List of Tables

Acronyms

AIG active ion gauge.

AOM acousto-optic modulator.

API application programming interface.

ARTIQ Advanced Real-Time Infrastructure for Quantum physics.

ATF amplitude transfer function.

AWG arbitrary waveform generator.

CAD computer-assisted drawing.

CE correction electrode.

CPT charge, parity, and time reversal.

CTF contrast transfer function.

DAC digital-to-analog card.

DC direct current.

DDS direct digital synthesizer.

DIO digital input/output.

EC end cap.

EMCCD electron-multiplying charge-coupled device.

EOM electro-optical modulator.

FFT fast Fourier transform.

FPGA field-programmable gate array.

FWHM full width at half maximum.

GE ground electrode.

GT gate valve.

GUI graphical user interface.

He:Ne helium-neon.

HV high voltage.

ICC ion Coulomb crystal.

LAN local area network.

MCP microchannel plate.

MT measurement trap.

MTF modulation transfer function.

NA numerical aperture.

Nd:YAG neodymium-doped yttrium aluminum garnet.

NDSP network device support package.

OFHC oxygen-free high conductivity.

OSW optical switch.

OTF optical transfer function.

PBS polarizing beam splitter.

PEEK polyether ether ketone.

PI-ICR phase-imaging ion-cyclotron-resonance.

PID proportional-integral-derivative.

PMT photomultiplier tube.

PnA pulse-and-amplify.

PnP pulse-and-phase.

ppb parts-per-billion.

ppm parts-per-million.

PSF point spread function.

PT preparation trap.

QED quantum electrodynamics.

QLS quantum logic spectroscopy.

RE ring electrode.

RF radio frequency.

RFQ radio-frequency quadrupole.

RGA residual gas analyser.

RMS root mean square.

RPC remote procedure call.

RRR residual-resistance ratio.

sCMOS scientific complementary metal–oxide–semiconductor.

SHE super-heavy element.

SIP sputter ion pump.

SNR signal-to-noise ratio.

TMP turbo-molecular pump.

ToF time-of-flight.

ToF-ICR time-of-flight ion-cyclotron-resonance.

TPMC test particle Monte Carlo.

TTL transistor–transistor logic.

UHV ultra-high vacuum.

USB universal serial bus.

VCO voltage-controlled oscillator.

WLM wavelength meter.

Chapter 1

Introduction

Since it was devised by Hans G. Dehmelt to directly measure the electron's magnetic moment [1], the Penning trap has become the tool of choice to perform high-precision measurements of fundamental properties of the confined particles. The high temporal and spatial stability of the trapping fields translates into unrivalled achievable precision in the measurement of the cyclotron and the Larmor frequencies, directly related to fundamental properties such as the mass and the magnetic moment. Some of the most precise measurements of fundamental properties of subatomic particles have been performed using Penning traps. A few examples are the electron and proton masses [2–4], the antiproton-to-proton charge-to-mass ratio [5], the fine-structure constant [6], and the magnetic moment of several particles and antiparticles [7–9]. Some of these values are used to test the predictions of quantum electrodynamics (QED) and the charge, parity, and time reversal (CPT) symmetry.

Penning traps are also the prime choice to determine atomic masses with high precision [10]. The mass of an atom or ion is a fundamental property directly related to its binding energy and therefore contains information about the interaction among its constituents. The ion's mass is extracted from a measurement of the cyclotron frequency, which is in turn related to the motional frequencies. Two well-established detection methods are usually employed: the ion is destructively detected after it has been ejected from the trap [11], or non-destructively through the current it induces on certain trap electrodes [12].

Techniques relying on destructive detection, such as time-of-flight ion-cyclotron-resonance (ToF-ICR) and phase-imaging ion-cyclotron-resonance (PI-ICR), have been extensively used in on-line facilities to measure the mass of short-lived nuclides. The main advantages are the speed and the operation at room temperature. ToF-ICR takes advantage of the magnetic-field gradient the ions undergo when are ejected from the trap to observe the motional excitation from the time of flight [13]. Precisions in the order of 10^{-7} - 10^{-9} have been achieved, enabling the study of nuclear structure, nucleosynthesis processes in astrophysics, or test the Standard Model [10]. The more recent PI-ICR tracks the phases of the ion's radial motions and allows to reach the 10^{-10} level [14].

Non-destructive techniques based on bolometric detection are preferred for stable nuclides. In the 1980s, the groups of Robert Van Dyck Jr. at the University of Washington (UW) [15] and David Pritchard at the Massachusetts Institute of Technology (MIT) developed single-ion motional-frequency measurement techniques which made possible to reach the 10^{-11} level. The MIT group developed the so-called pulse-and-phase (PnP) technique [16], which extracts the motional frequency from a phase measurement and was used to measure the atomic mass of 13 ion species from the proton to ^{133}Cs at the sub-ppb level [17, 18]. This technique is still successfully employed after the trap was moved to Florida State University (FSU) [19]. Its use with two ions confined simultaneously in the same trap in the same magnetron orbit has allowed to explore the 10^{-12} level [20, 21]. This level of precision has also been reached with single ions in other facilities like PENTATRAP at the Max Planck Institute for Nuclear Physics (MPIK) in Heidelberg [22] or at the former Mainz g-factor experiment [23].

Ion cooling is an important preparatory stage in most ion-trapping experiments to reduce the line broadening and frequency shifts in high-precision spectroscopy. Laser cooling is the most effective method to reduce the ion's kinetic energy in the range below the electronvolt. It was proposed by Theodor W. Hänsch and Arthur L. Schawlow for free atoms and a continuous Doppler spectrum (Doppler cooling) [24], and simultaneously by David J. Wineland and Hans G. Dehhmelt for trapped ions and a spectrum modulated by motional sidebands (sideband cooling) [25] in 1975. The first experimental demonstration on trapped ions took place in 1978, when Wineland's group at the National Institute of Standards and Technology (NIST) [26] and Peter E. Toschek's group in Heidelberg [27] reported at the same time Doppler cooling of Mg^+ in a Penning trap and Ba^+ in a Paul trap, respectively. Laser cooling to the ground state of motion was first demonstrated in 1989 by the NIST group on a Paul trap [28]. Sympathetic cooling of other species through the Coulomb interaction [29] is used, e.g., to prepare a two-ion crystal for quantum logic spectroscopy (QLS), a technique that enables spectroscopy of ions that do not have suitable transitions for state preparation and detection [30].

Although Doppler cooling was simultaneously demonstrated in a Penning and a Paul trap, the latter has been predominantly the preferred platform to perform experiments in which laser manipulation and fluorescence readout are employed. The main reason is the comparatively high experimental complexity of a Penning trap. Experiments are usually carried out inside a cryogenic superconducting magnet, which greatly complicates the optical access, and laser cooling also requires more elaborated schemes due to Zemann splitting and the instability of the so-called magnetron motion. The pioneering work was carried out by the Ion Storage Group at NIST, which currently can build and control 2D $^9Be^+$ ion Coulomb crystals that have been used to implement quantum simulations [31] or quantum sensing protocols [32] on hundreds of ions. The group at Imperial College was the first to demonstrate cooling to the ground state of a single $^{40}Ca^+$ ion in the axial [33] and radial [34] motions. The Penning-trap experiment at the University

of Granada also uses calcium ions but in a stronger magnetic field (7 T) than the one at the Imperial College (2 T). The main goal is to develop a novel technique to determine the cyclotron frequency of a target ion by laser addressing a sensor ion and carrying out optical detection [35]. Although the original proposal conceived the location of the target and sensor ions in different traps sharing a common electrode [36], a first implementation will take place in the same trap on a two-ion unbalanced crystal [37]. Compared to other techniques, it is universal and only needs one ion without restriction in the mass-to-charge ratio. In addition, the use of laser cooling in the preparatory stage, ideally to the ground state of all the eigenmotions, reduces the required motional amplitude for detection and therefore the associated systematic shifts [38]. It is worth mentioning that other groups like the BASE-Hannover collaboration [39], the BASE-Mainz collaboration [40], or IONPEN at ETH-Zürich [41] also investigate the use of laser cooling in Penning traps for precision experiments and quantum simulation and computation.

One possible field of application of the optical-detection technique might be on direct mass measurements of the heaviest elements. At present, SHIPTRAP at GSI is the only Penning-trap mass spectrometer coupled to a facility capable of producing transactinides, commonly known as super-heavy elements (SHEs) [42]. The determination of the binding energy of SHEs provides useful information about their internal nuclear structure, contributing sometimes with new hints about shell effects that are necessary to explain their existence [43]. ToF-ICR [44, 45] and PI-ICR [46] have been employed to directly measure the mass of nobelium, lawrencium, and rutherfordium ions. However, the minute production rates, of one ion per day already for rutherfordium, can make even PI-ICR impracticable when increasing the atomic number. Non-destructive techniques based on induced-current detection using superconducting coils have not reached mass-to-charge ratios higher than 65 u/C to date [18], while other approaches based on quartz crystals are under study [47–49].

One of the first ideas behind the optical method was the determination of the Q-value of certain nuclear β processes that are of interest in the field of neutrino physics [50]. The study of the electron energy in β^- decay and the X-ray spectrum in electron capture are the only direct methods to determine the neutrino mass. The comparison of the spectrum endpoint and the Q-value, which can be directly delivered to high precision by measuring the masses of the mother and daughter nuclides with a Penning trap, gives the absolute electron neutrino mass. For example, in the most precise upper bound of 0.8 eV/c^2 delivered by the KATRIN experiment [51] for the electron antineutrino in tritium β^- decay, the Q-value obtained can be contrasted with the mass difference measured by the FSU group with 22 meV/c^2 uncertainty using PnP [19]. In other experiments, such as ECHo [52] or HOLMES [53], the atomic de-excitation spectrum of the electron capture in ^{163}Ho is studied. A Q-value of this reaction has been measured at SHIPTRAP with 30 eV/c^2 uncertainty using PI-ICR [54]. Apart from the above-mentioned standard β processes, it is also possible to observe the weak second-order double

beta decay for some nuclides, such as $^{48}Ca^{+}$ [55]. The search for the neutrinoless double-beta decay attempts to unravel the Dirac or Majorana nature of the neutrino [56].

The development of the optical-detection technique (and therefore the facility) has a strong potential for optical-spectroscopy experiments usually carried out in Paul traps. Apart from the motional-frequency stability and the strong magnetic field, essential features in mass and g-factor measurements, Penning traps have also other advantages over Paul traps. The absence of micromotion within the whole trapping volume avoids detrimental effects such as unwanted Doppler shifts and ion heating [33]. The usually higher trap dimensions also imply lower heating rates when ions are cooled to the ground state of motion. Ion clocks are a particular application of precision spectroscopy in ion traps in which an internal atomic transition of a previously ground-state cooled ion is repeatedly interrogated [57]. The highest precision, below 10^{-18}, has been reached with an $^{27}Al^{+}$ ion that is sympathetically cooled and read out through a $^{25}Mg^{+}$ (control) ion using QLS [58]. A new generation of ion clocks based on laser addressing of a nuclear isomer that lays within the optical spectrum is currently under development using $^{88}Sr^{+}$ as control ion and a Paul trap as storage device [59]. The main advantage with respect to atomic transitions is the insensitivity to the noise coming from external electromagnetic fields, which currently dominates the uncertainty budget. The best candidate at present is ^{229}Th, which has a low-lying nuclear isomer, ^{229m}Th, with an energy of 8.338(24) eV (150 nm wavelength) [60]. This value is still far from precision spectroscopy on the corresponding magnetic dipole transition, and the laser technology for the very first experiments is currently under development. The facility at the University of Granada is at the stage where two-ion crystals containing $^{232}Th^{+}$ (and $^{40}Ca^{+}$) can be formed for motional-frequency studies aiming at cooling all modes to their ground state, studies that can be directly projected to $^{229}Th^{+}$.

This manuscript consists of seven chapters. Chapter 2 presents the fundamentals of ion trapping and laser cooling in a Penning trap and an overview of the main motional-frequency measurement techniques. Chapter 3 is devoted to the experimental setup, paying special attention to the parts that have been developed and improved: the ion sources, the customized cryogenic pump, the novel optical system, and the control and data-acquisition system. The installation of the cryogenic pump drastically improved the vacuum level, while the new optical system enabled the detection and visualization of single ions and crystalline structures. A comprehensive description of the design, characterization, and performance of the latter is given. Chapter 4 details the performance of the ion sources for the ion injection in the magnetic field and describes the characterization of the laser cooling of ions to the Doppler limit. Special attention is put into the cooling of the radial modes in single ions and two-ion crystals using axialization. Chapter 5 presents the characterization of the $^{40}Ca^{+}$ sensor ion under external electric fields and the mass ratios of several stable isotopes, employing the optical method for the first

time. For the cyclotron-frequency ratios presented, one ion is used at a time in the trap, and the measurements are taken alternating a reference ion and the ion of interest. Chapter 6 presents the first implementation of the optical method on a balanced ($^{40}Ca^{+}$ - $^{40}Ca^{+}$) and an unbalanced two-ion crystal ($^{42}Ca^{+}$ - $^{40}Ca^{+}$). The modelling of the system, the analysis of the data, and a thorough discussion about the current limitations of the technique due to the Coulomb anharmonicity are presented. The ways to overcome these limitations are also discussed.

Chapter 2

Optical detection of the motional frequencies in a Penning trap

2.1 Penning trap fundamentals

The confinement of charged particles can be achieved either by an oscillating radio frequency (RF) electric field or by the superposition of static magnetic and electric fields [61,62]. The first type is commonly known as RF or Paul trap, after Wolfgang Paul [63]. The second was developed by Hans G. Dehmelt inspired in the Penning ion gauge and is named after the latter [1].

In the ideal Penning trap, a spatially homogeneous magnetic field along the so-defined axial direction, $\vec{B} = B\hat{z}$, provides confinement on the perpendicular radial plane. The comparatively weak electric potential V, that enables trapping in the axial direction, has a quadrupolar shape and is usually built with rotational symmetry around the axial z axis,

$$V = \frac{V_0}{4d_0^2}\left(2z^2 - x^2 - y^2\right). \tag{2.1}$$

Figure 2.1 shows the hyperbolic Penning trap, an electrode arrangement that naturally creates harmonic electrostatic potential wells in the axial (confining) and radial (deconfining) directions. For this electrode geometry, V_0 is the potential difference between the endcaps and ring electrodes, and d_0 is the so-called characteristic distance of the trap. The Penning trap utilized in this thesis has a ring geometry that allows for laser addressing and fluorescence collection in the radial plane. It is presented in Sec. 3.1, and further details about the design and optimization can be found in previous theses of this group [64,65] or in Ref. [66].

2.1.1 Dynamics of a single trapped ion

The force exerted by the electromagnetic fields on a particle with charge q and velocity $\vec{v}$ is given by the Lorentz's law, $\vec{F} = q\left(\vec{E} + \vec{v} \times \vec{B}\right)$. The motional equations

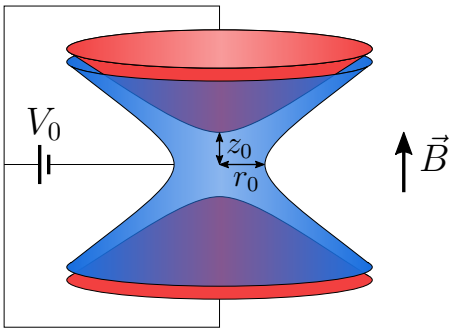

Figure 2.1. The hyperbolic Penning trap. The electric field is created by applying a potential difference V_0 between two endcaps (in red) and a ring electrode (in blue). The endcaps have the shape of a two-sheet hyperboloid, while the ring electrode is a one-sheet hyperboloid that shares the same asymptotic cone. The distances z_0 and r_0 are related to the trap's characteristic distance d_0 as $d_0^2 = \left(2z_0^2 + r_0^2\right)/4$.

of a single trapped ion of mass m in a Penning trap are

$$\ddot{x} - \omega_c \dot{y} - \frac{1}{2}\omega_z^2 x = 0, \tag{2.2a}$$

$$\ddot{y} + \omega_c \dot{x} - \frac{1}{2}\omega_z^2 y = 0, \tag{2.2b}$$

$$\ddot{z} + \omega_z^2 z = 0, \tag{2.2c}$$

where $\omega_c = 2\pi\nu_c$ is the cyclotron frequency of the ion in the bare magnetic field,

$$\omega_c = \frac{q}{m}B, \tag{2.3}$$

proportional to the charge-to-mass ratio q/m, and

$$\omega_z = \sqrt{\frac{qV_0}{md_0^2}}. \tag{2.4}$$

The axial motion is a simple harmonic oscillator with frequency $\omega_z = 2\pi\nu_z$. The two radial equations can be simplified by introducing the variable $u = x + iy$, giving rise to

$$\ddot{u} + i\omega_c \dot{u} - \frac{1}{2}\omega_z^2 u = 0 \tag{2.5}$$

and its complex conjugate. By setting $u = u_0 e^{i\omega t}$, it is found that the general solution of Eq. (2.5) is the superposition of two circular motions oscillating at frequencies

$$\omega_\pm = \frac{\omega_c}{2}\left[1 \pm \sqrt{1 - 2\left(\frac{\omega_z}{\omega_c}\right)^2}\right]. \tag{2.6}$$

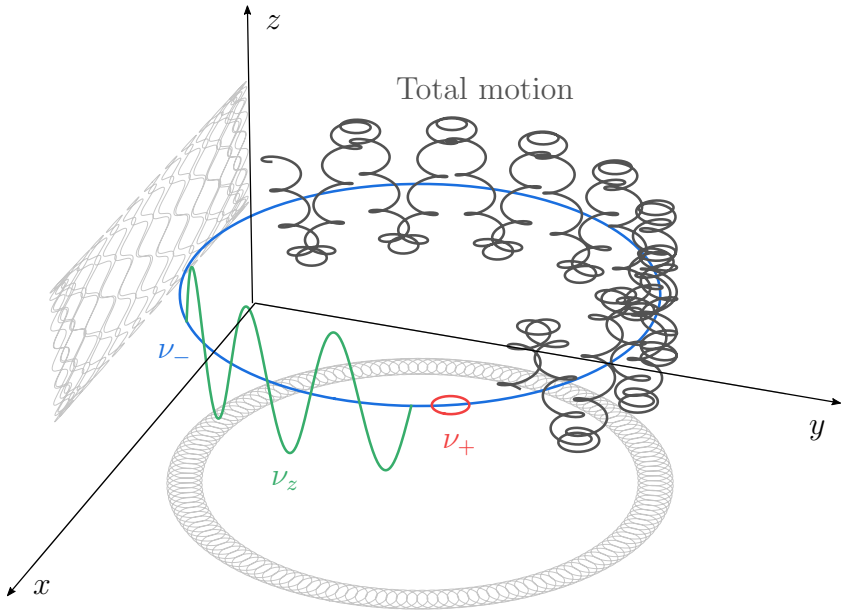

Figure 2.2. Motion of a single ion in a Penning Trap. The total motion and its decomposition in the three eigenmotions are represented. The radial xy and radial-axial xz projections are also plotted. $\omega_+/\omega_- = 15$, $\omega_z/\omega_- = 150$, $\rho_+/\rho_z = 0.75$, and $\rho_-/\rho_z = 10$.

The modified-cyclotron motion ($\omega_+ = 2\pi\nu_+$) originates from the cyclotron motion in the bare magnetic field (ω_c), slightly modified by the electric field. The magnetron motion ($\omega_- = 2\pi\nu_-$) results from the $\vec{E} \times \vec{B}$ drift. The motional equations for the three spatial coordinates are

$$x = \rho_+ \cos(\omega_+ t + \theta_+) + \rho_- \cos(\omega_- t + \theta_-), \tag{2.7a}$$
$$y = -\rho_+ \sin(\omega_+ t + \theta_+) - \rho_- \sin(\omega_- t + \theta_-), \tag{2.7b}$$
$$z = \rho_z \cos(\omega_z t + \theta_z), \tag{2.7c}$$

where ρ_u and θ_u represent the amplitude and phase, respectively [61,62]. Figure 2.2 shows the ion's motion in the Penning trap. The ion's energy can be derived using the Hamiltonian formalism and is given by [61]

$$E_{\text{total}} = \frac{1}{2} m\omega_z^2 \rho_z^2 + m\omega_1 \left(\omega_+ \rho_+^2 - \omega_- \rho_-^2\right), \tag{2.8}$$

where $\omega_1 = \omega_+ - \omega_-$. Note that a higher magnetron motional amplitude implies a lower energy, which might be interpreted as an unstable behaviour.

The cyclotron frequency can be directly derived from the radial frequencies as

$$\omega_c = \omega_+ + \omega_-. \tag{2.9}$$

A more powerful relationship that connects the three eigenfrequencies with the cyclotron frequency, valid even for first-order misalignment between the magnetic

and electric fields and first-order field ellipticity, is the invariance theorem [67], which reads

$$\omega_c^2 = \omega_+^2 + \omega_-^2 + \omega_z^2. \tag{2.10}$$

The real Penning trap is subject to field deviations from the ideal homogeneous $\vec{B}$ and harmonic $\vec{E}$ that cause the three eigenfrequencies to shift and therefore have an impact on the achievable accuracy. Some reasons are imperfections in the mechanization of the electrodes or their finite dimensions. Note that even the considered ideal Penning trap (Fig. 2.1) truncates the hyperboloids. Assuming cylindrical symmetry around the z axis, deviations from the ideal quadrupolar electric potential can be treated by a series expansion in terms of the Legendre Polynomials P_η,

$$V(r,z) = \frac{1}{2} C_\eta V_0 \left(\frac{r}{d_0}\right)^\eta P_\eta\left(\frac{z}{r}\right), \tag{2.11}$$

where $r = \sqrt{x^2+y^2+z^2}$ and C_η is a dimensionless coefficient [68]. If $C_2 = 1$ and $C_\eta = 0$ for $\eta \neq 2$, the electric potential of the ideal Penning trap, Eq. (2.1), is recovered. Given the absence of free currents near the centre of the trap, $\nabla \times \vec{B} = 0$ and the magnetic field can be derived as the gradient of a scalar potential Ψ, $\vec{B} = -\nabla\Psi$ [69]. Ψ can also be expanded in terms of Legendre Polynomials,

$$\Psi(r,z) = -\frac{1}{\eta+1} B_\eta r^{\eta+1} P_{\eta+1}\left(\frac{z}{\sqrt{r^2+z^2}}\right), \tag{2.12}$$

where B_η are coefficients with dimension of magnetic field strength times length raised to η [68]. The $\eta+1$ factors ensure the coefficient B_η is associated with a magnetic field of order η in the spatial coordinates. The magnitude of the motional amplitude-dependent frequency shifts, and thus the associated (systematic) uncertainty, can be estimated using perturbation theory. Mirror symmetry about the xy plane at the trap centre is assumed so that only even terms of the electric potential and magnetic field contribute. The frequency shifts originating from the quadrupolar component of the electric field are [68]

$$\Delta\omega_\pm = \mp \frac{C_4}{C_2}\frac{3}{2d_0^2}\frac{\omega_+\omega_-}{\omega_+-\omega_-}\left[2\rho_z^2 - \rho_\pm^2 - 2\rho_\mp^2\right], \tag{2.13a}$$

$$\Delta\omega_z = \frac{C_4}{C_2}\frac{3}{4d_0^2}\omega_z\left[\rho_z^2 - 2\rho_+^2 - 2\rho_-^2\right]. \tag{2.13b}$$

For the magnetic field [68],

$$\Delta\omega_+ = \frac{B_2}{4B_0}\omega_+\frac{\omega_+ + \omega_-}{\omega_+ - \omega_-}\left[\rho_z^2 - \rho_+^2 - \left(1 + \frac{\omega_-}{\omega_+}\right)\rho_-^2\right], \tag{2.14a}$$

$$\Delta\omega_- = -\frac{B_2}{4B_0}\omega_-\frac{\omega_+ + \omega_-}{\omega_+ - \omega_-}\left[\rho_z^2 - \left(1 + \frac{\omega_+}{\omega_-}\right)\rho_+^2 - \rho_-^2\right], \tag{2.14b}$$

$$\Delta\omega_z = \frac{B_2}{4B_0}\omega_z\frac{\omega_+ + \omega_-}{\omega_+\omega_-}\left[\omega_+\rho_+^2 + \omega_-\rho_-^2\right]. \tag{2.14c}$$

Precision Penning traps integrate compensation electrodes to mitigate these higher-order contributions and achieve an electric field as harmonic as possible.

The motional amplitudes and phases are routinely manipulated by applying external electric fields. A dipolar field resonant with a particular eigenfrequency is employed to address each of the motions separately. It can be used, e.g., to increase the amplitude of a previously cooled ion. A quadrupolar electric field oscillating at the sum (if both are stable) or difference (if the magnetron motion is involved) of frequencies is able to transfer energy between two eigenmotions [70].

2.1.2 Dynamics of a two-ion crystal

The dynamics of two ions simultaneously trapped in a Penning trap includes the Coulomb interaction. The ions are labelled as sensor (s) and target (t), and they are supposed to have the same charge. The motional equations can be written as [37, 65]

$$\ddot{x}_{s,t} - \omega_{cs,ct}\dot{y}_{s,t} - \frac{1}{2}\omega_{zs,zt}^2 x_{s,t} - \frac{1}{m_{s,t}}\frac{q^2}{4\pi\varepsilon_0}\frac{x_{s,t}-x_{t,s}}{|\vec{r}_s-\vec{r}_t|^3} = 0, \tag{2.15a}$$

$$\ddot{y}_{s,t} + \omega_{cs,ct}\dot{x}_{s,t} - \frac{1}{2}\omega_{zs,zt}^2 y_{s,t} - \frac{1}{m_{s,t}}\frac{q^2}{4\pi\varepsilon_0}\frac{y_{s,t}-y_{t,s}}{|\vec{r}_s-\vec{r}_t|^3} = 0, \tag{2.15b}$$

$$\ddot{z}_{s,t} + \omega_{zs,zt}^2 z_{s,t} - \frac{1}{m_{s,t}}\frac{q^2}{4\pi\varepsilon_0}\frac{z_{s,t}-z_{t,s}}{|\vec{r}_s-\vec{r}_t|^3} = 0, \tag{2.15c}$$

where ε_0 is the vacuum permittivity. If the kinetic energy is sufficiently low and $\omega_{zs}/\omega_{cs} < 1/\sqrt{3\mu}$ [65], with $\mu = m_t/m_s$, the two ions form an ordered structure referred to as Coulomb crystal: they occupy stable positions, aligned along the axis, and their relative distance is given by

$$d_{\text{ion-ion}} = \sqrt[3]{\frac{q^2}{2\pi\varepsilon_0 m_s \omega_{zs}^2}}. \tag{2.16}$$

For infinitesimal ions' amplitudes, the Coulomb force in Eq. (2.15) can be approximated to its first-order term in the Taylor series so that the motional equations become [37, 65]

$$\ddot{x}_{s,t} - \omega_{cs,ct}\dot{y}_{s,t} - \omega_{zs,zt}^2 x_{s,t} + \frac{1}{2}\omega_{zs,zt}^2 x_{t,s} = 0, \tag{2.17a}$$

$$\ddot{y}_{s,t} + \omega_{cs,ct}\dot{x}_{s,t} - \omega_{zs,zt}^2 y_{s,t} + \frac{1}{2}\omega_{zs,zt}^2 y_{t,s} = 0, \tag{2.17b}$$

$$\ddot{z}_{s,t} + 2\omega_{zs,zt}^2 z_{s,t} - \omega_{zs,zt}^2 z_{t,s} = 0. \tag{2.17c}$$

The axial motion is decoupled from the radial motion, and the frequencies of the two eigenmodes, namely the common and stretch modes, are [37, 65]

$$\omega_z^{\text{com,str}} = \omega_{zs}\sqrt{1 + \frac{1}{\mu} \pm \sqrt{1 + \frac{1}{\mu^2} - \frac{1}{\mu}}}, \tag{2.18}$$

where the +/− sign corresponds to common/stretch. The equations for the radial modes can be easily solved for the case of the balanced crystal ($m_t = m_s$), obtaining the frequencies [37, 65]

$$\omega_{\pm}^{\mathrm{com,str}} = \frac{\omega_{cs}}{2}\left[1 \pm \sqrt{1 - 2\left(\frac{\omega_z^{\mathrm{com,str}}}{\omega_{cs}}\right)^2}\right], \tag{2.19}$$

where the +/− sign stands for the modified-cyclotron/magnetron mode. For the general case, the frequencies of the radial eigenmodes can be also found analytically, but this entails solving a quartic equation.

Analogously to the case of a single ion, the six eigenfrequencies of the two-ion crystal, $\omega_u^{\mathrm{com,str}}$ with $u \in \{+, -, z\}$, can be related to the cyclotron frequencies of the two individual ions. The relationship, strictly valid only for infinitesimal amplitudes, is called generalized invariance theorem [41], and states

$$\omega_{cs}^2 + \omega_{ct}^2 = \sum_u \left(\omega_u^{\mathrm{com}}\right)^2 + \left(\omega_u^{\mathrm{str}}\right)^2. \tag{2.20}$$

2.2 Laser cooling fundamentals

Laser cooling achieves a net loss of the particle's momentum by the absorption and re-emission of photons near-resonant with an internal transition of the ion. Two situations can be considered depending on the relative magnitude of the ion's motional frequency ω_u and the natural linewidth of the transition Γ [71]. If $\omega_u \ll \Gamma$, the period of the ion's eigenmotion is much larger than the optical decay time, and the system is said to be in the weak-binding regime. During the oscillation period, the ion progressively explores the spectral line profile of the optical transition due to the Doppler effect. If $\omega_u \gg \Gamma$, the system is in the strong-binding regime. The spectrum seen by the ion is composed of the optical-transition frequency ω_{ge} and a series of equispaced sidebands at $n\omega_u$, with n an integer number [72].

The weak-binding regime occurs when addressing an electric dipole transition. For example, $\Gamma = 2\pi \times 22$ MHz for the dipole transition $3p^6 4s\,{}^2\mathrm{S}_{1/2} \Leftrightarrow 3p^6 4p\,{}^2\mathrm{P}_{1/2}$ in $^{40}\mathrm{Ca}^+$, while $\omega_c = 2\pi \times 2.7$ MHz in a 7-T Penning trap. Doppler cooling is accomplished by red-detuning the laser frequency so that momentum-loss collisions are fostered. This technique is very efficient below the electronvolt, with cooling times in the order of the millisecond. The ultimate temperature achieved is limited by the recoil energy from spontaneous emission. Cooling to the ground state of motion has been demonstrated in the strong-binding regime, e.g., employing the electric quadrupole transition $3p^6 4s\,{}^2\mathrm{S}_{1/2} \Leftrightarrow 3p^6 3d\,{}^2\mathrm{D}_{5/2}$ in $^{40}\mathrm{Ca}^+$ [28].

2.2.1 Doppler cooling in a Penning trap

The two radial motions in a Penning trap cannot be simultaneously cooled by red-detuned light. A net loss of momentum in a certain direction in the radial plane

implies a decrease of oscillation amplitude in the modified-cyclotron motion but an increase in the magnetron one, due to the unstable nature of the latter [73]. The two main techniques that have been developed to cool both motions simultaneously are summarized below.

Spatial intensity gradient

The laser beam of frequency ω_l and photon wavenumber $k_l = 2\pi\lambda$ is spatially offset in the radial plane so that there is an intensity gradient across the ion's orbit. Since many photons are scattered during one oscillation period in the weak-binding regime, the absorption can be modelled by a continuous force

$$F_{sc} = \hbar k_l R_{sc}, \tag{2.21}$$

where $\hbar$ is the reduced Planck's constant and R_{sc} is the scattering rate. The latter is given by

$$R_{sc} = \Gamma \frac{s/2}{1 + s + \left[2\Delta_{\text{eff}}/\Gamma\right]^2}. \tag{2.22}$$

$\Delta_{\text{eff}} = \omega_l - \omega_{ge} - \vec{k}_l \cdot \vec{v}$ is the effective detuning accounting for the Doppler shift. s is the (space-dependent) saturation parameter, defined as

$$s = \frac{I}{I_{\text{sat}}}. \tag{2.23}$$

Assuming a Gaussian beam travelling along the x axis and centred in $y = y_0$, the intensity I is given by,

$$I\left(y\right) = I_0 e^{-\frac{(y-y_0)^2}{2w_y^2}}, \tag{2.24}$$

where w_y is the so-called beam waist. The saturation intensity I_{sat} is given by

$$I_{\text{sat}} = \frac{2\pi\hbar c\Gamma}{3\lambda^3}, \tag{2.25}$$

where c is the speed of light.

The average momentum imparted by the emitted photons is zero since the spontaneous emission pattern is usually symmetric. However, the average energy, proportional to the squared momentum, increases linearly with the number of collisions. This random-walk problem has been studied using the so-called Fokker-Planck equation [74], which describes the evolution of a particle under the influence of damping and random forces, although it is beyond the scope of this work. The minimum temperature, usually referred to as the Doppler limit, is in the order of $\hbar\Gamma/2k_B$, with k_B the Boltzmann's constant [71]. For $^{40}Ca^+$, it corresponds to approximately 1 mK.

For small velocities and amplitudes, close to the final temperature, the scattering force (Eq. (2.21)) can be linearized in these two variables. The equation for

the axial motion is that of a damped harmonic oscillator. In the radial plane, the equations are

$$\ddot{x} - \omega_c \dot{y} - \gamma_v \dot{x} - \frac{1}{2}\omega_z^2 x + \gamma_y y = 0, \tag{2.26a}$$

$$\ddot{y} + \omega_c \dot{x} - \frac{1}{2}\omega_z^2 y = 0, \tag{2.26b}$$

where $\gamma_v = \left(\partial F_{sc}/\partial v_x\right)/m$ and $\gamma_y = \left(\partial F_{sc}/\partial y\right)/m$. Considering that $\gamma_v \ll \omega_c$ and $\gamma_y \ll \omega_z^2$, Eq. (2.26) can be analytically solved to first order [75], resulting in a variation of the modified-cyclotron and magnetron amplitudes given by

$$\rho_\pm(t) = e^{\mp \frac{\gamma_v \omega_\pm - \gamma_y}{4\omega_1} t} \rho_\pm(0). \tag{2.27}$$

The modified-cyclotron motion is cooled by a negative laser detuning (positive γ_v), while the magnetron motion is cooled by the position gradient if the laser beam is arranged in the configuration shown in Fig. 2.3 (positive γ_y). In order to cool the two motions simultaneously, $\omega_- < \gamma_y/\gamma_v < \omega_+$, or substituting the values of γ_y and γ_v,

$$\omega_- < \frac{(\Gamma/2)^2 + (\omega_{ge} - \omega_l)^2}{2k_l y_0 (\omega_{ge} - \omega_l)} < \omega_+, \tag{2.28}$$

where it is assumed the laser beam is placed to obtain a maximum gradient at the trap centre, i.e., $y_0 = w_y$ [73]. For $^{40}Ca^+$ in 7 T, $\omega_- = 2\pi \times 20$ kHz, $\omega_{ge} - \omega_l = \Gamma/2$, $I_0 = I_{\text{sat}}$, and $w_y = 100$ μm, $\gamma_v = 17$ kHz and $\gamma_y/\omega_1 = 1.5$ kHz. This implies cooling rates (argument of the exponential function in Eq. (2.27)) of 3.9 kHz and 0.34 kHz for the modified-cyclotron and magnetron motions, respectively.

Axialization

A quadrupolar electric field (see Fig. 2.3) at ω_c applied simultaneously with Doppler cooling allows for the cooling of the magnetron motion through the laser-cooled modified-cyclotron motion. The radial motional equations of the ion are

$$\ddot{x} - \omega_c \dot{y} - \gamma_v \dot{x} - \frac{1}{2}\omega_z^2 x + \kappa x \cos(\omega_{\text{quad}} t + \theta_{\text{quad}}) = 0, \tag{2.29a}$$

$$\ddot{y} + \omega_c \dot{x} - \frac{1}{2}\omega_z^2 y - \kappa y \cos(\omega_{\text{quad}} t + \theta_{\text{quad}}) = 0, \tag{2.29b}$$

where $\kappa = (q/m)\,\alpha_u V_{\text{quad}}/d_u^2$. V_{quad} is the quadrupolar excitation voltage, d_u the distance between electrodes with the same polarity, and $\alpha_u = E_{\text{quad}} d_u / V_{\text{quad}}$ is the surface correction factor, with E_u the electric field at the trap centre in the direction u created by V_{quad}. The dynamics of this system has been studied in Refs. [13] and [76] for a (linear) friction force originating from collisions buffer-gas atoms and laser cooling, respectively. For the case of strong ($\kappa \gg \omega_c \gamma_v$) and

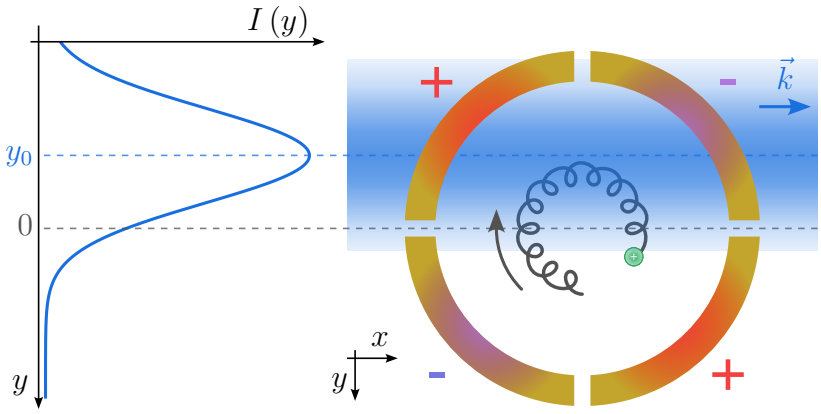

Figure 2.3. Scheme of Doppler cooling of the radial motion in a Penning trap. The spatial offset y_0 must prompt the photon absorption when the ion's magnetron motion (larger orbit in this figure) has the same direction as the laser wave vector. The Gaussian intensity profile is plotted on the left side. The polarity of a radially-segmented electrode that creates the quadrupolar field used in axialization is also illustrated.

resonant driving ($\omega_{\text{quad}} = \omega_c$), the amplitudes of the radial motion evolve with time as

$$\rho_{\pm}(t) = e^{-\gamma_v t}\left[\rho_{\pm}(0)\cos(\omega_B t) \mp \frac{i}{2}\frac{\rho_{\pm}(0)\,\gamma_v\omega_c + \rho_{\mp}(0)\,\kappa e^{\pm i\Delta\theta}}{\omega_1\omega_B}\sin(\omega_B t)\right], \quad (2.30)$$

where $\omega_B = \sqrt{\kappa^2 - \gamma_v^2\omega_c^2}/2\omega_1$ is the beat frequency between the modified-cyclotron and the magnetron motions and $\Delta\theta = \theta_{\text{quad}} - (\theta_+ - \theta_-)$. The amplitude of both motions is reduced at the same rate γ_v. The final stage of cooling is dominated by spontaneous emission, not taken into account in Eq. (2.29). The effect of the quadrupolar field is to homogenize the population in the two motions so that $\langle n_+\rangle \approx \langle n_-\rangle$ [77].

2.2.2 Calcium as optical detector

Calcium has six stable isotopes, namely, $A = 40, 42, 43, 44, 46, 48$. All of them except ^{43}Ca have zero nuclear spin, so they lack of hyperfine structure. In its singly ionized form, calcium (and the other alkaline-earth metals) has only one valence electron in the $4s$ shell.

Figure 2.4 shows the five lower-energy levels of the calcium even isotopes. For a 7-T magnetic field, the spin-orbit interaction still dominates over the effect of the external magnetic field. The otherwise degenerated fine-structure levels of total angular momentum $\vec{J}$ split into the magnetic quantum number M_J. The energy shifts were calculated using perturbation theory in M. J. Gutiérrez's thesis [65]. Up to the third order in the perturbation series is necessary to determine the energy shift with uncertainties below the lasers' linewidth. The second-order perturbation

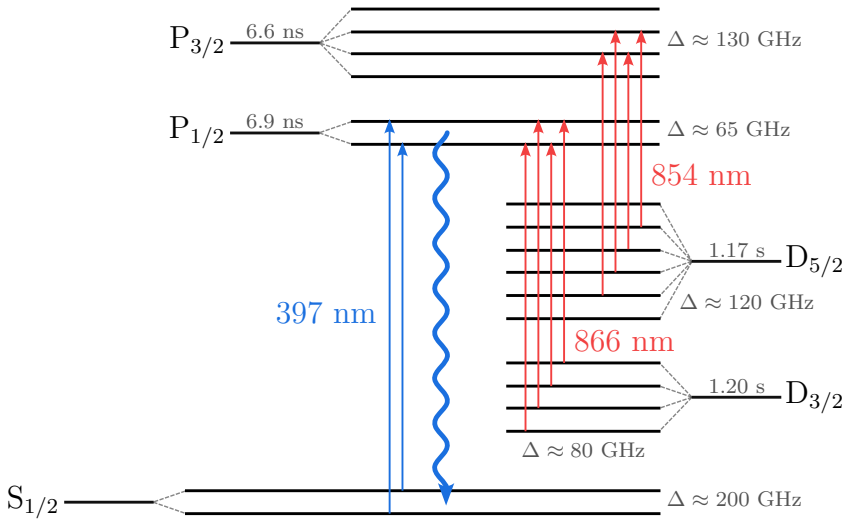

Figure 2.4. Atomic structure and relevant transitions of calcium even isotopes in the 7-T magnetic field. Δ denotes the order of the Zeeman splitting, which is asymmetric at gigahertz level in most cases [65]. The branching ratios for the decay of $3p^6 4p\,^2\mathrm{P}_{1/2}$ to $3p^6 4s\,^2\mathrm{S}_{1/2}$ and $3p^6 3d\,^2\mathrm{D}_{3/2}$ are 0.935 65(7) and 0.064 35(7), respectively [78]. The branching ratio for the decay to $3p^6 3d\,^2\mathrm{D}_{5/2}$ at 7 T is $\approx 1/50\,000$ [65, 79]. The lifetimes are taken from Refs. [80–82].

term predicts the coupling between levels of equal total angular momentum, breaking the weak-field approximation. In particular, the so-called J-mixing between $3p^6 3d\,^2\mathrm{D}_{3/2}$ and $3p^6 3d\,^2\mathrm{D}_{5/2}$ leads to a measurable population transfer between these states for $|M_J| \leq 3/2$ [79].

Table 2.1 provides a summary of the wavelength, linewidth and saturation parameter for the transitions shown in Fig. 2.4 in the absence of magnetic field. The frequency shifts due to the Zeeman effect in terms of the magnetic field strength can be found in Ref. [65]. The dipole transition $3p^6 4s\,^2\mathrm{S}_{1/2} \Leftrightarrow 3p^6 4p\,^2\mathrm{P}_{1/2}$ is used for Doppler cooling and fluorescence detection of 397-nm photons. The non-negligible probability of decaying into $3p^6 3d\,^2\mathrm{D}_{3/2}$ and the long decaying time from this

Table 2.1. Frequency ($\omega_{ge}/2\pi$), linewidth ($\Gamma/2\pi$) and saturation intensity (I_{sat}) of the transitions involved in Doppler cooling of $^{40}\mathrm{Ca}^+$. The saturation intensity has been calculated using Eq. (2.25). The 397-nm and 866-nm shifts for the rest of the stable even isotopes can be found in Ref. [83] and the 854-nm shifts in Ref. [84]. For an extensive review of the isotope shifts in singly-ionized calcium, see Ref. [85].

	$\omega_{ge}/2\pi$ (THz)	$\Gamma/2\pi$ (MHz)	I_{sat} (μW/mm^2)
$\mathrm{S}_{1/2} \Leftrightarrow \mathrm{P}_{1/2}$	755.222 765 896(88) [86]	21.57(8) [80]	451
$\mathrm{D}_{3/2} \Leftrightarrow \mathrm{P}_{1/2}$	346.000 234 867(96) [83]	1.482(8) [80]	2.99
$\mathrm{D}_{5/2} \Leftrightarrow \mathrm{P}_{3/2}$	350.862 882 823(82) [86, 87]	1.350(6) [88]	2.84

metastable state to the ground state (1.2 s) makes necessary to re-pump the population back to $3p^6 4p\,^2\mathrm{P}_{1/2}$ by 866-nm lasers. The J-mixing between the D-states makes also necessary to re-pump the population trapped in $3p^6 3d\,^2\mathrm{D}_{5/2}$ by 854-nm light. Although not used in this thesis work, the 729-nm quadrupole transition $3p^6 4s\,^2\mathrm{S}_{1/2} \Leftrightarrow 3p^6 3d\,^2\mathrm{D}_{5/2}$ is utilized for sideband cooling or to implement a qubit transition.

2.3 Precision measurement of the cyclotron frequency in a Penning trap: techniques in use

The techniques currently employed to determine the motional frequencies in a Penning trap can be classified into two groups, depending on whether the detection involves the loss of the particle or not. Destructive techniques usually detect the charged particle by impinging it on an electron-multiplying device, such as a microchannel plate (MCP), while in non-destructive techniques a dedicated circuit is normally attached to the trap to measure the current induced on an electrode.

Destructive techniques

The two most important destructive techniques in mass spectrometry are time-of-flight ion-cyclotron-resonance (ToF-ICR) [11,13] and phase-imaging ion-cyclotron-resonance (PI-ICR) [14]. Figure 2.5 shows the fundamentals of these two methods. In both of them, the ions' motional amplitudes are manipulated by external RF electric fields inside the Penning trap before the ejection through a magnetic-field gradient in a time-of-flight (ToF) section and detected with an MCP. In ToF-ICR, only the time between the ejection and the detection is recorded, while in PI-ICR the phase of the motion is also extracted by using a position-sensitive MCP with a delay-line anode.

In ToF-ICR, the ion is firstly excited to a particular magnetron amplitude by an electric dipolar field at ω_-. After that, an external electric quadrupolar field at variable frequency ω_{quad} is applied during a fixed time t_{exc} so that the motion partially becomes modified-cyclotron. At this point, the ion has a magnetic moment in the axial direction $\mu_z(\omega_{\mathrm{quad}})$ which is dominated by the modified-cyclotron component of the motion, since $\omega_+ \gg \omega_-$. When it is ejected and goes through the magnetic-field gradient, it experiences a force along the axial direction larger for a higher magnetic moment. This force will be maximum when $\omega_{\mathrm{quad}} = \omega_c$, i.e., for a more resonant quadrupolar field. Figure 2.5 shows a typical ToF-ICR signal, where the dip is centred around ω_c. The ToF can be calculated as

$$\mathrm{ToF}(\omega_{\mathrm{quad}}) = \int \sqrt{\frac{m}{2\left(E_0 - qV(z) - \mu_z(\omega_{\mathrm{quad}})\,B(z)\right)}}\,dz, \tag{2.31}$$

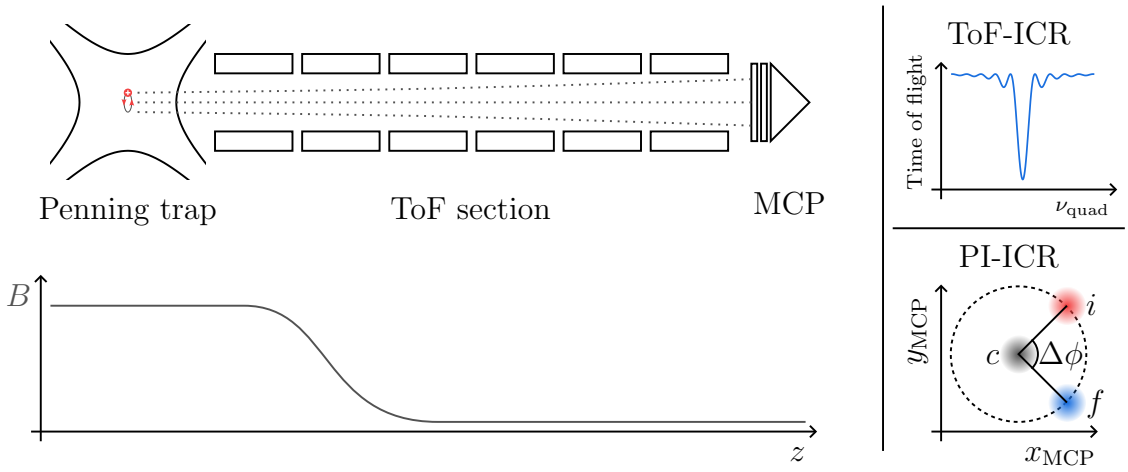

Figure 2.5. Pictorial description of mass-spectrometry techniques based on destructive detection.

where E_0 is the initial energy and $V(z)$ is the ToF-section electric potentials [13].

In PI-ICR, a radial eigenfrequency ω_u can be determined from two measurements of the motional phase [14]. If the ion is driven at a particular amplitude by an electric dipolar field and ejected straight away, it will originate a reference spot i at an angle ϕ_i on the MCP detector (see Fig. 2.5). If another ion is left to evolve for an accumulation time t_{acc} before it is ejected, the spot on the detector j will form an angle ϕ_j. The frequency ω_u can be calculated as

$$\omega_u/2\pi = \frac{N_{\text{acc}} + \Delta\phi_u/2\pi}{t_{\text{acc}}}, \tag{2.32}$$

where N_{acc} is the number of complete turns during t_{acc} and $\Delta\phi = \phi_f - \phi_i$. In this way, two spots are necessary to determine each radial eigenfrequency, and the cyclotron frequency is calculated using Eq. (2.9).

ToF-ICR routinely achieves a relative uncertainty of 10^{-8} for the usual single quadrupolar driving field, improving to the level of 10^{-9} using a Ramsey excitation scheme [89]. In the case of PI-ICR, the fact that the uncertainty is not limited by the properties of the Fourier transform but by the size of the spot makes possible to attain the 10^{-10} level [90].

Non-destructive techniques

Figure 2.6 shows a schematic of the bolometric technique [91], which relies on the detection of the image current induced by an oscillating ion on a pair of electrodes of the Penning trap,

$$I_{\text{ion}} = \alpha_u \frac{q v_u}{d_u}, \tag{2.33}$$

where v_u is the ion's velocity in the direction of detection u. The trap inherently contributes with a parasitic capacitance C_{trap} to the detection circuitry, so that

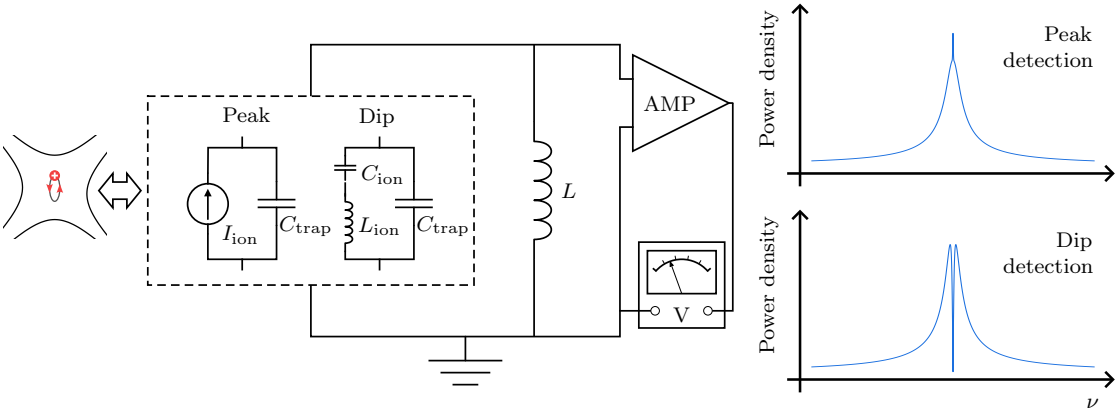

Figure 2.6. Pictorial description of mass-spectrometry techniques based on the detection of induced currents.

a proper value of the inductance L is chosen to build a parallel-LC tank circuit resonant with the ion's motional frequency ω_u. The inductance is usually provided by a superconducting coil operating at 4 K [92]. An alternative based on the use of quartz crystals at room temperature is under development, having already provided results for ion clouds [47,48]. At the resonance frequency ω_{LC}, this tuned circuit has an effective parallel resistance

$$R_p = \omega_{\text{LC}} L Q_{\text{LC}}, \tag{2.34}$$

where Q_{LC} is the quality factor, defined as the ratio between the energy stored in the resonator and the energy lost in one oscillation cycle, accounting for the parasitic resistances. The voltage drop produced by the induced current I_{ion}, $V_{\text{ion}} = R_p I_{\text{ion}}$, is usually amplified by low-noise field effect transistors. The resultant signal can be recorded by an oscilloscope or a spectrum analyser.

The effect of the ion in the Lorentzian lineshape of the resonant circuit can be seen differently depending on its relative temperature compared to the surroundings. If the ion is hotter, it acts as a current source, and its intensity is superimposed to the thermal component, therefore appearing as a peak at frequency ω_u (see Fig. 2.6). If the ion is at thermal equilibrium with the surroundings, it is excited by the thermal noise and damped by the induced current, following the dynamics of a driven damped harmonic oscillator. It can be modelled by a LC-series circuit so that the amplifier input impedance is given by

$$Z(\omega) = \left\{ \frac{1}{R_p}\left[1 + iQ_{\text{LC}}\left(\frac{\omega}{\omega_{\text{LC}}} - \frac{\omega_{\text{LC}}}{\omega}\right)\right] + \frac{1}{\frac{i}{\omega C_{\text{ion}}}\left(\frac{\omega}{\omega_u} - \frac{\omega_u}{\omega}\right)} \right\}^{-1}, \tag{2.35}$$

where $C_{\text{ion}} = \alpha_u q^2 / (m\omega_u^2 d_u^2)$. At the ion's oscillation frequency ω_u, it acts as a perfect conductor and the impedance vanishes to zero, giving rise to a dip feature

in the frequency spectrum (see Fig. 2.6) [49]. Another model based on two coupled oscillators has been recently developed in this group for experiments with quartz crystals [93].

The measurement of the dip spectrum can typically reach the 10^{-10} level of precision. Better values can be reached by phase-sensitive techniques. In pulse-and-phase (PnP) [16], the ion's amplitude is increased by a short dipolar excitation and it is then left to evolve during a certain accumulation time. The phase of the peak signal for different accumulation times is used to calculate the motional frequency in an equivalent way as in PI-ICR. Pulse-and-amplify (PnA) is a variation of PnP in which the dipolar field is partially substituted by a quadrupolar one with the aim of improving the accuracy [94]. The lowest uncertainty reached by these methods is in the order of 10^{-11} [5, 20–23, 95].

2.4 The optical method

The optical method relies on the use of a suitable ion for laser cooling as a sensor to determine the cyclotron frequency of the target ion in the Penning trap [35]. In this work, the optical method has been implemented on single ions and on a two-ion Coulomb crystal [37]. The photons scattered by an atomic electric dipole transition of the sensor ion are utilized to extract information about its motional state. For the two-ion crystal, the cyclotron frequency of the target ion in the bare magnetic field is calculated by means of the generalized invariance theorem, Eq. (2.20).

The simplest measurement protocol consists of an external dipolar electric excitation around each of the eigenfrequencies and subsequent Doppler cooling of the system. A photomultiplier tube (PMT) and an electron-multiplying charge-coupled device (EMCCD) located after a suitable optical system are used to record the fluorescence signal, as shown in Fig. 2.7. If the PMT is set to read from the time t_i, just after the excitation is switched off and laser cooling is turned on, until t_f, it will register a number of counts N_{PMT} given by

$$N_{\mathrm{PMT}} = \int_{t_i}^{t_f} R_{sc}\left(\vec{r},\vec{v}\right)\, dt, \tag{2.36}$$

where R_{sc} is the scattering rate given by Eq. (2.22). The ion's position $\vec{r}\,(t)$ and velocity $\vec{v}\,(t)$ can be obtained by solving the corresponding differential equations for the two-ion crystal, including the damping effect of Doppler cooling and axialization. During the same time interval, the EMCCD provides spatial resolution of the photon distribution. In particular, the recorded 2D photon array corresponds to the convolution of the spatial probability density function in the plane rz while the ion is being cooled, $\mathscr{P}\left(r,z\right)$, and the point spread function (PSF) of the optical system,

$$N_{\mathrm{EMCCD}}\left(r,z\right) = \mathscr{P}\left(r,z\right) * \mathrm{PSF}\left(r,z\right). \tag{2.37}$$

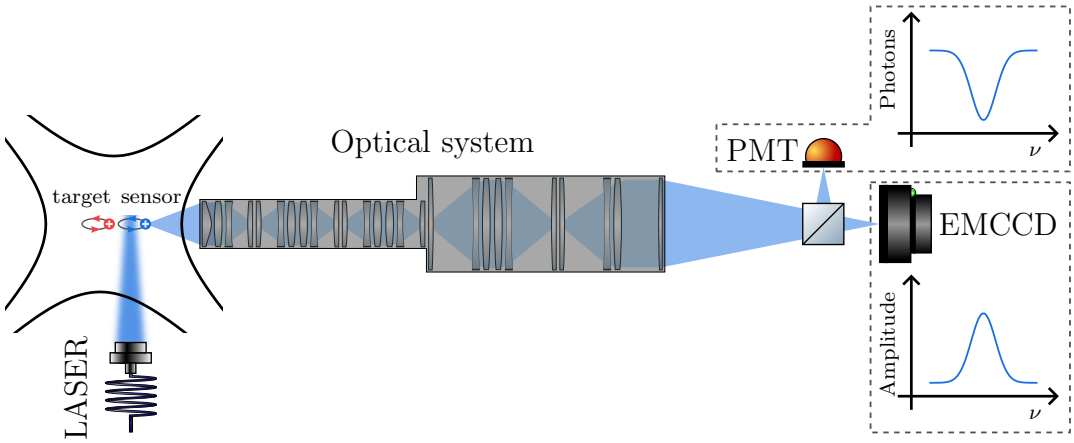

Figure 2.7. Pictorial description of the motional-frequency measurement using the optical method.

The registered photons N_{PMT} and $N_{\mathrm{EMCCD}}(r,z)$ do not present a trivial functional dependence on the external excitation frequency. In general terms, a resonant excitation will lead to a drop in N_{PMT} due to Doppler broadening, while the corresponding projection (r or z) in $N_{\mathrm{EMCCD}}(r,z)$ will become wider due to the increase of the ion's amplitude. A more detailed discussion of the particular parameters of this experiment is given in Sec. 5.1.

Compared with the destructive techniques presented in Sec. 2.3, the optical method has the advantage of demanding only one ion to measure the mass of the target specie. Laser cooling also allows the ion to be prepared at a much lower temperature, in contrast to the combination of buffer gas cooling and electric centring fields used in ToF-ICR and PI-ICR (amplitudes below the micron compared to about 90 μm in PI-ICR) [96]. This means lower motional amplitudes are required, which translates into lower systematic shifts for equivalent trapping fields.

The main advantage of the optical method compared with induced-current techniques comes from its universality. The resonant detection scheme used in the latter restricts the range of frequencies accessible. This can be partly overcome by tuning the trap parameters and/or by charge breeding to compensate for the frequency decrease when addressing heavy masses. Another benefit is laser cooling, which decreases the cooling time compared to resistive cooling and reduces the detectable ion's amplitude due to a lower initial temperature in the order of 1 mK compared to 4 K.

The main theoretical limitation of the optical method when the two ions are in the same trap has to do with the amplitude-dependent frequency shifts caused by the highly non-harmonic Coulomb interaction. If the generalized invariance theorem is applied to the six frequencies measured at arbitrary amplitudes, systematic shifts in the order of 10^{-7} per phonon are predicted [37]. This requires a full characterization of the amplitude dependence for the determination of the zero-amplitude eigenfrequencies. The latter is envisaged by implementing the op-

tical method in the quantum regime [38]. In the ground state of motion, the amplitude-dependent shifts due to the non-harmonic Coulomb potential will be highly reduced, and the application of an external field will lead to an increase in the phonon number that can be read out by means of the electron-shelving technique [97].

Chapter 3

Experimental setup

This chapter is devoted to the description of the Penning-trap beamline at the Ion Traps and Lasers Laboratory in Granada. An important part of this was built during J. M. Cornejo's thesis [64]. Several modifications and new implementations have been carried out within the thesis work presented in this manuscript: new ion sources, the improvement of the vacuum conditions, the laser system and beam access for Doppler cooling in all directions, and a new optical system for fluorescence detection. The latter is an important part of this thesis and a key aspect to detect single ions in the Penning trap. Besides this, the Penning-trap control system based on ARTIQ (Advanced Real-Time Infrastructure for Quantum physics), the development of which started during M. J. Gutiérrez's thesis [65], is also presented, focusing on the contributions made during this work.

3.1 The Penning-trap beamline

A three-dimensional computer-assisted drawing (CAD) of the Penning-trap beamline [98] is shown in Fig. 3.1. The 7-T superconducting magnet accommodates two Penning traps: the preparation trap (PT) and the measurement trap (MT). On the left side (upstream), a Paul-trap and a laser-ablation ion sources are located. The ions are guided from these sources to the traps through a transfer section. On the right side (downstream), a time-of-flight (ToF) section can be used to detect ions using a movable microchannel plate (MCP). The optical elements used for laser-beam preparation and the photon detectors are located behind the ToF section, outside the vacuum system.

The superconducting magnet[1] was energized in October 2012 and has been continuously running since then, being periodically refilled with cryogens (liquid helium and nitrogen). It has two 1-cm^3 regions of high homogeneity located 20 cm apart and centred in the bore, where the PT ($\Delta B/B < 10$ ppm) and the MT ($\Delta B/B \approx 0.1$ ppm) are placed. A detailed description of the magnet's specifications and its commissioning can be found in Ref. [64]. This magnet was replaced

[1] Agilent^{TM} 7T/160MM AS

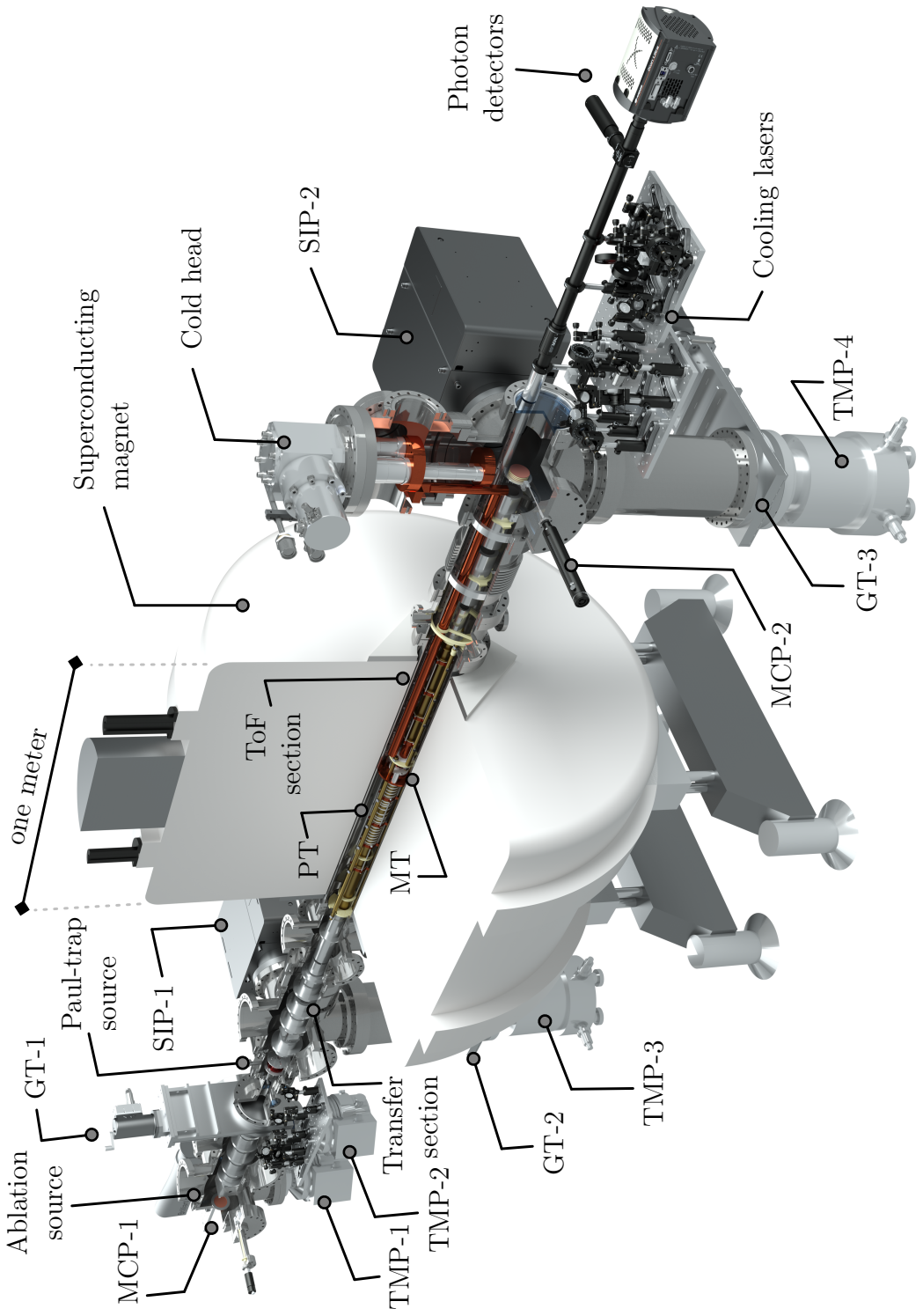

Figure 3.1. Three-dimensional technical drawing of the Penning-trap beamline. MCP: microchannel plate. GT: gate valve. TMP: turbo-molecular pump. SIP: sputter ion pump. PT: preparation trap. MT: measurement trap.

by a new cryogen-free superconducting one[2] in December 2022. The new magnet features one region with a field homogeneity of 0.1 ppm in a $15 \times 15 \times 15$ mm^3 cube and 2 ppm in a $15 \times 15 \times 60$ mm^3 parallelepiped, both centred in the magnet's bore. A new support assembly based on two U-shaped customized optical tables placed at both sides of the magnet has been designed to hold the whole beamline. Such a system includes a rail configuration that facilitates the maintenance operations in the whole Penning-trap beamline and minimizes the relative misalignment between the beam-access optics (mounted before in an independent optical table) and the MT.

DC potentials provided by high voltage (HV) power supplies[3] are used to guide the ions across the transfer section through Einzel lenses, steerers, and benders. The transmission values are optimized by measuring the counts detected on the MCP[4] located at the end of the beamline. The whole system is operated under ultra-high vacuum (UHV) conditions. To accomplish that, different types of pumps are used: turbo-molecular pumps (TMPs) backed by scroll pumps, sputter ion pumps (SIPs), and a customized cryopump. Further details about the vacuum system are given in Sec. 3.2.

The PT is a cylindrical Penning trap [64, 99] designed under the guidelines of the MATS experiment [100] that has been devoted to cool and purify samples from external ion sources. The MT is separated from the PT by a diaphragm with 2 mm in diameter and 23 mm in length. Further information about the design and a comparison with other Penning-trap geometries can be found in Ref. [65].

Figure 3.2 shows the MT. All the measurements presented in this manuscript were performed using this trap, so it is referred to as the Penning trap (or simply the trap) from Sec. 3.1.1 onwards. It consists of two symmetric sets of four concentric rings, and the electrodes are made of oxygen-free high conductivity (OFHC) copper and electrically separated by polyether ether ketone (PEEK) insulators. A new version of the MT made of gold-plated OFHC electrodes and sapphire insulators has been designed during this work. The new prototype, which improves mechanical stability, is planned to operate at cryogenic temperatures and will be installed in the Penning-trap beamline in the medium-term future. Further details can be found in Appendix A.

A two-dimensional cut of MT's open geometry is shown on the right side of Fig. 3.2. The harmonic electric field is generated using the electrodes EC, CE, and RE. It has been found both by simulations [65] and through induced-current measurements that the ratio $(V_{\mathrm{CE}} - V_{\mathrm{RE}})/(V_{\mathrm{EC}} - V_{\mathrm{RE}}) = 0.60\,(1)$ makes the field quadrupolar. The potential applied to RE is used to adapt the trap voltage to the energy of the incoming ions. A four-fold segmentation of RE allows for the application of external RF fields in dipolar or quadrupolar configurations. The DC

[2]Scientific Magnetics 7T240
[3]CAEN 1733N & N1470
[4]TOPAG Lasertechnik MCP-25-10

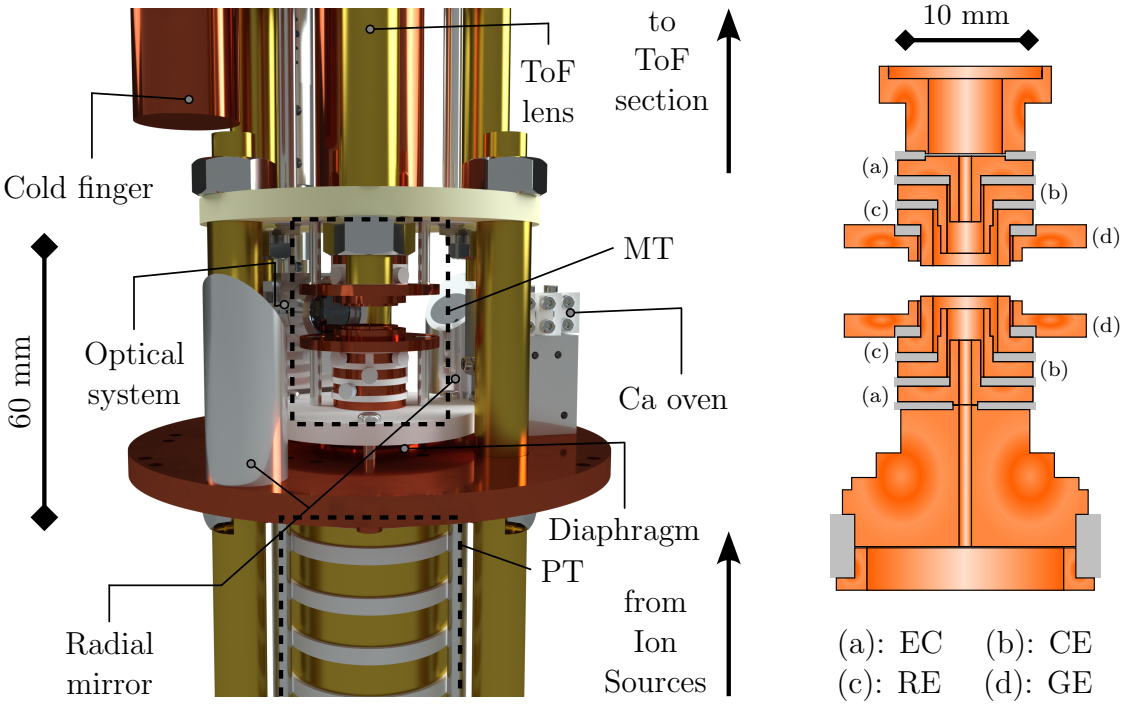

Figure 3.2. The measurement trap. Left: rendered drawing of the MT region within the beamline. Part of the last PT electrode (below) and part of the first ToF lens (above) are shown for completeness. Right: longitudinal section showing the open-ring geometry. EC: end cap. CE: correction electrode. RE: ring electrode. GE: ground electrode.

potential for the MT electrodes is supplied by a high-precision HV power supply[5]. Electrical switches[6] are used both to capture externally-produced ions and to eject unwanted ions.

The open-ring geometry features optical access in the axial and radial directions. In the case of radial access, two right-angle mirrors are used to allow the incoming beam to pass through the trap centre. The fluorescence emitted by the ion(s) is collected radially. The beginning of the optical system, with the first lens placed 22 mm apart from the trap centre (2.1 % collecting efficiency), is indicated in Fig. 3.2. It magnifies and translates the axial and radial projections from the trap centre to the detection systems, located outside the vacuum system (see Fig. 3.1).

The ions can be produced internally or using external sources. The internal source is shown in Fig. 3.2, and it consists of a calcium metal vapour sample that delivers calcium atoms by sublimation when heated by Joule effect (intensity within 3 - 5 A typically). The ionization is carried out through a two-step

[5]Stahl Electronics HV 200-16
[6]Stahl Electronics HS-200

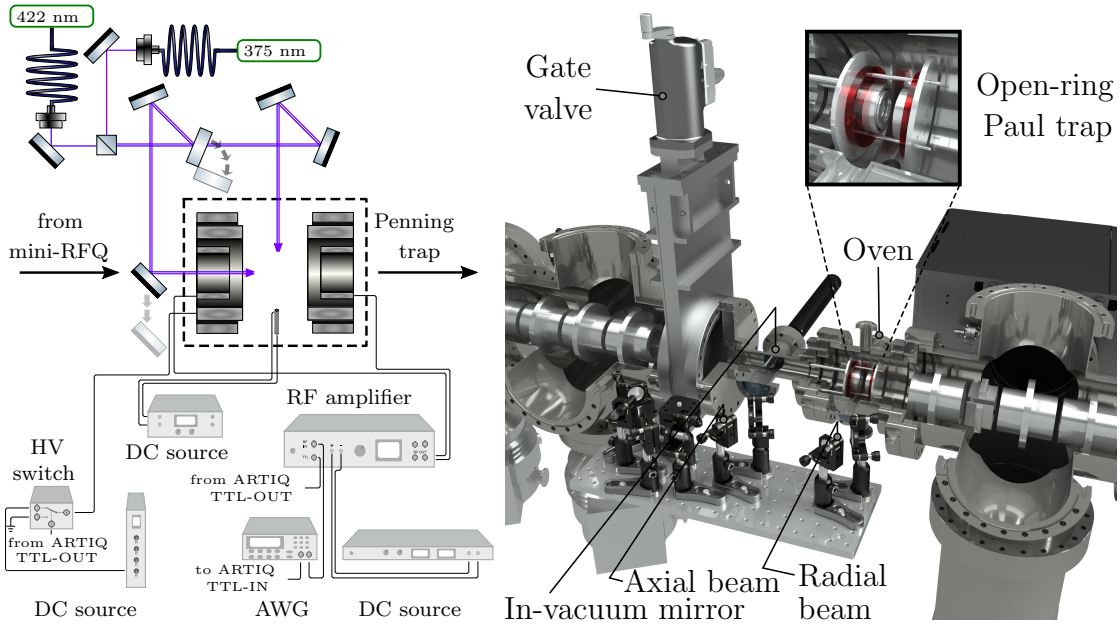

Figure 3.3. The Paul-trap ion source. Left: schematic including the photoionization beams and the power supplies. Right: realistic drawing of the ion source in the beamline.

resonant process [101]. A tunable 422-nm laser[7] is used to excite the transition $3p^6 4s^2\,{}^1\mathrm{S}_0 \Leftrightarrow 3p^6 4s4p\,{}^1\mathrm{P}_1$ and a free-running 375-nm laser[8] is used to move the excited electron to the continuum. Both laser beams are overlapped using a polarizing beam splitter (PBS).

The internal source was used for the first laser-cooling experiments since it provides slow calcium atoms (kinetic energy below 100 meV) that can be cooled within times well below 1 s. However, its operation at hundreds of degrees Celsius close to the MT increases the background pressure. Thus external ion sources, described in the following section, had to be developed.

3.1.1 Ion sources

Two ion sources have been developed and characterized during this thesis work. A Paul-trap ion source, placed close to the magnet (see Fig. 3.1), is used to provide calcium ions with high reproducibility in the loading process. A laser-ablation ion source is placed at the beginning of the beamline and can provide any kind of ion.

Figure 3.3 shows the Paul-trap ion source. It has the same open-ring geometry as the Penning trap, which allows for the injection of ions produced upstream in the beamline, e.g., by the laser-ablation source. This trap was used before in an independent setup to test the open-ring geometry in laser-cooling experi-

[7] Toptica DL pro
[8] Toptica iBeam smart

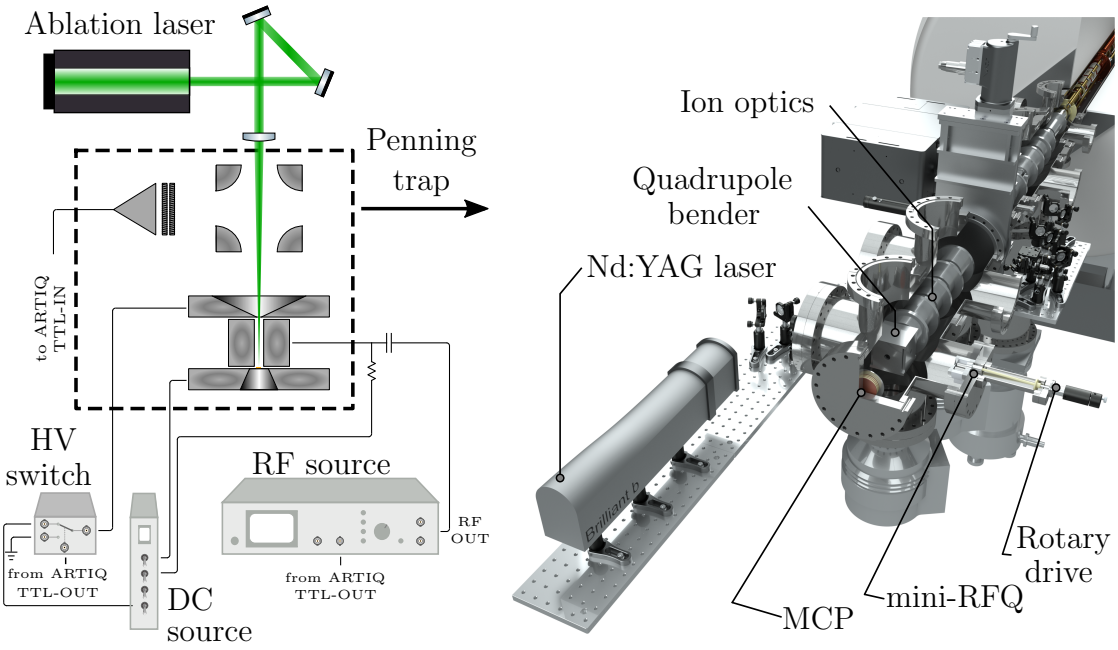

Figure 3.4. The laser-ablation ion source. Left: schematic including the ablation laser and the power supplies. Right: realistic drawing of the ion source in the beamline.

ments [66]. The RF field is applied to the inner electrodes. The signal from an arbitrary waveform generator[9] (AWG) feeds a non-resonant amplifier[10] to generate the RF voltage, the amplitude of which is provided by a DC source[11]. The typical operating values are $\nu_{\mathrm{RF}} = 600$ kHz and $V_{\mathrm{RF}} = 225\ \mathrm{V_{pp}}$, which correspond to Mathieu parameters [61, 62] of $q_{\mathrm{r}} = 0.243$ and $q_{\mathrm{z}} = 0.485$.

The ions are produced by photoionization. The overlapped laser beams can be directed axially, using a movable in-vacuum right-angle mirror, or radially. The first case is simpler and more efficient since there is no Doppler effect, but only the second configuration allows for the simultaneous operation of the two ion sources.

The RF trap can confine and accumulate calcium ions for several seconds before it saturates. The extraction takes place when a HV pulse is applied to the middle electrode on the upstream side of the trap. The HV pulse is provided by a general-purpose power supply[12], and the HV switch[13] features rising times below 1 μs. The TTLs triggering the extraction can be locked to the RF phase by feeding the control system with the AWG's synchronization signal. This makes the characteristics of the extraction similar between different cycles.

Figure 3.4 shows the laser-ablation ion source. It is based on the miniature

[9] Agilent 33210A
[10] Stahl Electronics HF-D 200 A
[11] Agilent N5752
[12] CAEN N1471
[13] BEHLKE HTS 151-01

Table 3.1. Specifications of the vacuum pumps shown in Fig. 3.1. TMP-1 and TMP-2 are both backed by an Edwards nXDS15i dry scroll pump. TMP-3 and TMP-4 are backed each by an Edwards XDS35i dry scroll pump. The pumping speeds are specified for N_2.

Pump	Manufacturer	Model	Speed (l/s)
TMP-1	Pfeiffer	HiPace 300	260
TMP-2	Edwards	STP-451 DN100CF	480
TMP-3/4	Edwards	STP 803C DN160CF	800
SIP-1	Gamma Vacuum	300 TV	300
SIP-2	Gamma Vacuum	600 TV	600

radio-frequency quadrupole (mini-RFQ) operating at SHIPTRAP [102]. The ions are produced directly by irradiating a solid sample with 532-nm pulsed laser light provided by a frequency-doubled Nd:YAG laser[14]. The pulse duration is 4 ns and the energy can be up to 300 mJ, with a repetition rate of 10 Hz. The discharge lamp's synchronization signal is used to trigger the control system when this ion source is used (see Sec. 3.5 for further details).

The targets are placed on a metallic plate biased to a certain voltage. This plate is attached to a rotary drive so that the target can be exchanged without breaking the vacuum. The system can be operated as an ion buncher if buffer-gas cooling is added and an RF field is applied[15] to the mini-RFQ so that the ions can be confined radially. A quadrupole bender is used either for introducing the ions in the beamline or for detection using an MCP.

3.2 Vacuum system

The specifications of the vacuum pumps shown in Fig. 3.1 are detailed in Tab. 3.1. Both TMPs and SIPs are used in a complementary way to reach the UHV regime. The Penning-trap vacuum system can be completely isolated from the outside and also from the laser-ablation ion source by closing gate valves[16]. The pressure is measured both using the SIPs themselves and two dedicated active ion gauges[17] (AIGs) located just above TMP-3 and TMP-4. A residual gas analyser[18] (RGA) can also be used to monitor the pressure and quantify the gas composition. The forepressure between the primary pump and the TMP is measured using a Pirani gauge[19].

[14] Litron Nano S 150-10
[15] Stahl Electronics HF-DR
[16] VAT UHV Gate Valve
[17] Edwards AIGX-S-DN40CF
[18] Leybold LEYSPEC view 100S
[19] Edwards APG100-XLS

Employing these pumps, pressures in the order of 10^{-9} mbar at the AIGs and several parts in 10^{-10} mbar at the SIPs were reached. However, a still-short ion's half-life (in the order of 30 s) motivated the investigation of the vacuum system performance. Simulations using Molflow+ [103] and the implementation of a custom cryogenic pump are detailed below.

3.2.1 Principles of vacuum simulation

The dynamics of a vacuum system strongly depends on the type of gas flow. Three main gas flow regimes can be identified for pressures ranging from atmospheric values to very low pressure [104]. The Knudsen number K_n, defined as the ratio of the mean free path l_{MFP} to the characteristic dimension of the vacuum chamber L_{pipe},

$$K_n = \frac{l_{\mathrm{MFP}}}{L_{\mathrm{pipe}}}, \tag{3.1}$$

is used to set the boundaries between the different regimes. The Penning-trap beamline operates in the so-called molecular regime, $K_n > 1$. The density is so low that the particles hardly interact with each other, behaving analogously to an ideal gas. The dynamics of the system is governed by the vessel geometry. The pumping speed S_{pump} is defined as the volumetric gas flux per unit time. The quantity of gas (at a fixed temperature) flowing across a specific cross-section per unit time is denoted by the throughput Q_{pipe}, and it can be related to S_{pump} as

$$pS_{\mathrm{pump}} = Q_{\mathrm{pipe}}, \tag{3.2}$$

where p is the equilibrium pressure. By analogy with an electrical circuit, the gas flow through a specific part of the vacuum system is controlled by the conductance C_{pipe}, a purely geometrical parameter [104]. An equivalent expression to the Ohm's law is

$$Q_{\mathrm{pipe}} = C_{\mathrm{pipe}}\,\Delta p, \tag{3.3}$$

where Q_{pipe} and the pressure difference Δp play the role of intensity and voltage drop, respectively, in an electrical circuit.

In principle, Eqs. (3.2) and (3.3) can be used to describe a vacuum system as a network of linearly connected elements, each characterized by a value of C_{pipe}. The outgassing sources are quantified by Q_{pipe}, while the vacuum pumps are described by S_{pump} (see Tab. 3.1). However, calculating the conductance for every geometry feature can already become a challenging task, and solving the corresponding linear problem for complex geometries using a standard computer might be unfeasible. Alternatively, computational tools based on the Monte Carlo method have been developed to determine pressure profiles and conductances.

Molflow+ is a software package based on the test particle Monte Carlo (TPMC) method [103]. TPMC independently calculates the trajectory of a large limited number of virtual test particles to get a picture of the system performance [105].

The geometry surfaces are represented by a series of polygons with associated physical parameters. Only one particle is simulated at a time in an event-driven way: the iteration is not over time, but over collision events, and the trajectory between wall hits is determined by ray tracing.

For each new virtual particle, the probability of choosing a certain starting point is proportional to the local particle flux $Q_{\text{pipe}}/k_B T$, with k_B the Boltzmann's constant and T the temperature, according to the ideal gas law. The particle direction probability is proportional to the cosine of the angle created with the surface normal, which is known as Knudsen's cosine law [104] and is also employed for subsequent rebounds. The determination of the velocity probability is based on the Maxwell-Boltzmann distribution [106]. All the polygons are assigned a sticking factor s_c, defined as the probability for the particle to be pumped out from the system. It is related to the pumping speed as

$$S_{\text{pump}} = \frac{1}{4} s_c \bar{v} A_{\text{pol}}, \tag{3.4}$$

where $\bar{v}$ is the mean speed of the particles and A_{pol} is the polygon's area [104].

The pressure on a specific surface is given by the orthogonal moment exchange with the particles [106]. Therefore, each polygon surface has a counter for the accumulated orthogonal momentum change $\sum I_\perp = \sum m v_\perp$, with m the particle's mass and $v_\perp$ the velocity component orthogonal to the surface. The pressure is calculated as the rate of momentum change per unit area,

$$p = \frac{1}{A_{\text{pol}}} \frac{dI_\perp}{dt} \approx \frac{1}{A_{\text{pol}}} K_{\text{MC}} \sum I_\perp, \tag{3.5}$$

where $K_{\text{MC}} = \left(dN_{\text{real}}/dt\right) / N_{\text{virtual}}$ is the ratio of the total particle flux rate to the number of virtual particles employed in the simulation [106].

3.2.2 Simulations at room temperature

Figure 3.5 shows the outcome of the vacuum simulations of the original system (without customized cryopump). A simplified version of the CAD drawing shown in Fig. 3.1 was implemented in Molflow+. The part of the beamline associated with the laser-ablation ion source (below GT-1 in Fig. 3.1) is not shown because the simulations were performed before attaching this module to the main beamline. Nevertheless, this region has a minimal effect on the trap's pressure since the CF40 tube placed just behind GT-1 strongly reduces the vacuum conductance between the two parts.

For the simulation shown in Fig. 3.5, a certain sticking factor is attributed to the pumps' inlet surface to reproduce the total pumping speed specified by the manufacturer according to Eq. (3.4). The surfaces of the vacuum chambers are simulated considering an outgassing rate per area of $3 \cdot 10^{-10}$ mbar·l/(s·cm^2) to reproduce the pressure readout at the different gauges locations. It also agrees

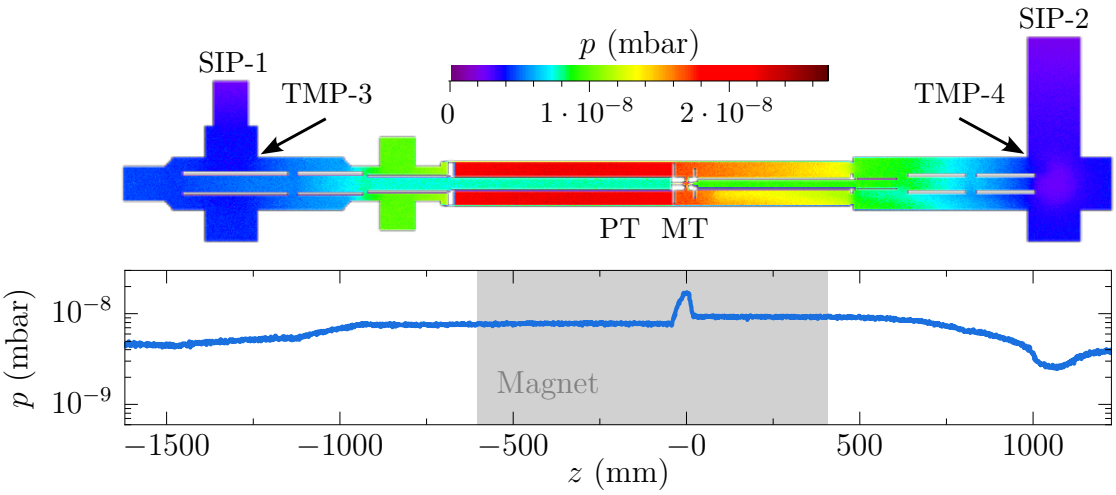

Figure 3.5. Vacuum simulations before installing the customized cryopump. The upper part corresponds to a top view of part of the system shown in Fig. 3.1, where the pump nomenclature was also explained. The electrodes and the contour of the vacuum chambers are displayed in white colour, indicating that no collisions occur. The ablation-source setup is not included. The lower part shows the pressure along the z axis, which is centred on the Penning trap and also serves for the colour map above.

with the literature values for the outgassing rate of non-baked stainless steel [107]. For the components made of copper and aluminium, the outgassing rate is set to $3 \cdot 10^{-12}$ mbar·l/(s·cm^2), according to Ref. [107].

From this simulation, the pressure in the Penning trap (MT in Fig. 3.5) was above 10^{-8} mbar, thus too high for the envisaged motional-frequency measurements. Such pressure leads to short coherence times in the ion's motion and even to the loss of the calcium ion, which can form an oxide due to the combination with oxygen background molecules. This vacuum level could not be improved with the existing TMP and SIP vacuum pumps, as they could not be moved closer to the trap due to the high-intensity magnetic field. Baking the vacuum chamber inside the bore was neither possible, so the implementation of a customized pump close to the Penning trap was found the only solution.

3.2.3 A customized cryogenic pump

Cryopumping is the action of evacuating residual gas by setting surfaces in a vacuum system at low temperatures. Two main mechanisms contribute to this [104]:

- Cryocondensation. It is the pumping mechanism due to the phase transition from gas to liquid or solid. The ultimate pressure achievable at a given temperature is the vapour pressure, i.e., the pressure exerted by the gas at equilibrium with the condensed phase.

- Cryosorption. If the surface is sufficiently cold, the gas particles impinging on it lose enough energy so that they stay attached to the surface by weak intermolecular Van der Waals forces. This mechanism can retain particles at a higher surface temperature than needed for cryocondensation. However, the sticking coefficient (Eq. (3.4)) is much lower, and only a few monolayers of particles are created.

- Cryotrapping. It refers to the possibility of employing a condensable gas to concurrently pump a non-condensable one by entrainment. The molecules of the non-condensable gas are caught and buried in the cryo-deposit of the more abundant condensable gas.

The customized cryopump consists in a one-meter long OFHC copper rod connected to the first stage of a cryocooler[20] ($T \approx 30$ K). The arrangement of the cryopump within the beamline is shown in Figs. 3.1 and 3.2. The temperature at the end of the rod, close to the trap, can be determined by assessing the system's heat load and the cryocooler's cooling power. The heat load by radiation is given by the Stefan-Boltzmann law applied to the rod,

$$dQ_{\mathrm{r}} = 4\pi\epsilon\sigma_{SB}T^4 r_{\mathrm{rod}} dx, \tag{3.6}$$

where ϵ is the surface's emissivity, σ_{SB} is the Stefan-Boltzmann constant, and r_{rod} is the rod's radius. The temperature profile along the rod can be calculated according to the Fourier's law,

$$Q_{\mathrm{c}} = k_{th}\frac{dT}{dx}, \tag{3.7}$$

where k_{th} is the rod's thermal conductivity. Combining Eqs. (3.6) and (3.7), and taking the average values of conductivity, a temperature of $T \approx 50$ K has been estimated at the end of the rod, ensuring the pumping of the residual water molecules by cryocondensation. Commercial or customized getter pumps were also considered, but discarded since the high activation temperature ($T = 400$ - 500 °C, typically) could have melted some of the plastic materials used in the setup or even caused the gold plating to diffuse into the copper.

Figure 3.6 shows the outcome from the vacuum simulations including the cryopump. A sticking factor of $s_c = 0.1$ was assigned to the cryopump. The criteria followed was again the reproducibility of the pressure measured at the gauge positions. An improvement in the pressure around the trap (MT in Fig. 3.6) by a factor of five is predicted. Experimentally, a clear increase in the typical trapping times was found: the ion always lasted for several minutes up to a few tens. Other solutions have been also worked out for the medium-term future. Further details can be found in Appendix A.

[20] Sumitomo RP-082B2

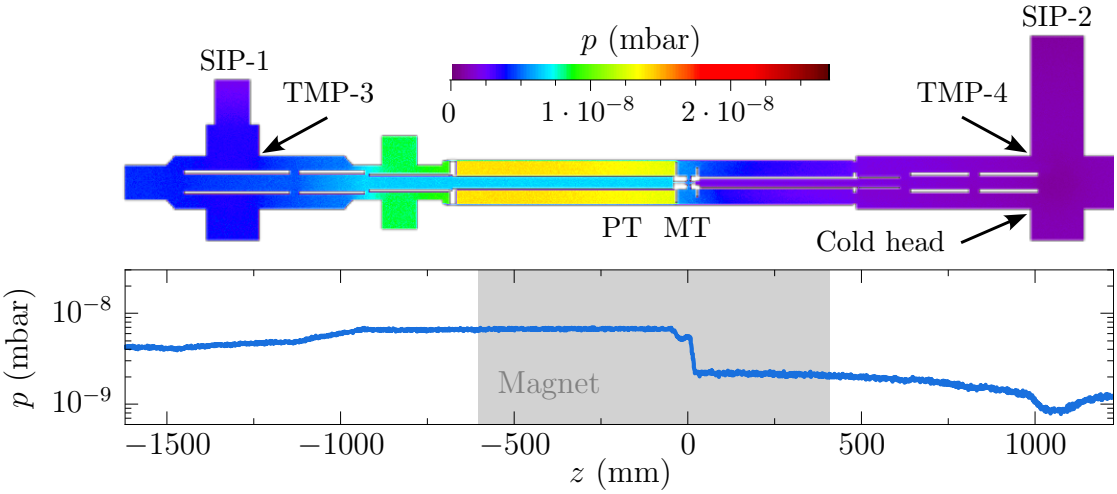

Figure 3.6. Vacuum simulations after installing the cryopump. The plot arrangement is identical to Fig. 3.5.

3.3 Laser system

The light fields required to excite the Doppler-cooling transitions are generated by diode lasers[21]. Their output power is in the order of tens of milliwatts, being possible to tune the frequency within a few nanometres with a mode-hop-free range of up to 20 GHz. As described in Sec. 2.2.2, it is necessary to address ten transitions to efficiently cool the ion to the Doppler limit in the 7-T magnetic field (see Fig. 2.4). In addition, some transitions must be addressed axially and radially to cool the three motional modes simultaneously. To meet these requirements, the laser system shown in Fig. 3.7 has been built. A total of nine tunable diode lasers are used. B1 and B2 produce the light to address one of the cooling transitions radially and axially, respectively. B3 generates the other two cooling beams. R1, R2, R3, and R4 are used to cover the four 866-nm repumping transitions. Finally, the light produced by R5 and R6 is passed through an electro-optical modulator[22] (EOM) to generate sidebands to drive the remaining four 854-nm repumping transitions [65].

All the lasers are regulated in frequency within 10 MHz absolute accuracy (according to 3σ criterion). 10% of the emitted power is fed into a wavelength meter[23] (WLM) via an optical switch (OSW) that allows for the sequential measurement of several lasers at the same time. The WLM is calibrated using a helium-neon (He:Ne) laser[24]. A proportional-integral-derivative (PID) algorithm is used to calculate the necessary output voltage delivered by a digital-to-analog card (DAC) PC board to be applied to the laser's piezo. Due to its limited reso-

[21] Toptica DL and DL pro
[22] EOSPACE PM-AV5-40-PFA-PFA-900
[23] HighFinesse WSU-10 (WLM-1) & WS8-10 (WLM-2)
[24] Sios SL 04

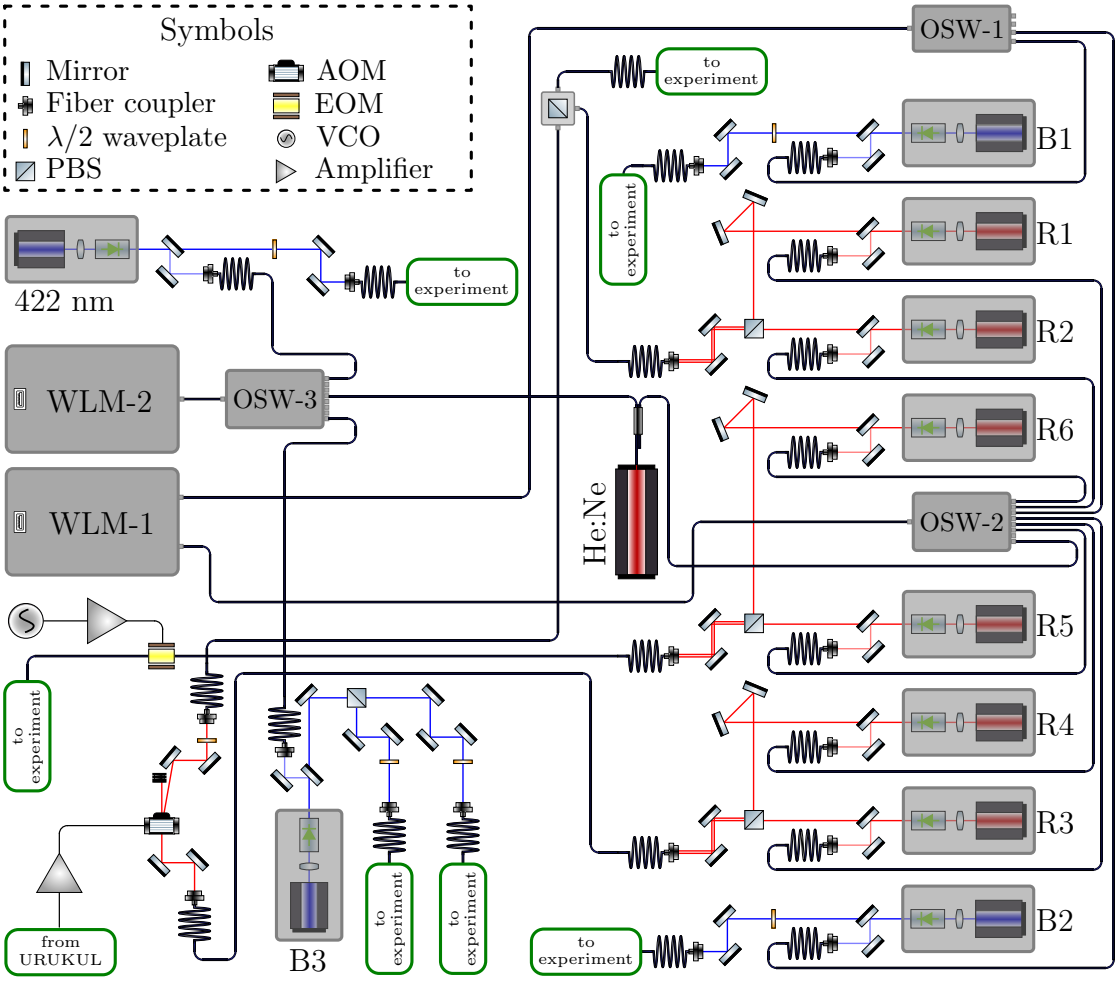

Figure 3.7. Optical table dedicated to preparing the Doppler-cooling laser beams.

lution (14 bits), a trade-off between the regulation's linewidth and range is found by inserting more or fewer voltage attenuators behind the DAC's output.

The four 397-nm light beams are transported separately to the Penning-trap setup using single-mode optical fibres. The four 866-nm beams are combined into a single fibre using PBSs and the same is done for the 854-nm laser beams. The combination of R3 and R4 laser beams is passed through an acousto-optic modulator[25] (AOM) mounted in single-pass configuration. This AOM is used to switch on and off laser cooling within 1 μs.

Figure 3.8 shows the setup devoted to the combination of the different light beams before they enter the vacuum. There are two optical tables dedicated to preparing the axial and radial beams. The former comprises all the repumping laser beams and the two cooling beams delivered by B1 and B3. A dichroic mirror is used to overlap 397- and 866-nm beams. The radial beam only contains 397-nm laser light. The beams' position in both directions can be monitored using a beam

[25] Crystal Technologies AOMO 3200-125

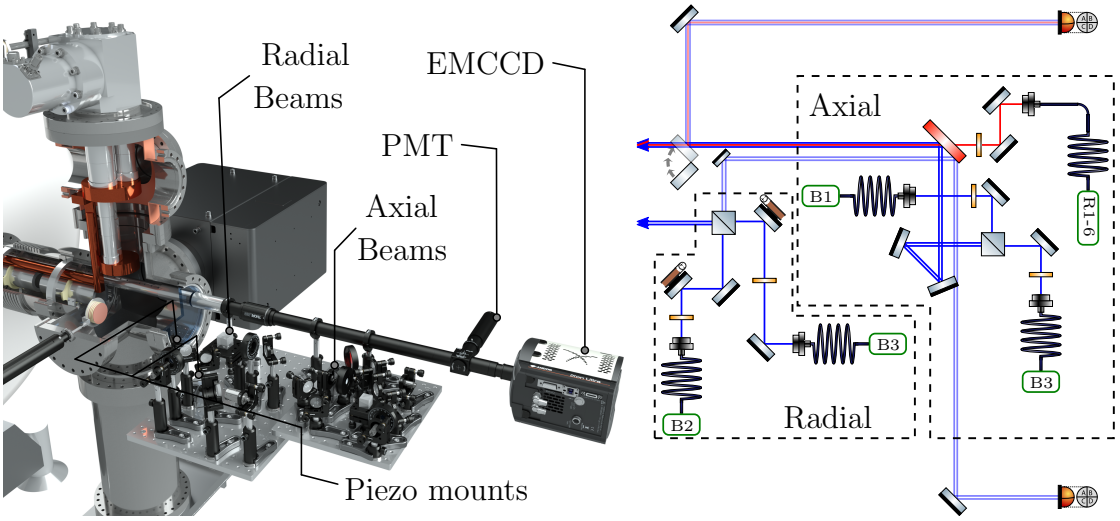

Figure 3.8. Entrance of the laser-cooling beams in the Penning-trap setup. Left: rendered drawing of the optical elements and detectors, placed at the beamline. Right: scheme showing laser-beam superposition.

profiler[26] located at the same distance as the trap centre. This sensor is used for adjusting the spot diameter and for estimating the beam displacement in the trap centre. Piezo motor-driven mirror mounts[27] are used to move the beams in the radial direction in 20-μm steps (0.001° resolution). It is operated together with the beam profiler to circumvent the piezo's hysteresis (0.01° repeatability).

3.4 Optical imaging system

A new optical system devoted to detecting individual ions and Coulomb crystals in the Penning trap has been designed, tested and successfully installed in the Penning-trap setup during this thesis work. The system magnifies the ion's photon distribution and projects it onto the detection devices: an electron-multiplying charge-coupled device[28] (EMCCD) and a photomultiplier tube[29] (PMT). These detectors complement each other in several ways. The EMCCD offers spatial resolution (1024 × 1024 pixels of 13 × 13 μm) but the processing time is in the order of only milliseconds even for regions tens-of-pixel wide. On the contrary, the PMT features sub-microsecond timing resolution but there is no position information. In the following, the necessary concepts of optical-system analysis are introduced before presenting the design guidelines and the computer simulations, to finally discuss the out-of- and in-vacuum performance of the system.

[26] Duma Beam Analyzer BA3-UV-USB
[27] Newport CONEX-AG-M100D
[28] Andor iXon Ultra 888
[29] Hamamatsu H11870-02

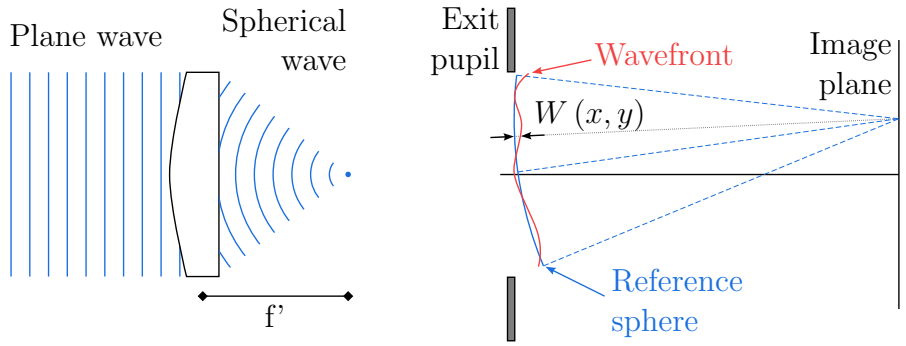

Figure 3.9. Wavefront transmittance of a single lens and the concept of wave aberration. Left: effect of a converging lens on a normally incident plane wave. Right: the graphical concept of wave aberration $W(x, y)$.

3.4.1 Principles of analysis

Image formation by an optical system can be studied at different levels of detail depending on the theory used. A simple picture is given by geometrical optics, where light propagation is described in terms of rays. However, certain optical effects such as interference or diffraction are not described in geometrical optics. The studies carried out in this section are based on the scalar diffraction theory, which describes the light field by a complex scalar potential U (complex amplitude of the electromagnetic field) and is valid for dimensions of the optical components much larger than the wavelength [108]. A brief description of the most important results of this theory can be found in Appendix B.

In a composite imaging optical system, the limiting aperture that gives rise to diffraction is called the aperture stop. The effect it has on the image can be directly analysed by applying diffraction theory to the exit pupil (image of the aperture stop formed by the part of the system which follows it), which can be modelled as a finite aperture on an infinite opaque screen [108]. The Huygens-Fresnel principle (Eq. (B.5)) states that every point on a wavefront can be regarded as the source of new spherical wavelets, and it might be applied to the exit pupil to calculate the complex scalar potential U at an observation point behind it. The Fresnel diffraction simplifies the spherical waves by parabolic ones, giving rise to

$$U(u, v) = \frac{e^{ikz}}{i\lambda z_0} \iint_{-\infty}^{+\infty} U(x, y)\, e^{i\frac{k}{2z}\left[(u-x)^2+(v-y)^2\right]}\, dx\, dy, \tag{3.8}$$

where $\{u, v\}$ and $\{x, y\}$ are the coordinates at the exit pupil and the observation point, respectively, both separated by a distance z_0. $k = 2\pi\lambda$ is the wavenumber, with λ the wavelength. The integral limits are expanded to the whole plane and U is assumed to be zero outside the exit pupil.

Apart from diffraction due to its finite size, an optical imaging system has a phase-transformation effect on the wavefront. The left side of Fig. 3.9 illustrates

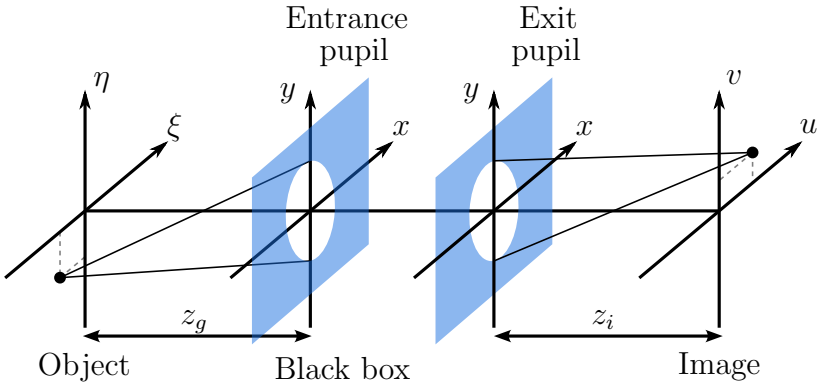

Figure 3.10. General model of an optical system as a black box. The transfer function is given by the transmittance (Eq. (3.9)) and the diffraction due to the stop aperture (Eq. (3.8)). Adapted from Ref. [109].

this for a single positive lens. The corresponding transmittance function $T(x, y)$ can be written as

$$T(x, y) = \mathcal{P}(x, y)\, e^{-i\frac{k}{2f'}\left(x^2+y^2\right)}, \tag{3.9}$$

where f' is the focal distance. $\mathcal{P}(x, y)$ is the generalized pupil function,

$$\mathcal{P}(x, y) = P(x, y)\, e^{ikW(x,y)}. \tag{3.10}$$

$P(x, y)$ is the pupil function, equal to one within the exit pupil and zero outside. $W(x, y)$ is the wave aberration, which quantifies the optical path difference between the reference sphere (ideal wavefront in the paraxial approximation) and the actual wavefront. The right side of Fig. 3.9 illustrates this concept graphically.

In general terms, an optical system can be treated as a black-box, as shown in Fig. 3.10. The evolution from the entrance pupil (image of the aperture stop formed by part of the system which precedes it [108]) to the exit pupil is given by a transmittance function (Eq. (3.9)) that captures the impact of all the optical components. Fresnel diffraction is applied on the exit pupil to account for the finite aperture stop. Given the linearity of the electromagnetic field, the image scalar field $U_i(u, v)$ produced by the optical system can be expressed in terms of the object scalar field $U_g(\xi, \eta)$ utilizing the superposition integral,

$$U_i(u, v) = \iint_{-\infty}^{+\infty} h_{\text{PSF}}(u, v; \xi, \eta)\, U_g(\xi, \eta)\; d\xi\, d\eta, \tag{3.11}$$

where $h_{\text{PSF}}(u, v; \xi, \eta)$ is the so-called point spread function (PSF) [109]. This function is analogous to the impulse response function in signal processing, describing the system's output at a point (u, v) in the image space for a Dirac-delta input at a point (ξ, η) in the object space. The point-source impulse wavefront U_{PSF} at the entrance pupil in the paraxial approximation is

$$U_{\text{PSF}}(x, y; \xi, \eta) = \frac{1}{i\lambda z_g} e^{i\frac{k}{2z_g}\left[(x-\xi)^2+(y-\eta)^2\right]}, \tag{3.12}$$

where z_g is the longitudinal distance between the object and the entrance pupil. If observation takes place on the paraxial image plane, i.e., the lens law is satisfied, the PSF can be expressed in terms of the optical-system pupil function as

$$h_{\text{PSF}}\left(u, v; \tilde{\xi}, \tilde{\eta}\right) = \frac{1}{\lambda^2 z_g z_i} \iint_{-\infty}^{+\infty} \mathcal{P}\left(x, y\right) e^{-i\frac{2\pi}{\lambda z_i}\left[\left(u-\tilde{\xi}\right)x+(v-\tilde{\eta})y\right]} dx\, dy, \tag{3.13}$$

where $\tilde{\xi} = M\xi, \tilde{\eta} = M\eta$ being M the magnification, and z_i is the distance between the exit pupil and the image plane [109]. Therefore, the PSF is precisely the Fraunhofer diffraction of the generalized pupil function [109]. Equation (3.13) also implies the space invariance of the PSF, since $h_{\text{PSF}}\left(u, v; \tilde{\xi}, \tilde{\eta}\right) \equiv h_{\text{PSF}}\left(u - \tilde{\xi}, v - \tilde{\eta}\right)$. The space-invariant PSF, $h_{\text{PSF}}\left(u, v\right)$, is the Fourier Transform of the generalized pupil function from the pupil coordinates (x, y) (at the exit pupil) to the spatial frequency coordinates $\left(\frac{u}{\lambda z_i}, \frac{v}{\lambda z_i}\right)$ (at the image plane).

In the ideal case of a non-aberrated circularly-symmetric optical system, the wave aberration W is zero, $\mathcal{P}\left(x, y\right)$ is constant over the exit pupil, and the PSF is the Airy disc [108]. In general, W can be expanded into the Zernike polynomials Z_n^m as

$$W\left(r, \phi\right) = \sum_{n} \sum_{m=-n}^{n} c_{nm} Z_n^m\left(r, \phi\right), \tag{3.14}$$

where r and ϕ are the radial distance and polar angle in spherical coordinates. The Zernike polynomials constitute a system of orthogonal polynomials in the unit circle that, for low orders, have a direct relation to the primary aberrations: defocus, astigmatism, comma, spherical, etc. They are defined as [108]

$$\begin{aligned} Z_n^m\left(r, \phi\right) &= R_n^m\left(r\right)\cos(m\phi) \quad \text{for} \quad m < 0, \\ Z_n^m\left(r, \phi\right) &= R_n^m\left(r\right)\sin(m\phi) \quad \text{for} \quad m > 0, \end{aligned} \tag{3.15}$$

where

$$R_n^m\left(r\right) = \sum_{s=0}^{\frac{n-m}{2}} (-1)^s \frac{(n-s)!}{s!\left(\frac{n+m}{2}-s\right)!\left(\frac{n-m}{2}-s\right)!} r^{n-2s}. \tag{3.16}$$

Coming back to Eq. (3.11), the image formation of an extended object will greatly depend on whether the source is coherent or incoherent. If a coherent light source is used, the system is linear in the electromagnetic field's amplitude. If the light source is incoherent, the system is linear in intensity [109]. The intensity in the image plane for the latter can be computed as

$$I_i\left(u, v\right) = \iint_{-\infty}^{+\infty} \left|h_{\text{PSF}}\left(u - \tilde{\xi}, v - \tilde{\eta}\right)\right|^2 I_g\left(\tilde{\xi}, \tilde{\eta}\right) d\tilde{\xi}\, d\tilde{\eta}. \tag{3.17}$$

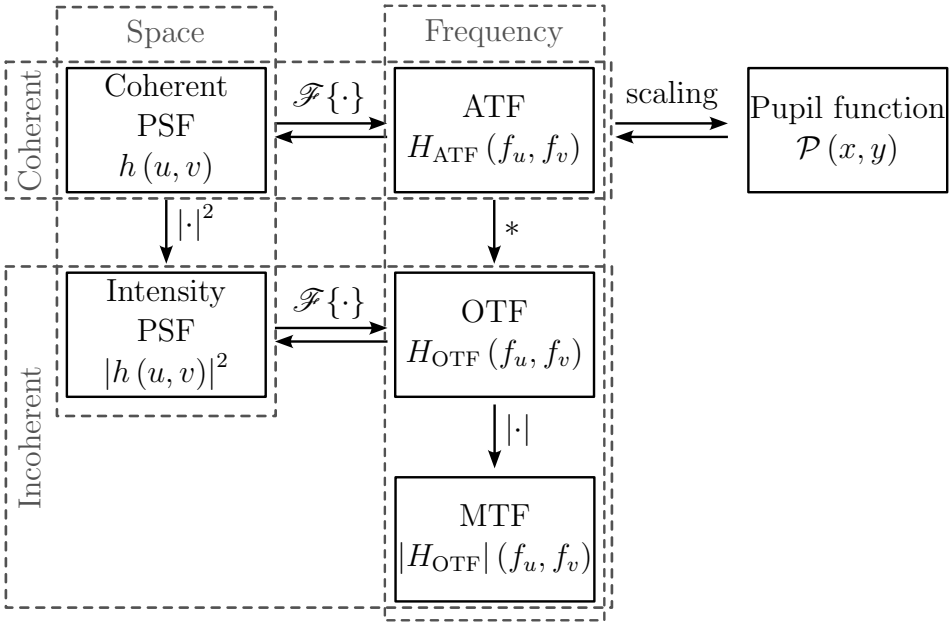

Figure 3.11. Relevant measures in Fourier optics. Note that an incoherent measure can be deduced from its coherent counterpart, but not vice versa.

Fluorescence emission by an ion Coulomb crystal is a clear example of incoherent illumination since there is no correlation between the different emission points.

The level of detail that the optical system can reproduce from an object can be quantified by studying the transmission of the spatial frequency f. The amplitude transfer function (ATF) is defined as the PSF's Fourier Transform, and it quantifies how well the system transfers spatially sinusoidal inputs at different frequencies when a coherent-light source is used. Taking into account that the PSF is a Fraunhofer diffraction pattern, it is possible to demonstrate that the ATF is proportional to the pupil function scaled with units of $\lambda z_i f$ [109]. The equivalent function for incoherent illumination is called optical transfer function (OTF),

$$H_{\mathrm{OTF}}(f_u,f_v)=\frac{\int_{-\infty}^{+\infty}\iint |h_{\mathrm{PSF}}(u,v)|^2\, e^{-i2\pi(f_u u+f_v v)}\,du\,dv}{\int_{-\infty}^{+\infty}\iint |h_{\mathrm{PSF}}(u,v)|^2\,du\,dv}. \tag{3.18}$$

Similarly to the ATF, the OTF also has a direct relation with the pupil function and can be computed as the normalized autocorrelation function of the latter. The module of the OTF is called modulation transfer function (MTF), and it provides the relative modulation of the image as a function of the input frequency. It can be demonstrated that aberrations always contribute to decreasing the MTF [109]. Figure 3.11 illustrates the connection among these optical measures. Assuming the Rayleigh criterion, an optical system can resolve the position of two points if the value of the MTF is higher than 0.2 for the corresponding spatial frequency.

3.4.2 Design and simulations

The new optical imaging system was designed with the assistance of Zemax[30]. This optical design software takes the geometrical specifications of the optical system as input and delivers multiple optical measures, such as the wave aberration (Eq. (3.10)), the PSF (Eq. (3.13)), or the OTF (Eq. (3.18)), which were used to assess whether the system's performance met the requirements imposed by the experiment.

Regarding the detection of fluorescence, the optical system had to spatially resolve the position of two laser-cooled trapped ions, which in the case of $^{40}Ca^{+}$ are separated 10 - 20 μm for typical axial frequencies in the range of 100 - 500 kHz. In addition, it had to provide enough magnification so that the two spots are a few pixels apart when projected into the EMCCD sensor (13×13 μm). The fluorescence collection efficiency had to be maximized. This is accomplished with a high numerical aperture, defined as $\mathrm{NA} = D/2f'$ with D the pupil diameter, and maximizing the transmission through the optical components for the operating wavelength, $\lambda = 397$ nm.

Regarding the Penning-trap setup, the optical system had to physically fit into the free space available inside the magnet bore. It had to magnify the axial and radial projections (optical axis perpendicular to $\vec{B}$) and collimate the image of the ion(s) downstream along the axial direction to the place where the detectors are located (see Fig. 3.1). It also had to operate under UHV conditions throughout 1.2 m, being rigidly anchored to the Penning-trap tower.

The maximum numerical aperture, limited by the ring Penning-trap geometry, is $\mathrm{NA}_{\mathrm{max}} \approx 0.29$. The use of a single spherical lens for such a value of the NA would have implied aberrations that prevent from achieving the resolution envisaged. One way to overcome this problem could have been using (spherical) lenses of different shapes and focal distances. Diffraction-limited objectives made of four lenses have been widely used for ion and optical traps. The first proposals were made in the early 2000s [110], and a comprehensive review for optical traps can be found in Ref. [111]. This type of system has also been used in Penning traps [112]. Another option was the use of a non-spherical or aspheric lens [113]. This kind of lens is flatter at its edge compared to spherical lenses, which reduces the refracting ray angle so that all the rays are brought to a common focus position [114].

For the Penning-trap optical system, commercial parts were preferred due to the high costs of custom components. The little space left inside vacuum made the use of standard 1" optics impossible, so 1/2"-diameter components were chosen for the parts inside the magnet bore. The new optical system is based on a first objective and then a series of relays. Using a single objective would have led to an intensity per pixel too low, and the system would have also been highly sensitive to misalignments since it is under vacuum and cannot be moved. The idea of reducing aberrations using an objective made of several lenses was also explored.

[30] Zemax OpticStudio® 2020

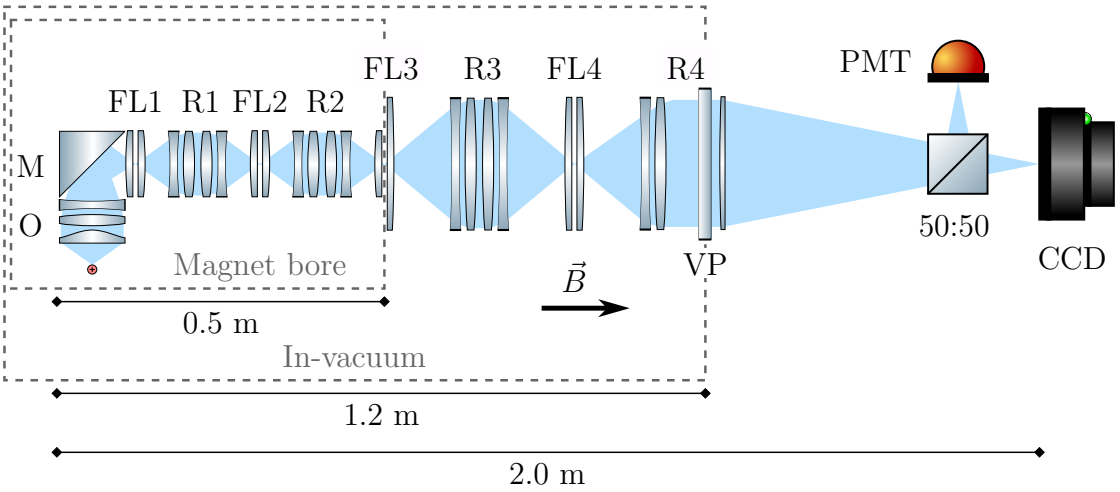

Figure 3.12. Cross-section sketch of the optical system (not-to-scale). O: objective; M: mirror; FL: field lens; R: relay; VP: viewport.

In the case of three lenses, it was possible to achieve an optimal configuration with commercial parts that fitted into the vacuum chamber, but the performance was not diffraction-limited. In the case of four lenses, the available space was not enough.

Figure 3.12 shows the final design. It consists of one objective that provides 5× and a series of relays that transport the image without magnification. The final factor 15× is achieved by adding a last single lens outside vacuum. The relays are doublets of plano-concave and bi-convex commercial lenses in which the relative distance was optimized to achieve diffraction-limited performance. The field lenses are pairs of plano-convex lenses centred on the image plane to avoid vignetting. Using a single bi-convex lens instead would perform the same but imaging imperfections might exist [115].

The objective's lenses specifications, including one of the field lenses of FL1 (see Fig. 3.12), are detailed in Tab. 3.2. The relative distances were optimized using Zemax, for which the wave aberration (see Eq. (3.10)) was used as the figure of merit to minimize. First, the asphere's focal point for $\lambda = 397$ nm was determined, giving rise to a working distance of 21.963 μm. Then, the relative distance in the doublet consisting of the bi-convex and the plano-concave lenses was optimized. The gap between the asphere and the doublet was chosen arbitrarily (5 mm in this case), and the field lens was likewise placed at a certain distance from the image plane. The effect the latter has on the image formation is minimal, and it only affects as a defocus. Finally, the optimization routine was run again for the two distances previously varied. Near on-axis diffraction-limited performance was achieved in all the cases, which was observed in the MTF (see Eq. (3.18)) or wave-aberration plots.

The specifications of the optical elements used for the relays are listed in Tab. 3.3. These parts are symmetric, so only half of the lenses are detailed. As in

Table 3.2. Objective's components and relative separation. The distance is defined between adjacent surfaces. All the lenses are commercial models from Thorlabs, Inc..

Type	Model	Separation (mm)
Object	-	21.963
Asphere	AL1225G-A	5
Bi-convex	LB1844-A	6.897
Plano-concave	LC4413-UV	84.723
Plano-convex	LA1207-A	2.5
Image	-	-

the case of the objective, one of the field lenses is included. A sequential procedure similar to the one explained for the objective's simulations was followed here. The last part of the optical system, called R4 in Fig. 3.12, consists of half of a one-inch relay plus a single lens with focal length $f' \approx 750$ mm (model LA1978-A of Thorlabs, Inc.). Although it is a simple plano-convex lens, it does not introduce further significant aberrations due to its small NA. All the lenses are made from N-BK7 or Fused Silica and have anti-reflective coating for $\lambda = 397$ nm.

Figure 3.13 shows a rendered image of the full optical system installed in the Penning-trap setup. The optical mounts are custom-designed and were machined by a local company. In general, the outer diameter is 17 mm for the half-inch components and 32 mm for the rest (the exceptions are the objective and the mounts at the magnet bore). The distance between these pieces is maintained using hollow tubes, with M14 $\times$ 0.5 mm and M27 $\times$ 0.75 mm very-fine threads to assure a good alignment. The material used is aluminium 6061-T6, employed in commercial lens tubes due to its good machining properties when it is threaded. All the pieces are perforated to pump the inner volume of the tubes. The optimal distances between lenses found in the simulations are physically defined by the

Table 3.3. Half- and one-inch relay's components and relative separation. The distance definition between elements is defined in Tab. 3.2. The lenses are commercial models from Thorlabs, Inc. (T) and Newport Corporation (N).

	Model		Separation (mm)	
Type	1”	1/2”	1”	1/2”
Object	-	-	2.5	3.75
Plano-convex	LA1207-A (T)	LA1461-A (T)	83.496	172.666
Plano-concave	LC4413-UV (T)	SPC025 (N)	7.227	14.814
Bi-convex	LB1844-A (T)	LB1676-A (T)	2.5	5
Image	-	-	-	-

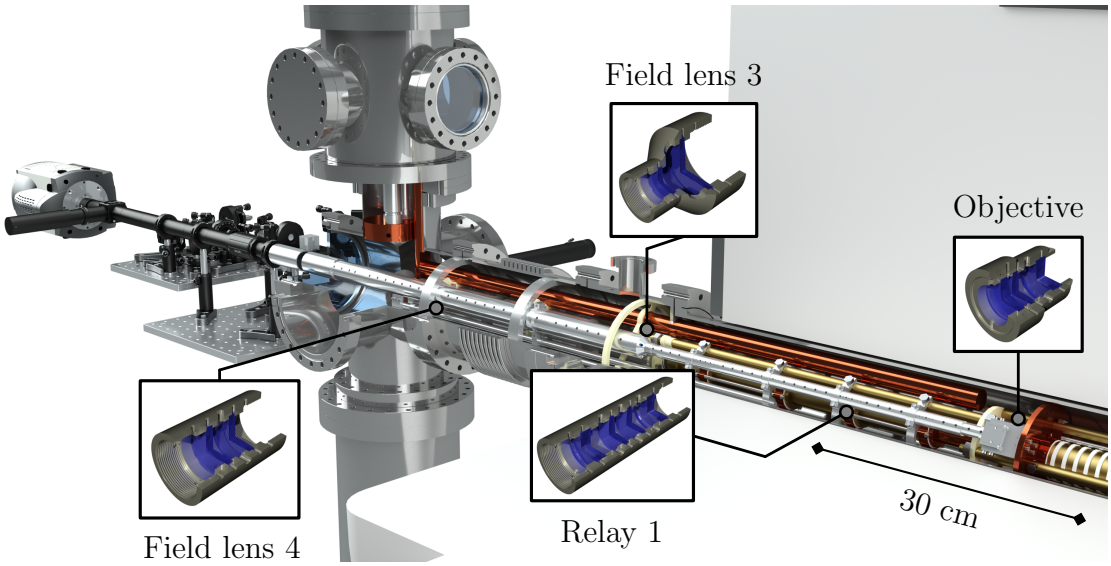

Figure 3.13. Rendered three-dimensional drawing of the optical system installed in the beamline. Several distinctive parts are zoomed in.

lens separators. These are rings with a thickness of 0.5 mm and 0.75 mm, having the shape of the corresponding spherical lens so that the contact is made on the full contour of the surface for better alignment. The optical system is attached to the Penning-trap tower at several positions inside the magnet bore (see Fig. 3.13).

Figure 3.14 shows some of the simulation results for the whole optical system. Zemax computes the optical system performance starting from the wave aberration (right side of Fig. 3.14). This function can be analytically calculated by simply knowing the shape of the lenses, listed in Tabs. 3.2 and 3.3. Then, the MTF, shown in the left part of Fig. 3.14, is calculated as the normalized autocorrelation of the pupil function (see Eqs. (3.10) and (3.18)). Although the system is diffraction-limited for on-axis performance, it cannot be moved once installed and under UHV, and thus it is important to know its off-axis performance. For that purpose, the impulse was placed at different field distances from the optical axis on the object plane. The particular line containing the object's position and the optical axis is called the tangential direction, while the perpendicular is the sagittal direction. The MTF and the root mean square (RMS) spot radius (inset) show that a position deviation of 200 μm, equivalent to a wave aberration of 1.5 λ, is the maximum affordable deviation to resolve 10 - 20 μm. In the case of the modulation, a value of 0.2 is equivalent to the Rayleigh criterion for two-point resolution.

3.4.3 Out-of-vacuum performance analysis

The optical system was experimentally tested before its installation in the Penning-trap setup. The response of the system to quadratic impulses using a 1951 USAF

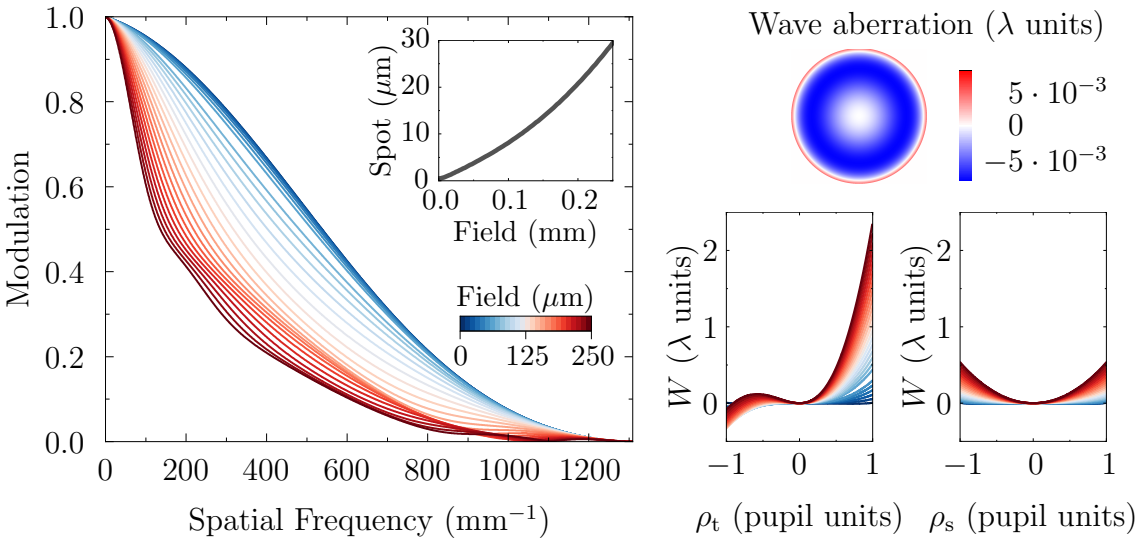

Figure 3.14. Simulation of the optical system. Left: MTF's tangential component for an object placed at different field positions and RMS spot radius (inset). The axis of abscissa represents the spatial frequency in the object plane. Top right: colour map representation of the on-axis wave aberration in wavelength units. Bottom right: tangential (left) and sagittal (right) cross sections of the wave aberration for an object placed at different field positions.

test target[31] was studied. As described on the right side of Fig. 3.15, the object, placed in the objective's focal plane, consisted of sets of two groups of three parallel bars, oriented in two perpendicular directions and separated by different distances. Measuring the maximum and minimum intensities, $I_{\max}$ and $I_{\min}$, it was possible to determine the contrast C_{opt}, defined as

$$C_{\text{opt}} = \frac{I_{\max} - I_{\min}}{I_{\max} + I_{\min}}. \tag{3.19}$$

The contrast can be considered analogous to the modulation (module of the OTF, Eq. (3.18)) for square impulses. The contrast transfer function (CTF) describes how well the system transfers square impulses of different spatial frequencies and is analogous to the MTF.

The system's performance was evaluated in two other ways based on its linear properties. If the set of square impulses is chosen as a complete and orthogonal basis, the contrast can be simply calculated as the inner product of the object and the image, both normalized to the total intensity. Another option is to work on the Fourier basis so that the convolution theorem can be applied,

$$|\mathscr{F}\{I_i\}| = |H_{\text{OTF}}| \cdot |\mathscr{F}\{I_g\}|\,, \tag{3.20}$$

[31] Thorlabs Inc. R1DS1P

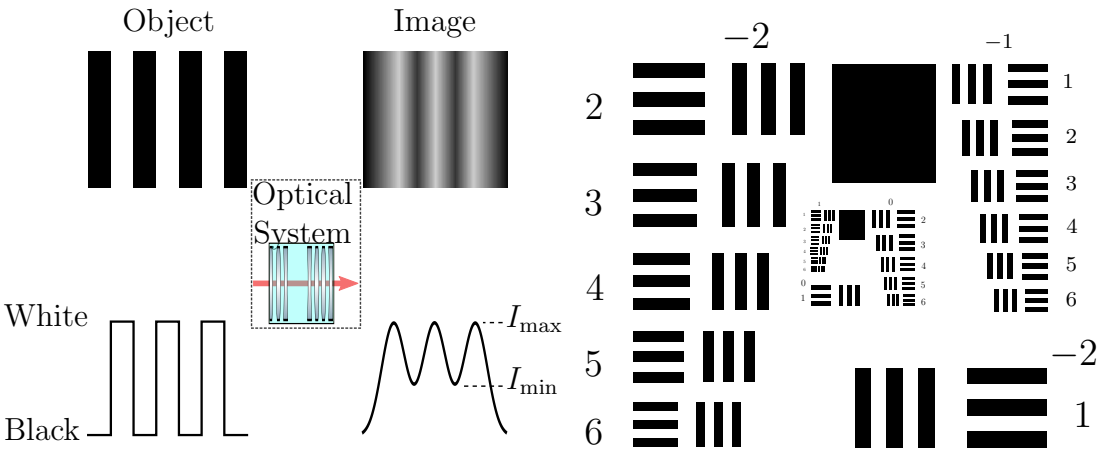

Figure 3.15. Investigation of the resolution using a square-impulse target. Left: pictorial description of the measurement of contrast of a square-impulse target. Right: 1951 USAF resolution test chart used in the experiment. Groups −2 to −1 are represented, comprising 6 elements each. The spatial frequency, in line pairs per millimetre, is calculated as $2^{\text{group}+(\text{element}-1)/6}$.

where I_g and I_i are the intensities in the object and image planes, respectively, and $|H_{\text{OTF}}|$ is the MTF. In principle, it should have been possible to fully recover the system's MTF using deconvolution techniques. However, the associated uncertainties became large for frequencies at which the object has a small component. In the case of square impulses, the frequency component is almost zero for even multiples of the fundamental frequency and maximum for odd multiples.

Figure 3.16 shows the characterization measurements for the whole optical system. For these tests, the optical system was fixed to an optical table, and the resolution target was mounted on a three-axis stage so that the region of interest could be placed at the focal point. The camera used was a scientific complementary metal–oxide–semiconductor (sCMOS) image sensor[32]. The target was illuminated with 397-nm light, and measurements were performed on groups 5, 6, and 7 of the USAF 1951 resolution target (see Fig. 3.15). The magnification obtained is 16.8(4)×. The square impulse analysis is shown on the left side of Fig. 3.16. The two types of analysis mentioned before were used and both yield similar results. The performance is close to the diffraction limit down to at least 5 μm of line separation. It was only possible to study frequencies as high as 228.1 mm^{-1} (7$^{\text{th}}$ group, 6$^{\text{th}}$ element) due to the features of the resolution target itself.

A deeper insight into higher frequencies was reached by employing the method using the deconvolution theorem to measure the system's MTF. In the analysis shown on the right side of Fig. 3.16, the fundamental frequency and the third harmonic were used, obtaining reliable results. From the relationship between the modulation and the Rayleigh criterion, the optical system is capable of resolving

[32] Andor Zyla 4.2 sCMOS

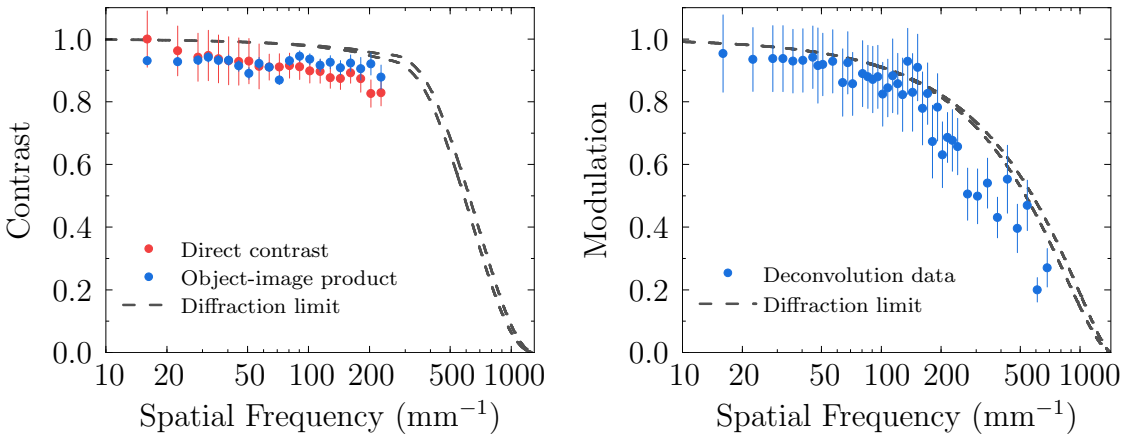

Figure 3.16. Frequency analysis of the measurements based on the 1951 USAF resolution target. Left: CTF measured directly and from the image-object product. Right: MTF calculated using the convolution theorem. The lower grey line includes the sensor (6.5 μm $\times$ 6.5 μm) frequency transmission [116]. In all the cases, the displayed data are the average of the performance for each two perpendicular bar sets of the test target (right part of Fig. 3.15).

two points separated by only 1.5 μm. Employing Eq. (3.20) for higher harmonics led to large uncertainties.

3.4.4 In-vacuum performance analysis

The final system's characterization was done using a trapped ion itself. A single trapped ion cooled to the Doppler limit is a perfect target to test the optical system's PSF. In the case of the Penning trap, the axial frequency was $\nu_z = 333$ kHz, which means a motional amplitude $z_{\max} \approx 300$ nm for $^{40}Ca^+$ at 1 mK (Doppler limit). This implies $z_{\max} < \lambda$, and the ion can be thus considered as a good approximation to a point-like source. In case the ion's temperature was higher, these results would be the worst-case scenario for the optical system performance.

The measured intensity PSF, $I_{\mathrm{PSF}} \equiv |h_{\mathrm{PSF}}|^2$, can be directly related with the Zernike polynomials through Eq. (3.13). Taking into account that Fraunhofer diffraction is a Fourier Transform,

$$I_{\mathrm{PSF}} = \left|\mathscr{F}\{e^{-ik\sum_{m,n} c_{nm} Z_n^m}\}\right|^2 . \tag{3.21}$$

Since the modulus is not a bijective function, a direct decomposition of I_{PSF} into the Zernike polynomials basis is not possible. In this sense, fitting algorithms have been developed to find the best approach [117,118]. This method has already been employed before in a Paul trap [119].

The outcome from the analysis of the ion image is shown in Fig. 3.17. The image has been rotated 131.7° here so that the trap's axial and radial axes match the page's horizontal and vertical axes, respectively. The magnification was calculated

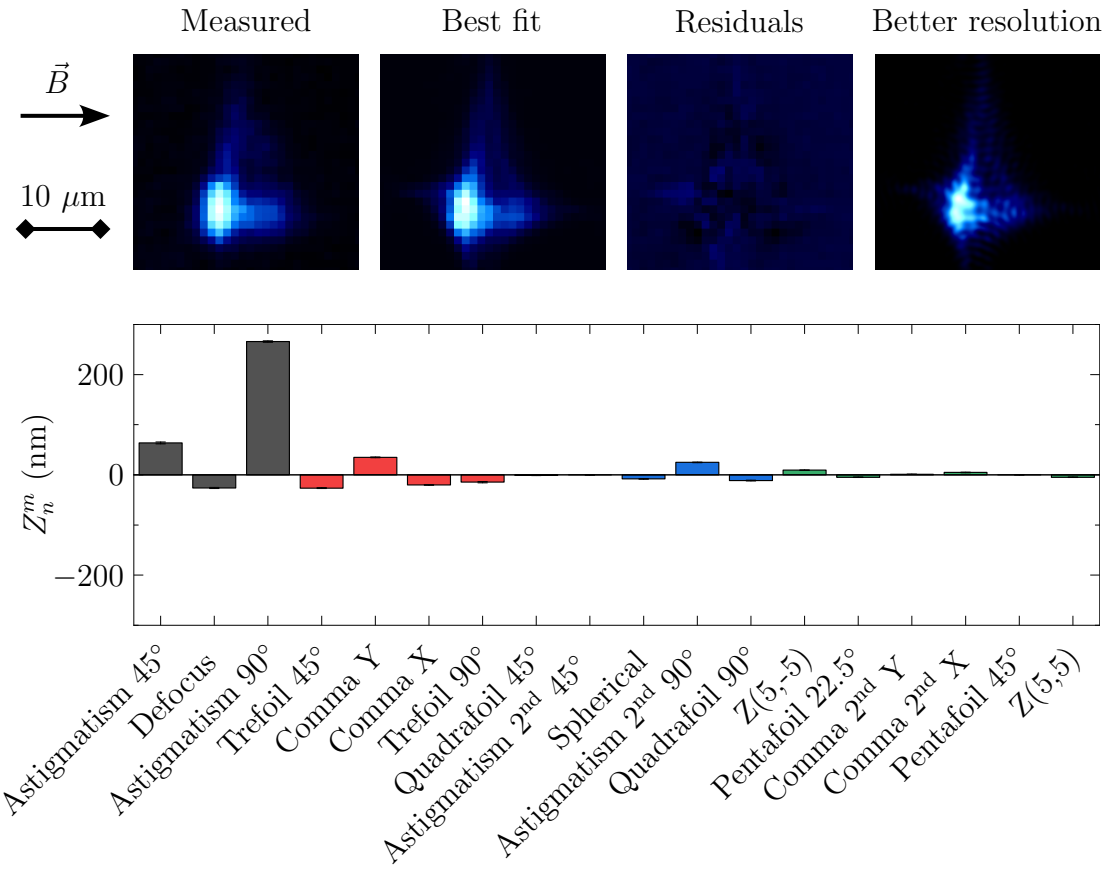

Figure 3.17. Wave aberration without external correction. Top: comparison between the measured image and the best fit, including a 100-factor increased resolution plot of the latter. The accumulation time for the measured image is 1 s. Bottom: weight of the first 21 (piston, X-, and Y-tilt are omitted) Zernike polynomials used in the best fit. The different colours stand for the five orders in the radial coordinate (see Eq. (3.16)).

from the ion-ion distance $d_{\text{ion-ion}}$ in a two-ion Coulomb crystal (Eq. (2.16)). The value obtained is 15.4(1)×, compatible with the design specifications. Compared to the diffraction-limited case, for which FWHM ≈ 0.8 μm, the measured image was much broader and strongly asymmetric. A total of 21 Zernike polynomials, up to fifth order in the radial coordinate, were used in the fitting procedure, for which a reduced chi-square of $\chi_\nu = 3.45$ was obtained. Introducing sixth-order Zernike polynomials did not improve the results significantly. A plot of the fitting results having a factor of 100 better spatial resolution is also shown to observe the interference patterns averaged by the sensor pixel size.

The Zernike polynomials decomposition revealed a strong astigmatism, noticeable even in its second-order component. The defocus can be used to find the least-confusion point, and should not be considered as an aberration. The second most prominent component was comma. Both types of aberration appear when

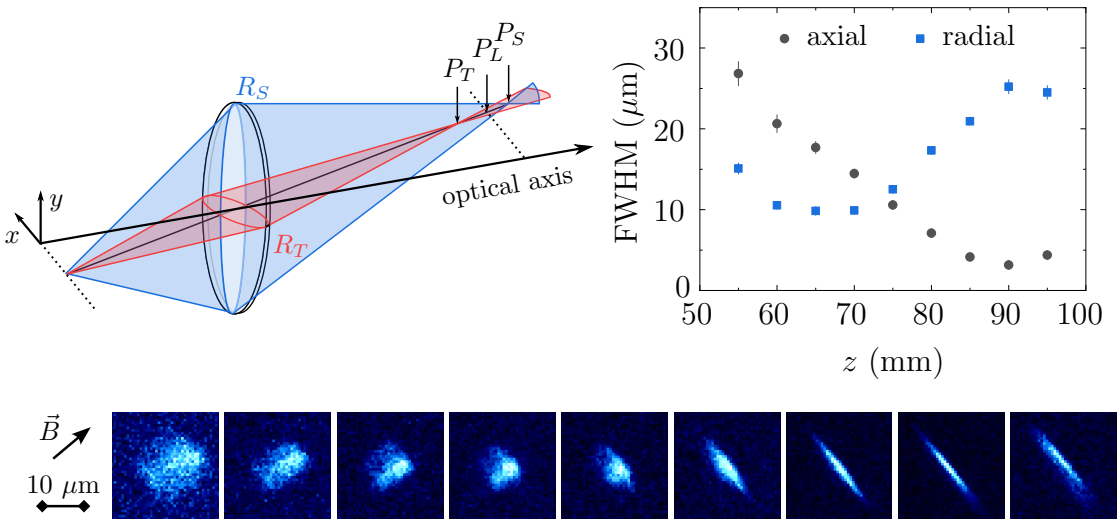

Figure 3.18. Study of the optical system's astigmatism. Top left: ray tracing showing the appearance of astigmatism in a spherical lens when the object is placed out of the optical axis. P_T: tangential focus. P_L: least confusion. P_S: sagittal focus. R_T: tangential radius. R_S: sagittal radius. Top right: variation of the ion image width in axial and radial directions when the EMCCD is scanned along the optical axis. Bottom: ion image recorded for the points analysed in the graph.

the object is not placed on the optical axis. This is consistent with a misalignment of the optical system with the trap due to machining tolerances in different anchoring points along the Penning-trap tower. The working distance was right since the magnification agrees with the design value.

Astigmatism can be easily identified by the appearance of two different focal positions for two perpendicular directions. Figure 3.18 illustrates the occurrence of this effect and the measurements carried out with a single ion. Due to the different radius of curvature seen by the off-axis object for the tangential and sagittal components of the light cone, two focal points appear where the image becomes sharp in either of these directions. Following the results shown in Fig. 3.17, a focus scan was performed around the least-confusion point. The analysed images in Fig. 3.18 confirmed that there was astigmatism in the optical system. A difference of 25 mm was observed between the tangential and sagittal focus. The tangential and sagittal directions nearly coincide with the trap's axial and radial directions, respectively, and a sharper focusing was obtained for the former ($z \approx 90$ mm) compared to the latter ($z \approx 65$ mm). These two observations indicate a lateral shift in the position of the optical system from the trap centre.

Astigmatism can be corrected using a cylindrical lens, which provides focusing only in one direction. A negative lens with $f' = -400$ mm was chosen, so that the first (tangential) focus point is forced to coincide with the second (sagittal). It was placed 110 mm before the image plane and the final configuration was found experimentally by minimizing the ion's spot radius.

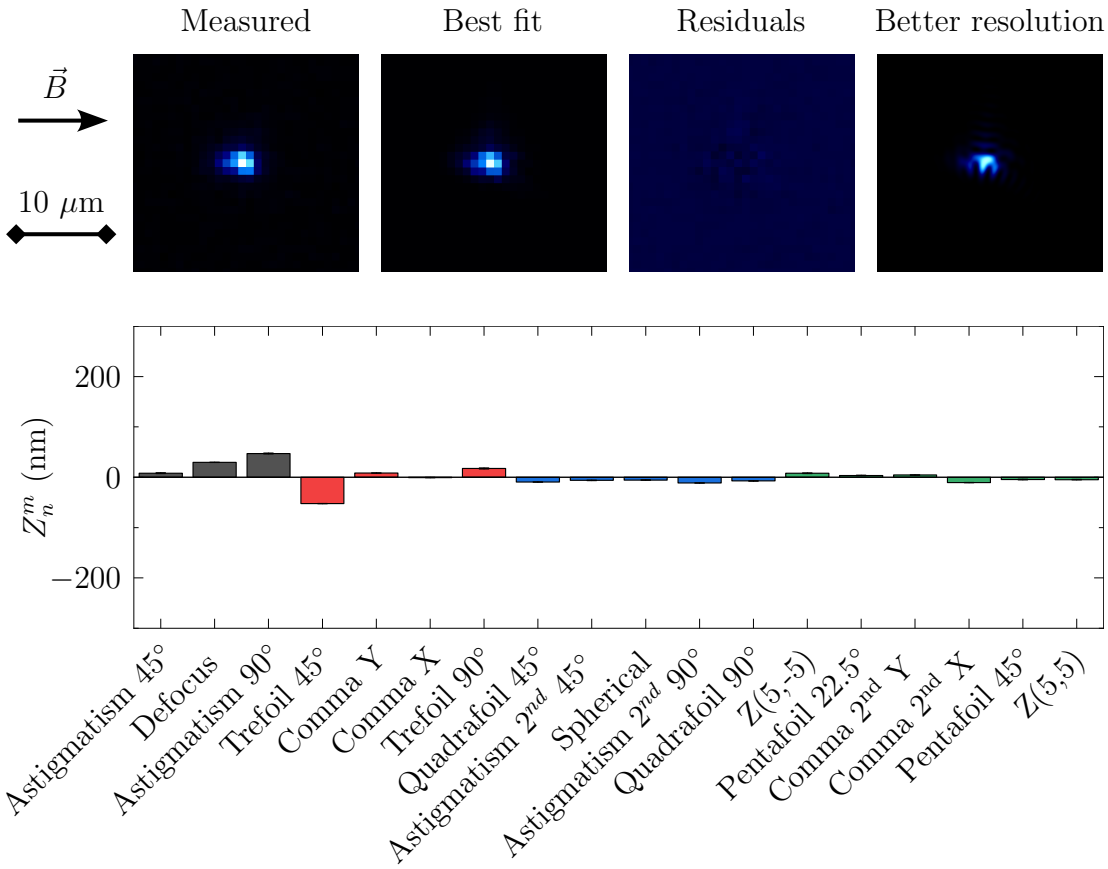

Figure 3.19. Wave aberration after implementing the cylindrical lens. The figure's layout is identical to Fig. 3.17.

The intensity PSF analysis of the optical system after inserting the cylindrical lens is shown in Fig. 3.19. The first 21 Zernike polynomials were used as in the previous analysis, just to allow a direct comparison. A reduced chi-square of $\chi_\nu = 13.1$ is obtained, although for the fitting using the first 15 polynomials, this value decreases to $\chi_\nu = 11.5$. The astigmatism is well attenuated compared to Fig. 3.17, and only some components of comma and trefoil remain. The magnification now becomes 17.9(1)×, larger than before, justified by the translation of the tangential focus point to the sagittal focus point utilizing the cylindrical lens.

Figure 3.20 shows the final performance in terms of the MTF and PSF. Both the images before and after the cylindrical lens inclusion are analysed. The MTF is calculated directly from the single-ion PSF using FFT (see Eq. (3.18)). The maximum spatial frequencies computed, 580 mm^{-1} (before the cylindrical lens correction) and 670 mm^{-1} (after), are limited by the pixel size of 13 μm. As was mentioned in Fig. 3.16, the effect of the detector pixel size is taken into account to establish the real diffraction limit performance (lower dashed line in Fig. 3.20). The resolution is detailed in Tab. 3.4. It must be mentioned that the intensities are normalized to the maximum value in the PSF comparison. Finally, a seven-ion

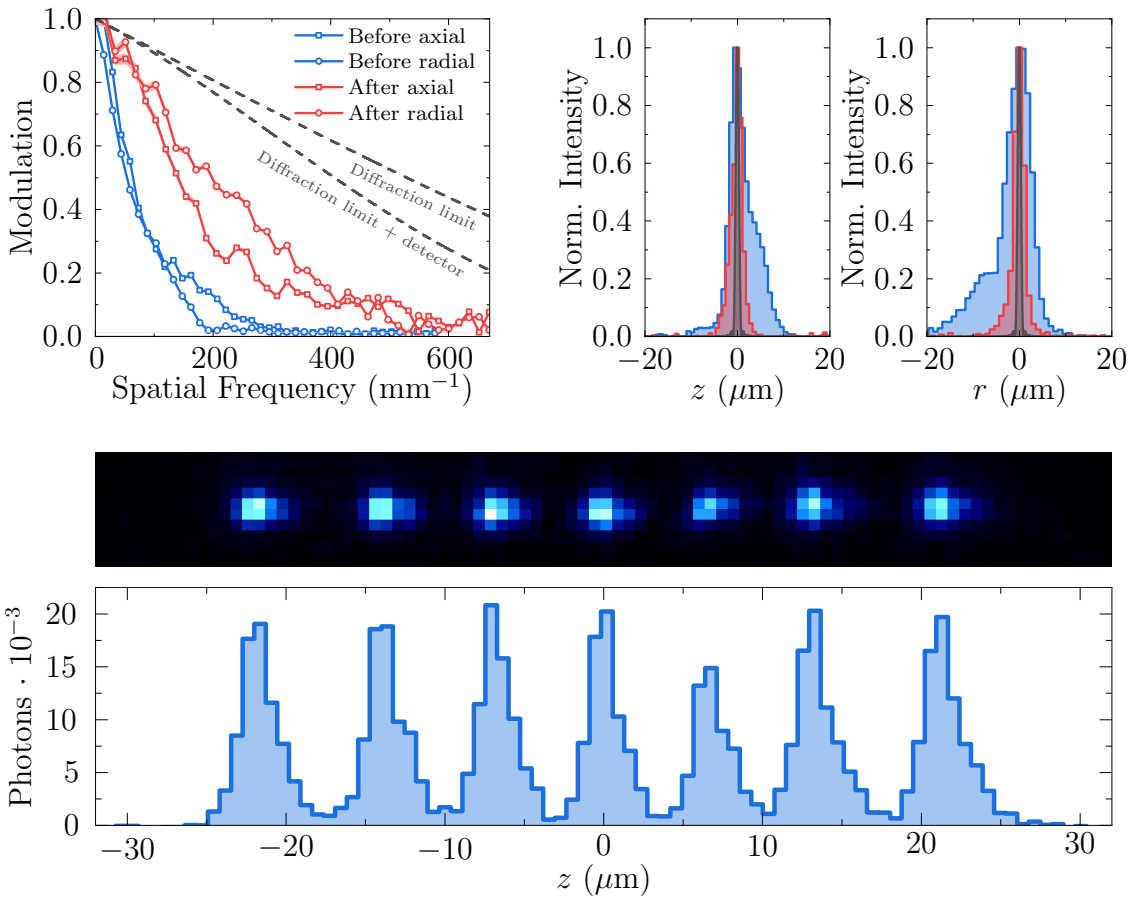

Figure 3.20. Final performance of the optical system. Top left: MTF before and after inserting the cylindrical lens compared to the ideal diffraction-limited case. Top right: axial and radial intensity PSF. Bottom: image of a seven-ion linear chain and profile along the axial axis.

linear chain is shown in the lower part of Fig. 3.20. In this particular case, the ions were oscillating at $\nu_z^{\text{com}} = 333\,(1)$ kHz, resulting in a ion-ion distance in the range $d_{\text{ion-ion}} = 8.01\,(16)$ - $6.77\,(17)$ μm. An equivalent expression to Eq. (2.16) for the ion-ion distance in a chain can be found in Ref. [120].

Table 3.4. Resolution of the optical system before and after inserting the cylindrical lens. These values are calculated from Fig. 3.20 using the Rayleigh criterion (modulation equal to 0.2).

	Resolution (μm)	
Situation	Axial	Radial
Before	6.96(5)	7.89(9)
After	3.69(3)	2.75(3)

3.5 Control and acquisition system

The control system of the Penning-trap setup is based on ARTIQ [121]. This open-source system provides both software (called ARTIQ as well) and hardware (Sinara boards) support to perform ion-trap experiments, and its use in the community is spreading rapidly. Python is used as a high-level programming language that facilitates the writing of experimental sequences. The associated hardware provides nanosecond timing resolution and sub-microsecond latency due to the use of a field-programmable gate array (FPGA) card where the code is compiled and run. External devices can be also integrated within ARTIQ's ecosystem by building a so-called network device support package (NDSP). This piece of software communicates with the specific device using the application programming interface (API) functions contained in the associated driver. Remote procedure calls (RPCs) using simple Python communications (SyPiCo) are employed for communications through the network.

Figure 3.21 shows a schematic of the Penning-trap control system and the interconnection among its different parts. ARTIQ's modular rack and other needed devices to perform motional-frequency measurements are shown. The experiments are scheduled and executed by the Master PC. The Client PC is usually used to develop the Python code. The graphical user interface (GUI) can be run on both PCs.

TTL, RF, and DC signals can be produced by ARTIQ with a precise timing (1 ns) by the FPGA[33]. TTLs are generated by three modules of eight digital input/output[34] (DIO) channels each. Four of these channels are configured as TTL-IN and can be used to determine the arrival time of an external TTL signal. The rest of the channels are configured in output mode and are used to trigger different devices across the experiment. Four direct digital synthesizers[35] (DDSs) produce RF signals from 1 MHz to 400 MHz with 0.25 Hz frequency resolution. The DC board[36] can provide ±10 V with 4 ppm stability.

Both ARTIQ's RF and DC boards need to be complemented with other devices to meet all the experiment's requirements. AWGs[37] are used to excite the ion's motional modes, since $\nu_z, \nu_- < 1$ MHz. Urukul is used to apply the quadrupolar excitation at ν_c and also to drive the AOM utilized to switch on and off laser cooling. As discussed in Sec. 3.1, all the voltages along the beamline are provided for dedicated general-purpose and high-precision DC sources.

The NDSPs for the EMCCD, the AWGs, and one of the HV DC sources were developed in a previous thesis work [65]. During this work, drivers for the PMT's counting unit[38], the Penning trap's DC power supplies, and the other HV DC

[33] Kasli v1.0
[34] DIO BNC
[35] Urukul AD9910
[36] Zotino v1.0
[37] Agilent 33210A
[38] Hamamatsu C8855-01

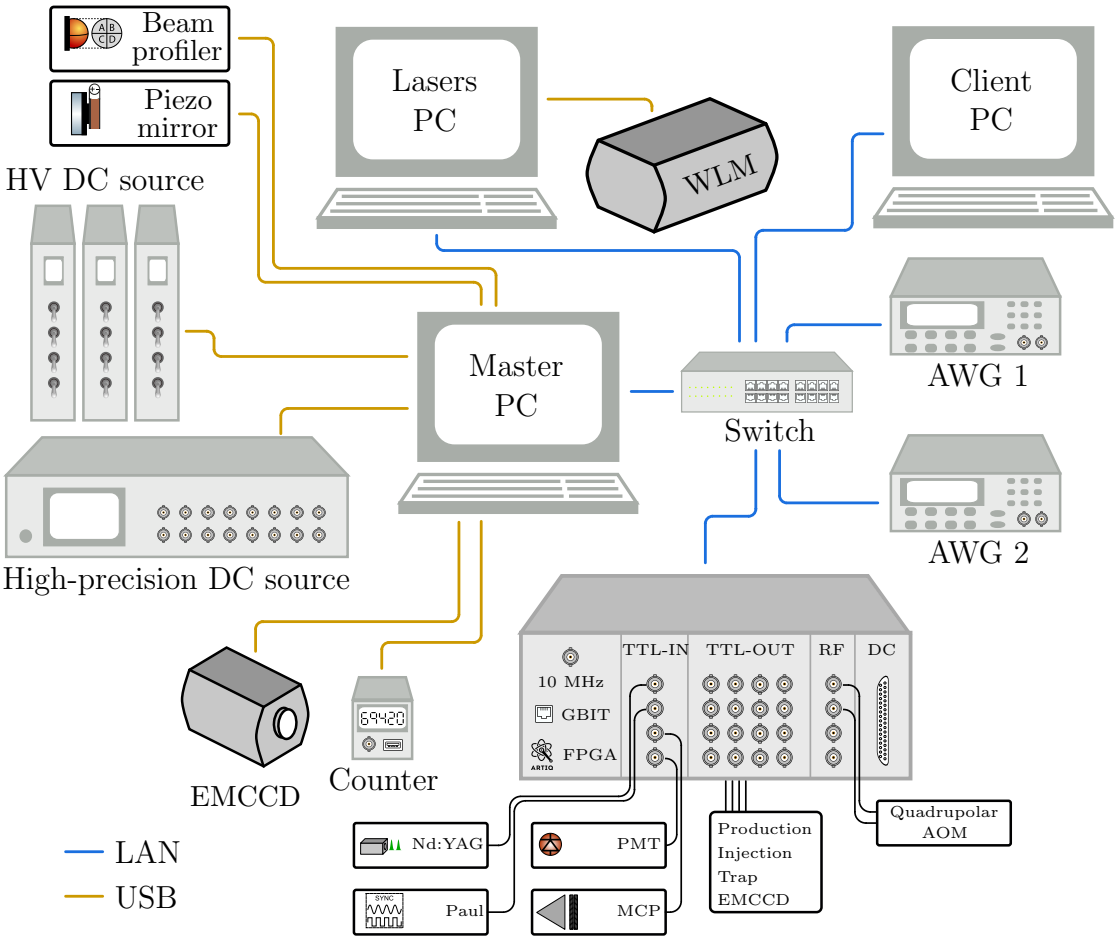

Figure 3.21. ARTIQ control system and peripheral devices. LAN connection is used where possible due to the higher speed and lower latency compared to USB.

source have been developed. A similar procedure as used before for the EMCCD's driver based on Python's module ctypes and the dynamic-link library (DLL) provided by the manufacturer was employed here. Although the WLM is not fully integrated within ARTIQ's environment, a communication protocol based on Python's socket module has also been developed. This protocol is used to vary the lasers' frequency through the PID regulation protocol during some experimental sequences. A server is continuously running in the WLM PC that receives commands from the ARTIQ program that runs in the Master PC. It communicates with the WLM employing the DLL the manufacturer provides and returns the status afterwards.

The necessary scripts to perform motional-frequency measurements developed during this thesis work use TTL-OUT channels and DC sources to transport and adapt the trap to the ions' energy, RF modules and the AWGs to apply the motional excitations, and the EMCCD and PMT to measure the ion's motional amplitude. Of particular importance has been the development of code to use TTL-IN channels in the experiment. Temporal synchronization in the two ion

Listing 3.1. Python readout method used to register the PMT and MCP output TTLs.

```
def readout(self):

    ref    = now_mu()
    cursor = self.ttl0.gate_rising(self.extraction_time)

    for i in range(self.nmax): self.tof_register[i] = -1
    i = 0
    while True:
        tof = self.ttl0.timestamp_mu(cursor)
        if tof == -1: break
        self.tof_register[i] = self.core.mu_to_seconds(tof-ref)
        i += 1
```

sources is achieved using this hardware. In the Paul-trap ion source, the extraction pulse can be locked to a specific phase of the RF trapping field. In the laser-ablation ion source, the Nd:YAG laser is running continuously, and any script involving the use of this source is paused until a pulse from the laser lamp is detected. TTL-IN channels are also used to read the output signals from the PMT and the MCP. Both systems can be operated by dedicated hardware (PMT's control unit and MM6 control system [122]), but the integration in ARTIQ's environment is much easier using TTL-IN channels. Listing 3.1 shows the excerpt of code used to read and save in `self.tof_register` the arrival times of TTL signals produced by the PMT or the MCP. Here, the channel `ttl0` is set to register rising edge events during a time interval between `now_mu()` and `now_mu()+self.extraction_time` in the future. The arrival times are determined with nanosecond resolution, retrieved sequentially by `timestamp_mu()` and stored in `tof_register`.

Although TTL-IN methods are very useful and flexible to precisely quantify TTL arrival times, limitations appear when detecting high count rates or locking quickly to an external trigger. The system needs ≈ 2 μs to process one event and its memory is only able to allocate 64 events. If the readout (`while` loop) is not fast enough to remove one event before the 65^{th} arrives, a so-called overflow exception is raised and the experiment stops. The aforementioned processing time also imposes a minimum delay of a few microseconds between an incoming trigger and the system's response. For lower delays, an underflow exception appears.

Chapter 4

Preparation and characterization of a single ion in the Doppler limit

The implementation of two major technical improvements, namely the new optical system (see Sec. 3.4) and the customized cryopump (see Sec. 3.2), has been key to the successful operation of the Penning-trap experiment. The optical system has enabled the detection of single ions, while the cryopump and the external ion production have contributed to reducing the background pressure so that lifetimes in the order of several minutes made possible to perform precision measurements.

In this chapter, the ion production and its cooling to the Doppler limit are characterized. The performance of two ion sources developed during this thesis work is also studied. This is followed by the characterization of the crystallization process, starting from large ion clouds to reach the single-ion case. Finally, a detailed study of axialization, used to efficiently cool the radial eigenmotions, is presented, together with spectroscopy measurements to accurately define the frequencies of the repumping transitions from the observation of dark resonances. Most of the results presented in this chapter have been published in Ref. [77].

4.1 Ion injection in the magnetic field

4.1.1 Paul-trap ion source

The geometry and operational parameters of the Paul-trap ion source can be found in Sec. 3.1.1. The ions were produced by two-step resonant photoionization [123, 124] of atoms evaporated from a metal vapour source that is heated by the Joule effect. Typical currents of 5 - 6 A were used in this setup, which correspond to temperatures of 850 - 900 K [125] and ion kinetic energies around 110-120 meV for the calcium isotopes. The transition $4s^2\,{}^1\mathrm{S}_0 \Leftrightarrow 4s4p\,{}^1\mathrm{P}_1$ is resonantly addressed by 422-nm laser light, with a typical power of 12 mW is delivered over 500 μm at the

trap centre, which implies a saturation parameter $s \approx 15$ (see Eq. (2.25)). A 375-nm laser with a similar beam waist and delivering around 10 mW provides the remaining energy to remove one electron. The ionization process has a cross-section of 60 - 280 Mb [126], leading to an overall efficiency of $\sim 10^{-3}$.

The photoionization laser beams can be directed along the axial or radial directions of the Paul trap, as shown in Fig. 3.3. Photoionization in the axial direction is approximately five times more efficient, but only the radial configuration allows for the injection of ions produced by the ablation source (see Fig. 3.3). In the latter, the 422-nm laser frequency has to be detuned from resonance since the laser beams propagate in opposite direction to the ions, shifting the resonant frequency in the ion's reference frame due to the Doppler effect [101]. A shift of 0.75 pm/A was measured in the interval 5 - 6 A applied to the atom oven.

The trap saturates after ≈ 3 s of continuous ion production. Assuming a spherical potential shape, the maximum number of ions contained in a Paul trap can be estimated as

$$N_{\max} = \frac{4\pi\varepsilon_0 r_0}{q\bar{D}}, \tag{4.1}$$

where ε_0 is the vacuum permittivity, r_0 is the trap's characteristic dimension (see Fig. 2.1), q is the ion's charge, and $\bar{D} = (qV_0^2) / (4mr_0^2\omega_{\mathrm{RF}}^2)$ is the average potential depth, with m the ions' mass, and V_0 and ω_{RF} the voltage and frequency of the oscillating field, respectively [62]. Considering the trapping parameters $V_0 = 112.5$ V and $\omega_{\mathrm{RF}} = 2\pi \times 600$ kHz, and the trap dimension $r_0 = 12.5$ mm (see Sec. 3.1.1), $N_{\max} \approx 2.5 \cdot 10^6$.

The electrostatic voltages applied along the transfer section to guide and inject the ions in the magnetic field are shown on the left side of Fig. 4.1. Ions were typically created in the Paul-trap source during 1 s. Afterwards, a 575-V pulse was applied to the middle electrode on the upstream side of the trap (for the trap's geometry, see Fig. 3.3). The extraction-pulse potential was chosen so that the ions' energy matches the voltages applied to the Penning-trap electrodes to be in-flight captured. The voltages applied to the Einzel lenses in the transfer section are detailed in Tab. 4.1. These values have been found experimentally. The time sequence is shown on the right side of Fig. 4.1. The trapping voltage produced by a non-resonant amplifier decays within one period of the signal; specifically, it drops exponentially to half its maximum value within 735 ns. The details about the phase locking of the trapping field during extraction are given in Sec. 3.5.

One of the most important features of an ion source is its energy spread. Sharp energy distributions are beneficial to maximize the trapping efficiency and to have well-defined initial conditions before any cooling method is applied. In the Paul-trap ion source, the energy spread was strongly affected by the delay time t_{delay} between the oscillating trapping potential being switched off and the extraction pulse being turned on. In the left side of Fig. 4.2, the time-of-flight (ToF) signals of $^{40}Ca^+$ ions extracted using different delay times are shown. The ions were sent through the magnetic field in transmission and detected in MCP2 (z_3 in Fig. 4.1).

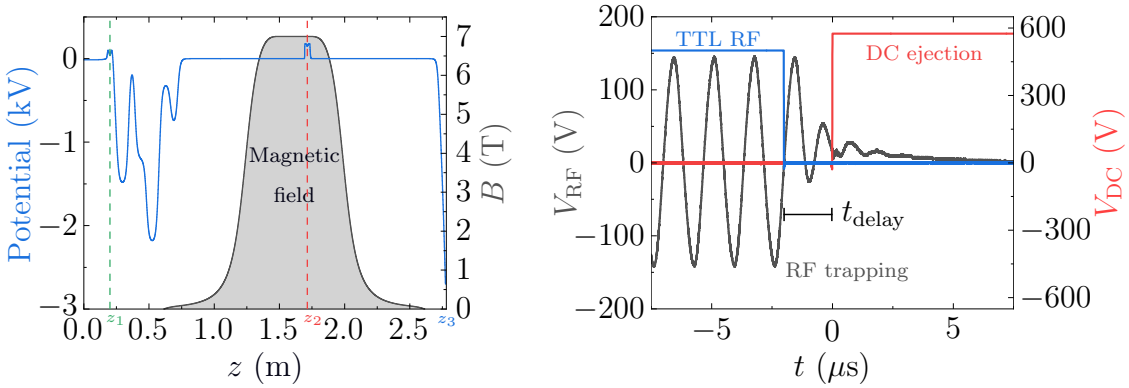

Figure 4.1. Ion transport and injection in the magnetic field. Left: electric potentials (left axis) and magnetic-field strength (right axis) along the Penning-trap beamline. The positions of the Paul-trap ion source, z_1, and the Penning trap, z_2, are indicated by a green and a dashed red line, respectively. Right: Paul-trap voltages during the extraction process. The trapping voltage of 225 V_{pp} oscillates at 600 kHz. The blue line represents the TTL pulse (in arbitrary units) controlling the non-resonant amplifier switch (see Fig. 3.3). The solid red line is the ejection pulse at 575 V.

For a short t_{delay}, the ToF signal is wide due to the residual trapping voltage. For a long t_{delay}, the ions start to disappear due to the absence of confinement force. In these experiments, the delay time was fixed to $t_{delay} = 2.8$ μs, resulting in an energy spread of 22.3(25) eV (FWHM) for the measurements shown in Fig. 4.2.

The Paul-trap ion source can deliver several naturally abundant calcium isotopes. Figure 4.3 shows transmission ToF signals of $^{A}Ca^{+}$ for $A = 40, 42, 44, 48$. The optimal laser frequency for the resonant transition was chosen based on isotope-shift measurements carried out with ions produced by the internal ion source located inside the magnet (see Fig. 3.2) [65]. While a clean signal of each isotope was obtained by applying dipolar excitations to remove other isotopes from the trap, some of the ions of interest were also lost. This could be attributed to the proximity of their motional frequencies compared with the frequency resolution in the Paul trap. Nevertheless, the isotopic separation can be accomplished by properly tuning the transfer time to the Penning trap. In particular, transfer times of 47/48.2/49.3/51.5 μs have been used for $A = 40/42/44/48$.

The ions delivered by the Paul-trap source were captured in-flight by rapidly

Table 4.1. Voltages used in the transfer section. L10 to L16 are consecutive Einzel lens placed between the Paul-trap ion source and the magnet.

Lens	L10	L11	L12	L13	L14	L15	L16
Potential (V)	-1500	-1200	-2200	-300	-800	0	0

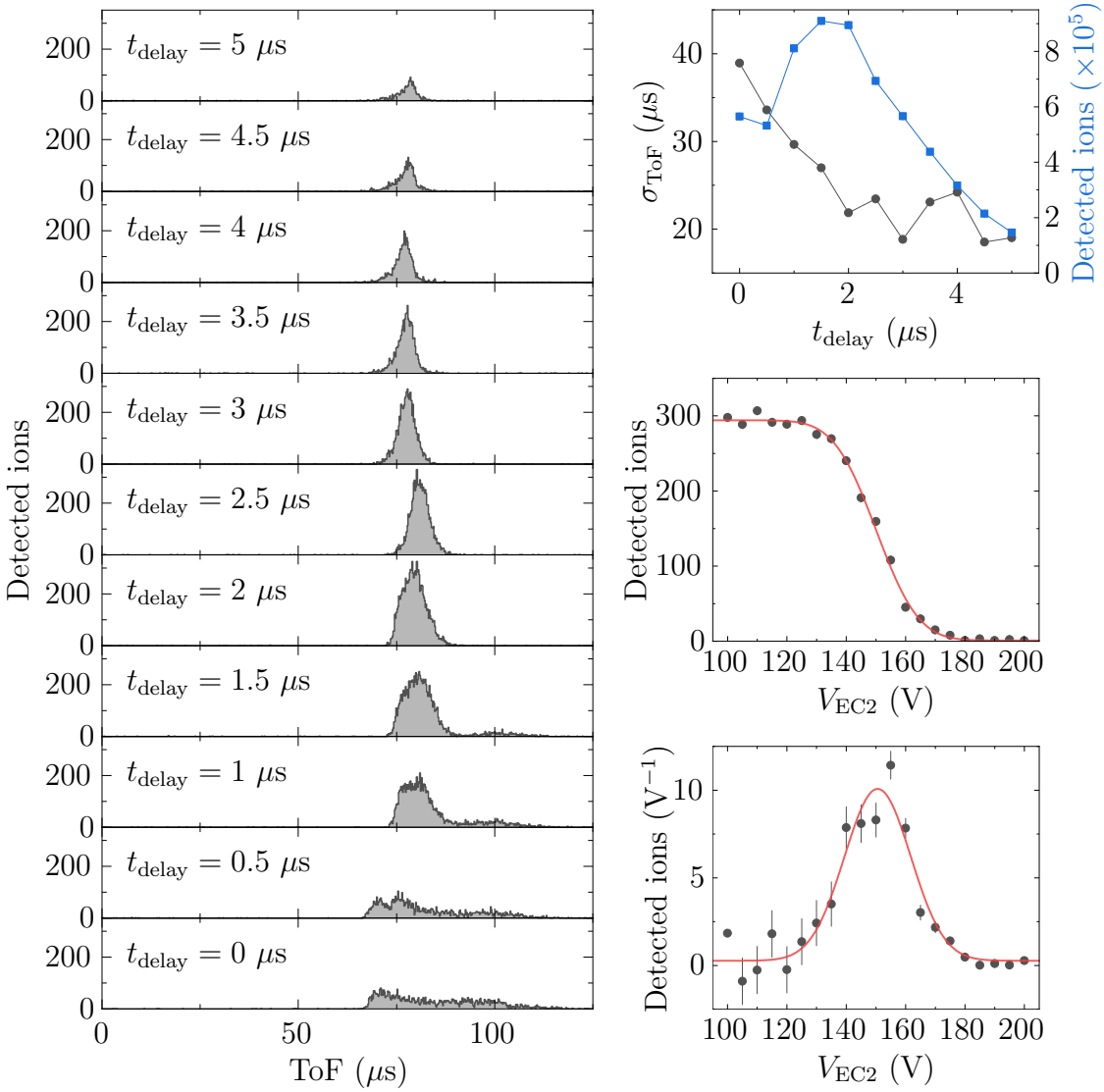

Figure 4.2. Extraction process in the Paul-trap ion source. Left: ToF signal of ions ejected from the Paul-trap source for different values of t_{delay}. Upper right: standard deviation (grey circles) and total number of detected ions (blue squares) of the ToF signals shown on the left side. Middle right: number of detected ions in the MCP detector at the end of the beamline vs voltage applied to EC2 (see Fig. 3.2) to create a potential barrier. The data are fitted to the Gaussian cumulative distribution function. $t_{delay} = 2.8\ \mu s$ for these measurements. Lower right: energy spread of the ions produced in the Paul-trap source calculated as the derivative of the data in the middle right panel. The data are fitted to a Gaussian distribution.

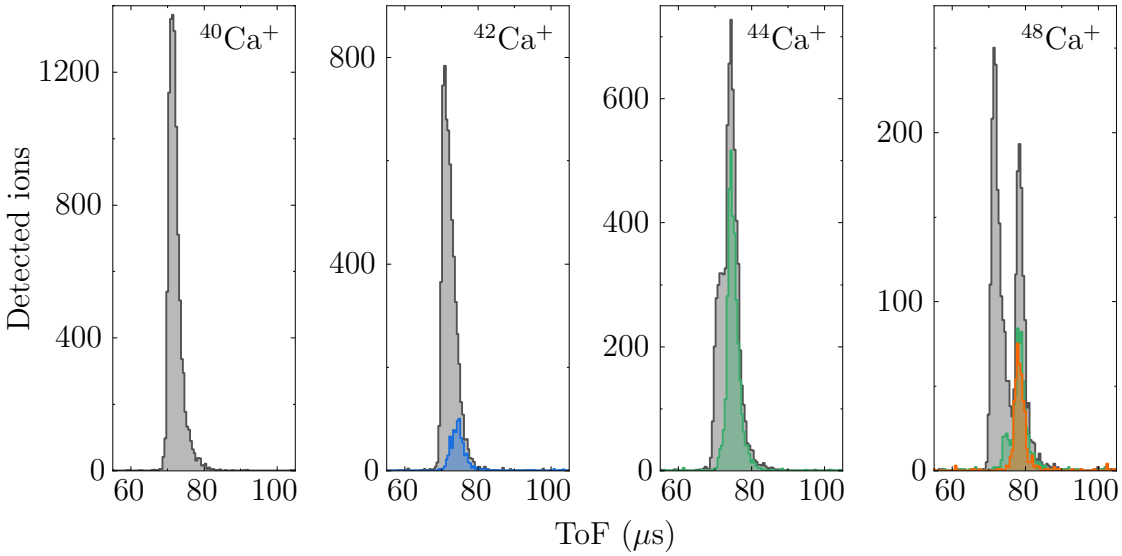

Figure 4.3. Production of calcium isotopes by the Paul-trap ion source. The grey-shaded spectra are obtained when the resonant photoionization 422-nm laser is detuned 390/790/1530 MHz for $A = 42/44/48$ from $^{40}Ca^+$ to produce more efficiently the ion of interest. The coloured-shaded data are obtained when a dipolar excitation at the axial motional frequency of $^{40}Ca^+$ (and $^{44}Ca^+$ for the yellow-shaded data in the $^{48}Ca^+$ spectrum) is superimposed to the trapping field to remove unwanted isotopes.

switching (within 1 μs) one of the Penning trap's halves between two voltages. The trapping voltages were $V_{EC} = 180$ V, $V_{CE} = 168$ V, and $V_{RE} = 150$ V (see Fig. 3.2 for the Penning trap's geometry), while the lower voltage in all the electrodes was 150 V for injection and extraction. The energy distribution has been studied by scanning the lower voltage of the trap when extracting the ions. The injection potentials and several extraction configurations used in this study are shown in the upper-left panel of Fig. 4.4. The trapping efficiency is ≈ 30 %, calculated as the ratio between the number of ions ejected from the Penning trap and the detected ions in transmission. The upper-right panel shows the number of ions vs voltage applied to EC2. The ions' energy spread is shown in the lower panels. The energy distribution is asymmetric, and it is centred in 17.5 eV with FWHM = 1.75(15) eV. The trap depth could not be decreased to 0 V by only scanning EC2. Only when the trap was fully open (dash-dotted red line in the upper-right panel), the count rate increased by 14(2) % due to low-energy ions.

4.1.2 Ablation ion source

The ablation ion source was tested using a dedicated setup with a one-meter ToF section before it was coupled to the Penning-trap beamline. This setup was also used to study the production of molecular ions [127]. As it is explained in Sec. 3.1.1,

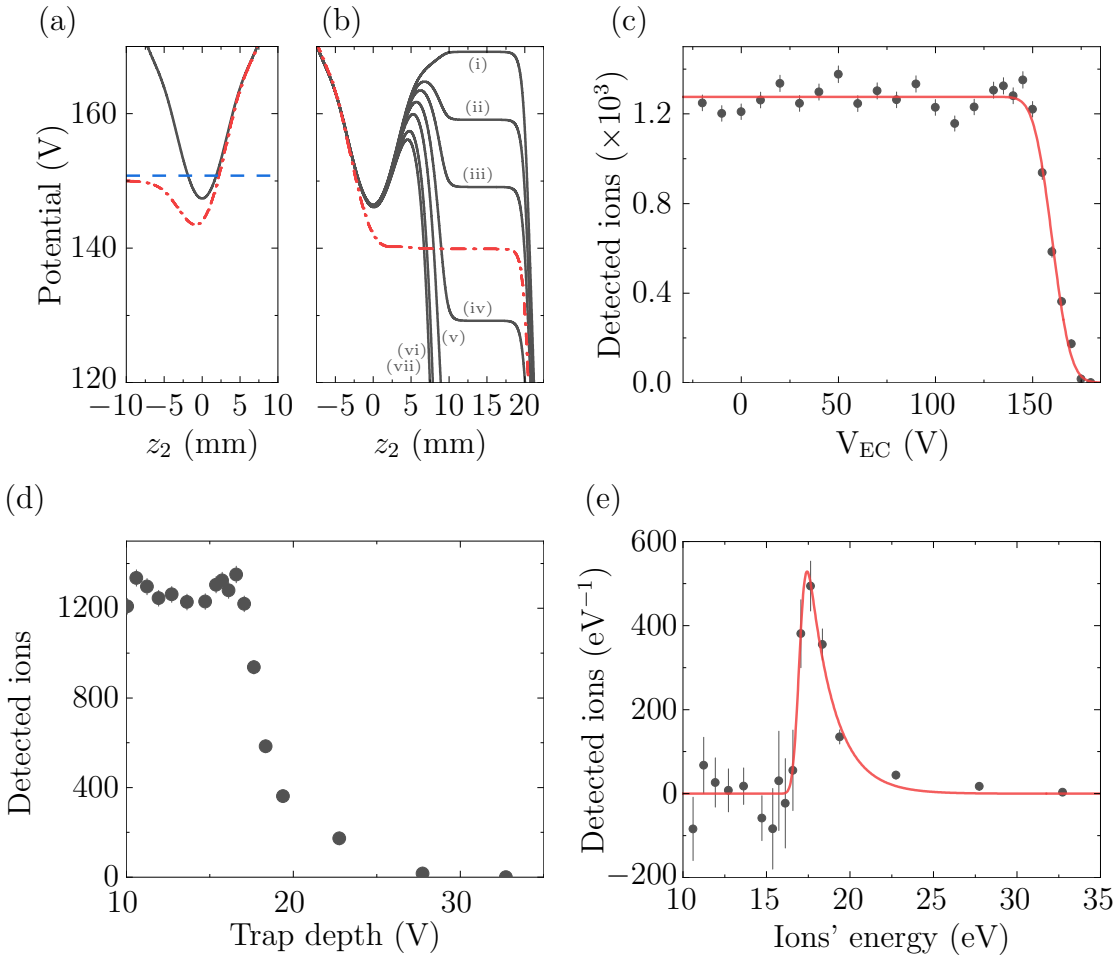

Figure 4.4. Energy characterization of ions produced by the Paul-trap source and captured in the Penning trap. Upper left: potentials applied for injection (a) and extraction (b) used for the energy characterization of the trapped ions. Only a few cases are shown: (i) $V_{EC} = 170$ V, (ii) $V_{EC} = 160$ V, (iii) $V_{EC} = 150$ V, (iv) $V_{EC} = 140$ V, (v) $V_{EC} = 130$ V, (vi) $V_{EC} = 100$ V, (vii) $V_{EC} = 40$ V, and (vii) $V_{EC} = 0$ V. The horizontal dashed blue line (a) represents the mean ions' kinetic energy from the measurements presented in Fig. 4.2. The dash-dotted red lines represent the potential configuration for injection (a) and the configuration to extract all the ions from the trap (b). Upper right (c): number of detected $^{40}Ca^+$ ions for different values of V_{EC} (some of them are shown in the upper left part of this figure). The red line is the fit using a Gaussian cumulative distribution function. Lower left (d): number of detected ions vs the effective trap depth, extracted from SIMION simulations. Lower right (d): negative derivative of the number of detected ions vs their energy in the trap. The red line is the fit using an exponentially modified Gaussian distribution.

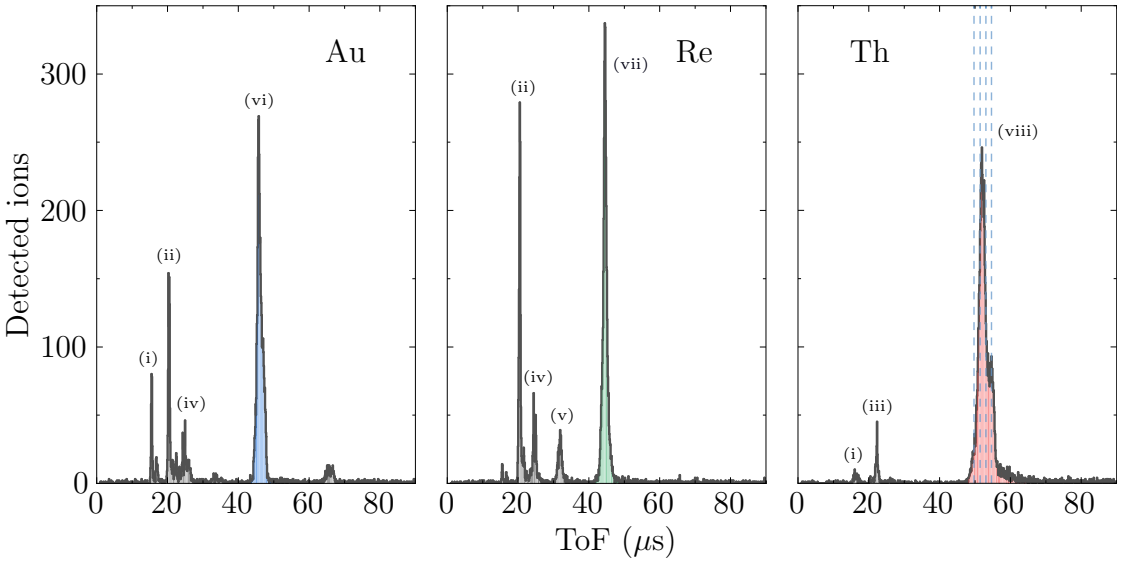

Figure 4.5. ToF spectra from the laser-ablation ion source using a dedicated setup. Samples of gold (vi), rhenium (vii), and thorium (viii) were used. The four blue vertical dashed lines in the thorium spectrum mark the expected mean ToF for $^{232}Th^+$ and the oxides $^{232}ThO^+$, $^{232}ThO_2{}^+$, and $^{232}ThO_3{}^+$. The peaks (i) - (v) are contaminants. Based on the gold peak, their masses are estimated to be (i) 23.6(33) u, (ii) 39.4(17) u, (iii) 46.9(16) u, (iv) 57.4(97) u, and (v) 95.3(60) u. The targets are biased to 1000 V.

a rotary feedthrough swaps between different targets without the need to open the vacuum system. Natural samples of gold, rhenium, and thorium were installed. Gold was used for calibration since it has only one stable isotope, ^{197}Au. Rhenium was installed because of the interest to complement studies of the β^- decay of ^{187}Re in the context of neutrino mass determination [50]. The study of the natural isotope ^{232}Th is the first step in this laboratory towards the investigation of the nuclear isomer ^{229m}Th, the unique candidate to implement an optical clock based on an isomeric nuclear transition [59].

Figure 4.5 shows the ToF spectra measured for gold, rhenium, and thorium at a kinetic energy of 1000 eV. The mean ToFs for gold and rhenium are 46.0(15) μs and 44.56(96) μs, respectively. The uncertainty given is one standard deviation of the ToF distribution. The two abundant and stable rhenium isotopes, $^{185}Re^+$ (37.4 %) and $^{187}Re^+$ (62.6 %), are not resolved at 1000 eV, although the two peaks should be distinguished at higher energies [50]. The thorium peak is compatible with $^{232}Th^+$ and also with oxide compounds with up to three oxygen atoms ($^{232}ThO_3{}^+$) based on the gold and rhenium reference measurements. Contaminant peaks labelled (i) - (v) are of unknown origin and not relevant in the experiments.

The energy distribution of the ablation ion source was studied in the same way as with the ions from the Paul-trap source. The Penning trap's EC2 electrode was used to create a potential barrier for the ions transmitted through the

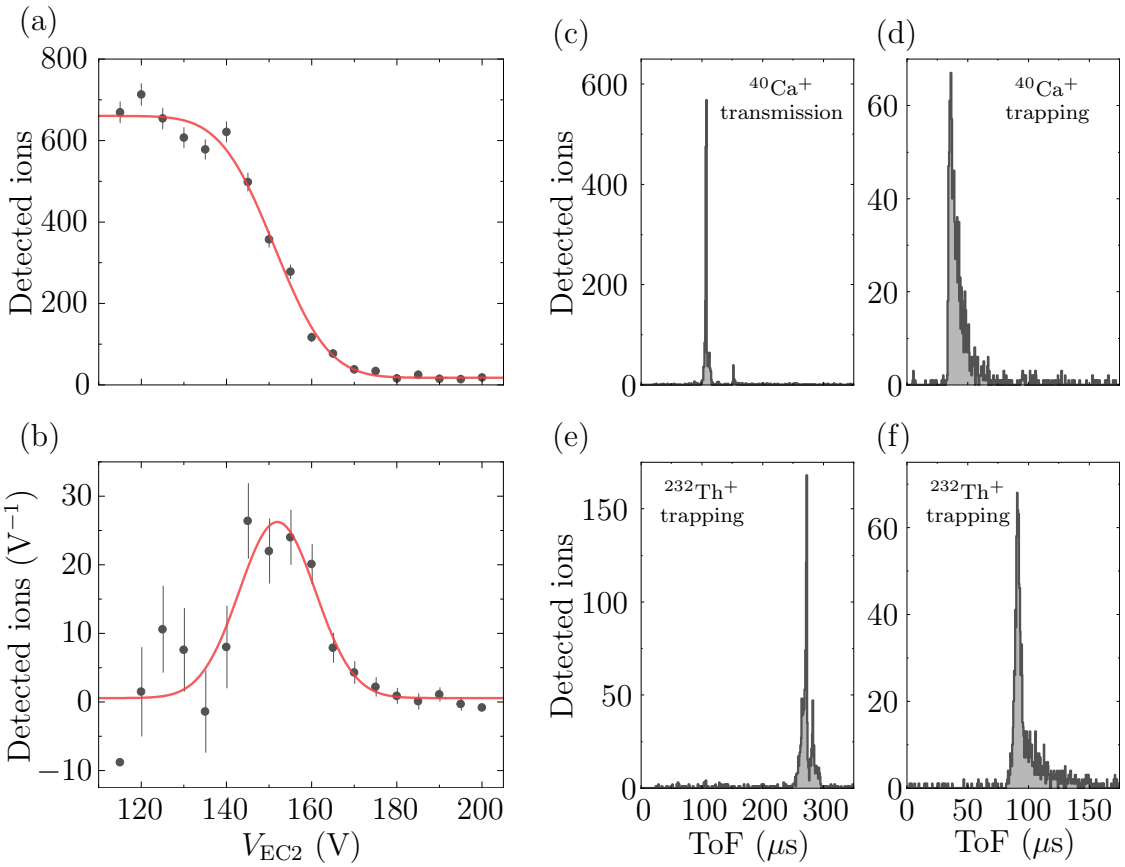

Figure 4.6. Characterization of the laser-ablation ion source in the Penning-trap beamline. Upper left (a): number of detected ions as a function of the potential applied to the EC2 electrode of the Penning trap. A Gaussian cumulative distribution function is used to fit the data. Lower left (b): ions' energy spread, calculated as the negative derivative of the data shown in the panel above. The data are fitted to a Gaussian function. Right: ToF measurement of the ions delivered by the ablation ion source when the targets are metallic calcium (c,d) and thorium (e,f). In the trapping spectra (d,f), the ions are in-flight captured and trapped for 20 ms before they are ejected from the Penning trap to the detector.

magnetic field so that the cumulative distribution function of the ions' energy can be obtained from the number of detected counts in MCP2. Figure 4.6 shows the results. An energy spread of 21.1(38) eV (FWHM) is obtained. The distribution is centred in 152.0(14) eV (target plate biased to 150 V) to capture the ions in the Penning trap using the voltage configuration employed for the Paul-trap source (see Fig. 4.4).

The ions were in-flight captured in the Penning trap using the same scheme shown in Fig. 4.4. The transfer times between the ablation source and the Penning trap for $^{40}Ca^+$ and $^{232}Th^+$ were 85 μs and 205 μs, respectively. The acquisition system was locked to the ablation-laser repetition rate, as it is explained in

Secs. 3.1.1 and 3.5. ToF spectra of calcium and thorium ions, both directly transmitted through the magnetic field and trapped in the Penning trap for 20 ms, are shown in Fig. 4.6. A laser fluence of 44(15) mJ/cm^2 and 50(17) mJ/cm^2 was used in these measurements. Several peaks are visible in the thorium ToF transmission spectrum, being the highest one compatible with the expected ToF for $^{232}ThO_2{}^+$.

4.2 Laser cooling of a single ion to the Doppler limit

4.2.1 Cooling parameters

The laser setup is described in Sec. 3.3, and the $^{40}Ca^+$ energy levels and relevant transitions for Doppler cooling are shown in Fig. 2.4. A total of twelve laser beams are used to cover the 397-nm (×4), 866-nm (×4), and 854-nm (×4) optical transitions in the 7-T magnetic field. Figure 4.7 shows a pictorial representation of the laser beams associated with transitions, including the specific nomenclature used in this work. The power P delivered by each laser beam, the estimated spot diameter at the trap centre w, and the saturation parameter s (Eq. (2.25)) are given in Tab. 4.2. The 866-nm and 854-nm transitions are strongly addressed, which assures a fast repumping from the metastable states and thus a high level of fluorescence. The two cooling transitions are also addressed above saturation. It has been checked that a higher saturation parameter could result in ion heating, something detected from the widening of the ion image observed with the electron-multiplying charge-coupled device (EMCCD). A lower value of s may lead to lower temperatures but decreases the fluorescence signal. The spot diameter of the radial laser beams at the ion location must fulfil Eq. (2.28) to perform cooling efficiently. In the case of $^{40}Ca^+$ oscillating at $\nu_+ = 2.679$ MHz and $\nu_- = 10$ kHz, the radial spot diameter must lie within 1.7 and 460 μm. In general, the smaller the spot size the more efficient the magnetron cooling. Although the spot diameter of B2 is higher than 460 μm, this laser also contributes to cooling the ion when axialization is applied (see Sec. 2.2.1).

As it is shown in Sec. 4.1.1, the mean initial energy of $^{40}Ca^+$ ions in the Penning trap is 17.5 eV. A cooling time of 165(64) s was observed in a series of 17 measurements with a single ion. According to Ref. [128], the time t needed to cool a single ion is related to its initial energy E as

$$t = \frac{4}{3} t_0 \sqrt{r} \left(\frac{E}{E_0} \right)^{3/2}, \tag{4.2}$$

where $t_0 = 2\,(1+s)\,/s\Gamma$ and Γ the cooling-transition linewith. $r = (\hbar k)^2\,/\,(2mE_0)$ with $\hbar$ the reduced Planck's constant, k the photon wave number, m the ion's mass, and $E_0 = (\hbar\Gamma)\,/2\sqrt{1+s}$ the recoil energy. The cooling lasers were detuned $\Gamma/2$ from the resonance frequency. Taking the saturation parameters of Tab. 4.2, it is

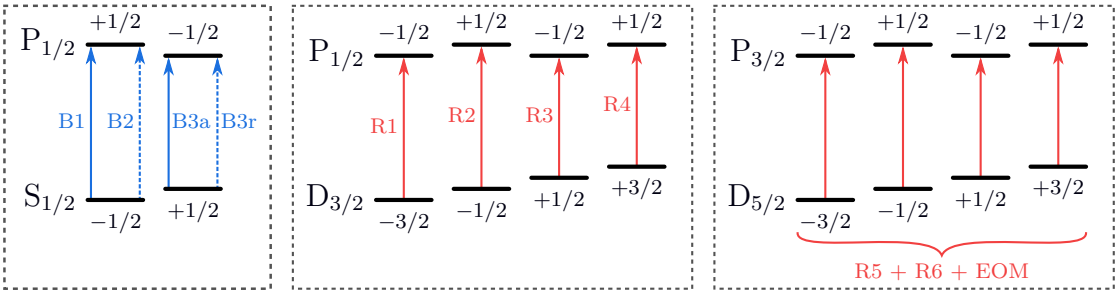

Figure 4.7. Laser-driven transitions to perform Doppler cooling of calcium ions in 7 T [98]. The boxes gather the transitions according to the fine structure. The cooling transitions are addressed both in the axial (parallel to the magnetic field) and radial (dashed lines) directions. The repumping laser beams are directed parallel to the magnetic field since their influence on the momentum transfer during the cooling process is small compared to the 397-nm transition. The calculations to address the four 854-nm transitions using two lasers and an electro-optical modulator (EOM) can be found in Ref. [65].

possible to deduce a lower limit for E of 4.2(2.3) eV, which does not coincide with the value of 17.5 eV obtained in Sec. 4.1.1. The energy difference was removed by the interaction between the ions and the residual-gas atoms. To prove this, laser cooling was switched on at time t_B after ion capture. The subsequent time needed for the ion to be laser-cooled to the Doppler limit was shorter for longer times t_B. For a total of 16 measurements with t_B ranging from 0 to 200 s, it was possible to extract a decay-time constant of about 225 s. The presence of this background gas is beneficial to shorten the cooling time of an initially hot ion but prevents a long coherence time in the motional-frequency measurement. To achieve faster cooling without the need for gas cooling, the frequencies of the axial cooling lasers B1 and B3a were scanned starting after loading the ion from 8 GHz to about 10 MHz below resonance, which is equivalent to a change in the kinetic energy of the ions from 2 eV to $3 \cdot 10^{-6}$ eV (Doppler limit). If the initial ion's energy is below 2 eV, the cooling is boosted at the time the laser frequency matches the maximum frequency shift, and the ion is progressively brought to the Doppler limit by the frequency ramp.

Table 4.2. Power, spot diameter, and saturation parameter of the Doppler-cooling laser beams. The saturation is determined using Eq. (2.25) and the values in Tab. 2.1.

Laser	B1	B2	B3a	B3r	R1	R2	R3	R4	R5	R6
P (mW)	0.52	0.34	0.28	1.4	0.75	1.4	0.40	0.32	2.3	2.2
w (mm)	0.50	0.85	0.50	0.22	1.6	1.6	1.6	1.6	1.6	1.6
s	11	7.0	6.1	29	230	420	120	100	710	680

4.2.2 From ion Coulomb crystals to a single ion

Figure 4.8 shows a few examples of ion clouds ranging from several thousand to one single ion. Spatially ordered structures known as ion Coulomb crystals (ICCs) are observed. Note that these images were collected using the non-corrected optical system, thus suffering from several optical aberrations that are explained in Sec. 3.4. The number of ions N_{ion} given in the caption of Fig. 4.8 is determined based on the volume of an ellipsoid as

$$N_{\text{ion}} = \frac{\pi}{6} N_z N_r^2, \tag{4.3}$$

where N_z and N_r are the number of layers in the axial and radial directions, respectively. The value obtained using Eq. (4.3) is compared with the ratio between the fluorescence photons from the cloud and one ion, and the difference is used to quote the uncertainty. The layers can be readily determined by taking the projection across the axial and radial directions at the cloud centre, as shown in the right side of Fig. 4.8. The number of registered photons at the centre position is higher for the ICC than for a single ion due to the contribution of the other layers of ions. In the case of the ICC, the peaks are likewise not fully resolved due to the background fluorescence contribution from other layers. The ions' equilibrium positions are defined by the equilibrium between the repulsive Coulomb interaction and the attractive force exerted by the trapping fields. In the case of a two-ion crystal, their relative distance along the z axis $d_{\text{ion-ion}}$ is given by Eq. (2.16). For these measurements, $d_{\text{ion-ion}} = 18.3$ μm.

Although the ion cloud always exhibits a crystalline structure in the measurements presented in Fig. 4.8 that can be considered as a solid structure, configurations where the cloud behaves like a liquid or a gas have also been reported [129–131]. The transition between these phases is governed by the Coulomb correlation parameter Γ_C, defined as the ratio between the electrostatic energy of neighbouring charges and the thermal energy. It can be calculated as

$$\Gamma_C = \frac{1}{4\pi\varepsilon_0} \frac{q^2}{a_{\text{WS}} k_{\text{B}} T}, \tag{4.4}$$

where a_{WS} is the Wigner-Seitz radius defined by $(4\pi/3)\, n_0 a_{\text{WS}}^3 = 1$, with n_0 the particle density, k_{B} is the Boltzmann's constant, and T is the cloud temperature [132, 133]. If $\Gamma_C \ll 1$, the system is said to be weakly correlated and the ions move independently. Numerical simulations have shown that ordering characteristics of liquids appear at $\Gamma_C \approx 2$ [134]. $\Gamma_C \gg 1$ denotes a strong coupling among the ions, with a relevant correlation between the dynamic variables of the particles. Crystallization occurs at $\Gamma_C \approx 178$ [135, 136], and the ICC aspect ratio r_0/z_0 depends in a non-trivial way on the specific eigenfrequencies and the laser cooling rate [137]. Using this lower limit for Γ_C, it is possible to find an upper limit of $T \approx 5$ mK for the ICC's temperature.

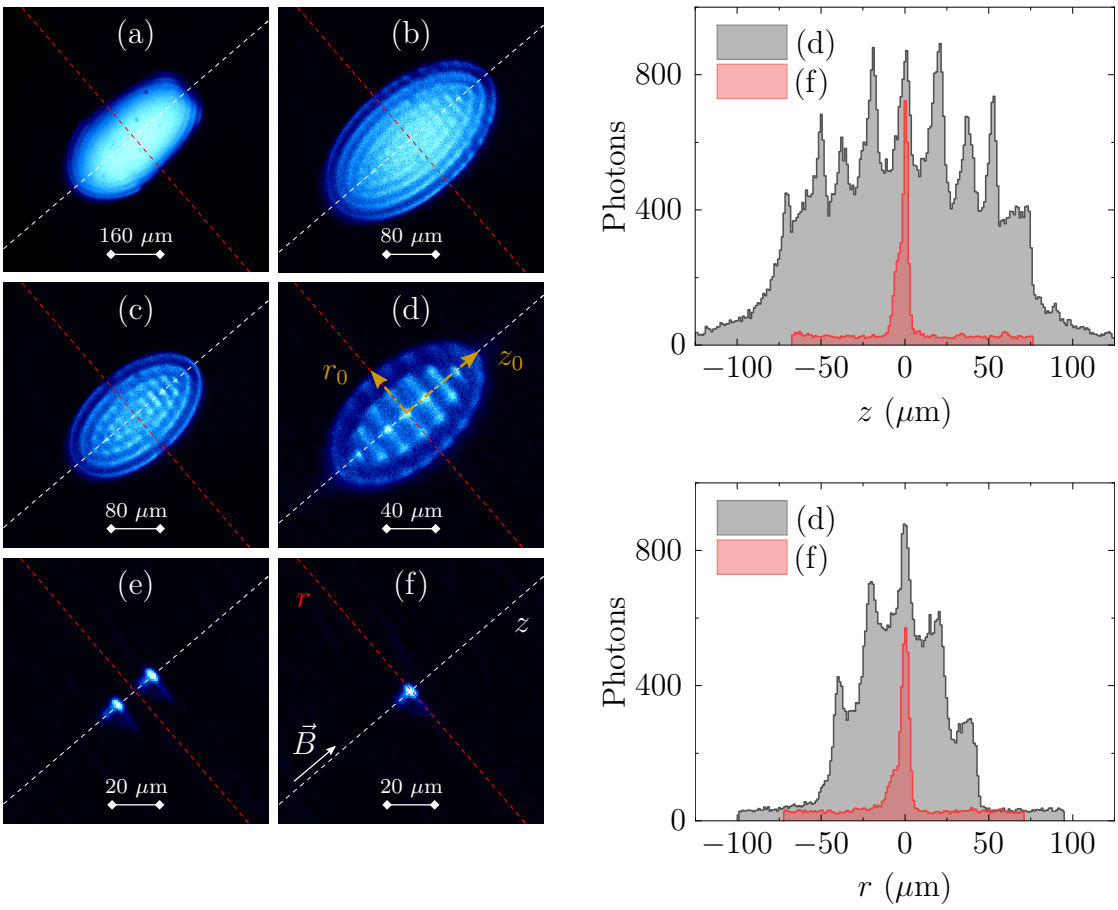

Figure 4.8. Ion Coulomb crystals. Left: EMCCD images of ICCs in the 7-T Penning trap formed by different amount of ions N_{ion}. (a) $N_{\text{ion}} = 5000(400)$, (b) $N_{\text{ion}} = 1200(100)$, (c) $N_{\text{ion}} = 550(50)$, (d) $N_{\text{ion}} = 117(3)$, (e) $N_{\text{ion}} = 2$, and (f) $N_{\text{ion}} = 1$. The exposure time is 1 s. The crystal structure becomes clearly visible from (b). In these cases, the ions were created inside the trap using the internal ion source. The Penning trap was operated with an axial oscillation frequency for a single $^{40}Ca^{+}$ ion of $\nu_z = 170$ kHz. Right: projections (sum of ten pixels around the trap's centre) along the magnetic field axis (top) and the radial direction (bottom) of the crystal (d) and of the single ion (f) shown on the left side.

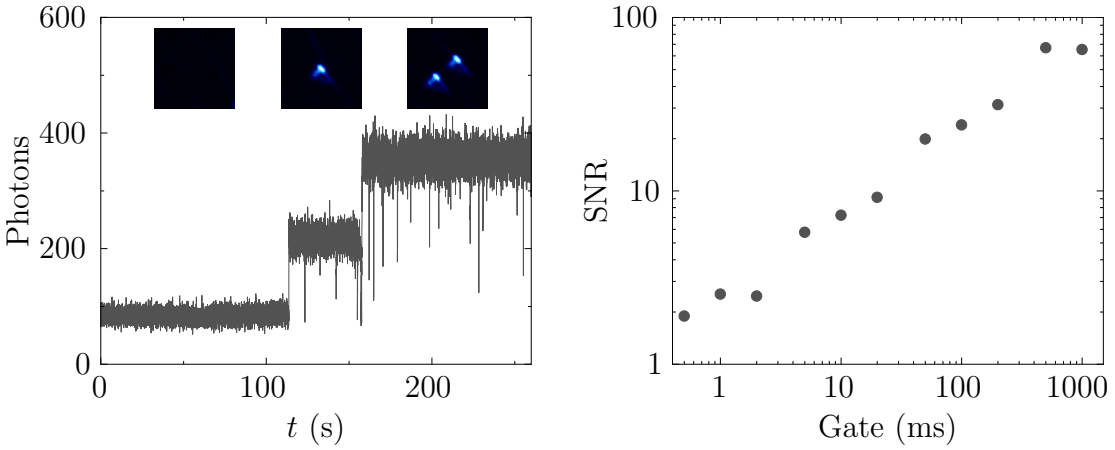

Figure 4.9. Characterization of the PMT signal. Left: PMT 397-nm detected photons for a time window of 260 s and a gate of 5 ms when two ions are loaded and sequentially cooled in the trap. Right: SNR from a single laser-cooled $^{40}Ca^{+}$ ion in the Penning trap as a function of the PMT gate.

4.2.3 PMT characterization

As described in Sec. 3.4, half of the fluorescence collected by the optical system is directed towards the photomultiplier tube (PMT). A typical PMT signal where two ions were sequentially cooled is shown on the left side of Fig. 4.9. The detection of the first ion at $t \approx 115$ s and the second at $t \approx 160$ s gives rise to two discrete levels in the fluorescence signal. The signal-to-noise ratio (SNR) can be calculated as

$$\mathrm{SNR} = \frac{S - B}{\mathrm{FWHM}_B}, \tag{4.5}$$

where S and B are the signal and background noise height, respectively, and FWHM_B is the full width at half maximum of the noise distribution sample. In the right side of Fig. 4.9, the SNR is studied as a function of the gate time. The higher the gate time, the higher the SNR, but at the expense of a slower performance.

The drops observed in the fluorescence signal (left side of Fig. 4.9) were due to elastic collisions with the background gas molecules at room temperature. In these collisions, the electric field created by the trapped ion polarizes the molecules, with a collision cross section σ_{col} that depends on the molecule's polarizability α_{pol} [138] and velocity v_{mol} as

$$\sigma_{\mathrm{col}} = \pi\Gamma\left(1/3\right)\left[\frac{\alpha_{\mathrm{pol}} q^2}{16\varepsilon_0 \hbar v_{\mathrm{mol}}}\right]^{2/3}, \tag{4.6}$$

where $\Gamma(a)$ is the gamma function with argument a [139]. The collision rate γ_{col} depends on the gas density n_0 and the collision cross section as $\gamma_{\mathrm{col}} = n_0 \langle \sigma_{\mathrm{col}} v_{\mathrm{mol}} \rangle$, where the average is over the thermal distribution. It can be calculated in international units as $\gamma_{\mathrm{col}} = 1.23 \cdot 10^5 \alpha_{\mathrm{pol}}^{2/3} (\tilde{v})^{1/3}$, being $\tilde{v} = (2k_{\mathrm{B}}T/\mu)^{1/2}$ the reduced

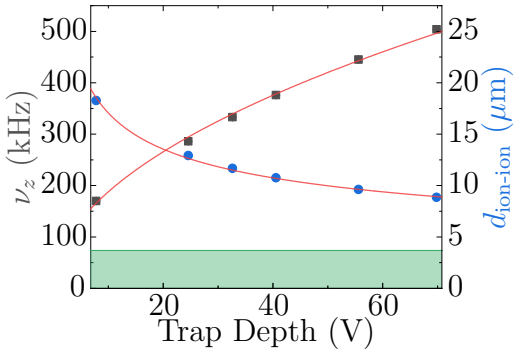

Figure 4.10. Characterization of the axial trapping frequency. Evolution of the measured common-mode axial frequency (grey squares) and optically-determined ion-ion distance (blue circles) vs trap depth. The solid red lines fit the data points. The fitting function for the frequency data is proportional to the square root of the trap depth, while that for $d_{\text{ion-ion}}$ is inversely proportional to the cube root. The green-shaded area marks the limit to resolve two ions.

velocity and μ the reduced mass of the two-particle system [139]. The background pressure can be calculated from n_0 using the ideal-gas equation. The most abundant molecules below 10^{-8} mbar are H_2O and H_2, due to the difficulty of pumping them out. In this experiment, $\gamma_{\text{col}} \approx 0.1$ s^{-1}, which means a background pressure $p \approx 3 \cdot 10^{-10}$ mbar if the drops in the fluorescence signal were caused, as assumed, by collisions with H_2O or H_2.

4.2.4 Trap characterization

Figure 4.10 shows the distance $d_{\text{ion-ion}}$ in a two-ion crystal as a function of the trap potential, covering a common-axial mode frequency from 170 kHz to 500 kHz. The dependency of $d_{\text{ion-ion}}$ on the axial frequency is given by Eq. (2.16). If these results are extrapolated to higher frequencies, even a two-ion crystal at the maximum axial-mode frequency the trap can be operated, $\nu_z = 1.902$ MHz, could be spatially resolved by the optical system. For such a frequency, $d_{\text{ion-ion}} = 3.65$ μm.

4.2.5 Cooling of the radial modes. Axialization

As it was stated in Sec. 2.2, the modified-cyclotron and the unstable magnetron motions can be cooled simultaneously by tuning the position of the laser beam in addition to its frequency. Experimentally, this has been achieved by scanning the beam position in small steps (20 μm) around the trap centre. The final position was a compromise between the maximum fluorescence signal observed from the trap centre and the minimum width in the projection of the photon radial distribution. However, this method presented several drawbacks. In the Penning-trap setup, the outputs of the laser beams from fibre collimators are located 1.5 m away from the

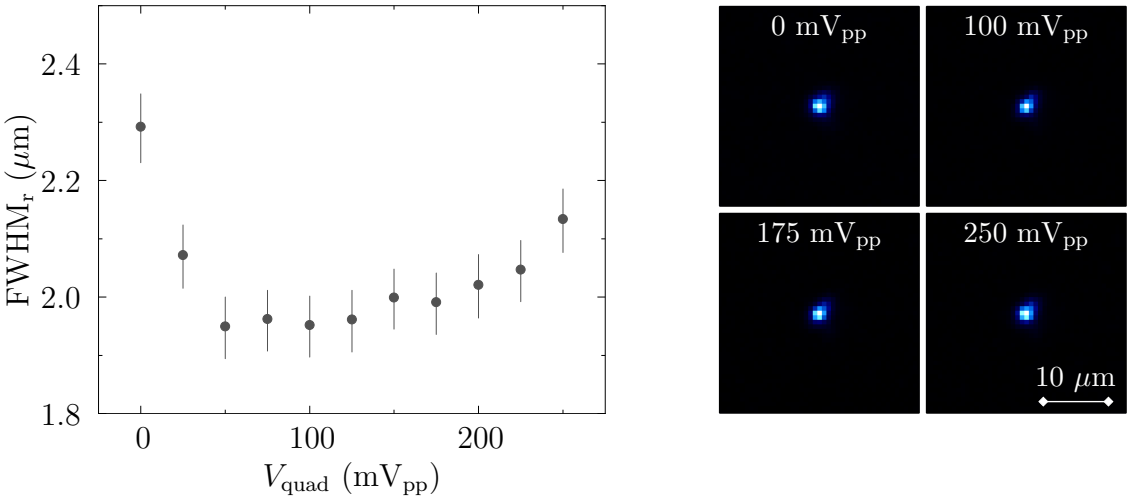

Figure 4.11. Axialization of a single ion. Left: evolution of the radial FWHM of a single ion as a function of the axialization voltage. The axialization frequency was always $\nu_{quad} = 2\,689\,365$ Hz. The quadrupolar field was created by alternating opposite polarity. Right: EMCCD images of a single ion for different axialization voltages. These images are the average of ten consecutive measurements with 1-s exposure time.

trap (see Fig. 3.8) on an optical table physically separated from the beamline structure. This made the final position of the radial laser-cooling beam very sensitive to mechanical instabilities. With the cooling parameters given in Tab. 4.2, and using Eq. (2.27), the ratio between the cooling rates for the oscillation-amplitude of the modified-cyclotron and magnetron motions is $\left(d\left\langle\rho_-^2\right\rangle/dt\right) / \left(d\left\langle\rho_+^2\right\rangle/dt\right) \approx 0.025$. This means a much slower energy reduction in the magnetron mode. A quadrupolar field at $\nu \approx \nu_c$ was applied simultaneously with the laser interaction to speed up the cooling of the two radial motions. This field produces an energy exchange between the two motions allowing to efficiently cool the magnetron through the modified-cyclotron. This technique is normally called axialization since the ion's motion is squeezed into the axial axis. Its first experimental implementation is reported in Ref. [140].

In Fig. 4.11, the axialization technique is studied for a single $^{40}Ca^+$ ion. The minimum radial width obtained is FWHM$_r$ (100 mV$_{pp}$) = 1.87(9) μm, compared to FWHM$_r$ (0 mV$_{pp}$) = 2.25(17) μm when axialization is not applied. Once a steady state has been reached for strong axialization (see Sec. 2.2.1), the phonon numbers $n_\pm$ in the two radial motions become equal due to the energy exchange induced by the interaction with the quadrupolar field [77]. Assuming this equilibrium condition, upper values can be given for each of the amplitudes of the radial motions based on the EMCCD-image projections. Starting from the radial motional equation, Eq. (2.7), the measured FWHM can be related with the ion's motional amplitudes ρ_+ and ρ_- as FWHM $= 2\sqrt{\ln 2}\sqrt{\rho_+^2 + \rho_-^2}$. Taking into account the dependence of the ion's energy on the motional amplitudes (Eq. (2.8)), $\rho_+ = \rho_-$

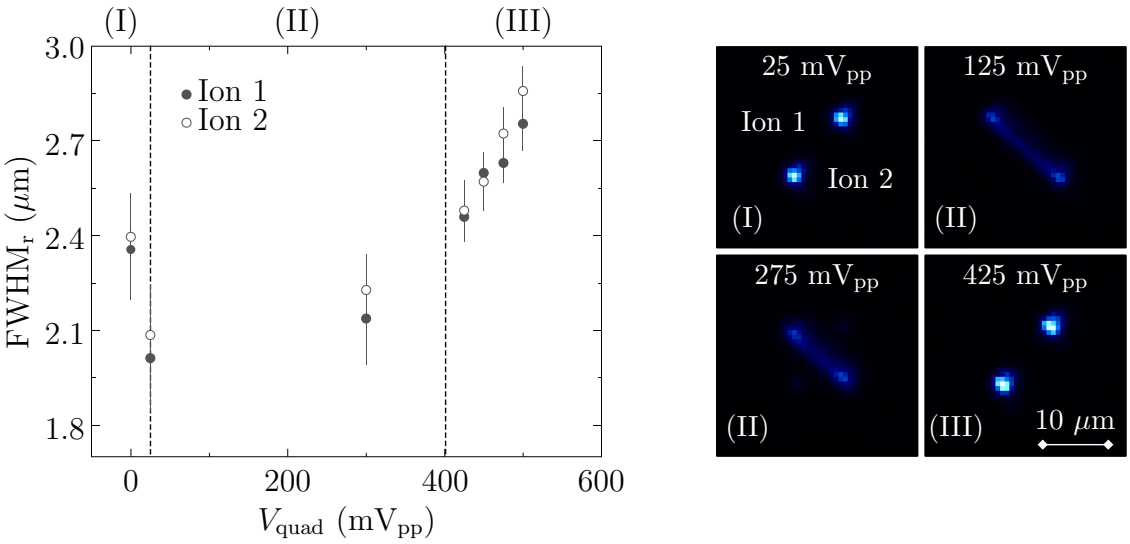

Figure 4.12. Axialization of a two-ion crystal. Left: evolution of the radial FWHM of a two-ion crystal as a function of the axialization voltage. Right: EMCCD images of a two-ion crystal for different axialization voltages. The crystal was stable along the axial direction in regions (I) and (III). In the region (II), the crystal oriented most of the time in the radial plane.

in the steady state. Thus, each of the radial-motion amplitudes can be directly calculated from the image width as

$$\rho_{\pm} = \frac{\text{FWHM}}{2\sqrt{2\ln 2}}. \tag{4.7}$$

An amplitude $\rho_{\pm} < 674(32)$ nm is estimated.

According to Ref. [13], the cooling rate achieved by axialization should increase monotonically with the voltage and tend to a maximum value limited by the laser cooling rate of the modified-cyclotron motion. However, an increase of the ion's amplitude is observed in Fig. 4.11 for high V_{quad}, which could be attributed to a residual dipolar field originated as a consequence of misalignments between the electrodes.

Figure 4.12 shows a similar analysis to that presented in Fig. 4.11 but for a $^{40}Ca^{+}$ - $^{40}Ca^{+}$ balanced crystal. The minimum radial amplitude for ion 1 is FWHM$_r$ (25 mV$_{pp}$) = 2.09(16) μm, compared to FWHM$_r$ (0 mV$_{pp}$) = 2.40(14) μm when axialization is not applied, and for ion 2 FWHM$_r$ (25 mV$_{pp}$) = 2.01(17) μm, compared to FWHM$_r$ (0 mV$_{pp}$) = 2.36(16) μm obtained when axialization is not applied. Using again the hypothesis that the number of phonons is shared for the radial modes, an amplitude $\rho_{\pm} < 753(36)$ nm is estimated.

Three regions can be identified in Fig. 4.12 depending on the crystal orientation. In regions (I) and (III), the crystal is axially oriented as expected when it is cooled to temperatures in the range of millikelvin. However, in region (II) the two-ion

crystal is oriented radially in a much higher angular-momentum configuration. No fundamental reason has been found that could explain this behaviour, which would need further investigation.

4.2.6 Spectroscopy on the $D_{3/2} \Leftrightarrow P_{1/2}$ transition. Dark resonances

The atomic level scheme of $^{40}Ca^{+}$ in the 7-T magnetic field can be found in Fig. 2.4. In the experiments presented in the following, one of the repumping 866-nm lasers was scanned around resonance while the rest of the lasers used in Doppler-cooling remained at a steady frequency. It was possible to observe dark resonances (drops in the fluorescence level) superimposed to the Lorentzian profile of the cooling transition when a Λ-type transition between the 866-nm laser and one of the others was formed [141, 142]. The left side of Fig. 4.13 shows a four-level model representing the relevant states involved in the dark-resonance phenomenon. In the cooling scheme used in this experiment, each of the $P_{1/2}$ Zeeman sublevels ($|2\rangle$ in Fig. 4.13) is connected to one of the $S_{1/2}$ ($|1\rangle$) and to two $D_{3/2}$ Zeeman sublevels ($|3\rangle$ and $|4\rangle$). Therefore, two dark resonances are observed for each repumping-laser frequency sweep (right side of Fig. 4.13).

The dynamics of the system is described by a Hamiltonian consisting of two components,

$$\mathcal{H} = \mathcal{H}_A + \mathcal{H}_I. \tag{4.8}$$

$\mathcal{H}_A$ is the atomic Hamiltonian,

$$\mathcal{H}_A = \sum_{a=1}^{4} \hbar\omega_a \left|a\right\rangle \left\langle a\right|, \tag{4.9}$$

where ω_a is the Bohr frequency of the state $|a\rangle$. $\mathcal{H}_I$ accounts for the ion-laser interaction,

$$\begin{aligned} \mathcal{H}_I = & \frac{1}{2}\hbar\Omega_{12}\left(\left|2\right\rangle\left\langle 1\right| e^{-i\omega_{12}t} + \left|1\right\rangle\left\langle 2\right| e^{i\omega_{12}t}\right) + \\ & \frac{1}{2}\hbar\Omega_{32}\left(\left|2\right\rangle\left\langle 3\right| e^{-i\omega_{32}t} + \left|3\right\rangle\left\langle 2\right| e^{i\omega_{32}t}\right) + \\ & \frac{1}{2}\hbar\Omega_{42}\left(\left|2\right\rangle\left\langle 4\right| e^{-i\omega_{42}t} + \left|4\right\rangle\left\langle 2\right| e^{i\omega_{42}t}\right), \end{aligned} \tag{4.10}$$

where ω_{ab} and Ω_{ab} are the transition and Rabi frequencies of the lasers addressing $|a\rangle \Leftrightarrow |b\rangle$ [143]. Ω_{ab} is defined in terms of the electric dipole moment $\vec{D}_{ab}$ and the electric field amplitude $\vec{E}_{ab}$ as $\hbar\Omega_{ab} = \vec{D}_{ab} \cdot \vec{E}_{ab}$. In the interaction picture [143], and having established $\hbar\omega_2$ as the zero point of energy, the total Hamiltonian

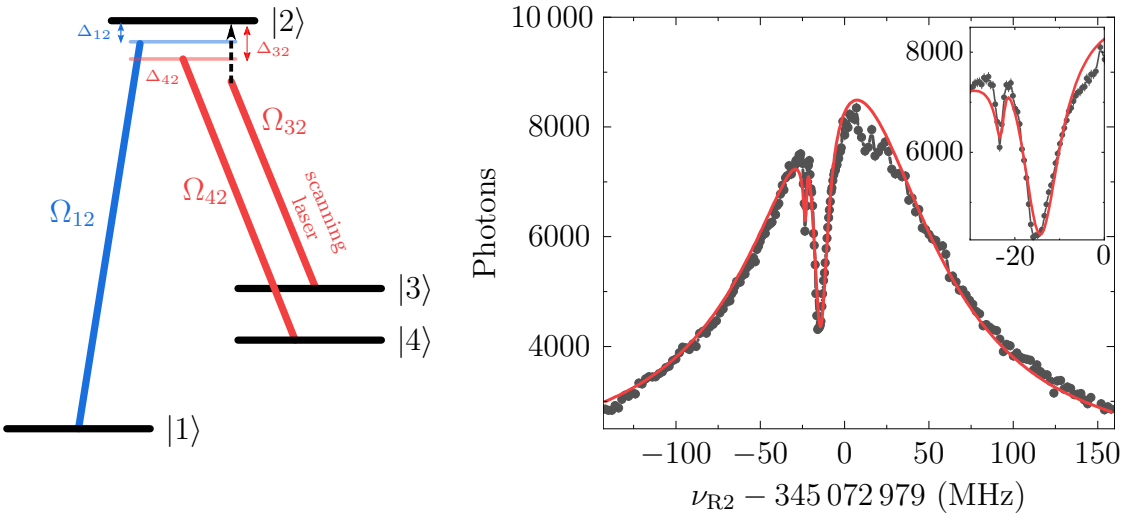

Figure 4.13. Dark resonances in the 7-T magnetic field. Left: the four-level system used to describe the observation of dark resonances. $|1\rangle$ represents one of the $S_{1/2}$ Zeeman sublevels connected to the corresponding $P_{1/2}$ sublevel $|2\rangle$ by a 397-nm laser field detuned Δ_{12} from the resonance frequency. Levels $|3\rangle$ and $|4\rangle$ represent $D_{3/2}$ Zeeman sublevels. $|3\rangle$ is connected to $|2\rangle$ by 866-nm light detuned Δ_{42} from the resonance frequency, while the laser frequency of the transition $|3\rangle \Leftrightarrow |2\rangle$ is scanned around resonance (vertical dashed line). Right: number of registered photons from the $S_{1/2} \Leftrightarrow P_{1/2}$ transition as a function of the frequency of one of the $D_{3/2} \Leftrightarrow P_{1/2}$ lasers. The inset zooms the region where the two dark resonances appear. In this particular case, the scanning laser was RE2, according to the nomenclature established in Fig. 4.7. See the text for more details about the fitting.

matrix representation is

$$\mathcal{H} = \begin{pmatrix} \Delta_{12} & \frac{\Omega_{12}}{2} & 0 & 0 \\ \frac{\Omega_{12}}{2} & 0 & \frac{\Omega_{12}}{2} & \frac{\Omega_{42}}{2} \\ 0 & \frac{\Omega_{32}}{2} & \Delta_{32} & 0 \\ 0 & \frac{\Omega_{42}}{2} & 0 & \Delta_{42} \end{pmatrix}, \tag{4.11}$$

where Δ_{ab} is the detuning of the lasers addressing the transitions $|a\rangle \Leftrightarrow |b\rangle$. The diagonal elements correspond to $\mathcal{H}_A$ and the rest to $\mathcal{H}_I$ [144].

To encompass the dissipative and incoherent processes originating from the spontaneous emission and the laser finite linewidth, it is necessary to study the interaction of the ion with the surrounding [145]. Since the complete quantum system belongs to an infinite-dimension Hilbert space, as the radiation field has infinite modes, the usual approach is to model the ion as an open quantum system. Under these circumstances, a statistical description of the system, provided by the density-matrix formalism, becomes necessary. The density matrix $\hat{\rho}$ is a generalization of the wave function to describe the state of the system. While the latter

can only represent pure states, $\hat{\rho}$ can be used to describe a statistical ensemble consisting of different pure states prepared with certain probabilities. The evolution of a quantum open system is given by the Lindblad master equation [145],

$$\frac{d\hat{\rho}}{dt} = -\frac{i}{\hbar}\left[\mathcal{H}, \hat{\rho}\right] + \mathcal{L}\left(\hat{\rho}\right), \tag{4.12}$$

where $\mathcal{L}\left(\hat{\rho}\right)$ is the Lindblad operator defined as

$$\mathcal{L}\left(\hat{\rho}\right) = \sum_{k}\left[C_i\hat{\rho}C_i^{\dagger} - \frac{1}{2}\left(C_i^{\dagger}C_i\hat{\rho} + \hat{\rho}C_i^{\dagger}C_i\right)\right], \tag{4.13}$$

with the transition operators C_i describing the different dissipative processes. The spontaneous decay from $|2\rangle$ to $|1\rangle$, $|3\rangle$, and $|4\rangle$ is described by [146]

$$C_{ba} = \sqrt{\Gamma_{ba}}\,|a\rangle\langle b|, \tag{4.14}$$

where $b \equiv 2$ and $a \equiv 1, 3, 4$. The finite laser linewidths are also accounted as a dissipative operator as [146]

$$C_{aa} = \sqrt{\Gamma_{la}}\,|a\rangle\langle a|, \tag{4.15}$$

where $a \equiv 1, 3, 4$ and $\Gamma_{la} = 2\pi\sigma_a$ with σ_a the linewidth of the laser addressing the transition $|a\rangle \Leftrightarrow |2\rangle$.

Equation (4.12) leads to a set of ten differential equations known as optical Bloch equations [143]. The stationary state is found by imposing $\left(d\hat{\rho}\right)/\left(dt\right) = 0$, which implies finding the solution of a linear system comprising ten equations to find the density matrix elements, for which Mathematica[1] was used. The number of 397-nm photons detected in the experiment is proportional to the population in the upper state $\hat{\rho}_{22}$.

In the right side of Fig. 4.13, a functional form proportional to $\hat{\rho}_{22}$ is used to fit a frequency scan of laser R2. Qualitatively, a dip in the fluorescence profile appears when $\Delta_{32} = \Delta_{42}, \Delta_{12}$, and its width and depth are governed by the operators C_{ba} and C_{aa}, associated to the natural linewidth of the transition and the laser linewidth, respectively. Three parameters of the laser beam are extracted from the fit: detuning, saturation, and linewidth. While saturation and linewidth can be experimentally estimated by optical power and wavelength meters, respectively, this is the more reliable way to fix the detuning. In general, the cooling and repumping lasers are set to 15 MHz and 20 MHz below resonance, respectively, in order to achieve the lowest ion temperature [147]. For the particular case shown in Fig. 4.13, $\Delta_{12} = -2\pi \times 14.48(50)$ MHz and $\Delta_{42} = -2\pi \times 23.1(11)$ MHz.

[1] Wolfram Mathematica 12.2.0.0

Chapter 5

Cyclotron-frequency ratios of $^{42,44,48}Ca^+$ and $^{40}Ca^+$

The cyclotron-frequency ratios of the calcium isotopes $^{42,44,48}Ca^+$ - $^{40}Ca^+$ have been precisely determined using the optical detection method for the first time. Since all these isotopes can be laser cooled, the measurements have been performed using one single ion at a time in the trap, alternating between one of the isotopes and $^{40}Ca^+$. Most of the results presented in this chapter have been recently published in Ref. [148]. The general case, i.e., measurements with a two-ion crystal, is presented in Chapter 6.

The values obtained in this thesis work agree within 1σ with the literature values [149], although similar precision is only obtained in the case of $^{44}Ca^+$. These results, however, constitute the first characterization of the sensor ion [35] in the Penning trap before the implementation of the optical detection method on an unbalanced crystal [37], and they have been used to estimate the ultimate precision achievable with the existing apparatus.

The optical detection method is described in the first part of the chapter, presenting the optimization of the experimental parameters. The full analysis process of a complete mass-ratio measurement is shown, and the results obtained from all the motional eigenfrequencies applying the invariance theorem are compared with the case using only the radial ones. Afterwards, the analysis procedure of the frequency ratios of the pairs $^{42,44,48}Ca^+$ - $^{40}Ca^+$ is presented, showing a direct measurement of the ion position and amplitude for each measurement. The ultimate precision limit is discussed, and the mutual dependence of the three eigenfrequencies is studied through a correlation analysis. Finally, and beyond its application in mass spectrometry, the potential exploitation of this technique in the fields of force sensing [32, 150] and to probe fundamental symmetries [83, 151] are underlined.

5.1 Motional frequency measurements on a laser-cooled ion

The use of the fluorescence signal from a dipolar transition employed for Doppler cooling in the field of Penning-trap mass spectrometry was proposed and first tried in the 80s [152]. An approach of this idea has been exploited in Paul traps for the identification of molecular ions, reaching a typical mass resolution of $\sim 10^{-4}$ [153–158]. In the Ions Traps and Lasers Laboratory at the University of Granada, previous studies using that approach have been carried out with an open-ring Paul trap with a single ion [159] and a two-ion balanced crystal [160]. In Penning traps, it has been only tried with ion ensembles [161, 162] with outcomes far away from the level of precision reached using other techniques based on bolometric detection [91]: ion-balance technique [20], pulse-and-phase (PnP) [163], or pulse-and-amplify (PnA) [23]. In this thesis work, a suitable measurement protocol has been developed for the determination of the three ion's eigenfrequencies in the Penning trap using the optical signal registered on a electron-multiplying charge-coupled device (EMCCD) and a photomultiplier tube (PMT).

5.1.1 Measurement procedure

The measurement protocol is described in Fig. 5.1. A full measurement of any mass ratio comprised the determination of the cyclotron frequency ν_c of both the reference ion and the ion of interest, which play an analogous role to that of the sensor and target ions in the Coulomb crystal. The value obtained from the reference ion (whose mass is well known) was used to calibrate the magnetic field so that the charge-to-mass ratio of the ion of interest can be directly calculated from its cyclotron frequency according to Eq. (2.3).

In the experiment, the ion was loaded from the external Paul-trap source (see Secs. 3.1.1 and 4.1.1) and cooled to the Doppler limit. During the in-flight trapping sequence, the Penning trap was biased to 150 V, matching the ion's kinetic energy (see Fig. 4.2). After the capture, the trap potentials were adiabatically reduced to reach 0 V in the ring electrode. To achieve the Doppler limit within a few seconds, the frequencies of the cooling lasers were ramped towards resonance to match the ion's Doppler shift due to its initial energy (see Sec. 4.2). The motional frequency measurement was triggered once the ion's fluorescence was observed with the EMCCD.

The measurement sequence has been fully automated in ARTIQ and/or the Master PC (see Sec. 3.5). Several measurements of each eigenfrequency were carried out, as shown in the green box of Fig. 5.1, with 5/3/5 runs for $\nu_+/\nu_-/\nu_z$ in this case. The relative number of measurements for each eigenfrequency depends on its contribution to the overall uncertainty of the cyclotron frequency. The values chosen are discussed in Sec. 5.1.3, where the dependence on the excitation time is presented.

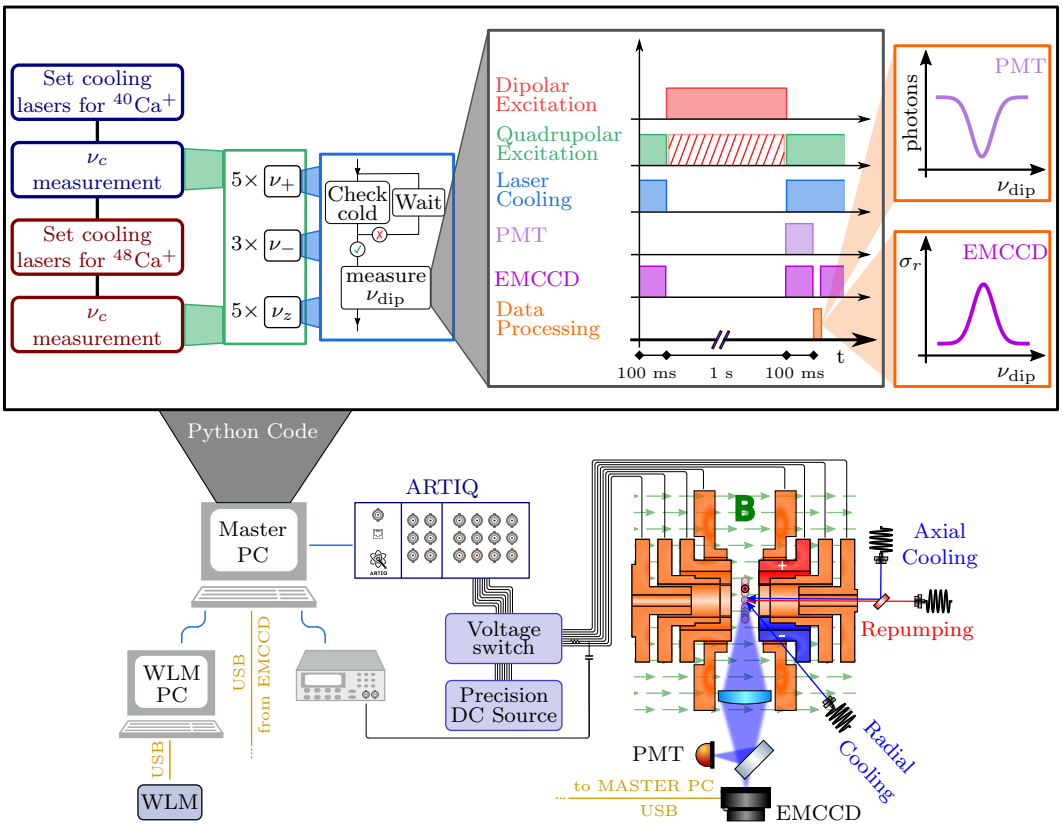

Figure 5.1. Measurement protocol. A block diagram of a complete mass- or cyclotron-frequency ratio measurement is presented in the upper part, including the time sequence used for each individual cycle. All the information contained in this box is scheduled in a Python script compiled and executed both in the Master PC and ARTIQ's FPGA. A detailed description of the experimental setup was presented in Chapter 3.

The timing sequence for each measurement is depicted in the blue box of Fig. 5.1. Each ion's eigenfrequency was determined by scanning the frequency of an external electric dipolar field applied to one of the segments of the trap's ring electrode RE2 (see Sec. 3.1) around the resonance value. Before probing the ion, it was checked to be cold (orange box in Fig. 5.1). For that purpose, the script states a minimum number of photons to be detected on a specific region of the EMCCD before it launches the frequency scan. A quadrupolar field oscillating at the cyclotron frequency was applied in the radial direction for axialization (see Sec. 4.2.5). Once the three ion's eigenmotions were cooled, the excitation was turned on and laser cooling was switched off. To accomplish the latter in less than 1 ms, an acousto-optic modulator (AOM) was used on two of the four 866-nm repumping lasers (see Sec. 3.3). After the dipolar excitation was turned off, the cooling lasers were switched on again to observe the ion's motional amplitude through the scattered photons. The photons scattered by the ion show a widened

fluorescence image in the EMCCD along the excitation direction and/or a drop of the number of detected photons in the PMT. The first observation is a direct consequence of the ion's higher orbit and the second is due to Doppler broadening. If a collision with a background molecule occurred, the number of detected photons decreased below a specific threshold, and the measurement was discarded and repeated.

Since laser cooling was switched off while probing the eigenfrequency, the linewidth is not broadened due to the damping force of the cooling laser. Therefore, these experiments have yielded more precise measurements than previous experiments with Penning traps [152, 161, 162], or other experiments carried out in the laboratory with a Paul trap [159, 160], where the cooling laser was never switched off.

5.1.2 Data analysis

As mentioned above, the oscillation amplitude of the ion after the excitation was read out through the fluorescence photons scattered on the cooling transition ($3p^6 4s\,{}^2\mathrm{S}_{1/2} \Leftrightarrow 3p^6 4p\,{}^2\mathrm{P}_{1/2}$ in the case of ${}^{40,42,44,48}\mathrm{Ca}^+$) and recorded by the EMCCD and the PMT. The time evolution of the ion image in the EMCCD after it was resonantly excited at the modified-cyclotron frequency is shown in Fig. 5.2. At $t = 0$, the excitation amplitude is $\rho_+ = 27(5)$ μm, while the photon signal in the PMT remains constant all the time. It was necessary to excite the ion to higher amplitudes ($\rho_+ > 50$ μm) to observe a drop of counts in the PMT. This behaviour can be explained based on two main points. First, the radial cooling rate was low enough to observe a time evolution in the order of milliseconds, even when axialization and the position of the radial beams were optimized. This allowed for the observation with the EMCCD, impossible if the cooling dynamics had taken place within microseconds. Second, the scattering rate was dominated by the interaction with the axial beams (see Tab. 4.2). Thus, the level of fluorescence remained basically unaltered for small radial excitations. For the magnetron motion, the situation is equivalent.

The only limit in sensitivity for the radial eigenmotions was the resolution of the optical system, which is 2.75(3) μm (see Tab. 3.4), and the time constant of the evolution of the ion's amplitude, shown on the right side of Fig. 5.2, equal to 80(23) ms. The latter has been used to estimate the ion's amplitude just after the excitation is turned off. In the actual experiment, the minimum radial amplitude that can be measured with reasonable statistics has been limited to 10 μm by the fluctuations in the scattering rate, which may arise from changes in the cooling rate.

In order to extract the ion's radial eigenfrequencies, the EMCCD images have been automatically analysed using a Python script. The first image with 75-ms accumulation time (upper left corner in Fig. 5.2) is used for the analysis. The image has been rotated for the analysis, as shown in Fig. 5.3 (a,b). The most

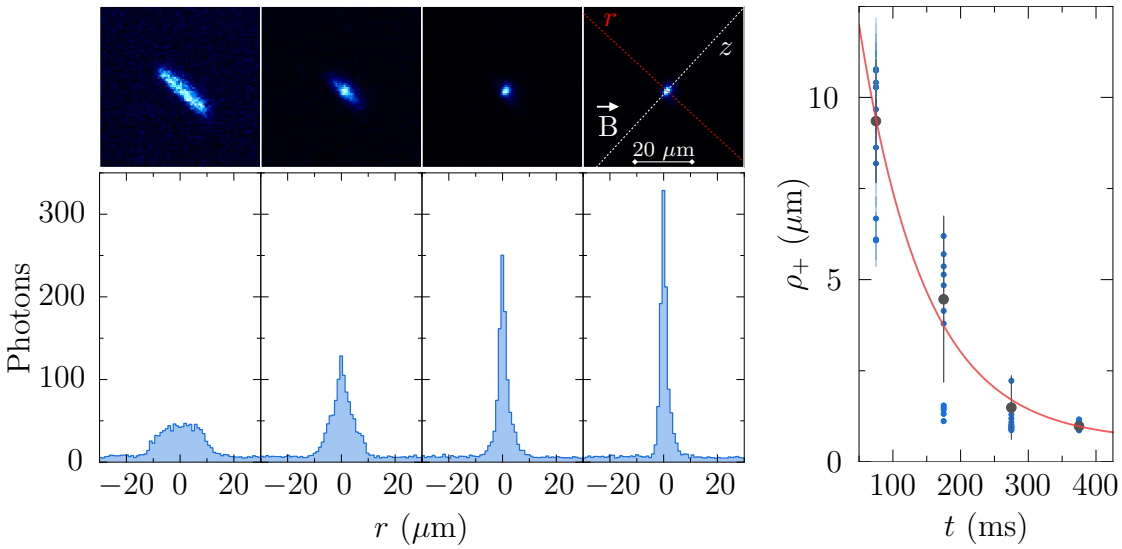

Figure 5.2. Time evolution of the EMCCD image after excitation. The exposure time is 75 ms, and the start time for each frame is triggered every 100 ms. Left: images and projections along the radial plane r (sum of 10 pixels along the axial axis). Right: radial width as a function of time for several measurements on resonance with the modified-cyclotron motion. The small blue solid circles are individual measurements, and the big dark grey ones are their average. They are fitted to an exponential decay function.

important parameter is the width of the radial distribution. Two ways have been considered to determine the uncertainty: weighting the data points by the photon count statistical uncertainty (square root of total number of registered photons, according to Poisson distribution) or weighting the data points uniformly. In the first case, Gaussian error propagation has been used to estimate the uncertainty of the width from the photons' projection in the radial direction. In the second case, the necessary amount of error to obtain a good fit featuring $\chi^2 = 1$ has been associated with the data points, and Gaussian error propagation is likewise applied. The first method calculates the fitting internal uncertainty while the second calculates the external uncertainty. The larger of these two values has been used as the uncertainty associated with the extracted ion's amplitude.

The resonance curve has been built by representing these amplitudes as a function of the excitation frequency, as shown in the right side (e) of Fig. 5.3, where a Gaussian function is used to fit the data. The procedure using internal and external fitting uncertainties discussed above has been applied to estimate the uncertainty associated with the central frequency. The analysis has been carried out both using Gaussian (like in Fig. 5.3) and sinc functions, obtaining equivalent results in terms of the central frequency and its associated uncertainty.

In the case of the axial motion, the PMT was more sensitive to axial amplitude variations than the EMCCD: the cooling rate in the axial motion, well below the

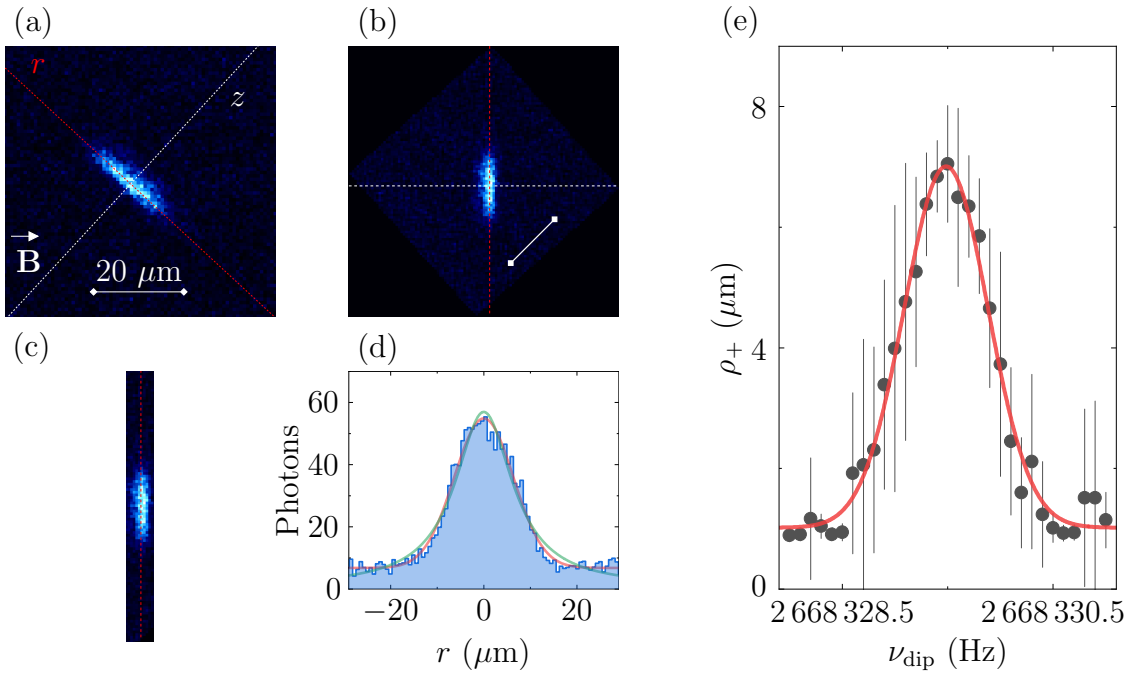

Figure 5.3. Analysis of the EMCCD data. Left: analysis steps to extract the ion's radial width. The original tilted image (a) is rotated to the natural matrix axis using interpolation methods (b). Gaussian and Lorentzian fittings are performed to a ten-pixel wide projection along the radial plane (c,d). The ion's amplitude is estimated as half of the full width at half maximum (FWHM) from the fit. Right (e): radial amplitude as a function of the excitation frequency. Each point is obtained by performing the analysis described on the left side of the figure. The excitation time was 1 s and the excitation voltage was 6 μV_{pp}.

75-ms EMCCD acquisition window, was much higher than in the radial ones. It was also easier to see a drop in the number of fluorescence photons due to the Doppler modulation since most of the scattered photons arose from the interaction with the axial laser beams. To observe changes in the EMCCD image, either a higher amplitude or a smaller cooling power would have been needed. In the first situation, the systematic effects originated by the field imperfections would have increased. In the second case, much higher statistics would have been necessary to overcome the loss of signal-to-noise ratio (SNR) (Eq. (4.5)).

The analysis procedure has been automated by a Python script, like in the case of the EMCCD images. The number of photons is registered within a time window from the instant the lasers are switched on to a few milliseconds later. This is indicated by the yellow dashed line on the left side of Fig. 5.4. The resulting resonance curve has a dip around resonance, as shown in the right side of Fig. 5.4. Equivalently to the analysis of the radial eigenmotions, both Gaussian and sinc functions have been used to fit the resonances, obtaining analogous results.

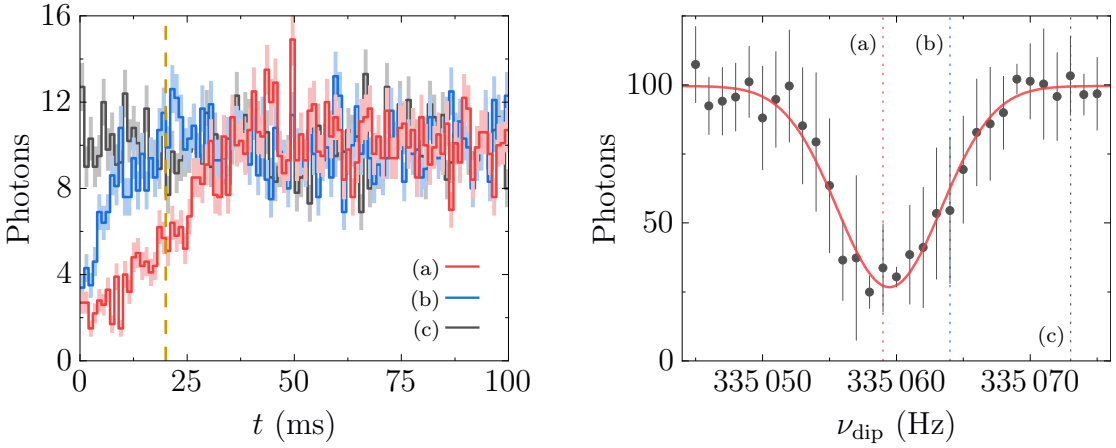

Figure 5.4. Analysis of the PMT data. Left: photon histograms for three different excitation frequencies (the letters (a)-(c) indicate the correspondence with the right side). If the excitation frequency coincides with the ion's motional frequency, the red line is obtained. The grey and blue lines represent the out-of-resonance and intermediate cases, respectively. The binning is 1 ms. Right: number of accumulated photons during a time delimited by the yellow dashed line (left side) as a function of the excitation frequency. The excitation time is 100 ms.

5.1.3 Optimization of the excitation time and voltage

A higher excitation time implies a better frequency resolution, by the properties of the Fourier transform. However, instabilities and drifts limit this time. Resonance curves are shown on the left side of Fig. 5.5 for three different excitation times. The excitation voltage was modified accordingly so that the product of the excitation time and voltage, $t^{+}_{\mathrm{dip}} \cdot V^{+}_{\mathrm{dip}}$, was kept constant. In principle, the ion's amplitude ρ_{+} at the resonance frequency should be the same for all the excitation times, but an increase in the data dispersion and a decrease of the mean value have been observed for longer times, which is attributed to the above-mentioned frequency instability.

To determine the optimum excitation time, a normalized time-independent frequency uncertainty was calculated as

$$\Delta\Omega_u = \Delta\nu_u \sqrt{\frac{t^u_{\mathrm{dip}}}{t_0}\frac{N}{N_0}}, \tag{5.1}$$

where $\Delta\nu_u$ is the uncertainty obtained in a measurement with excitation time t^u_{dip} that is repeated N times, and t_0 and N_0 are a reference time and number of measurements, respectively. $\Delta\Omega_u$ represents the uncertainty that would be obtained if scans using an excitation time t^u_{dip} were performed during the same time it takes to complete N_0 scans using an excitation time t_0. $\Delta\Omega_{+}$ is shown on the right side of Fig. 5.5 for different excitation times, including those plotted on the left side. $t_0 = 1$ s and $N_0 = 5$ in this case. The normalization factor in

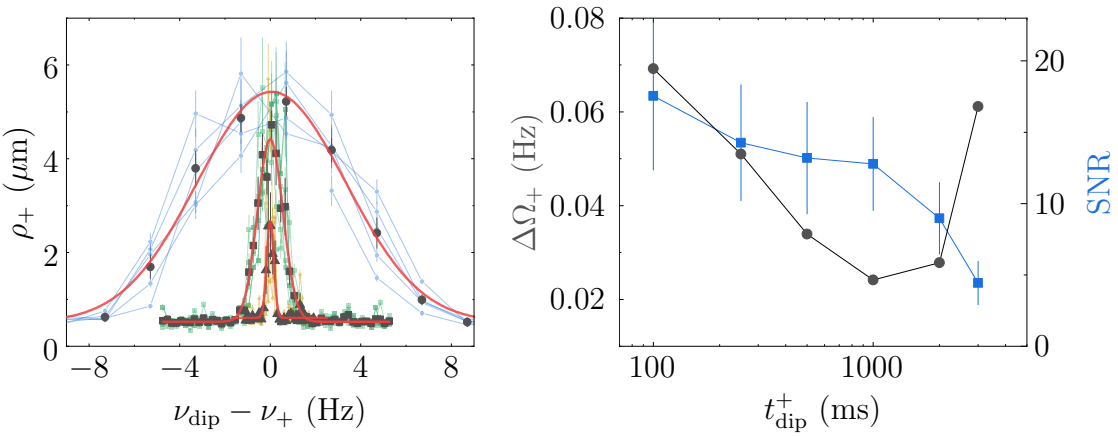

Figure 5.5. Optimization of the excitation time. Left: modified-cyclotron resonances for 100 ms, 500 ms, and 2 s excitation time. The longer the excitation time, the smaller the resonance width. Five scans were taken for each excitation time. The average data are plotted in grey and the solid lines represent the Gaussian fits. Right: normalized uncertainty (Eq. (5.1)) obtained for the central frequency and SNR for the different excitation times. For these measurements, $\nu_+ \approx 2\,685\,578$ Hz.

Eq. (5.1) (root-squared term) has been applied according to the evolution of the uncertainty of the mean value in a Gaussian distribution. The optimal excitation times for $\nu_+/\nu_-/\nu_z$ are 500-1000/100-200/50-100 ms.

The invariance theorem (Eq. (2.10)) has been used to determine the cyclotron frequency ν_c, so the propagation of each eigenfrequency ν_u uncertainty goes as

$$\frac{\partial \nu_c}{\partial \nu_u} = \frac{\nu_u}{\nu_c}. \tag{5.2}$$

The higher the frequency the more its contribution to the overall uncertainty of the cyclotron frequency. The optimal excitation time for each eigenfrequency was used, and the number of scans N performed was adjusted to reduce the statistical uncertainty as needed.

The final value of the eigenfrequency has been calculated as the weighted mean of the individual eigenfrequency measurements ν_i obtained from the fit in each scan,

$$\bar{\nu} = \frac{\sum_N w_i \nu_i}{\sum_N w_i}, \tag{5.3}$$

where $w_i = 1/\left(\Delta\nu_i\right)^2$ is the weighting factor. Two uncertainties can be associated with the sample: internal and external [164]. The internal uncertainty, defined as

$$\Delta\nu_{\mathrm{int}} = \sqrt{\frac{1}{\sum_N w_i}}, \tag{5.4}$$

is calculated from Gaussian error propagation on the data sample. If the uncertainties are well estimated for each ν_i, $\Delta\nu_{\text{int}}$ is a good estimate of the eigenfrequency uncertainty. The external uncertainty $\Delta\nu_{\text{ext}}$, defined as

$$\Delta\nu_{\text{ext}} = \sqrt{\frac{\sum_N w_i \left(\nu_i - \nu\right)^2}{(N-1)\sum_N w_i}}, \tag{5.5}$$

accounts for the statistical dispersion of the sample ν_i. The eigenfrequency uncertainty is chosen as $\Delta\nu = \max\left(\Delta\nu_{\text{int}}, \Delta\nu_{\text{ext}}\right)$.

For low statistics, the probability of finding the ion's frequency in the interval $[\bar{\nu} - \sigma_s, \bar{\nu} + \sigma_s]$, with σ_s the standard deviation of ν, is lower than expected for a Gaussian distribution centred in ν and with standard deviation $\Delta\nu$. In particular, the random variable $(\nu - \bar{\nu})/\sqrt{\sigma_s^2/N}$ has a Student's t-distribution with $N-1$ degrees of freedom [165, 166]. Given the symmetry of this distribution, the probability of finding the frequency ν within a certain interval around the average value can be expressed in terms of the Student's cumulative distribution as

$$P\left(\bar{\nu} - c_s\frac{\sigma_s}{\sqrt{N}} < \nu < \bar{\nu} + c_s\frac{\sigma_s}{\sqrt{N}}\right) = 1 - 2P\left(\frac{\nu - \bar{\nu}}{\sqrt{\sigma_s^2/N}} > c_s\right), \tag{5.6}$$

where c_s is a coefficient that determines the interval size in units of $\sigma_s/\sqrt{N}$. For a confidence level of 68.3 %, the coefficient c_s corresponds to the 84.1^{th} percentile of the Student's t-distribution. The eigenfrequency uncertainty $\Delta\nu$ has consequently been multiplied by c_s to obtain a realistic estimate of the uncertainty even for a low number of measurements N. c_s is always higher than one, decreases monotonously with N, and tends to one for $N \to \infty$ [166].

The other basic parameter that has been optimized is the excitation voltage. For the detection of the radial eigenmotions using the EMCCD signal, a compromise has been found between a desirable small amplitude to attenuate the systematic effects due to the field imperfections and a good SNR. In the left side of Fig. 5.6, the FWHM of the ion image in the radial plane is plotted for different excitation voltages maintaining the excitation time fixed. For low voltages, the fluctuations in the fluorescence signal led to poor SNRs. This is pointed out by the chi-squared test, where $\chi^2 < 1$ confirms that it is improperly fitting noise. On the contrary, for high ion amplitudes, the signal became blurry, since the number of photons registered in each individual pixel was very low. This translates into a high value of χ^2 which suggests that the uncertainties are being underestimated. An optimal configuration was found for $V_{\text{dip}}^{+} \approx 4 - 8\ \mu\text{V}_{\text{pp}}$ in this case. A similar compromise was obtained for the PMT detection in the axial eigenmotion.

As discussed in Sec. 2.1, the motional frequencies varies with the ion's amplitude as a consequence of the imperfections of the magnetic and electric field. To quantify this deviation, the axial frequency was measured for different excitation voltages. The results are shown on the right side of Fig. 5.6. The frequencies

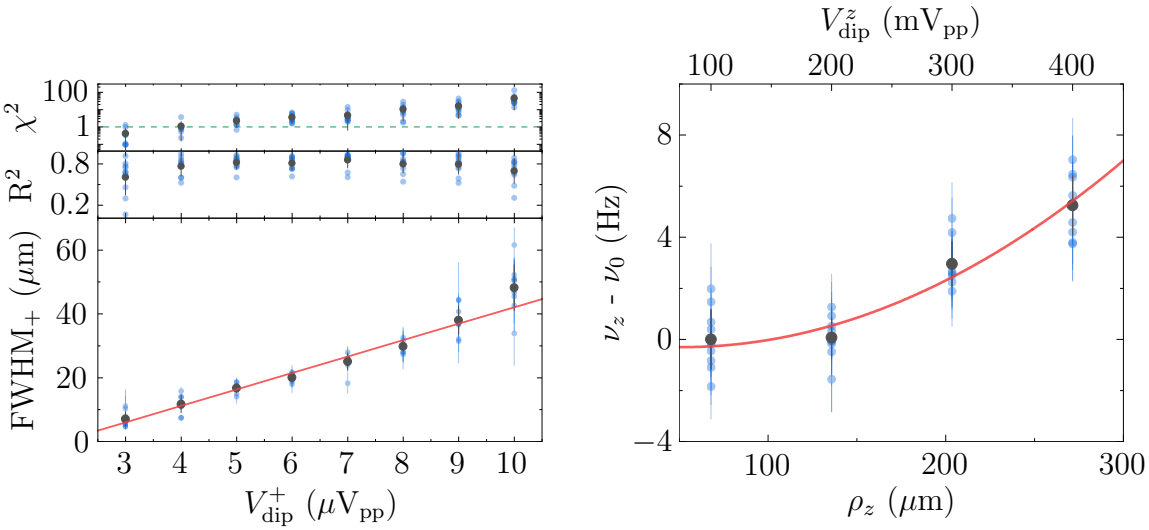

Figure 5.6. Optimization of the excitation voltage. The blue smaller solid circles and the bigger grey ones represent the individual and average data, respectively. Left: FWHM of the modified-cyclotron distribution as a function of the excitation voltage. In the upper part, both the R^2 (coefficient of determination) and the reduced chi-squared statistics are plotted. Right: axial frequency as a function of the axial oscillation amplitude (bottom x axis) and dipolar excitation voltage (top x axis). The data points are obtained from the fits of the resonance curves as shown in Fig. 5.4. $\nu_0 = 271\,329.748$ Hz.

have been corrected to take into account the drift of the electric field during the measurement. The axial amplitude has been estimated as

$$\rho_z = \frac{1}{2}\frac{E_z}{E_r}\frac{\nu_1}{\nu_z}\left(\rho_+\frac{V_{\mathrm{dip}}^{z}}{V_{\mathrm{dip}}^{+}}\frac{t_{\mathrm{dip}}^{+}}{t_{\mathrm{dip}}^{z}} + \rho_-\frac{V_{\mathrm{dip}}^{z}}{V_{\mathrm{dip}}^{-}}\frac{t_{\mathrm{dip}}^{-}}{t_{\mathrm{dip}}^{z}}\right), \tag{5.7}$$

where $E_{r,z}$ are the radial and axial components of the electric field in the trap centre (calculated using SIMION[1]), $\nu_1 = \nu_+ - \nu_-$, and $\rho_{+,-}$ are the modified-cyclotron and magnetron amplitudes obtained from the EMCCD images. $V_{\mathrm{dip}}^{+,-,z}$ are the excitation voltages and $t_{\mathrm{dip}}^{+,-,z}$ the excitation times. Comparing the results from the fit in the right side of Fig. 5.6 with Eq. (2.13b), a coefficient ratio $C_4/C_2 = 1.23(20)\cdot 10^{-2}$ is obtained.

5.1.4 Filtering of spurious data

Some of the experiments threw faulty data on the ion's amplitude or the scattered photons, mostly originating from the collisions with background particles during the excitation time. These data needed to be deleted during the analysis. For this purpose, each of the values obtained for the ion's width (EMCCD) or the scattered

[1]SIMION Ion and Electron Optics Simulator v8.0

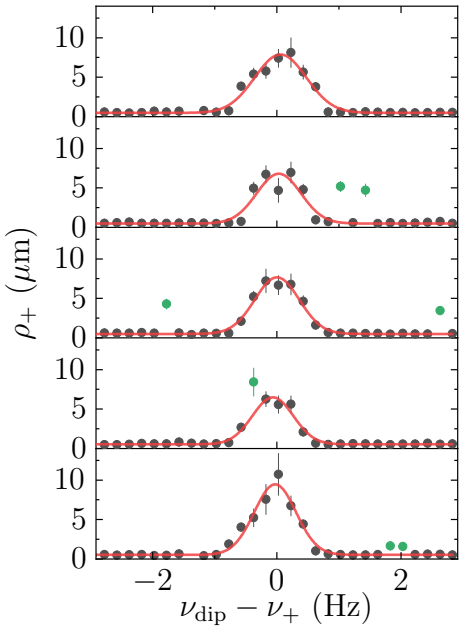

Figure 5.7. Filtering of faulty measurements in a set of consecutive scans. The points which deviate more than a fixed number of standard deviations (around five) from the mean (green solid circles) are discarded. $\nu_+ = 2\,675\,607.174(25)$ Hz.

photons (PMT) have been compared with the rest of the data taken under the same circumstances in other frequency scans. A specific data point has been discarded when it differs more than a number of standard deviations (around ten) from the mean value of the rest of the experiments applying the same excitation frequency and voltage. An example of this kind of filtering of faulty measurements is shown in Fig. 5.7.

In addition to the filtering of individual erroneous experiments, full scans have been also discarded when the expected fit using a sinc/Gaussian functional form is not possible. In most of these cases, the ion was lost in the middle of a frequency scan and the resonance curve was not fully completed. In other cases, some preparation steps in the experiment may have failed, such as the laser regulation, but it was detected at the time.

5.1.5 Determination of the cyclotron frequency

The cyclotron frequency has been calculated from direct measurements of the three eigenfrequencies by means of the invariance theorem (Eq. (2.10)) since this relationship is satisfied even for first-order misalignments between the trapping fields or for a certain degree of trap ellipticity [167]. Nevertheless, the straightforward connection between the cyclotron frequency and the radial eigenfrequencies (Eq. (2.9)) has also been explored. In that case, the modified-cyclotron frequency ν_+ was also measured directly, but the magnetron frequency ν_- was determined through its

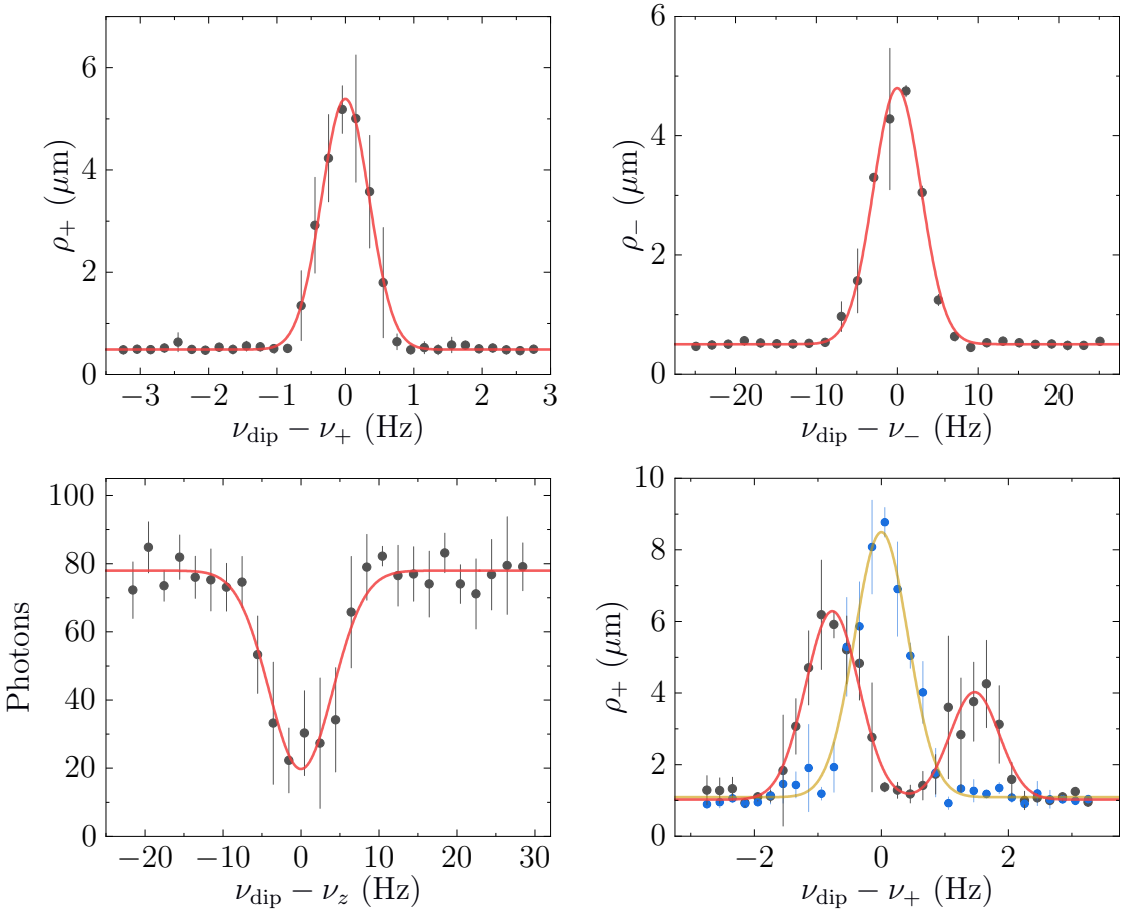

Figure 5.8. Direct eigenfrequency measurements theorem and coupling of the radial motions. Resonance curves for the three ion's eigenmotions and a measurement of the sidebands around the modified-cyclotron frequency. The centre values for the direct measurements are $\nu_+ = 2\,672\,839.214(37)$ Hz, $\nu_- = 16\,524.82(22)$ Hz, and $\nu_z = 297\,226.67(25)$ Hz. For the double-peak measurement, $\nu_{RS} = 2\,672\,829.975(29)$ Hz, $\nu_{BS} = 2\,672\,832.234(62)$ Hz, and $\nu_+ = 2\,672\,830.772(41)$ Hz. Using Eq. (5.8), the magnetron frequency is $\nu_- = 16\,533.563(80)$ Hz. The excitation times are $t^+_{dip} = 1$ s, $t^-_{dip} = 100$ ms, and $t^z_{dip} = 100$ ms, and the excitation voltages $V^+_{dip} = 6\ \mu V_{pp}$, $V^-_{dip} = 60\ \mu V_{pp}$, and $V^z_{dip} = 100\ \mu V_{pp}$. In the double-peak measurement, $\nu_{quad} = 2\,689\,365$ Hz and $V_{quad} = 25\ mV_{pp}$.

coupling to ν_+ by an external quadrupolar electric field oscillating at $\nu_{quad} \approx \nu_c$. The formalism used to describe this coupling between two of the Penning-trap eigenmotions can be found in Ref. [70]. It can be shown that two sidebands at frequencies ν_{RS} and ν_{BS} around ν_+ appear as a consequence of this coupling. The magnetron frequency can be calculated as

$$\nu_- = \nu_{quad} + \nu_+ - \nu_{RS} - \nu_{BS}. \tag{5.8}$$

Table 5.1. Cyclotron frequency of $^{40}Ca^{+}$ obtained by three different methods: the invariance theorem (Eq. (2.10)), the sum of the radial eigenmotions measured directly (Eq. (2.9)), and the same but determining the magnetron frequency from the coupling of the radial motions (Eq. (5.8)).

	Invariance	Direct	Double-peak
ν_c (Hz)	2 689 365.394(46)	2 689 364.03(22)	2 689 364.34(11)

The distance between the sidebands is controlled by the voltage of the external quadrupolar field, while its frequency regulates the relative height of the two sideband peaks.

Figure 5.8 shows an example of the determination of the three eigenfrequencies both directly and through the double-peak signal obtained in the coupling between radial motions. In this case, 5/3/5/5 frequency scans of the eigenmotions $\nu_+/\nu_z/\nu_-/\left(\nu_+ \leftrightarrow \nu_-\right)$ were performed. The cyclotron-frequency values obtained are presented in Tab. 5.1. As it can be seen, the two methods using only the radial modes agree, but they disagree with the invariance theorem results leading to a systematic shift of $4 \cdot 10^{-7}$. This can be used to estimate misalignment between the magnetic and electric field θ_{trap} or a certain degree of trap ellipticity ϵ_{trap} (lack of symmetry around the magnetic field). Following Ref. [168],

$$\frac{9}{4}\theta_{\text{trap}} - \frac{1}{2}\epsilon_{\text{trap}}^2 = \frac{2\nu_+\nu_-}{\nu_z^2} - 1. \tag{5.9}$$

For all the measurements presented throughout this thesis, the cyclotron frequency calculated using only the radial motions is lower than the value using the invariance theorem, which means that the left side of Eq. (5.9) is negative. Therefore, ellipticity is a predominant phenomenon here over misalignments. Assuming $\epsilon_{\text{trap}} \gg \theta_{\text{trap}}$, $\epsilon_{\text{trap}} = 0.7374(10)^{\circ}$. This value did not change over time (it only depends on the mechanical structure of the apparatus), and it could be used to correct the double-peak cyclotron-frequency value by $\nu_-\epsilon_{\text{trap}}^2/2$ [168].

Since the use of the invariance theorem is more robust against systematic effects for the determination of the cyclotron frequency, it has been employed for all the measurements presented in the following. For the data presented in Fig. 5.8, the contributions of each eigenfrequency to the cyclotron frequency uncertainty, $\left(\Delta\nu_c\right)_u = \left(\partial\nu_c\right)/\left(\partial\nu_u\right)\Delta\nu_u$, are $\left(\Delta\nu_c\right)_+ = 37$ mHz, $\left(\Delta\nu_c\right)_- = 1.3$ mHz, and $\left(\Delta\nu_c\right)_z = 46$ mHz. Since these quantities are quadratically added to calculate the cyclotron-frequency uncertainty, the magnetron contribution is negligible. The most relevant contributions come from ν_+ and ν_z. They are usually of the same order, so the same number of scans has been performed for the determination of these two eigenfrequencies.

5.1.6 Determination of the mass ratio

Cyclotron frequency measurements of two calcium isotopes were performed in an alternating way to determine their frequency ratio. Figure 5.9 shows an example of this. One of the isotopes was used as a reference so that the series begins and ends with a measurement of it. In this way, the cyclotron frequency of the reference ion can be precisely obtained at any time t_i at which the ion of interest is studied. Linear interpolation between the two nearest reference-ion measurements, $\nu_c^{\mathrm{ref}}(t_{i-1})$ and $\nu_c^{\mathrm{ref}}(t_{i+1})$, has been used:

$$\nu_c^{\mathrm{ref}}(t_i) = \nu_c^{\mathrm{ref}}(t_{i-1}) + \frac{t_i - t_{i-1}}{t_{i+1} - t_{i-1}} \left[\nu_c^{\mathrm{ref}}(t_{i+1}) - \nu_c^{\mathrm{ref}}(t_{i-1})\right]. \tag{5.10}$$

Using Gaussian error propagation, the uncertainty in the cyclotron frequency of the reference ion at t_i can be estimated as

$$\Delta\nu_c^{\mathrm{ref}}(t_i) = \sqrt{\left[\frac{t_i - t_{i-1}}{t_{i+1} - t_{i-1}} \Delta\nu_c^{\mathrm{ref}}(t_{i+1})\right]^2 + \left[\left(1 - \frac{t_i - t_{i-1}}{t_{i+1} - t_{i-1}}\right) \Delta\nu_c^{\mathrm{ref}}(t_{i-1})\right]^2}. \tag{5.11}$$

A value of the frequency ratio R has been obtained for each measurement of the ion of interest, $\nu_c^{\mathrm{int}}(t_i)$. It has been calculated as

$$R(t_i) = \frac{\nu_c^{\mathrm{ref}}(t_i)}{\nu_c^{\mathrm{int}}(t_i)}, \tag{5.12}$$

with an uncertainty given by

$$\Delta R(t_i) = R(t_i) \sqrt{\left[\frac{\Delta\nu_c^{\mathrm{ref}}(t_i)}{\nu_c^{\mathrm{ref}}(t_i)}\right]^2 + \left[\frac{\Delta\nu_c^{\mathrm{int}}(t_i)}{\nu_c^{\mathrm{int}}(t_i)}\right]^2}. \tag{5.13}$$

The final value of the cyclotron-frequency ratio has been calculated as the weighted mean of the individual ratios, $R_i \equiv R(t_i)$:

$$\bar{R} = \frac{\sum_N w_i R_i}{\sum_N w_i}, \tag{5.14}$$

with $w_i = 1/(\Delta R_i)^2$. The uncertainty analysis is described in Sec. 5.1.3 for the eigenfrequency determination. An internal (Eq. (5.4)) and external (Eq. (5.5)) uncertainty can be associated with the sample of frequency ratios:

$$\Delta R_{\mathrm{int}} = \sqrt{\frac{1}{\sum_N w_i}}, \quad \Delta R_{\mathrm{ext}} = \sqrt{\frac{\sum_N w_i (R_i - R)^2}{(N-1)\sum_N w_i}}. \tag{5.15}$$

The largest one has been taken as the statistical uncertainty ΔR_{stat}. The final uncertainty associated with the cyclotron-frequency ratio is calculated by adding quadratically the systematic uncertainty ΔR_{sys},

$$\Delta R = \sqrt{\Delta R_{\mathrm{stat}}^2 + \Delta R_{\mathrm{sys}}^2}. \tag{5.16}$$

A discussion about the different systematic effects and the associated uncertainties can be found in Sec. 5.5.

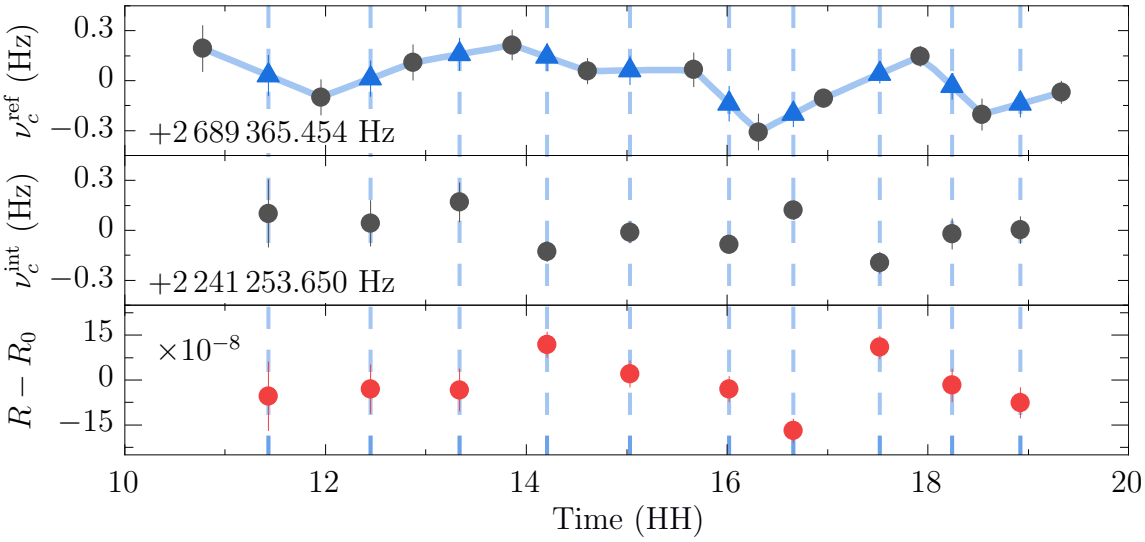

Figure 5.9. Determination of the frequency ratio. The cyclotron frequency of the reference ion, $^{40}Ca^+$ in this case, is plotted in the upper panel (solid circles). The cyclotron frequency of the ion of interest, $^{48}Ca^+$ in this case, is plotted in the middle panel. The cyclotron frequency of the reference ion at the time the ion of interest is measured is determined from linear interpolation (blue solid triangles in the upper panel). The frequency ratio is represented in the lower panel, where R_0 is the mean value.

5.2 Frequency ratio of $^{48}Ca^+$ and $^{40}Ca^+$

^{48}Ca is a neutron-rich (0.187 % natural abundance) isotope of calcium which contains 20 protons and 28 neutrons, which are both magic numbers and contribute to an unusually high half-life of $6.4(14) \cdot 10^{19}$ years [169]. The only observed disintegration pathway is the weak second-order process of double-beta decay $^{48}Ca \rightarrow {}^{48}Ti + 2e^- + 2\bar{\nu}_e$ [55]. Two neutrons in the atomic nucleus decay in two two protons emitting two electrons and two antineutrinos. This decay does not violate lepton number conservation and is allowed in the Standard Model. There is, however, another type of double-beta decay hypothesized, known as neutrinoless double-beta decay, emitting only electrons, which is only possible if the neutrino is considered as a Majorana particle [170]. The detection of the neutrinoless double-beta decay would be a remarkable discovery by itself, clarifying the nature of the neutrino [171, 172].

^{48}Ca is a particularly interesting nucleus since it has the highest Q-value (4267.98(32) keV [173]) of any proposed double-beta decaying isotope. This Q-value can be used in neutrinoless double-beta decay to precisely delimit the energy window in the search of events. Penning traps can provide a precise value of this quantity by measuring the atomic mass of the mother and daughter nuclei, which constitutes a relevant motivation for the implementation of the optical method [50].

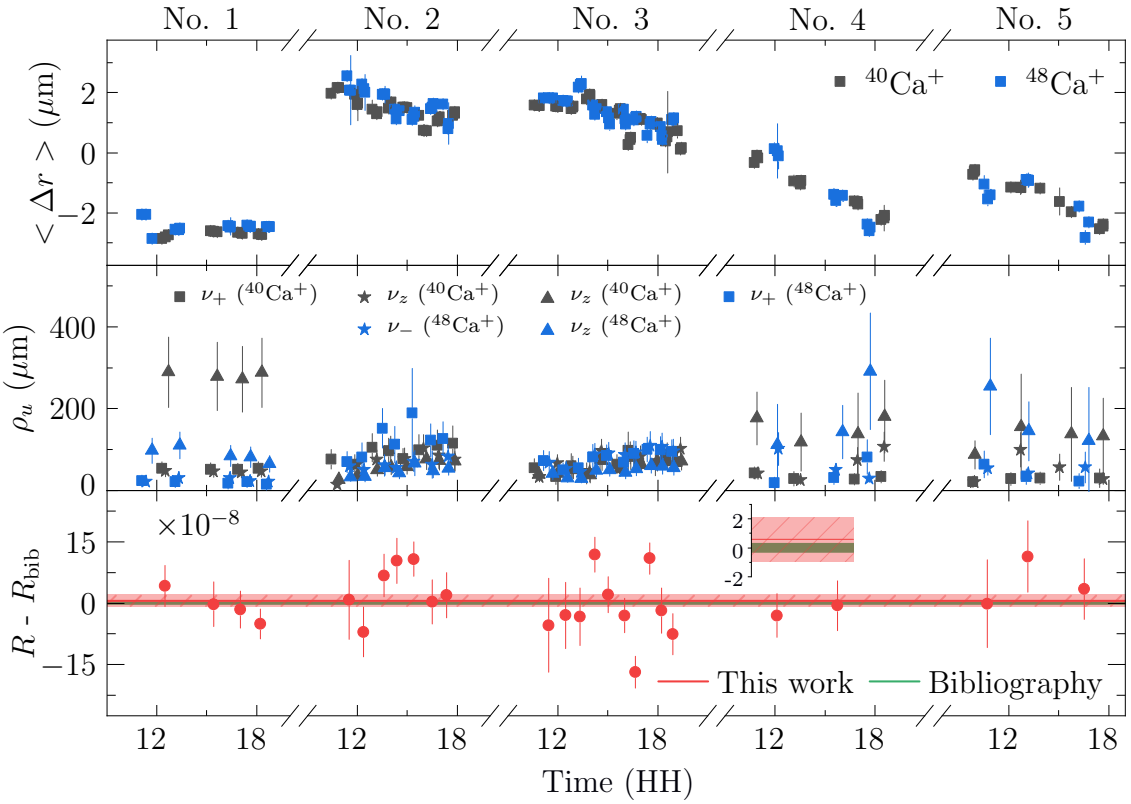

Figure 5.10. ^{48}Ca$^+$ - ^{40}Ca$^+$ mass ratio, ion position, and motional amplitude. The frequency ratios are plotted in the lower panel, where the weighted mean is compared with the bibliography value [149]. The three ion's motional amplitudes after excitation are represented for the two ions in the middle panel. The average position around the centre of the trap monitored in the radial direction is plotted in the upper panel. The day number is marked on the top.

Figure 5.10 shows the cyclotron-frequency ratios measured in this work along with the fluctuations of the position of the ion in the radial direction and the motional amplitudes after excitation. It comprises a total of five days of measurements taken in three different periods and using different trap configurations listed in Tab. 5.2. The first day corresponds to data taken the 13$^{\rm th}$ of July of 2022, using trap configuration 1. A total of four ratios were obtained from these measurements. The second and third days shown in Fig. 5.10 correspond to the 13$^{\rm th}$ and the 14$^{\rm th}$ of September, using configuration 2. The trap configuration was changed due to the appearance of unknown noise at the modified-cyclotron frequency that heated the ion while laser cooling was switched off. The last two days of measurements on ^{48}Ca$^+$ were the 19$^{\rm th}$ and the 20$^{\rm th}$ of October. For these measurements, a new trap configuration (number 3 in Tab. 5.2) was explored, trying to mitigate the impact of the electric-field instability on the cyclotron-frequency uncertainty.

The final value of the cyclotron-frequency ratio is $R = 1.199\,938\,029(15)$. For the different trap configurations 1, 2, and 3 listed in Tab. 5.2, the values obtained

are $R = 1.199\,938\,011(20)$, $1.199\,938\,030(23)$, and $1.199\,938\,038(27)$. The literature value R_{bib} is calculated from the atomic masses of the reference and interest ion, m_{ref} and m_{int}, as

$$R_{\mathrm{bib}} = \frac{m_{\mathrm{int}} - m_e + E_B^{(1)}}{m_{\mathrm{ref}} - m_e + E_B^{(1)}}, \tag{5.17}$$

where $m_e = 0.000\,548\,579\,909\,067(17)$ u [3] is the (atomic) mass of the electron and $E_B^{(1)} = 6.113\,155\,47(25)$ eV [174] is the ionization energy of calcium. For $^{48}Ca^+$ - $^{40}Ca^+$, $R_{\mathrm{bib}} = 1.199\,938\,024\,55(81)$ [149]. The literature value of the atomic mass of ^{48}Ca was directly measured in the Penning-trap mass spectrometer SHIPTRAP by comparing the cyclotron frequency of $^{48}Ca^+$ with that of $^{12}C_4{}^+$ using the PI-ICR technique [175]. For $^{40}Ca^+$, the ratio $^{40}Ca^{17+}$ - $H_2{}^+$ was measured using ToF-ICR in the Penning-trap mass spectrometer SMILETRAP [176]. For a brief introduction to the techniques PI-ICR and ToF-ICR, see Sec. 2.3.

In addition to the central frequency, the ion's motional amplitude and position have also been extracted from the analysis procedure. These values are plotted in the upper panel of Fig. 5.10. The radial amplitudes for the modified-cyclotron and magnetron motions after excitation can be extracted directly from the EMCCD data used to obtain the ion's radial eigenfrequencies. The initial axial amplitude after excitation has been estimated from Eq. (5.7). The mean values of the amplitudes obtained for the three eigenmotions are $\langle\rho_+\rangle = 30(20)$ μm, $\langle\rho_-\rangle = 30(12)$ μm, and $\langle\rho_z\rangle = 46(40)$ μm.

The mean radial position of the ion shown in the upper panel of Fig. 5.10 describes the spatial drift of the trap centre. It takes into account both modified-cyclotron and magnetron data. During a whole day of measurements (around 8 hours), the mean value of the position changed 1 - 2 μm. This is not a problem since the time needed for one cyclotron measurement was around thirty minutes. During such time intervals, only changes of tens of nanometers are observed.

Figure 5.11 shows the individual eigenfrequencies corresponding to the measurements presented in Fig. 5.10. As can be observed, all the frequencies from day two to five evolve every day following a capacitor charge curve. The relative frequency shifts during a full day are quite high: $9.1(14)\cdot10^{-7}$ for the modified-cyclotron motion, $1.71(45)\cdot10^{-4}$ for the magnetron motion, and $6.9(1.5)\cdot10^{-5}$ for

Table 5.2. Motional frequencies and excitation times of $^{40}Ca^+$ for the three trap configurations.

Config.	ν_+ (MHz)	ν_- (kHz)	ν_z (kHz)	ν_+/ν_c	ν_-/ν_c	ν_z/ν_c	t^+_{dip} (ms)	t^-_{dip} (ms)	t^z_{dip} (ms)
1	2.673	16.5	297	0.9939	0.0061	0.111	1000	100	100
2	2.676	13.8	271	0.9949	0.0051	0.101	1000	100	100
3	2.686	3.8	142	0.9985	0.0014	0.053	500	100	100

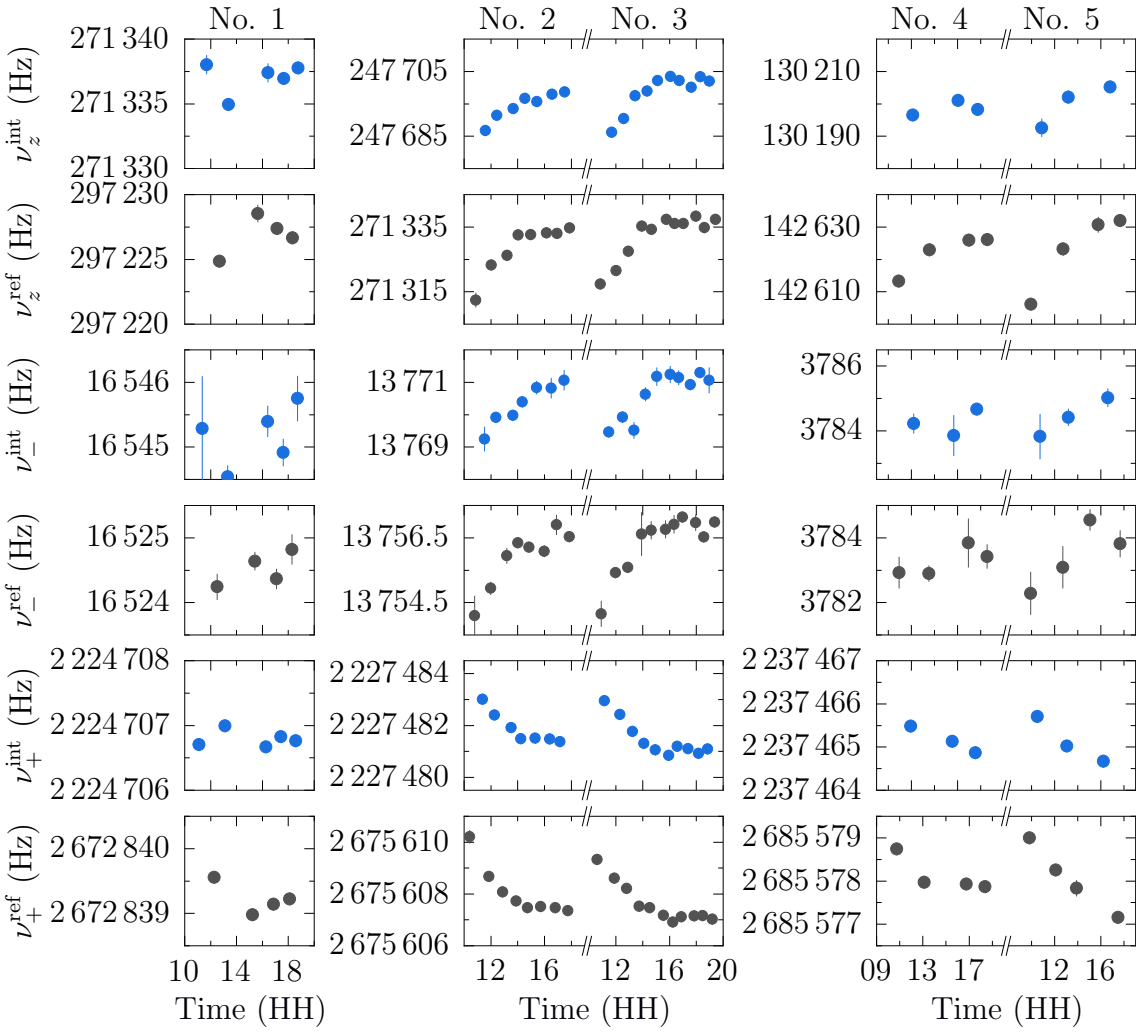

Figure 5.11. Eigenfrequencies of $^{48}Ca^+$ and $^{40}Ca^+$. The three eigenfrequencies used to compute the cyclotron frequency in Fig. 5.10 are plotted as a function of the measurement time. The day number is marked on the top.

the axial motion. These shifts did not affect individual ν_c measurements due to their shorter timescale. However, an additional uncertainty taking into account this drift became necessary, especially for the measurements taken when it is more pronounced (measurements in the morning). In that sense, the frequency variation during the cyclotron-frequency measurement has been estimated for each of the three eigenfrequencies by linear interpolation with the neighbouring values; extrapolation has been used for the first and last measurements. This variation has been added quadratically to the statistic uncertainty obtained from the analysis procedure.

This drift seems originated from noise of an electrical nature since it is visible in the axial motion, which only depends on the electric field. In addition, the observed drift in the radial eigenfrequencies can be fully explained by the electric

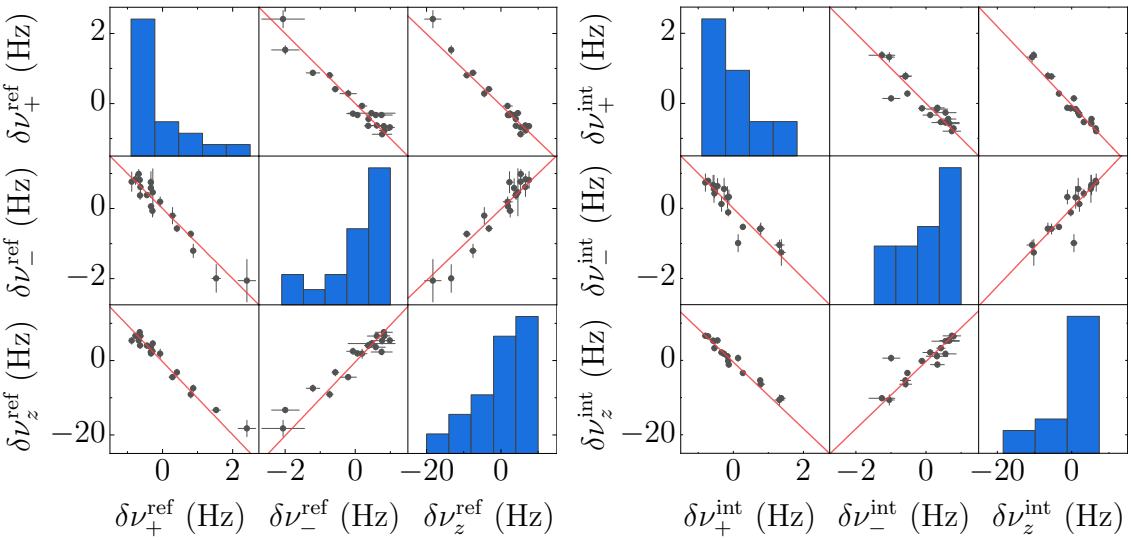

Figure 5.12. Correlation matrix of the $^{48}Ca^+$ - $^{40}Ca^+$ eigenfrequency data. In the off-diagonal plots, the mutual dependence between the different eigenfrequencies of the same cyclotron-frequency measurement is studied. The fitting functions are given by Eq. (2.6) (radial motions in terms of the axial eigenfrequency) and its inverse function. The diagonal plots show frequency histograms. The matrix on the left side is built from the $^{40}Ca^+$ data while the one on the right side is built from $^{48}Ca^+$. For $^{40}Ca^+$, $\delta\nu_+^{\mathrm{ref}} = \nu_+^{\mathrm{ref}} - 2\,675\,607.798$ Hz, $\delta\nu_-^{\mathrm{ref}} = \nu_-^{\mathrm{ref}} - 13\,756.150$ Hz, and $\delta\nu_z^{\mathrm{ref}} = \nu_z^{\mathrm{ref}} - 271\,330.731$ Hz. For $^{48}Ca^+$, $\delta\nu_+^{\mathrm{int}} = \nu_+^{\mathrm{ref}} - 2\,227\,481.636$ Hz, $\delta\nu_-^{\mathrm{int}} = \nu_-^{\mathrm{ref}} - 13\,770.506$ Hz, and $\delta\nu_z^{\mathrm{int}} = \nu_z^{\mathrm{ref}} - 247\,696.884$ Hz.

field fluctuations manifested in the axial motion. In particular, the dependence of $\nu_\pm$ on the axial frequency is

$$\frac{\partial\nu_\pm}{\partial\nu_z} = \mp\frac{\nu_z}{\nu_c}\frac{1}{\sqrt{1-2\left(\frac{\nu_z}{\nu_c}\right)^2}}. \tag{5.18}$$

Assuming $\nu_z \ll \nu_c$, the relative fluctuations in the radial and axial eigenfrequencies can be related as

$$\frac{\Delta\nu_\pm}{\nu_\pm} = \frac{\nu_z^2}{\nu_c\nu_\pm}\frac{\Delta\nu_z}{\nu_z}, \tag{5.19}$$

which means the electric-field fluctuations affect the frequencies $\nu_+/\nu_-/\nu_z$ in a proportion 0.010/1.99/1. The difference between maximum and minimum frequency observed in Fig. 5.11 are in proportion 0.0132(47)/2.5(1.2)/1. Another possible source might be the collisions with the residual gas molecules, although this would mean a dependence of the collision rate with the mean free path yielding a shorter lifetime for the faster motion, opposite to the observations.

In order to gain insight into these drifts, a correlation matrix to study the interdependence of the three eigenfrequencies has been built for both $^{40}Ca^+$ and

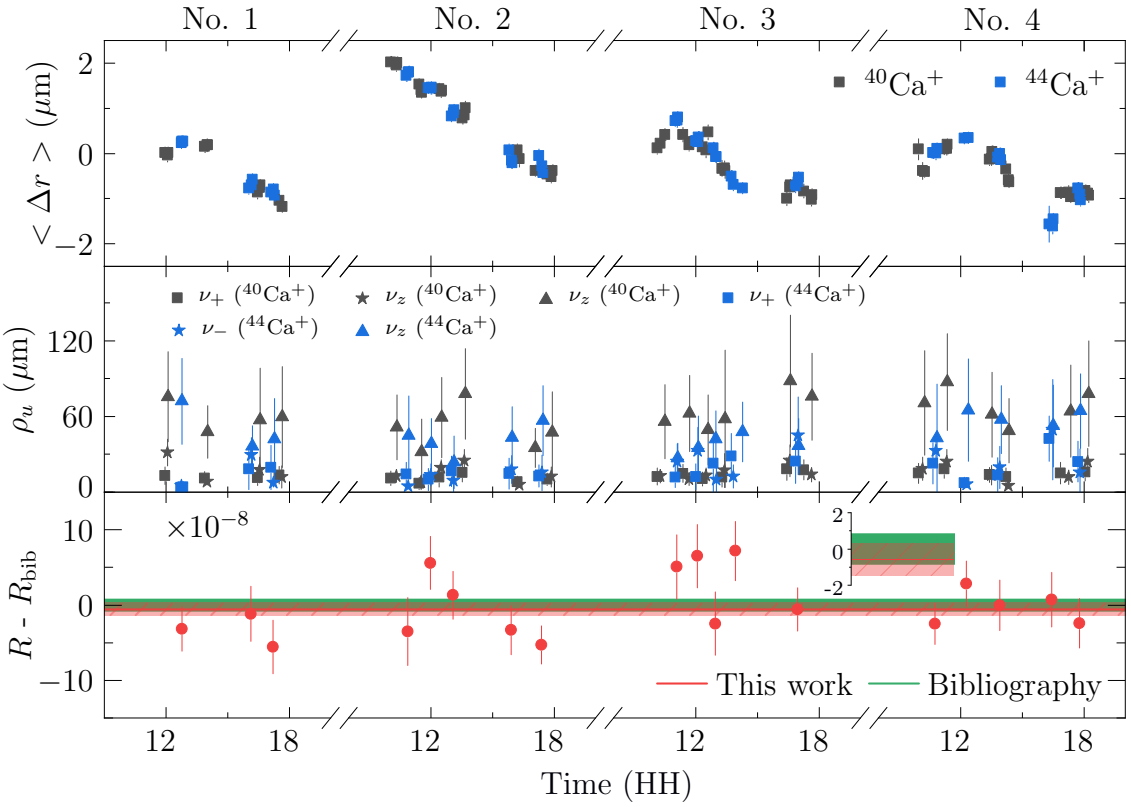

Figure 5.13. ^{44}Ca$^+$ - ^{40}Ca$^+$ mass ratio, ion position, and motional amplitude. The panels show the same kind of results as in Fig. 5.10.

^{48}Ca$^+$. The results are shown in Fig. 5.12. The Pearson correlation coefficients for the pairs $(\nu_+, \nu_-)/(\nu_+, \nu_z)/(\nu_-, \nu_z)$ are -0.96/-0.98/0.96 and -0.92/-0.98/0.89 for ^{40}Ca$^+$ and ^{48}Ca$^+$, respectively. The high anti-correlation (negative slope) between ν_z and ν_+, and the correlation between ν_z and ν_-, corroborate the hypothesis of an electric noise source.

The magnetic field was more stable than the electric field: the relative variation during an entire day of measurements has been $\Delta B/B = 1.47(80) \cdot 10^{-7}$ (from ν_c data) and $\Delta E/E = 2.2(16) \cdot 10^{-4}$ (from ν_z data). Equation (2.6) has been used with ν_c as the only free parameter to fit the frequency correlations in Fig. 5.12. A value of $\nu_c = 2\,689\,365.49(50)$ Hz is extracted from these fittings for ^{40}Ca$^+$, which is compatible and has a comparable uncertainty to that obtained using the interpolation method, $\nu_c = 2\,689\,365.480(44)$ Hz.

5.3 Frequency ratio of ^{44}Ca$^+$ and ^{40}Ca$^+$

^{44}Ca$^+$ is the second most abundant isotope (2.09 %) of calcium. Prior to this work, its atomic mass had only been determined from nuclear reactions [177, 178]. The data shown in Fig. 5.13 correspond to the measurements carried out on the pair

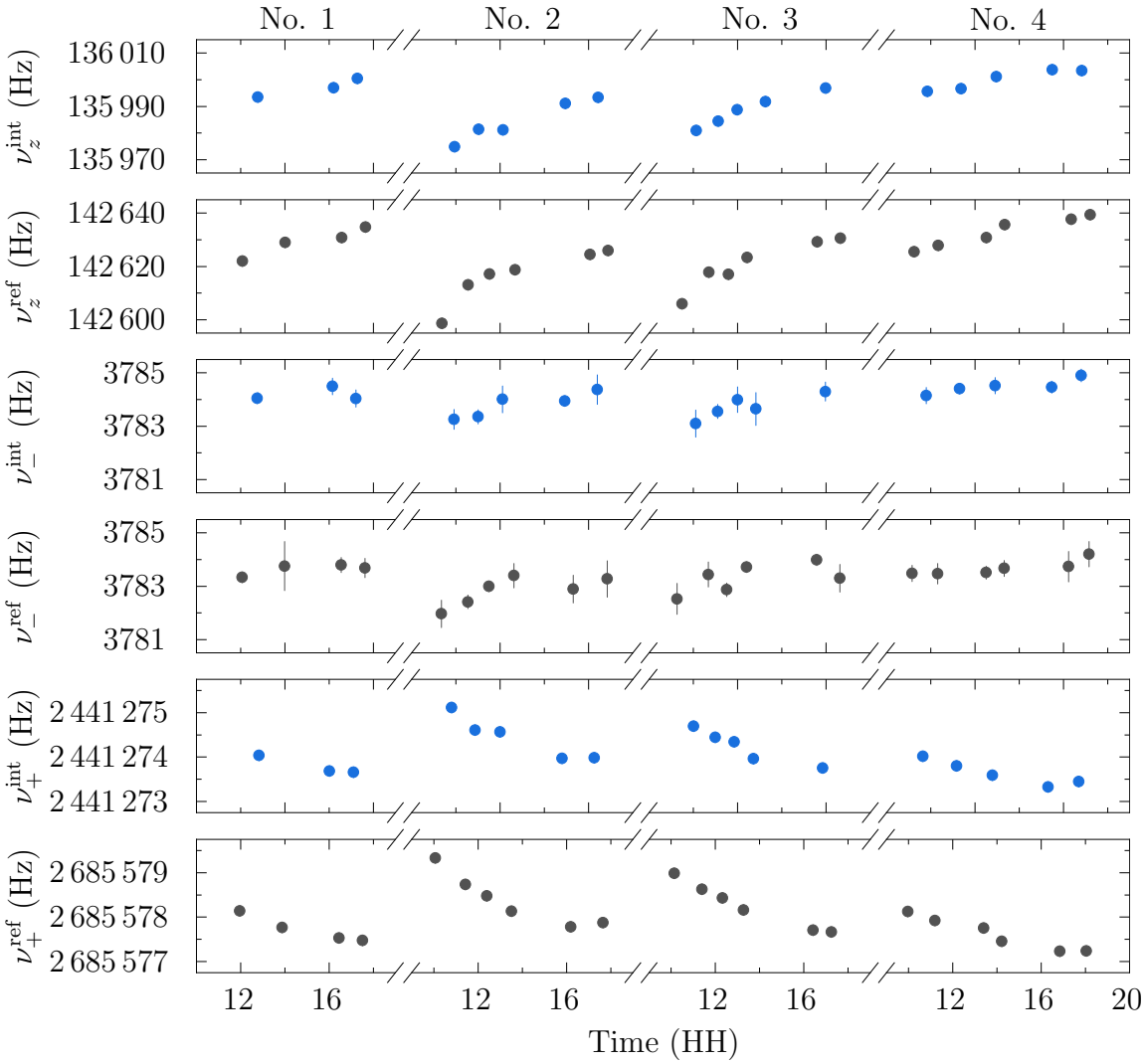

Figure 5.14. Eigenfrequencies of $^{44}Ca^+$ and $^{40}Ca^+$. As in Fig. 5.11, the three eigenfrequencies are plotted as a function of the measurement time, but now only trap configuration 3 was used.

$^{44}Ca^+$ - $^{40}Ca^+$ from the 21th to the 24th of October 2022. A total of 18 individual cyclotron-frequency ratio measurements have yielded $R = 1.099\,917\,0772(89)$. The relative uncertainty is $8.1 \cdot 10^{-9}$, better than the value obtained for $^{48}Ca^+$. The literature value is $R_{bib} = 1.099\,917\,0830(88)$ [149] (see Eq. (5.17)), in agreement with the measured value in this work and with similar uncertainty.

For these measurements, the trap configuration 3 (see Tab. 5.2) was used. As was already stated in the previous section, the aim of lowering the axial frequency was to improve the cyclotron-frequency uncertainty. According to Eq. (2.10), a smaller value of the axial frequency leads to a smaller impact of its uncertainty on the cyclotron frequency. Although the ion of interest is different, a comparison between the results on the pair $^{48}Ca^+$ - $^{40}Ca^+$ (most of the data were measured

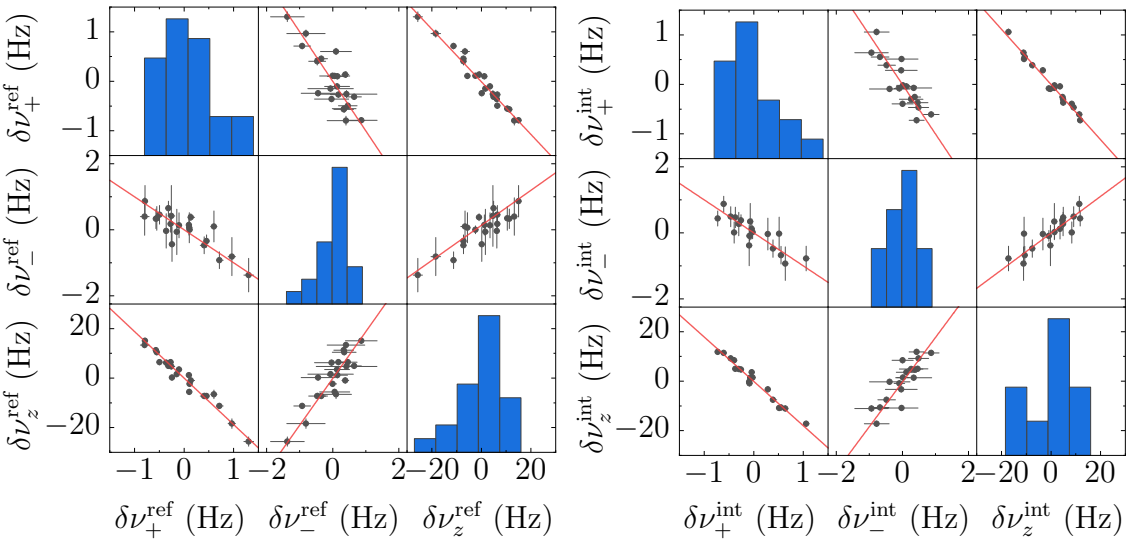

Figure 5.15. Correlation matrix of the ^{44}Ca$^+$ - ^{40}Ca$^+$ eigenfrequency data. The structure is the same as for Fig. 5.12. The fitting function is likewise given by Eq. (2.6). For ^{40}Ca$^+$ (left panels), $\delta\nu_+^{\mathrm{ref}} = \nu_+^{\mathrm{ref}} - 2\,685\,578.023$ Hz, $\delta\nu_-^{\mathrm{ref}} = \nu_-^{\mathrm{ref}} - 3\,783.336$ Hz, and $\delta\nu_z^{\mathrm{ref}} = \nu_z^{\mathrm{ref}} - 142\,624.313$ Hz. For the measurements of ^{44}Ca$^+$ (right panels), $\delta\nu_+^{\mathrm{int}} = \nu_+^{\mathrm{ref}} - 2\,441\,274.055$ Hz, $\delta\nu_-^{\mathrm{int}} = \nu_-^{\mathrm{ref}} - 3\,784.029$ Hz, and $\delta\nu_z^{\mathrm{int}} = \nu_z^{\mathrm{ref}} - 135\,991.971$ Hz.

using $\nu_z > 270$ kHz) and the pair ^{44}Ca$^+$ - ^{40}Ca$^+$ ($\nu_z = 142$ kHz) data shows an improvement in the cyclotron frequency uncertainty.

Figure 5.14 shows the measured eigenfrequencies, observing drifts with the same trend as in Fig. 5.11. The correlation matrices have also been plotted in Fig. 5.15 to certify the electric nature of the noise source. For these measurements, the Pearson correlation coefficients for the pairs $(\nu_+, \nu_-)/(\nu_+, \nu_z)/(\nu_-, \nu_z)$ are -0.84/-0.98/0.88 and -0.86/-0.99/0.86 for ^{40}Ca$^+$ and ^{44}Ca$^+$, respectively.

5.4 Frequency ratio of ^{42}Ca$^+$ and ^{40}Ca$^+$

^{42}Ca$^+$ is the third most abundant calcium isotope (0.647 %). The measurements presented in Fig. 5.16 were taken from the 25$^{\mathrm{th}}$ to the 28$^{\mathrm{th}}$ of October 2022. A total of 11 individual measurements of the cyclotron-frequency ratio have yielded $R = 1.049\,948\,070(11)$, with a relative uncertainty is $1.0 \cdot 10^{-8}$, compared to the literature value $R_{\mathrm{bib}} = 1.049\,948\,0720(41)$ [149] obtained using Eq. (5.17). The mass of ^{42}Ca$^+$ in Ref. [179] was not obtained from direct measurements but deduced from spectroscopy data. For the experiments presented here, the trap configuration 3 was also used. Although a worse relative uncertainty is obtained compared to the pair ^{44}Ca$^+$ - ^{40}Ca$^+$, the dispersion of the data is of the same order: $5.4 \cdot 10^{-8}$ against $4.0 \cdot 10^{-8}$ for ^{44}Ca$^+$. Similar results for the frequencies and correlations to those already presented in Figs. 5.14 and 5.15 are obtained.

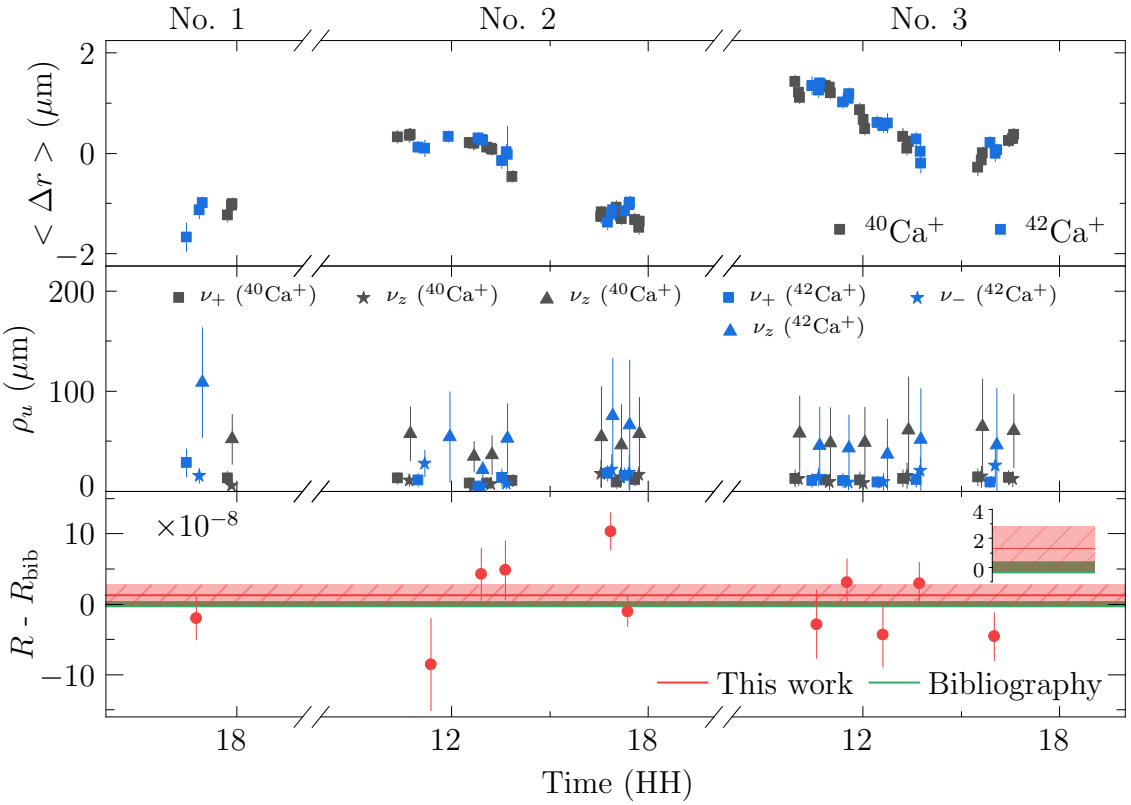

Figure 5.16. $^{42}Ca^+$ - $^{40}Ca^+$ mass ratio, ion position, and motional amplitude. The structure is the same as for Figs. 5.10 and 5.13.

5.5 Evaluation of systematic uncertainties

The uncertainties presented in Figs. 5.10, 5.13, and 5.16 are statistical, and thus can be reduced with the number of measurements. They are related to the concept of precision, and in case the cyclotron-frequency ratio R has a Gaussian distribution, $\Delta R \sim 1/\sqrt{N}$, being N the number of measurements. In addition, there are always sources of systematic uncertainties that cannot be avoided and limit the final accuracy of the measurement. In motional-frequency measurements with Penning traps, there are several sources of systematic effects inducing frequency shifts, mostly arising from the simplifications assumed when modelling mathematically the trapped ion and its environment.

One source of systematic frequency shifts is the finite amplitude of the ion during its excitation in the measurement cycle. A spatially homogeneous magnetic field and a perfect harmonic electric potential are assumed when obtaining the motional equations of the ion. However, it is necessary to quantify how much these hypotheses are satisfied in the real Penning trap. To do that, the electric and magnetic fields are expanded in a power series, and perturbation theory is applied to quantify how much the eigenfrequencies are shifted by higher-order components [68]. The expressions for the frequency shifts caused by the quadrupolar

and dipolar components of the electric potential and magnetic field, respectively, can be found in Sec. 2.1.1.

Taking into account that in a single eigenfrequency measurement the two eigenmotions that were not probed had negligible oscillation amplitudes compared to the one that is excited, the shifts due to the electric field imperfections can be calculated as

$$\Delta\nu_{\pm} = \pm\frac{C_4}{C_2}\frac{3}{2d_0^2}\frac{\nu_-}{1-\nu_-/\nu_+}\rho_{\pm}^2 \tag{5.20}$$

for the radial eigenfrequencies and

$$\Delta\nu_z = \frac{C_4}{C_2}\frac{3}{4d_0^2}\rho_z^2\nu_z \tag{5.21}$$

for the axial one (see Eq. (2.13)). C_2 and C_4 are dimensionless coefficients accounting for the harmonic and quadratic components of the potential, respectively, and d_0 is a characteristic dimension of the trap (see Eq. (2.4)).

The eigenfrequency shifts propagate into the cyclotron frequency as

$$\begin{aligned}\Delta\nu_c &= \sqrt{(\nu_+ + \Delta\nu_+)^2 + (\nu_- + \Delta\nu_-)^2 + (\nu_z + \Delta\nu_z)^2} - \sqrt{\nu_+^2 + \nu_-^2 + \nu_z^2} \\ &\approx \nu_c\left(\sqrt{1 + 2\frac{\nu_+\Delta\nu_+ + \nu_-\Delta\nu_- + \nu_z\Delta\nu_z}{\nu_c^2}} - 1\right) \\ &\approx \frac{\nu_+\Delta\nu_+ + \nu_-\Delta\nu_- + \nu_z\Delta\nu_z}{\nu_c},\end{aligned} \tag{5.22}$$

where $\Delta\nu_u \ll \nu_u$ has been used in the last step.

Combining Eqs. (5.22), (5.20), and (5.21), the frequency shift on the cyclotron frequency due to the imperfections of the electric field can be quantified as

$$\Delta\nu_c = \frac{C_4}{C_2}\frac{3}{2d_0^2}\frac{1}{\nu_c}\left(\rho_+^2\nu_+\nu_- - \rho_-^2\nu_-^2 + \frac{1}{2}\rho_z^2\nu_z^2\right). \tag{5.23}$$

The amplitudes of the radial eigenmotions have been directly determined from the EMCCD images. The amplitude of the axial eigenmotion has been calculated using Eq. (5.7). Figure 5.17 shows a histogram of the relative cyclotron frequency shift in the measurements presented in the previous sections. The comparison with other experiments shows that the optical method outperforms the electronic detection technique for an equivalent mass-to-charge ratio even when there is still room for improvement, as shown in the figure. The current limitation arises from the measurement of the axial eigenfrequency since this motion had to be excited to $\rho_z > 100$ μm in some cases. A way to diminish this systematic shift would be to decrease the ion's motional amplitude during the eigenfrequency measurements. In this respect, Fig. 5.23 shows the best situation that can be achieved by the technique developed during this work (UGR at Doppler limit) and the shifts that would be obtained for an ion excited at 1 mK (in all modes). Another possible

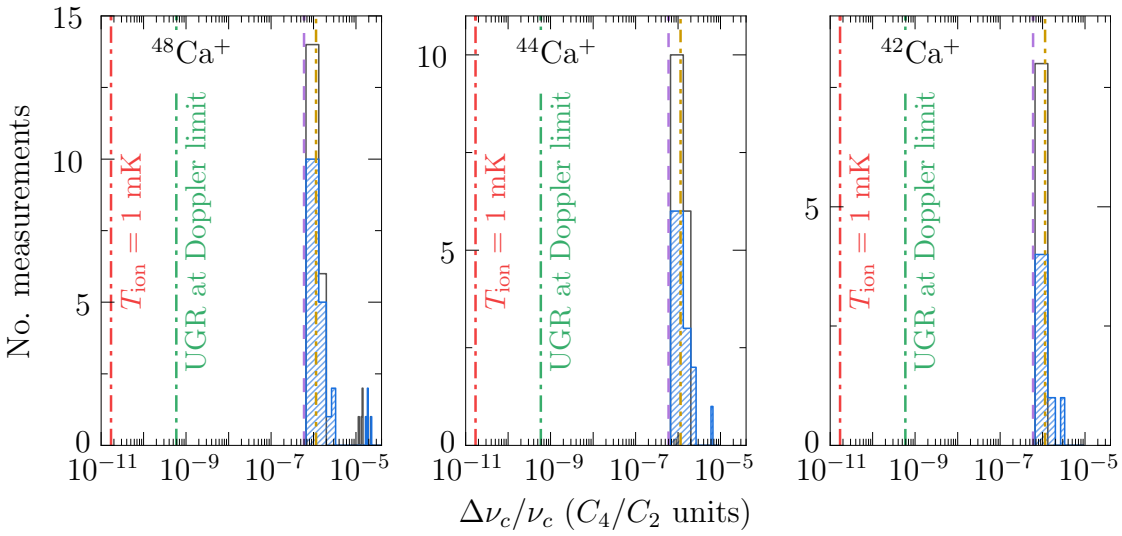

Figure 5.17. Systematic frequency shifts due to electric field imperfections. Histograms of the cyclotron frequency shift caused by the imperfections of the electric field according to Eq. (5.23). The empty bars correspond to $^{40}Ca^+$ and the ones filled with the blue pattern to the ion of interest. The amplitude data presented in Figs. 5.10, 5.13, and 5.16 are used. The shifts are expressed in terms of C_4/C_2 units, according to Sec. 2.1.1 and Ref. [68]. The green dashed-dotted line indicates the best possible performance of the technique, assuming the ion is excited to a minimum detectable initial oscillation amplitude of $\rho_\pm \approx 4.2$ μm, while for the red dashed-dotted line ρ_u corresponds to 1 mK in all the eigenmotions. The yellow dashed-double-dotted line estimates the shift in the Penning trap spectrometer PENTATRAP at the Max-Planck Institute for Nuclear Physics in Heidelberg for $m/q \approx 40$ u/C, according to the frequency and amplitude data in Ref. [180]. The purple dashed line indicates the frequency shift in the experiment at Florida State University [181].

strategy would be to compensate the amplitudes of the different eigenmotions to minimize the term between parenthesis in Eq. (5.23).

The systematic shifts due to imperfections in the magnetic field can be quantified as

$$\Delta\nu_\pm = -\frac{1}{2}\frac{B_2}{B_0}\nu_\pm\rho_\pm^2 \tag{5.24}$$

for the radial eigenmotions while $\Delta\nu_z = 0$ for the axial one, where Eq. (2.14) (based on Ref. [68]) has been followed and a non-negligible amplitude has only been considered for the eigenmotion that was probed in that specific measurement. Combining Eq. (5.24) with Eq. (5.22), the systematic shift on the cyclotron frequency due to magnetic field imperfections is

$$\Delta\nu_c = \frac{1}{2}\frac{B_2}{B_0}\frac{1}{\nu_c}\left(-\rho_+^2\nu_+^2 - \rho_-^2\nu_-^2\right). \tag{5.25}$$

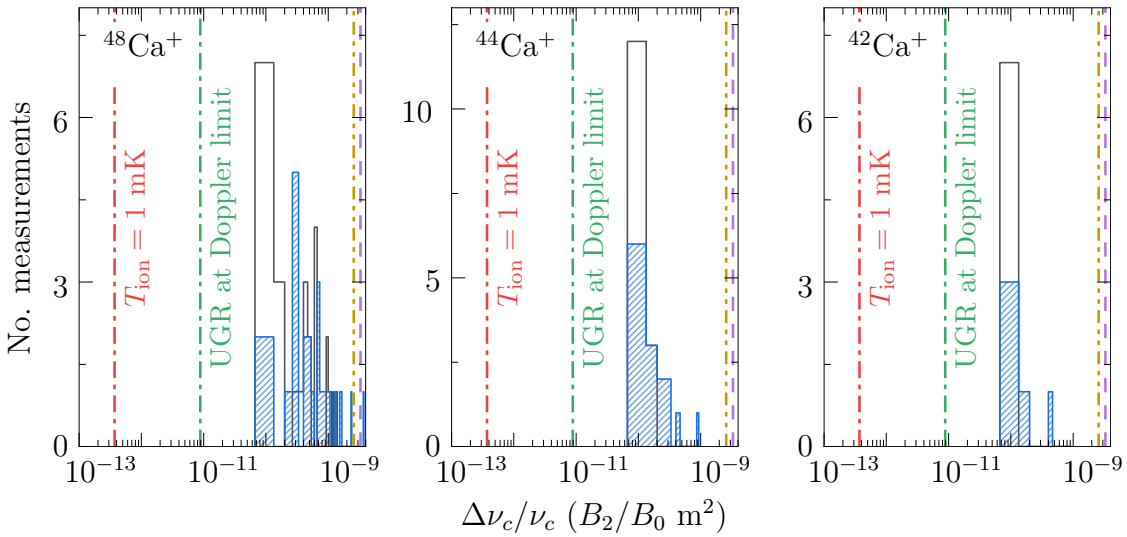

Figure 5.18. Systematic frequency shifts due to magnetic field imperfections. Histograms of the cyclotron frequency shift due to imperfections of the magnetic field according to Eq. (5.25). The bar style and the vertical lines are analogous to Fig. 5.17. The shifts are expressed in terms of B_2/B_0, according to Sec. 2.1.1 and Ref. [68].

Figure 5.18 shows the systematic shifts due to the imperfections of the magnetic field for the measurements presented in the previous sections. Under similar conditions of mass-to-charge ratio, the shifts obtained are about one order of magnitude lower than for other techniques, mainly due to the lack of contribution of the axial-motion amplitude.

The shifts on the cyclotron frequencies ν_c^{ref} and ν_c^{int} propagate to the frequency ratio R as

$$\begin{aligned}\Delta R &= \frac{\nu_c^{\mathrm{ref}} + \Delta\nu_c^{\mathrm{ref}}}{\nu_c^{\mathrm{int}} + \Delta\nu_c^{\mathrm{int}}} - \frac{\nu_c^{\mathrm{ref}}}{\nu_c^{\mathrm{int}}} \\ &= \frac{\nu_c^{\mathrm{ref}}}{\nu_c^{\mathrm{int}} + \Delta\nu_c^{\mathrm{int}}} \left(\frac{\Delta\nu_c^{\mathrm{ref}}}{\nu_c^{\mathrm{ref}}} - \frac{\Delta\nu_c^{\mathrm{int}}}{\nu_c^{\mathrm{int}}} \right) \\ &\approx \frac{\nu_c^{\mathrm{ref}}}{\nu_c^{\mathrm{int}}} \left(\frac{\Delta\nu_c^{\mathrm{ref}}}{\nu_c^{\mathrm{ref}}} - \frac{\Delta\nu_c^{\mathrm{int}}}{\nu_c^{\mathrm{int}}} \right).\end{aligned} \tag{5.26}$$

If $\Delta\nu_c^{\mathrm{ref}} = \Delta\nu_c^{\mathrm{int}} \equiv \Delta\nu$,

$$\begin{aligned}\frac{\Delta R}{R} &\approx \Delta\nu \left(\frac{1}{\nu_c^{\mathrm{ref}}} - \frac{1}{\nu_c^{\mathrm{int}}} \right) \\ &= \Delta\nu \frac{\nu_c^{\mathrm{int}} - \nu_c^{\mathrm{ref}}}{\nu_c^{\mathrm{ref}} \nu_c^{\mathrm{int}}} \propto \Delta m,\end{aligned} \tag{5.27}$$

which constitutes the so-called mass-dependent shift [182]. Using the value of the ratio C_4/C_2 estimated in Sec. 5.1.3 (see Fig. 5.6), a relative systematic shift in the

ratio of $4.3 \cdot 10^{-9}$, $2.3 \cdot 10^{-9}$, and $1.7 \cdot 10^{-9}$ has been estimated for $^{48}Ca^{+}$, $^{44}Ca^{+}$, and $^{42}Ca^{+}$, respectively. Considering a spatial homogeneity of 0.1 ppm over 1 cm^3 in the Penning trap, a ratio $B_2/B_0 \approx 0.2$ m^{-2} has been estimated, which translates into a relative systematic shift in the ratio of $8.0 \cdot 10^{-11}$, $2.6 \cdot 10^{-11}$, and $8.2 \cdot 10^{-12}$ for $^{48}Ca^{+}$, $^{44}Ca^{+}$, and $^{42}Ca^{+}$, respectively.

Two more sources of systematic uncertainties must be quantified: relativistic and image-charge frequency shifts. The fact of considering a non-relativistic model for the description of the ion's motion can also lead to the appearance of a systematic shift. The mass of the ion at rest increases due to its velocity v as $m_{\mathrm{rel}} = m/\sqrt{1-(v/c)^2}$. Since $\nu_+ \gg \nu_z, \nu_-$, the modified-cyclotron motion contributes dominantly to this shift. The relative shift in the cyclotron frequency can be calculated as

$$\frac{\Delta\nu_c}{\nu_c} = \frac{m}{m_{\mathrm{rel}}} - 1 = \sqrt{1 - \left(\frac{\nu_+\rho_+}{c}\right)^2} - 1. \tag{5.28}$$

Considering that $\nu_+ = 2.7$ MHz and that the maximum value of the amplitude is $\rho_+ \approx 69$ μm, a relative systematic shift in the cyclotron frequency of the calcium isotopes of $1.3 \cdot 10^{-13}$ is estimated.

The image charge the ion induces on the electrodes alters the total electric potential, causing a shift in the ion's eigenfrequencies. Following Ref. [183], the relative shift in the cyclotron frequency is given by

$$\frac{\Delta\nu_c}{\nu_c} \approx \frac{m}{4\pi\varepsilon_0 B^2 r_0^3}, \tag{5.29}$$

where ε_0 is the vacuum permittivity and r_0 is the trap radius. Substituting the parameters of this experiment, a relative systematic shift in the cyclotron frequency and in the ratio of $9 \cdot 10^{-11}$ and $2 \cdot 10^{-11}$ are obtained, respectively.

In the experiments presented in this chapter, two 866-nm repumping lasers were switched off while applying the external excitation. Since the 397-nm cooling lasers were not switched off, the ion was not in the ground state, but in some of the $D_{3/2}$-manifold states. In terms of energy, this means a difference of 1.69 eV, which represents a relative change of $4.5 \cdot 10^{-11}$ in the mass of $^{40}Ca^{+}$. This is not critical for the precision achieved in this work. If better precision is envisaged, this shift can be removed by preparing the ion in the ground state before the excitation and switching off all the cooling lasers during this period.

5.6 Other studies

The values of the atomic mass extracted from isotope ratios measured in this thesis can be calculated using Eq. (5.17) and are compared with the literature values in Tab. 5.3. The final uncertainty is dominated by the statistical contribution. As shown in Sec. 5.5, the main source of systematic frequency shifts, which limit the attainable accuracy, are the imperfections of the electric field, in the order of 10^{-9}

Table 5.3. Atomic mass of the calcium isotopes. The bibliography data are extracted from the 2020 Atomic Mass Evaluation [149].

	This work		Bibliography	
Isotope	m_{int} (u)	$\Delta m_{\text{int}}/m_{\text{int}}$	m_{int} (u)	$\Delta m_{\text{int}}/m_{\text{int}}$
^{48}Ca	47.952 522 82(60)	$1.3 \cdot 10^{-8}$	47.952 522 654(19)	$4.0 \cdot 10^{-10}$
^{44}Ca	43.955 481 31(36)	$8.1 \cdot 10^{-9}$	43.955 4815(3)	$6.8 \cdot 10^{-9}$
^{42}Ca	41.958 617 74(44)	$1.0 \cdot 10^{-8}$	41.958 617 78(16)	$3.8 \cdot 10^{-9}$

and mainly due to the axial oscillation amplitude. Nevertheless, this value could be reduced in the future by properly tuning the trapping potentials to make the trap more harmonic and choosing a convenient ratio of the ions' amplitude according to Eqs. (5.23) and (5.26). Moreover, this systematic shift could be treated as a correction shift since the ion's amplitude can be directly determined for each individual cyclotron-frequency measurement.

The statistical uncertainty could be reduced either by performing more measurements or by increasing the excitation time. The first strategy scales as $1/\sqrt{t}$ and the second as $1/t$. However, larger measurement times are also more affected by the system instabilities, leading to lower SNRs. As it was previously investigated by the correlation analysis (see Secs. 5.2 and 5.3), the main source of statistical noise comes from the electric field.

The DC power supply was measured to feature long-term relative stability of $4.5 \cdot 10^{-5}$. For this, the magnetron frequency was monitored, since its relative fluctuation is a direct measurement of the electric-field fluctuation (Eq. (5.19)). In this sense, the reduction of the axial frequency, which implies a lower dependence of the cyclotron frequency on the electric field, led to an increase in precision. For ^{44}Ca$^+$ and ^{42}Ca$^+$, the dispersion of the cyclotron-frequency ratios are $4.0 \cdot 10^{-8}$ and $5.4 \cdot 10^{-8}$, respectively, lower than $8.8 \cdot 10^{-8}$ for ^{48}Ca$^+$.

Fundamental studies with calcium isotopes

The precise knowledge of the masses of the stable calcium isotopes has a special interest in the field of isotope-shift spectroscopy for King-plot analysis. In particular, the dependence between the isotope shift of two internal transitions is studied. The observation of a non-linear relation between these frequencies could be interpreted as an indication of the existence of new physics beyond the Standard Model [184]. Besides calcium, with five stable isotopes featuring zero nuclear spin ($A = 40, 42, 44, 46, 48$), Sr$^+$, Ba$^+$, and Yb$^+$ are also promising candidates, with three ($A = 84, 86, 88$), five ($A = 130, 132, 134, 136, 138$), and five ($A = 168, 170, 172, 174, 176$) available isotopes, respectively [184, 185].

The isotope frequency shift $\delta\nu_i^{A,A'}$ of a transition i in the isotope A with respect to the isotope A' can be divided into a component due to the nuclear mass, $\delta\nu_{i,\text{MS}}^{A,A'}$,

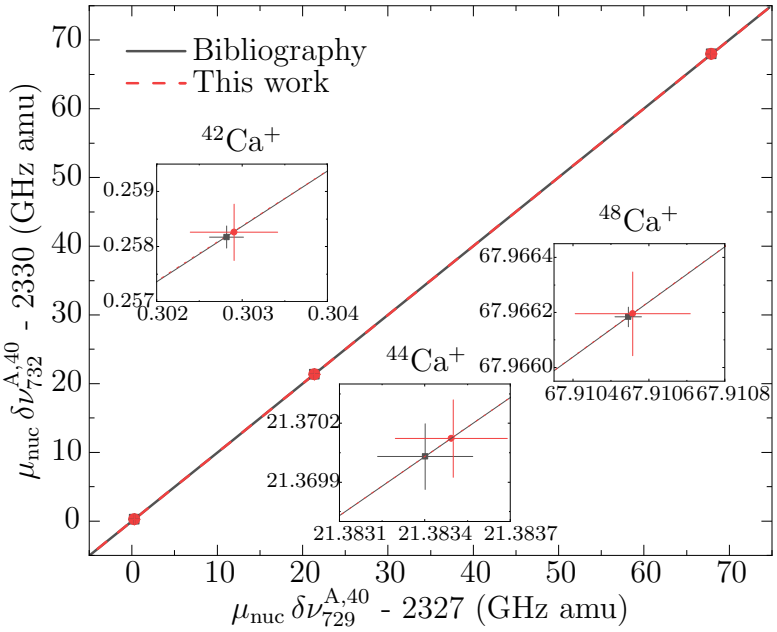

Figure 5.19. King plot of the calcium isotopes. The dark-grey solid circles are obtained using literature values [151]. The results using the mass values of this thesis are represented by the red solid circles.

and another due to the nuclear charge radius, $\delta\nu^{A,A'}_{i,\mathrm{FS}}$. It can be written as

$$\delta\nu_i^{A,A'} = \delta\nu_{i,\mathrm{MS}}^{A,A'} + \delta\nu_{i,\mathrm{FS}}^{A,A'} = K_i\left(\frac{1}{m_{A,\mathrm{nuc}}} - \frac{1}{m_{A',\mathrm{nuc}}}\right) + F_i\delta\left\langle r_c^2\right\rangle^{A,A'}, \tag{5.30}$$

where K_i and F_i are the so-called mass and field shift constants, respectively, and $\delta\left\langle r_c^2\right\rangle^{A,A'} = \left\langle r_c^2\right\rangle^{A} - \left\langle r_c^2\right\rangle^{A'}$ is the difference of the mean squared nuclear-charge radii. m_A and $m_{A'}$ are the nuclear masses of the two isotopes, calculated as

$$m_{A,\mathrm{nuc}} = m_A - Zm_e + E_B, \tag{5.31}$$

where Z is the atomic number, and E_B is the total binding energy, which is 18510(4) eV for calcium [186]. Although the isotope masses and certain internal transitions can be determined to a high level of precision, the nuclear-charge radii are currently determined with an uncertainty of 10^{-4} - 10^{-3} [83, 187]. Therefore, two internal transitions are measured so that the nuclear charge radii term can be left out. A relation between the isotope shifts of the two transitions i, j and masses of the ions can be deduced [188]:

$$\mu\delta\nu_i^{A,A'} = \mu\delta\nu_j^{A,A'} + (K_i - K_j), \tag{5.32}$$

where $\mu_{\mathrm{nuc}} = (m_{A,\mathrm{nuc}}m_{A',\mathrm{nuc}})\,/\,(m_{A',\mathrm{nuc}} - m_{A,\mathrm{nuc}})$ is the relative mass change. This relationship constitutes the King plot, and it is represented in Fig. 5.19. In the case of calcium the best results are obtained for the two electric quadrupole transitions

$3p^6 4s\,{}^2\mathrm{S}_{1/2} \Leftrightarrow 3p^6 3d\,{}^2\mathrm{D}_{5/2}$ and $3p^6 4s\,{}^2\mathrm{S}_{1/2} \Leftrightarrow 3p^6 3d\,{}^2\mathrm{D}_{3/2}$, measured in Refs. [151, 189] by means of the electron shelving technique [190] and direct frequency-comb Raman spectroscopy [191]. As expected, the results coincide with those using the literature values, but the level of uncertainty is not improved. In any case, the mass appears linearly in the two axes of Fig. 5.19, which attenuates its impact on the deviations from linearity of the King plot.

Force sensing

In the experiments presented in this chapter, the ion can be considered an extremely sensitive radiofrequency fluorescence detector. The sensitivity is commonly used to quantify the detector performance, and it is defined as the minimum discernible force that can be measured per frequency bandwidth. The force exerted by the external field on the ion to increase the phonon number in the mode u, F^u_{dip}, is directly calculated from the measured motional amplitudes as

$$F^u_{\mathrm{dip}} = \frac{2m\omega\rho_u}{t^u_{\mathrm{dip}}}, \tag{5.33}$$

where $\omega \equiv \omega_z$ for the axial motion and $\omega \equiv \omega_1$ for the radial ones. The force detection sensitivity is calculated as

$$S_d = \frac{F^u_{\mathrm{dip}}}{\sqrt{B}}, \tag{5.34}$$

where F^u_{dip} is the detected force in the mode u and $B = \left(t^u_{\mathrm{dip}} + t_{\mathrm{det}}\right)^{-1}$ is the measurement bandwidth, with t_{det} the detection time. The sensitivity is usually normalized to the signal-to-noise ratio as $\bar{S}_d = S_d/\mathrm{SNR}$.

From the measurements presented in this thesis, a minimum normalized sensitivity of $\bar{S}_d = 7.4(35)$ yN/$\sqrt{\mathrm{Hz}}$ and $\bar{S}_d = 24.9(99)$ yN/$\sqrt{\mathrm{Hz}}$ is reported in the modified-cyclotron and axial motion, respectively. For the modified-cyclotron motion, $S_d = 50(14)$ yN/$\sqrt{\mathrm{Hz}}$ is obtained with SNR = 6.8(13). For the axial motion, $S_d = 97(26)$ yN/$\sqrt{\mathrm{Hz}}$ and SNR = 3.9(5). The excitation times are $t^+_{\mathrm{dip}} = 1$ s and $t^z_{\mathrm{dip}} = 100$ ms, and the detection time is $t_{\mathrm{det}} = 75$ ms. This is the best value reported to date for an experiment in the classical regime. As a comparison, the Penning-trap experiment at NIST reported in 2010 a value of 390(150) yN/$\sqrt{\mathrm{Hz}}$ at 867 kHz from an experiment realized in the classical regime using the axial mode of a $\approx$ 100-ion two-dimensional planar array [150]. In 2021, the same group reported a value of 5.76(24) yN/$\sqrt{\mathrm{Hz}}$ at 1.59 MHz using again the axial mode of a two-dimensional Coulomb crystal but now cooled to the ground-state and applying quantum-based schemes [32]. These results could be improved by orders of magnitude by a single ion cooled to the ground state of motion. The equivalent classical force to prompt a change of a single quantum might be calculated by using the classical motional amplitudes corresponding to $n = 0$ and $n = 1$, with n the phonon number, in Eq. (5.33). Assuming $\nu_+ \approx \nu_c$, forces in the order of

$3 \cdot 10^{-3}$ yN could be detected with a singly-charged particle in a 7-T magnetic field. As an example, one-quantum modified-cyclotron jumps of an electron oscillating at 150 GHz are measured within cycles of 5 s in the g-factor experiment presented in Ref. [192], which implies a force detection sensitivity in the order of $7 \cdot 10^{-3}$ yN/$\sqrt{\text{Hz}}$.

Chapter 6

A test over the generalized invariance theorem

The use of a two-ion crystal in a Penning trap as a platform to perform high-precision mass measurements was first proposed in Ref. [37]. This method is a particularization of the general idea presented in Ref. [35], where the ions are located in different traps. As it was stated in Sec. 2.4, the two main advantages of this method are its sensitivity and universality: it only requires one target ion to determine the frequency ratio and it can be implemented for any ion species.

The link between the six modes' eigenfrequencies and the cyclotron frequencies of the two individual ions is provided by the generalized invariance theorem (Eq. (2.20)), theoretically proposed for Penning traps [41] but not yet experimentally demonstrated. This relationship is strictly correct only for infinitesimal ion amplitudes since the Coulomb interaction introduces amplitude-dependent shifts in the motional frequencies.

In this chapter, motional frequency measurements of the six eigenmodes of a balanced ($^{40}Ca^{+}$ - $^{40}Ca^{+}$) crystal are presented. The level of accuracy reached by the generalized invariance theorem is evaluated by comparing with single-ion cyclotron-frequency measurements of $^{40}Ca^{+}$ using the technique developed in Chapter 5. The anharmonicities arising from the Coulomb potential are clearly visible when probing the eigenmodes in the case of the unbalanced crystal. They are treated as a perturbation to the harmonic potential, and the method of multiple scales is used to calculate the dynamics of the system (see Appendix C). The first measurements on an unbalanced crystal ($^{42}Ca^{+}$ - $^{40}Ca^{+}$) are also presented, underlining the differences in the analysis procedure with respect to the balanced crystal. The results are subject to improvement, issues that are also discussed.

6.1 Preparation of the two-ion crystal

The two constituents of the crystal can be produced separately by the two dedicated ion sources (see Sec. 3.1.1). The Paul-trap ion source, located closer to the

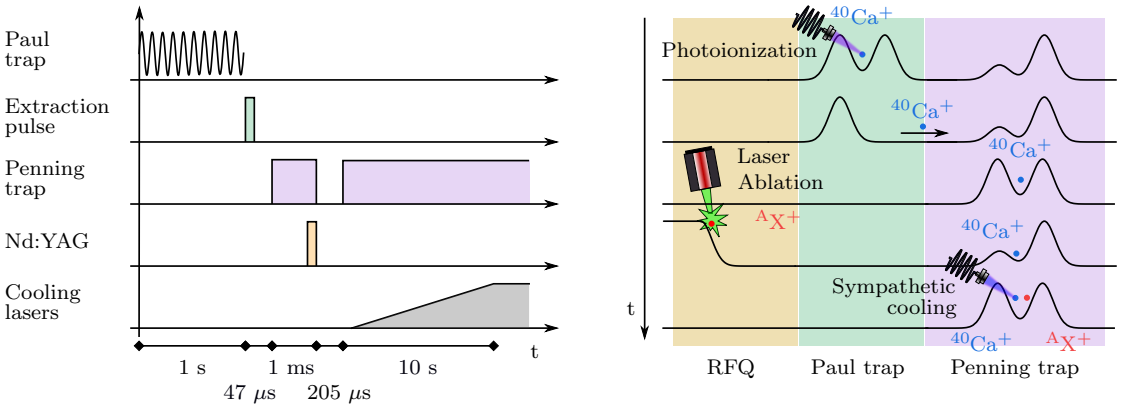

Figure 6.1. Injection scheme to form a two-ion crystal in the Penning trap. Left: time sequence showing the steps to load the two ions in the Penning trap. Right: pictorial description showing the sequential production using the two ion sources and the Penning-trap voltage adjustment. $^{A}X^{+}$ represents any ion species that is produced with the ablation laser source, particularly in this chapter $^{40,42}Ca^{+}$. A crystal $^{40}Ca^{+}$ - $^{232}ThO_2{}^{+}$ is shown in the outlook (Chapter 7).

magnet, was used to produce the $^{40}Ca^{+}$ sensor ion and other calcium isotopes, while the ablation source supplied the target ion (see Fig. 3.1 for a general view of the beamline). Figure 6.1 shows the injection scheme. The simultaneous in-flight trapping was not possible since the sensor ion was lighter. The coolant sensor ion was trapped first, and the Penning trap was later partially opened for 2 μs to capture the target ion. The lower voltage was 2 V above the trap's bottom potential so that laser-cooled ions remained in the trap. The trap was set to 180/168/150 V in EC/CE/RE (see Sec. 3.1) to match the kinetic energy of the incoming ions. Afterwards, the potentials were lowered to 7/4.2/0 V, which corresponds to an axial frequency of 143 kHz for a single $^{40}Ca^{+}$ ion.

The target ion was sympathetically cooled through the Coulomb interaction with the laser-cooled $^{40}Ca^{+}$. Sympathetic cooling was first demonstrated in a Penning trap [29], although it has been more widely used in Paul traps with a high number of coolant ions [193] for spectroscopic studies on molecular ions [194] or highly-charged ions [195], and in a more particular way in the preparation of a two-ion crystal for quantum logic spectroscopy [196]. In Penning traps, it has only been previously used for spectroscopy studies [197] and with prospects to cool highly-charged ions [198]. While cooling times of about 90 s were obtained for the $^{40}Ca^{+}$ - $^{40}Ca^{+}$ balanced crystal ($E_0 = 17.5(1.8)$ eV, see Sec. 4.1.1), in agreement with the studies carried out in Ref. [199], much higher and impracticable values are predicted for the sympathetic cooling of one arbitrary ion by a single $^{40}Ca^{+}$.

Figure 6.2 shows the fluorescence detection of a $^{42}Ca^{+}$ - $^{40}Ca^{+}$ crystal. The two constituents were individually laser-cooled, which could be quickly done by software commands since the isotope shift was smaller than the diode-lasers mode hop-free range. Figure 6.2 also shows a ToF spectrum of simultaneously trapped

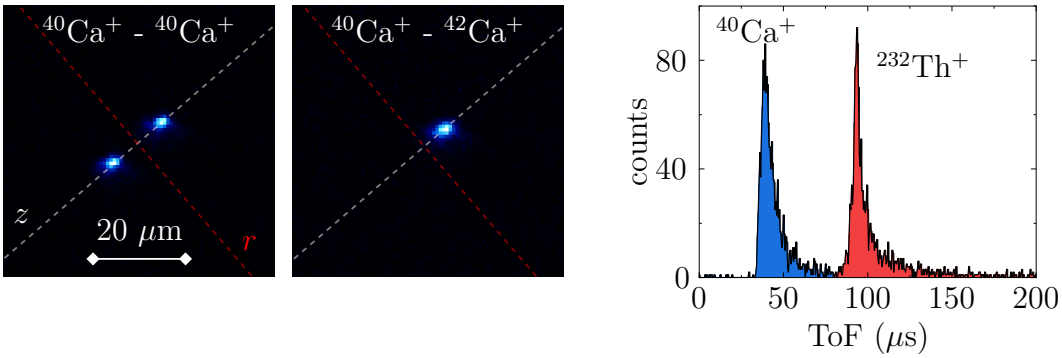

Figure 6.2. Identification of the ion crystals. Left: balanced crystal, clearly observed from the fluorescence of the two ions. Middle: fluorescence image of an unbalanced $^{42}Ca^+$ - $^{40}Ca^+$ crystal. The distance between the two ions does not depend on the mass since only electrostatic forces are involved at rest. In this case, the identification was possible without probing any mode, by tuning the cooling lasers first for $^{40}Ca^+$ and later for $^{42}Ca^+$. Right: ToF distributions resulting from 1000 measurements of simultaneously trapped $^{40}Ca^+$ and $^{232}Th^+$ (an/or oxide compounds), delivered by the Paul-trap and the ablation source, respectively. This detection is useful when no fluorescence from the target ion can be observed under any circumstances.

$^{40}Ca^+$ and $^{232}Th^+$ ions. Sympathetic cooling of $^{232}Th^+$ and its oxide compounds has also been accomplished (see Chapter 7), requiring times in the order of minutes to reach the Doppler limit.

6.2 Measurement scheme

The measurement protocol used to determine the crystal's eigenfrequencies is generally analogous to the one developed in Chapter 5 for the single-ion measurements: for each mode, the frequency of an external electric field was scanned around the resonance value so that the eigenmode's amplitude was consequently excited. However, there are two distinctive features of the two-ion crystal: the charge distribution in the stretch modes and the anharmonicities arising from the Coulomb interaction. Figure 6.3 depicts these two features for the axial mode.

In the common mode, the two ions carry out in-phase small displacements from the equilibrium positions. Therefore, a spatially homogeneous (or dipolar) electric field, such that $\vec{E}_1 \approx \vec{E}_2$ at the two equilibrium positions, increases the oscillation amplitude of both ions when driven around the mode resonance frequency. In the stretch mode, the ions move in opposite phases, so an optimal coupling is achieved if $\vec{E}_1 \approx -\vec{E}_2$, which is accomplished by a quadrupolar field.

The dynamics of the two-ion crystal when the Coulomb interaction is approximated by a linear restoring force is studied in Ref. [37]. This model was developed in M. J. Gutiérrez's thesis [65], and a brief summary can be found in Sec. 2.1.2.

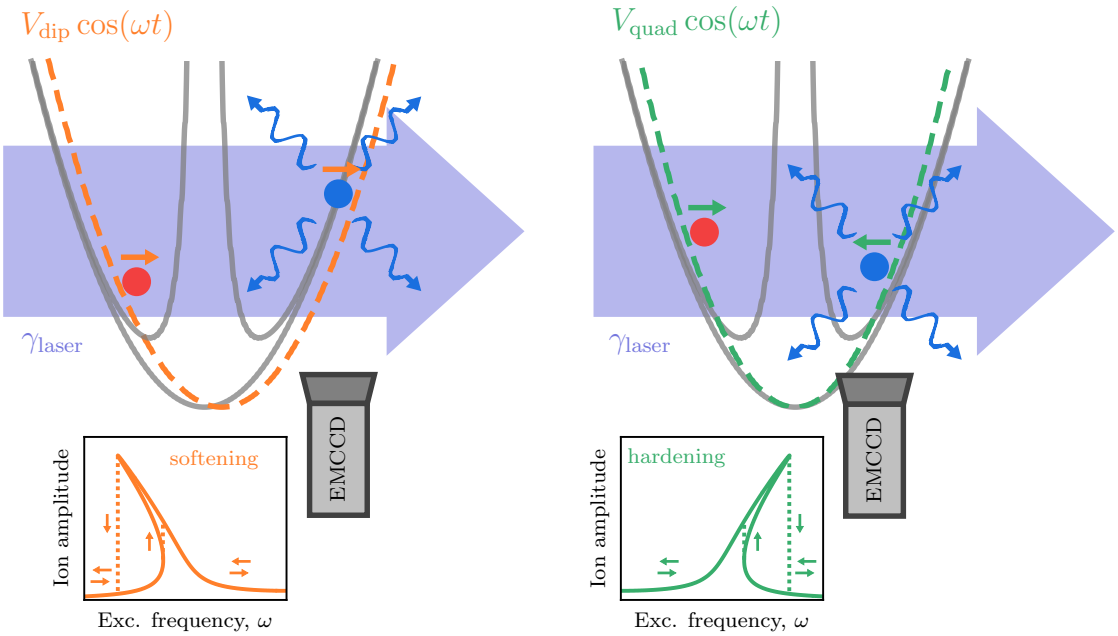

Figure 6.3. Measurement of the axial eigenmodes of an unbalanced crystal. Left: common mode. Right: stretch mode. The grey lines represent the trap and the total potential. Dashed lines are used when the dipolar/quadrupolar excitation field is added for the common/stretch mode. Laser cooling is applied if the amplitude-dependent frequency shift is much larger than the resonance width. A Duffing-type resonance is obtained for the bright-ion oscillation amplitude. There is a region with three possible oscillation amplitudes for the same frequency. Only the maximum and minimum amplitudes are observed depending on the scanning direction, which is indicated by the arrows.

Although it is only strictly valid for infinitesimal oscillation amplitudes, it can be used as an approximation if they are much smaller than the equilibrium distance between the ions, $d_{\text{ion-ion}}$ (Eq. (2.16)). For the measurements presented in this chapter, $d_{\text{ion-ion}} = 20.5(2)$ μm (see Sec. 4.2.4 for the characterization of the trap's frequencies), while the ions had to be excited to several micrometres to detect a peak/dip signal in the EMCCD/PMT. With these values, frequency shifts have been already observed, especially in the stretch modes. A new model including the third- and fourth-order terms in the Taylor series expansion of the Coulomb potential has been developed to describe these deviations from the harmonic approximation.

The Lagrangian of the two-ion crystal can be written as

$$\mathcal{L}_{\text{crystal}} = \frac{1}{2}m_s\dot{p}_s\dot{\bar{p}}_s - \frac{1}{4}m_s\omega_{zs}^2\left(2z_s^2 - p_s\bar{p}_s\right) + \frac{i}{4}m_s\omega_{cs}\left(p_s\dot{\bar{p}}_s - \bar{p}_s\dot{p}_s\right) + \tag{6.1}$$

$$\frac{1}{2}m_t\dot{p}_t\dot{\bar{p}}_t - \frac{1}{4}m_t\omega_{zt}^2\left(2z_t^2 - p_t\bar{p}_t\right) + \frac{i}{4}m_t\omega_{ct}\left(p_t\dot{\bar{p}}_t - \bar{p}_t\dot{p}_t\right) - V, \tag{6.2}$$

where s and t stand for sensor and target, respectively. m is the mass, $p = x + iy$,

and V is the Coulomb potential. The crystal motional equations are presented in Sec. 2.1.2. Within the harmonic approximation, the axial direction and the radial plane are decoupled (see Eq. (2.17)). Moreover, the axial modes can be diagonalized so that the differential equations obtained for the common and stretch modes are decoupled. The motional equation for any of the axial eigenmodes Z_λ with eigenvalue Ω_λ becomes

$$\begin{aligned}\ddot{Z}_\lambda + \Omega_\lambda^2 Z_\lambda + \frac{1}{2}\frac{\partial}{\partial Z_\lambda}\Big[\sum_{i,j,k} \frac{\partial^3 V}{\partial u_i \partial u_j \partial u_k}\Big|_{\text{eq}} e_i^\alpha e_j^\beta e_k^\gamma U_\alpha U_\beta U_\gamma + \\ \sum_{i,j,k,l} \frac{\partial^4 V}{\partial u_i \partial u_j \partial u_k \partial u_l}\Big|_{\text{eq}} e_i^\alpha e_j^\beta e_k^\gamma e_l^\delta U_\alpha U_\beta U_\gamma U_\delta \Big] = 0,\end{aligned} \tag{6.3}$$

where e represents the change-of-basis matrix from the spatial coordinates $\{u_i\}$ to the eigenvectors $\{U_\alpha\}$. The radial eigenmodes are not decoupled in the harmonic approximation. If the radial eigenmode P_λ is expressed in terms of $p_{s,t}$ as $P_\lambda = \delta_\lambda^s p_s + \delta_\lambda^t p_t$, where δ represents the change-of-basis matrix from the radial spatial coordinates $\{p_{s,t}, \bar{p}_{s,t}\}$ to the eigenvectors $\{P_i\}$, the motional equation for P_λ can be written as

$$\begin{aligned} & m_s\delta_s^\lambda \sum_k \delta_s^k \ddot{\bar{P}}_k + m_t\delta_t^\lambda \sum_k \delta_t^k \ddot{\bar{P}}_k \\ & + i m_s\omega_{cs}\delta_s^\lambda \sum_k \delta_s^k \dot{\bar{P}}_k + i m_t\omega_{ct}\delta_t^\lambda \sum_k \delta_t^k \dot{\bar{P}}_k \\ & - m_s\omega_{zs}^2\delta_s^\lambda \sum_k \delta_s^k \bar{P}_k - m_t\omega_{zt}^2\delta_t^\lambda \sum_k \delta_t^k \bar{P}_k \\ & - \frac{1}{2} m_s\omega_{zs}^2\delta_s^\lambda \sum_k \delta_t^k \bar{P}_k - \frac{1}{2} m_t\omega_{zt}^2\delta_t^\lambda \sum_k \delta_s^k \bar{P}_k \\ & + \frac{1}{2}\frac{\partial}{\partial P_\lambda}\Bigg[\sum_{i,j,k} \frac{\partial^3 V}{\partial u_i \partial u_j \partial u_k}\Big|_{\text{eq}} e_i^\alpha e_j^\beta e_k^\gamma U_\alpha U_\beta U_\gamma + \\ & \sum_{i,j,k,l} \frac{\partial^4 V}{\partial u_i \partial u_j \partial u_k \partial u_l}\Big|_{\text{eq}} e_i^\alpha e_j^\beta e_k^\gamma e_l^\delta U_\alpha U_\beta U_\gamma U_\delta \Bigg] = 0. \end{aligned} \tag{6.4}$$

Equations (6.3) and (6.4) couple in principle all the six eigenmodes. However, taking into account that the amplitude of the frequency-scanned mode $u \in \{Z_\lambda, P_\lambda\}$ is much higher than that of any of the other eigenmodes, the motional equation of the axial modes can be reduced to one of the type

$$\ddot{u} + \omega_0^2 u + \alpha_2 u^2 + \alpha_3 u^3 = 0 \tag{6.5a}$$

while for the radial modes

$$\ddot{u} - i\omega_c \dot{u} - \omega_0^2 u + \alpha_2 u^2 + \alpha_3 u^3 = 0. \tag{6.5b}$$

The parameters α_2 and α_3, derived from the Coulomb-potential Taylor series, quantify the non-linearity. Since the second-order frequency shifts average zero over the whole oscillation period due to its even parity, the third order is also included. Multiple-scale analysis [200] is used to solve Eqs. (6.5) in Appendix C. This method is a generalization of the standard perturbation theory where several independent time variables are included in the hypothetical solution to describe dynamics at disparate time scales.

In the cases where amplitude-dependent frequency shifts were discernible, the laser was left on during the excitation period. This made possible to detect lower amplitudes but increased the linewidth of the resonance. The mode amplitude u_0 obeys the implicit equation

$$\left\{\left[(\omega-\omega_0)-F\left(\alpha_2,\alpha_3\right)u_0^2\right]^2+\gamma_{\text{laser}}^2\right\}^2 u_0^2=\frac{E_0^2}{4\omega_0^2}, \tag{6.6}$$

where $F\left(\alpha_2,\alpha_3\right)$ is a real number that depends on the coefficients α_2 and α_3, γ_{laser} quantifies the laser-cooling damping, and E_0 accounts for the external-field amplitude oscillating at frequency $\nu=\omega/2\pi$. Equation (6.6) predicts the frequency spectra depicted in Fig. 6.3, which is the characteristic resonance of a Duffing oscillator. This kind of system has already been studied in Paul traps [201, 202]. There is a region where three values of the motional amplitude coexist, and the observation of two of them (maximum and minimum) depends on the scanning direction, which can be considered as a hysteresis behaviour. A positive $F\left(\alpha_2,\alpha_3\right)$ describes a hardening oscillator, in which the frequency increases with the amplitude, and gives rise to a rightward-tilted curve. $F\left(\alpha_2,\alpha_3\right)<0$ corresponds to a softening oscillator. Equation (6.6) has been solved numerically using `fsolve` from the Python's package `scipy.optimize`.

6.3 The balanced $^{40}Ca^+$ - $^{40}Ca^+$ crystal: a test over the generalized invariance theorem

The balanced $^{40}Ca^+$ - $^{40}Ca^+$ crystal was chosen for the first experimental tests in which all the eigenfrequencies of a two-ion crystal are measured in a Penning trap. The production and injection of $^{40}Ca^+$ into the Penning trap was well controlled (see Chapter 4 and Ref. [77]) and the cooling time was much shorter than for an unbalanced crystal. The results have been used for the first tests of the generalized invariance theorem.

A total of three measurements were carried out in November 2022. All the resonances of one of these measurements are shown in Fig. 6.4. Analogously to the measurements presented in Chapter 5, several frequency sweeps (5-10) were performed to determine each eigenfrequency. The fluorescence signal of both ions has been analysed, and the mean value of the number of photons and the ions' width has been used to build the resonance curves. The study of the individual

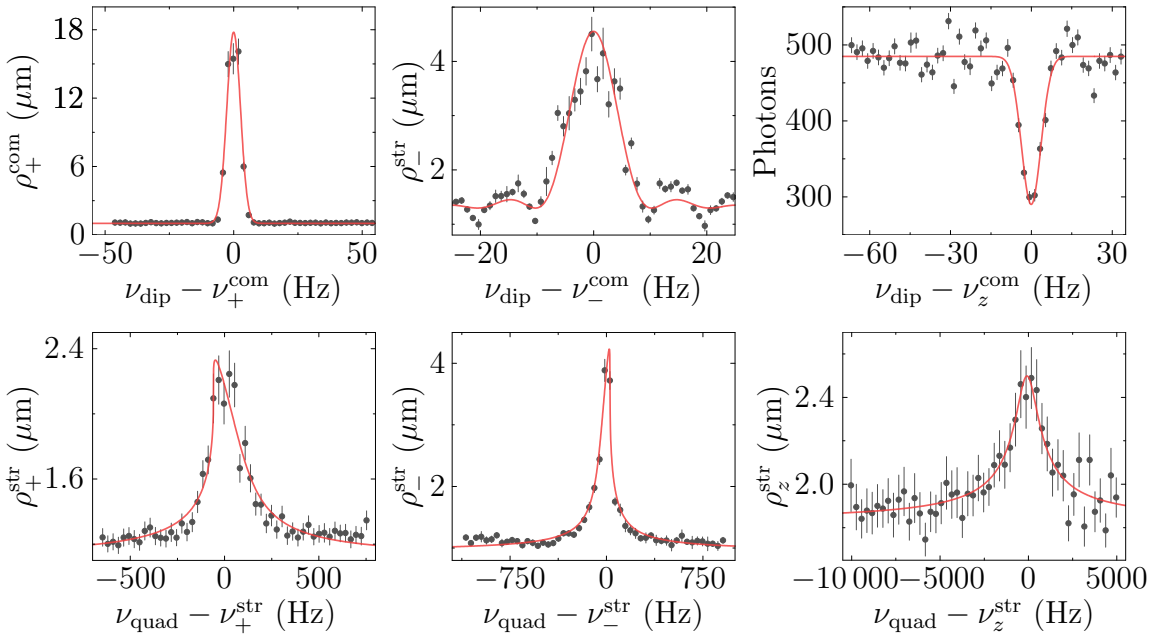

Figure 6.4. Eigenfrequency measurements of a balanced $^{40}Ca^+$ - $^{40}Ca^+$ crystal. The common and stretch modes are shown in the upper and lower rows, respectively. From left to right: modified-cyclotron, magnetron, and axial modes. The excitation voltages were $V_{dip} = 80/400/180$ μV_{pp} for $\nu_+^{com}/\nu_-^{com}/\nu_z^{com}$ and $V_{quad} = 250/100/100$ mV_{pp} for $\nu_+^{str}/\nu_-^{str}/\nu_z^{str}$. The excitation time in the common modes was $t_{dip} = 100$ ms. The stretch modes were measured in the steady state with laser cooling on. The data has been fitted to Gaussian/sync functions for the common modes and to Eq. (6.6) for the stretch modes. The centre values correspond to the first experiment listed in Tab. 6.1.

scans or the average data has led to equivalent results. The uncertainty treatment procedure discussed in Secs. 5.1.2 and 5.1.3 has been also applied here. Note that the modified-cyclotron modes are sometimes referred to as simply cyclotron modes throughout this chapter for clarity.

The laser-pulsed measurement technique presented in Chapter 5 was used for the common modes, extracting the ions' motional amplitudes from the EMCCD images for the radial modes and from the PMT counts for the axial mode. In the common modes, the ions move in phase and with the same amplitude due to symmetry. The equations of motion are fully solvable and the three eigenfrequencies are those of a single ion, not observing any amplitude-dependent shift due to the Coulomb interaction [37, 65].

For the stretch modes, the steady-state measurement scheme was used, applying laser cooling while the ion was excited. Analogously to the pulsed measurements, 75-ms accumulation-time images were taken by the EMCCD for each excitation frequency. It was not possible to locate the resonance peak using the laser-pulsed technique. Taking as a reference the measurements in Chapter 5,

Table 6.1. Eigenfrequencies of the balanced $^{40}Ca^+$ - $^{40}Ca^+$ crystal. ν^{com} and ν^{str} stand for the common and stretch eigenfrequencies, respectively. $\Delta\nu^{com}$ and $\Delta\nu^{str}$ are the frequency shifts with respect to the zero-amplitude value predicted based on the single-ion measurements. $(\nu_c)_{single}$ is the single-$^{40}Ca^+$-ion cyclotron frequency used as calibration. The common-mode frequencies calibration values are not affected by the motional amplitude and are exactly those of a single ion. The stretch axial eigenfrequency is $\sqrt{3}$ times the common-mode one, and the radial frequencies can be calculated using the single-ion relationship (Eq. (2.6)). $(\nu_c)_{crystal}$ is the $^{40}Ca^+$ cyclotron-frequency value calculated using the generalized invariance theorem. The frequency shift with respect to the single-ion calibration value is also shown.

	ν^{com} (Hz)	ν^{str} (Hz)	$\Delta\nu^{com}$ (Hz)	$\Delta\nu^{str}$ (Hz)
ν_+	2 685 576.13(24)	2 677 947.0(95)	0.00(26)	-19.6(95)
ν_-	3 785.53(49)	11 493.1(70)	0.20(50)	94.9(70)
ν_z	142 651.74(67)	247 030(190)	0.9(13)	-040(190)
$(\nu_c)_{single}$	2 689 364.75(10)			
$(\nu_c)_{crystal}$	2 689 353(20)		-12(20)	

	ν^{com} (Hz)	ν^{str} (Hz)	$\Delta\nu^{com}$ (Hz)	$\Delta\nu^{str}$ (Hz)
ν_+	2 685 577.144(53)	2 677 935.1(98)	0.27(17)	-34.0(98)
ν_-	3 783.30(68)	11 448.4(72)	0.35(71)	52.3(72)
ν_z	142 638.3(31)	247 050(150)	-6.5(35)	000(150)
$(\nu_c)_{single}$	2 689 365.36(74)			
$(\nu_c)_{crystal}$	2 689 348(17)		-17(17)	

	ν^{com} (Hz)	ν^{str} (Hz)	$\Delta\nu^{com}$ (Hz)	$\Delta\nu^{str}$ (Hz)
ν_+	2 685 576.719(72)	2 677 937(15)	0.00(11)	-31(15)
ν_-	3 783.72(48)	11 444(37)	0.08(63)	47(37)
ν_z	142 642.43(98)	247 042(190)	-1.6(20)	-025(190)
$(\nu_c)_{single}$	2 689 364.98(41)			
$(\nu_c)_{crystal}$	2 689 349(23)		-16(23)	

the stretch mode needs to be excited to tens of micrometres. The corresponding amplitude-dependent frequency shifts have been calculated using the formalism employed in Ref. [37], where the cross-coupling matrix that connects the frequency shift on a specific mode with the phonon number of the rest of the modes is presented [203]. For the stretch axial mode of $^{40}Ca^+$ - $^{40}Ca^+$, a frequency shift above 2 kHz is already predicted for $\rho_z^{str} = 1$ μm.

Note the difference of several orders of magnitudes between the excitation volt-

ages applied for dipolar and quadrupolar excitations used for the common and stretch modes, respectively. On the one hand, the stretch-mode excitation needs to overcome the laser damping while no resistance is found in the pulsed scheme used in the common modes. On the other hand, the dipolar coupling in the common modes is stronger than the quadrupolar interaction in the stretch modes.

Table 6.1 shows the measured eigenfrequencies for the three experiments carried out with $^{40}Ca^+$ - $^{40}Ca^+$. The first group of data corresponds to the measurements presented in Fig. 6.4. It took typically one hour to perform each eigenfrequency measurement, spending most of the time on the loading and formation of the two-ion crystal. Cyclotron-frequency measurements of single $^{40}Ca^+$ ions were performed before and after each of the crystal series, and linear interpolation has been used to estimate the single-ion calibration frequency at the time the crystal was measured. The cyclotron frequency calculated using the generalized invariance theorem agrees in all three cases with the single-ion value with a relative uncertainty of $7 \cdot 10^{-6}$.

The uncertainties obtained in the common mode are comparable to those obtained in the single-ion measurements presented in Chapter 5, of the order of $4.5 \cdot 10^{-8}/1.5 \cdot 10^{-5}/1.1 \cdot 10^{-6}$ for $\nu_+^{\mathrm{com}}/\nu_-^{\mathrm{com}}/\nu_z^{\mathrm{com}}$. The frequencies agree with those of a single ion ($\Delta\nu^{\mathrm{com}}$ column in Tab. 6.1), and a relative uncertainty in the cyclotron frequency of $4.7 \cdot 10^{-8}$ is obtained.

The uncertainty of the stretch modes clearly prevails over those of the common modes in the final value obtained through the generalized invariance theorem. The relative values for $\nu_+^{\mathrm{str}}/\nu_-^{\mathrm{str}}/\nu_z^{\mathrm{str}}$ are $4.3 \cdot 10^{-6}/1.5 \cdot 10^{-3}/7.2 \cdot 10^{-4}$. The main reason is the damping effect of laser cooling, leading to a linewidth of 201(12)/87.6(75)/2530(870) and a linear damping coefficient (see Eq. (C.1)) of 70(30)/21.8(61)/1440(210) Hz for $\nu_+^{\mathrm{str}}/\nu_-^{\mathrm{str}}/\nu_z^{\mathrm{str}}$. From these values, it can be seen that the axial mode was the most efficiently cooled, and that, even using axialization, the modified-cyclotron mode was still cooled faster than the magnetron one. Although the highest relative uncertainty is obtained in the magnetron mode, the major contribution to the final uncertainty through the generalized invariance theorem comes from the axial and modified-cyclotron modes. The uncertainties of these would need to be reduced by about an order of magnitude to gain an equivalent factor in the cyclotron frequency determination.

A negative frequency shift of $6 \cdot 10^{-6}$ is always observed in the cyclotron frequency, which suggests a systematic shift that could have been better discernible

Table 6.2. Mean phonon number for each eigenmode of the crystal $^{40}Ca^+$ - $^{40}Ca^+$ in the Doppler limit. The magnetron modes are assumed to be cooled by axialization.

n_+^{com}	n_+^{str}	n_-^{com}	n_-^{str}	n_z^{com}	n_z^{str}
3.4	3.6	3.4	3.6	73	42

with higher statistics. This is clearly visible for the values of $\Delta\nu_{+,-}^{\mathrm{str}}$ in the last column of Tab. 6.1. In fact, none of these values agrees with the prediction based on the one-ion or the common-mode measurements, but the final cyclotron frequency uncertainty is increased by the stretch-mode uncertainty so that it does agree with the calibration measurement. Stretch cyclotron and magnetron eigenfrequencies were measured for different excitation voltages, but an amplitude-dependent shift has not been observed within the uncertainty obtained. The frequency shift observed in a given mode can also be caused by a finite amplitude of any of the others. The mean phonon number for each eigenmode when the crystal is cooled to the Doppler limit is shown in Tab. 6.2. For the case of $^{40}Ca^{+}$ - $^{40}Ca^{+}$, the cross-coupling matrix [37, 203] reads

$$\begin{pmatrix} \Delta\nu_{+}^{\mathrm{com}} \\ \Delta\nu_{+}^{\mathrm{str}} \\ \Delta\nu_{-}^{\mathrm{com}} \\ \Delta\nu_{-}^{\mathrm{str}} \\ \Delta\nu_{z}^{\mathrm{com}} \\ \Delta\nu_{z}^{\mathrm{str}} \end{pmatrix} = \begin{pmatrix} 0 & 0 & 0 & 0 & 0 & 0 \\ 0 & 0.0050 & 0 & 4.8503 & 0 & -0.1062 \\ 0 & 0 & 0 & 0 & 0 & 0 \\ 0 & 4.8503 & 0 & -2.4049 & 0 & 25.519 \\ 0 & 0 & 0 & 0 & 0 & 0 \\ 0 & -0.1062 & 0 & 25.519 & 0 & 0.1987 \end{pmatrix} \begin{pmatrix} n_{+}^{\mathrm{com}} \\ n_{+}^{\mathrm{str}} \\ n_{-}^{\mathrm{com}} \\ n_{-}^{\mathrm{str}} \\ n_{z}^{\mathrm{com}} \\ n_{z}^{\mathrm{str}} \end{pmatrix} \mathrm{Hz}. \quad (6.7)$$

The common modes do not suffer from any amplitude-dependent frequency shift since the distance between the ions is constant (see Eq. (2.15) for $m_s = m_t$). The negative frequency shift observed in the stretch cyclotron, $\Delta\nu_{+}^{\mathrm{str}} = -28.2(62)$, can be explained considering, e.g., $n_z^{\mathrm{str}} = 420(59)$, and assuming that the stretch magnetron mode was cooled to the Doppler limit (see Tab. 6.2), which is equivalent to $T_z^{\mathrm{str}} = 10.0(14)$ mK. $\Delta\nu_{-}^{\mathrm{str}} \approx 1$ kHz is predicted after all the eigenmodes are cooled to the Doppler limit mostly due to the contribution of n_z^{str}, much smaller than the values of Tab. 6.1, $\Delta\nu_{-}^{\mathrm{str}} = 65(21)$ kHz. An amplitude of the stretch magnetron mode $\rho_{-}^{\mathrm{str}} > 140$ nm, compatible with the observations with the EMCCD, could explain this frequency shift.

The stretch axial mode clearly features a dependency of the frequency on the mode amplitude. The ions explore closer relative distances for higher motional amplitudes, which translates into a positive frequency shift and a hardening nonlinear response (see Fig. 6.3). Figure 6.5 shows the resonance curves obtained for several excitation voltages. For values higher than 200 $\mathrm{mV_{pp}}$, there is a region where the resolution of the implicit relation used for fitting the data, Eq. (6.6), predicts three possible motional amplitudes. Since the scanning direction in Fig. 6.5 is towards higher frequencies, the highest amplitude was observed in the three-solution region (see Fig. 6.3). A sudden amplitude drop takes place at the point where Eq. (6.6) predicts only one solution again. In the case of scanning the excitation frequency in the opposite direction, the low-amplitude solution would be experimentally observed until a break would happen likewise to go over the one-solution region of lower frequencies.

The upper-right panel of Fig. 6.5 shows the magnitude of the sinusoidal force applied to obtain the resonance curves on the left side. The lower-right panel shows

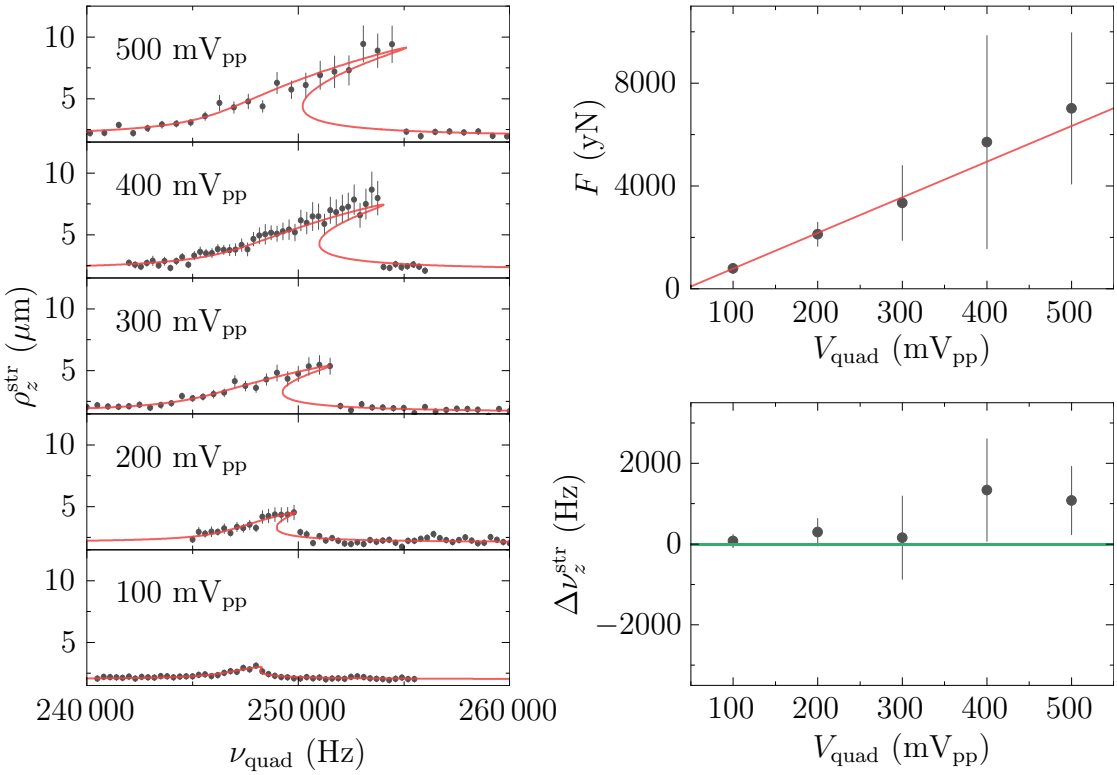

Figure 6.5. Studies of the amplitude-dependent frequency shift in the stretch axial mode of $^{40}Ca^+$ - $^{40}Ca^+$. Left: resonance curves for different excitation voltages. Right: force applied over the two-ion system and resonance frequency, both extracted from the fit to the amplitude deduced in Eq. (6.6). The reference stretch axial frequency in the lower-right plot is 247 068 Hz.

the zero-amplitude frequency obtained from the fitting routine. It agrees with the single-ion calibration value for low voltages ($V_{quad} \leq 200$ mV$_{pp}$). However, the uncertainty obtained is generally higher if the excitation voltage is increased.

6.4 The unbalanced $^{42}Ca^+$ - $^{40}Ca^+$ crystal

$^{42}Ca^+$ - $^{40}Ca^+$ is the first two-ion unbalanced crystal for which all the six eigenfrequencies have been directly probed in a Penning trap. It was the easiest crystal to prepare in the experiment since the lasers could be tuned to cool $^{40}Ca^+$ or $^{42}Ca^+$ by a simple software instruction in the control system. In the loading procedure, the $^{42}Ca^+$ ion was cooled first to avoid heating of $^{40}Ca^+$ when tuning the lasers since the cooling frequencies are higher for the latter. $^{40}Ca^+$ and $^{42}Ca^+$ single-ion cyclotron-frequency measurements were performed before and after the crystal studies. $^{40}Ca^+$ has been used as the sensor ion, while the $^{42}Ca^+$ data has been used to check the validity of the crystal measurements.

Two complete measurements of the six eigenfrequencies were performed in

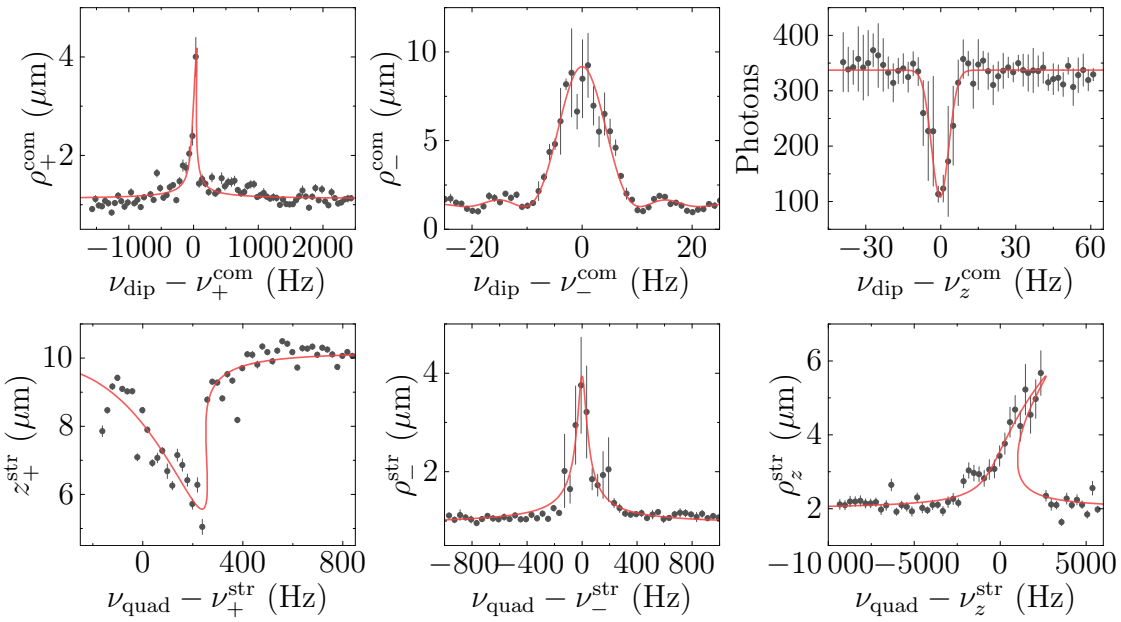

Figure 6.6. Eigenfrequency measurements of an unbalanced $^{42}Ca^+$ - $^{40}Ca^+$ crystal. The same arrangement as in Fig. 6.4 is used. The excitation voltages were $V_{\mathrm{dip}} = 3000/200/300$ μV_{pp} for $\nu_+^{\mathrm{com}}/\nu_-^{\mathrm{com}}/\nu_z^{\mathrm{com}}$ and $V_{\mathrm{quad}} = 30/100/200$ $\mathrm{mV_{pp}}$ for $\nu_+^{\mathrm{str}}/\nu_-^{\mathrm{str}}/\nu_z^{\mathrm{str}}$. The excitation time in the common magnetron and axial modes was $t_{\mathrm{dip}} = 100$ ms. Unlike the usual motional amplitude or number of detected photons, the axial distance to the trap centre is monitored for the stretch cyclotron mode. More details can be found in the text. The centre values correspond to the second experiment listed in Tab. 6.3.

November 2022. Figure 6.6 shows the resonances from one of them. For these experiments, the laser-pulsed measurement scheme used in Chapter 5 could only be used for the common axial and magnetron modes. The steady-state measurement scheme keeping laser cooling on had to be used for the common cyclotron mode, where non-linearities were observed. The stretch axial mode presents a clearly tilted resonance, while the stretch magnetron spectrum anharmonicity is not discernible at these amplitudes.

The stretch cyclotron is a singular case. It has been found that $^{40}Ca^+$, bright and lighter ion in this case, moved towards the trap centre as the resonance frequency was approached. According to the simulations presented in Ref. [37], the oscillation amplitude of $^{42}Ca^+$ in the stretch cyclotron mode is around 20 times higher than that of the $^{40}Ca^+$ ion. Therefore, the low-amplitude hypothesis was not valid any more when this mode was driven by an electric field to detect the oscillation amplitude of the $^{40}Ca^+$ ion with the EMCCD. During the frequency scan, the crystal was generally not aligned along the axial axis defined by the magnetic field even for a small $^{40}Ca^+$ oscillation amplitude. This would have needed to be well below one micrometre to satisfy the hypothesis aforementioned. Assuming the $^{40}Ca^+$ amplitude was negligible compared to the one of $^{42}Ca^+$, the force balance

Table 6.3. Eigenfrequencies of the unbalanced $^{42}Ca^+$ - $^{40}Ca^+$ crystal. The same nomenclature as in Tab. 6.1 is used here.

	ν^{com} (Hz)	ν^{str} (Hz)	$\Delta\nu^{\text{com}}$ (Hz)	$\Delta\nu^{\text{str}}$ (Hz)
ν_+	2 681 340(150)	2 553 568(87)	-540(140)	-156(87)
ν_-	3 785.98(36)	11 474(17)	-1.01(36)	80(17)
ν_z	140 898.0(13)	243 800(980)	32.0(13)	-370(980)
$(\nu_{cs})_{\text{single}}$	2 689 364.867(60)			
$(\nu_{ct})_{\text{single}}$	2 561 426.552(90)			
$(\nu_{ct})_{\text{crystal}}$	2 560 670(140)		-750(140)	

	ν^{com} (Hz)	ν^{str} (Hz)	$\Delta\nu^{\text{com}}$ (Hz)	$\Delta\nu^{\text{str}}$ (Hz)
ν_+	2 681 447(76)	2 553 686(30)	-441(76)	-38(30)
ν_-	3 784.80(40)	11 433(87)	-2.20(40)	39(87)
ν_z	140 889.0(11)	244 850(870)	23.0(11)	720(870)
$(\nu_{cs})_{\text{single}}$	2 689 364.87(22)			
$(\nu_{ct})_{\text{single}}$	2 561 426.55(20)			
$(\nu_{ct})_{\text{crystal}}$	2 561 002(82)		-425(82)	

between the trap confinement and the Coulomb interaction for the first is

$$m_s \left(\omega_z^{\text{str}}\right)^2 z_+^{\text{str}} = \frac{q^2}{4\pi\varepsilon_0} \frac{2z_+^{\text{str}}}{\left[(2z_+^{\text{str}})^2 + (r_+^{\text{str}})^2\right]^{3/2}}, \tag{6.8}$$

where z_+^{str} is the axial distance of any of the ions to the trap centre ($^{40}Ca^+$ is monitored here) and r_+^{str} is the radial distance of the $^{42}Ca^+$ to the trap centre. Resolving for the axial position of the bright ion,

$$z_+^{\text{str}} = \frac{1}{2}\sqrt{d_{\text{ion-ion}}^2 - (r_+^{\text{str}})^2}, \tag{6.9}$$

where $d_{\text{ion-ion}}$ is the two-ion equilibrium distance defined by Eq. (2.16). Analogously to the motional amplitudes of other modes, r_+^{str} is assumed to follow the non-linear oscillator model, Eq. (6.6). The resonance described by Eq. (6.9) is an asymmetric dip, as can be seen in the lower-left plot of Fig. 6.6.

Table 6.3 shows the resonance frequencies obtained from the fits for the two complete measurements. The cyclotron frequency presents a statistical relative uncertainty of $4 \cdot 10^{-5}$, mainly dominated by the stretch axial and common cyclotron frequencies, determined with $3.8 \cdot 10^{-3}$ and $4.2 \cdot 10^{-5}$ relative uncertainty, respectively. However, the value of ν_c determined through the generalized invariance theorem from the crystal six-eigenmode measurements is negatively shifted several hundreds of hertz in both measurements, giving rise to a systematic relative uncertainty in the order of $2 \cdot 10^{-4}$.

Systematic shifts are perceptible in all the eigenmodes, as can be observed in the two rightmost columns of Tab. 6.3. Analogously to the case of the $^{40}Ca^+$ - $^{40}Ca^+$ crystal, these frequency shifts can be explained by a non-zero population of other modes. The cross-coupling matrix [37, 203] for the crystal $^{42}Ca^+$ - $^{40}Ca^+$ reads

$$\begin{pmatrix} \Delta\nu_+^{\mathrm{com}} \\ \Delta\nu_+^{\mathrm{str}} \\ \Delta\nu_-^{\mathrm{com}} \\ \Delta\nu_-^{\mathrm{str}} \\ \Delta\nu_z^{\mathrm{com}} \\ \Delta\nu_z^{\mathrm{str}} \end{pmatrix} = \begin{pmatrix} 0.001 & -0.002 & 0 & 2.229 & -0.000 & -0.053 \\ -0.002 & 0.001 & 0 & 2.512 & -0.000 & -0.052 \\ 0 & 0 & -0 & -0 & 0 & 0 \\ 2.229 & 2.512 & -0 & -2.347 & 0.033 & 24.53 \\ -0.000 & -0.000 & 0 & 0.033 & -0.000 & 0.000 \\ -0.053 & -0.052 & 0 & 24.53 & 0.000 & 0.194 \end{pmatrix} \begin{pmatrix} n_+^{\mathrm{com}} \\ n_+^{\mathrm{str}} \\ n_-^{\mathrm{com}} \\ n_-^{\mathrm{str}} \\ n_z^{\mathrm{com}} \\ n_z^{\mathrm{str}} \end{pmatrix} \mathrm{Hz}, \tag{6.10}$$

where the arrangement is identical to Eq. (6.7). The matrix elements associated to $\Delta\nu_-^{\mathrm{com}}$ are null up to the third digit. The mean phonon number in the Doppler limit is the same as listed in Tab. 6.2 for $^{40}Ca^+$ - $^{40}Ca^+$. In the following, the population of the modes originating the cross-coupling terms is estimated from the observed systematic frequency shifts.

The common and stretch cyclotron eigenfrequencies tend to increase with the amplitude, as can be seen from the two first on-diagonal terms in the matrix of Eq. (6.10). The frequency shifts $\Delta\nu_+^{\mathrm{com}} = -491(50)$ Hz and $\Delta\nu_+^{\mathrm{str}} = -97(59)$ Hz observed from the measurements presented in Tab. 6.3 might be explained considering, e.g., $T_z^{\mathrm{str}} \approx 200$ mK and $T_z^{\mathrm{str}} \approx 50$ mK, respectively, assuming the rest of the modes were cooled to the Doppler limit.

The stretch magnetron eigenfrequency tends to decrease when the oscillation amplitude increases, as can be seen from the fourth on-diagonal term in the matrix of Eq. (6.10). A frequency shift $\Delta\nu_-^{\mathrm{str}} = 940$ Hz is predicted when the ion crystal is cooled to the Doppler limit against the observed value of $\Delta\nu_-^{\mathrm{str}} = 60(21)$ Hz. This can be explained by $\rho_z^{\mathrm{str}} = 2.0$ μm, which is compatible with the oscillation amplitude observed with the EMCCD.

The frequency shift in the stretch axial mode due to its own amplitude is positive since the relative distance between the ions decreases with the amplitude, as can be confirmed from the last on-diagonal element in the matrix of Eq. (6.10). The statistical uncertainty of $4 \cdot 10^{-4}$, does not allow, however, to draw any conclusion. In the common mode, the positive frequency shift $\Delta\nu_z^{\mathrm{com}} = 27.5(4.5)$ Hz can be explained from the mean number of phonons either in the stretch magnetron mode or in the stretch axial mode or a combination of both. A thorough quantification of this could be carried out after cooling the crystal to the ground state and using quantum-based protocols with a number of phonons as low as possible.

6.5 Prospects for first precision frequency ratios

The generalized invariance theorem has been tested to a relative uncertainty of $7 \cdot 10^{-6}$ using a $^{40}Ca^+$ - $^{40}Ca^+$ balanced crystal. The current limitation is set

by systematic shifts coming from cross-coupling between different modes. In these experiments, one-dimensional frequency scans were performed. Thus, the model presented in Sec. 6.2 was only able to correct for frequency shifts due to the amplitude associated to the excited eigenmotion. These shifts are more remarkable for the $^{42}Ca^{+}$ - $^{40}Ca^{+}$ unbalanced crystal. From the two experiments carried out so far, the generalized invariance theorem only holds up to $4 \cdot 10^{-5}$.

The technique and analysis procedure presented in this chapter could still provide better results if the eigenfrequencies are determined using the lowest field amplitudes. Assuming all the eigenfrequencies were measured at the Doppler limit, a relative uncertainty of $3.7 \cdot 10^{-6}$ would be obtained, improving the current results by an order of magnitude. Nevertheless, it will be necessary to cool the crystal to the ground state to perform competitive measurements. In that scenario, by applying resonant fields at each of the crystal's eigenfrequencies, one can see changes in the sideband spectrum due to the increase in the number of phonons. By controlling this quantity, it will be possible to obtain the systematic shift as a function of the phonon number of the rest of the modes, yielding a precise quantification of the systematic shift. Another variant of this approach consists in applying separated fields with opposite phases after the crystal is cooled to the ground state, as proposed in Ref. [38], or after preparing it in a Fock state, a method developed in RF traps [204]. To illustrate this method, the very first candidate will be $^{42}Ca^{+}$ - $^{40}Ca^{+}$ since both ions can be laser-cooled. The extension of the technique to a crystal with a target ion non-laser coolable will require further investigations to characterize sympathetic cooling.

Chapter 7

Summary and outlook

This thesis presents the first measurements of cyclotron-frequency ratios using optical detection in a Penning trap. The technique has been implemented on single calcium isotopes and two-ion Coulomb crystals. The first scenario has served for the characterization of the sensor ion, and it has rendered the first mass ratios using this technique. The experiments with balanced and unbalanced crystals have yielded useful data to test the validity of the generalized invariance theorem, and they constitute the first universal implementation of the method. In addition to these results, this manuscript details technical improvements implemented in the Penning-trap setup and the characterization of ion production and laser cooling. In the following, the main results and conclusions of this thesis work are summarized, discussing at the end the perspectives of the experiment in the short-term future.

Technical developments

The Penning-trap experiment in the Ion Traps and Lasers Laboratory at the University of Granada [98] was built in the course of previous theses [64, 65]. Part of the work presented here has been devoted to the design and commissioning of technical improvements which enabled the implementation the optical method.

Two new external sources to deliver ions to the Penning trap have been installed and characterized. The first one is a ring Paul trap used to deliver calcium isotopes created by photoionization with high reproducibility. The second one is a laser-ablation source which has been tested with gold, rhenium, and thorium, among other species. These external sources can create and inject two different species to generate any unbalanced crystal in the Penning trap. Before this thesis work, the calcium ions were generated inside the Penning trap, preventing reaching better vacuum conditions in the trapping region.

Further improvements of the vacuum in the Penning trap have been accomplished by installing a customized cryogenic pump, increasing the ion lifetime up to tens of minutes, which agrees with the expected background pressure in the order of 10^{-9} mbar obtained from simulations using Molflow+ [103].

The new (in-vacuum) optical system has been an important breakthrough. It

has been designed for collecting the ions' fluorescence and projecting the image on the PMT and EMCCD. Simulations of the performance have been carried out with Zemax. Out-of-vacuum measurements of the modulation transfer function and the contrast transfer function using square impulses have shown the near-diffraction-limited performance of the system on the optical axis. For the in-vacuum characterization, a single ion has been used as a point-like source to measure the point spread function of the system. Wave-aberration retrieval techniques have been employed to quantify the weight of each type of aberration on the Zernike polynomial basis. The strong astigmatism aberration initially observed has been corrected by adding a suitable cylindrical lens. The final resolutions in the axial and radial directions are 3.69(3) μm and 2.75(3) μm, respectively.

The acquisition and control system based on ARTIQ has been completed for the envisaged experiments in the Doppler limit. Most of the measurement protocols have been automated: in-flight ion trapping has been synchronized with the ion-sources ejection phase to improve reproducibility; the lasers' frequencies and the AOM's output can be tuned from the measurement scripts; the readouts of the PMT and MCP have been implemented directly through ARTIQ's hardware, which adds to the already-included EMCCD and AWGs [65].

Detection and characterization of laser-cooled ions

The implementation of the above-mentioned technical developments has made laser-cooling and detection of ions at the Doppler limit possible [77]. The creation of large ion Coulomb crystals, small chains, and single ions has been demonstrated in the experiment. In particular, the observation of crystallization in ensembles of up to thousands of ions implies temperatures below 5 mK.

The Penning trap has been characterized in terms of its axial frequency for a broad range of trapping voltages by optically measuring the distance between the two ions of a balanced $^{40}Ca^{+}$ crystal. The photon detection sensitivity has been pushed to its limit, obtaining signal-to-noise ratios above the unity for readout times of milliseconds. The collision rate in fluorescence measurements suggests an actual pressure in the trapping region around $3 \cdot 10^{-10}$ mbar, improving the expected gain from the customized cryopump.

Laser cooling of the radial modes of a single ion and a two-ion crystal has been studied in detail. The axialization technique [140] has been applied to circumvent the unstable magnetron mode and cool both radial modes simultaneously. The optimum conditions have been searched by monitoring the ions' motional amplitude, measured optically from the ion image provided by the EMCCD, as a function of the axialization voltage. An upper limit of 753(36) nm is estimated for the modified-cyclotron and the magnetron modes of a two-ion balanced $^{40}Ca^{+}$ crystal, respectively.

Results: frequency ratios of single calcium isotopes

The optical method has been utilized to measure the mass ratio of several calcium isotopes ($A = 42, 44, 48$) and $^{40}Ca^+$ [148]. Single ions of each isotope have been sequentially loaded in the trap and their three eigenfrequencies have been measured to determine their cyclotron frequencies.

A readout protocol has been devised to determine the ion's amplitude after exciting each eigenmotion by a dipolar field during a time interval in which laser cooling is switched off. The oscillation amplitude after excitation is reconstructed by applying laser cooling again and observing the time evolution of the spatial distribution and the number of photons, recorded with the EMCCD and the PMT, respectively. Each eigenfrequency has been directly determined by performing a frequency sweep on the external dipolar field and monitoring the ion's amplitude. The resultant peak (EMCCD) or dip (PMT) is centred at the ion's motional frequency. The invariance theorem is used to obtain the cyclotron frequency from ν_+, ν_-, and ν_z.

The three measured cyclotron-frequency ratios agree within 1σ with the literature values [149]. In the case of $^{44}Ca^+$, the 18 ratio measurements yield a value of 1.099 917 0772(89), which matches the current literature uncertainty of $8.1 \cdot 10^{-9}$. For $^{48}Ca^+$, a value of 1.199 938 029(15) is calculated from 26 ratios, with a relative uncertainty of $1.3 \cdot 10^{-8}$. This isotope has been measured in different Penning-trap experiments, and the current and high-precision value (a factor of 20 better) is quoted using the PI-ICR technique [175]. The 11 frequency measurements of $^{42}Ca^+$ deliver a ratio of 1.049 948 070(11), with an uncertainty of $1.0 \cdot 10^{-8}$ which is 2.5 times higher than the literature value.

The unique feature of the optical method of direct monitoring of the ion's amplitude allows for a direct estimation of the systematic uncertainty arising from high multipolar components of the trapping fields. Furthermore, for equivalent mass-to-charge ratios, the optical method exhibits a better performance than those based on bolometric detection. The minimum detectable amplitude, estimated to be around 4 μm, is only limited by the resolution of the optical imaging system and the cooling rate, against the 10 μm needed using induced currents [205].

The current limiting factor in precision is the stability of the electric field. The long-term stability deduced from the evolution of any of the eigenfrequencies is in the order of $4.5 \cdot 10^{-5}$. This value could be improved provided more stable voltage sources are available and presumably by better isolation from external noise.

Results: test of the generalized invariance theorem and first implementation on an unbalanced crystal

The optical method has been implemented in the Coulomb crystals $^{40}Ca^+$ - $^{40}Ca^+$ and $^{42}Ca^+$ - $^{40}Ca^+$. The measurement protocol differs from that on a single ion in applying laser cooling during the excitation for those modes where the Coulomb force leads to large amplitude-dependent frequency shifts. In these cases, the

system may be described in equilibrium by a non-harmonic damped and forced oscillator and the eigenmode amplitude can be extracted directly from the ions' image. A new model that contains second- and third-order terms of the Coulomb force expanded in the Taylor series has been developed to fit the measured asymmetric spectra. The corresponding differential equation has been solved using the method of multiple scales. In addition, a quadrupolar field must be used for the excitation of the stretch modes to achieve an effective coupling with the crystal eigenmode.

Three complete measurements of the six eigenfrequencies of $^{40}Ca^{+}$ - $^{40}Ca^{+}$ have been collected and analysed. In this balanced crystal, amplitude-dependent shifts have only been observed for the stretch axial mode. Duffing hardening resonances are observed for this particular eigenmode. A frequency region where three different values of amplitude are the solution of the differential equation leads to a hysteresis effect. The measurements on this balanced crystal certify the validity of the generalized invariance theorem [41] up to $7 \cdot 10^{-6}$.

First measurements of the eigenfrequencies of the unbalanced $^{42}Ca^{+}$ - $^{40}Ca^{+}$ crystal in which $^{40}Ca^{+}$ plays the role of sensor ion have been presented. The asymmetries arising from the amplitude-dependent shifts are more pronounced than for the balanced crystal. The modified-cyclotron stretch mode must be analysed differently due to the factor-of-20 larger amplitude of the heavier (blind) $^{42}Ca^{+}$ ion which breaks the low-amplitude approximation in which the crystal aligns along the axial axis. These first measurements are subject to further improvements, although they have yielded the cyclotron frequency of $^{42}Ca^{+}$ calculated via the generalized invariance theorem with a relative uncertainty of $4 \cdot 10^{-5}$.

Perspectives

The mass-ratio values of the calcium isotopes could be improved by using an ultra-stable voltage source. The precision can be increased by exciting the ion for a longer period provided a good signal-to-noise ratio is maintained. The systematic shifts associated with the field imperfections can be attenuated by minimizing and adjusting the relative amplitudes of the eigenmodes.

Mass values are a necessary input for the construction of the so-called King plot, which studies the linearity of the isotopic shift between two internal transitions. Combining high-precision mass measurements of several isotopes that can be cooled by laser could be used to unveil deviations from the predicted linear behaviour that would be evidence of new physics beyond the Standard Model [184]. Two quadrupolar transitions have been recently measured with an accuracy of 20 Hz [151, 189] to build a King plot using the calcium isotopic chain. Further improvements in the uncertainty of these spectroscopic values may require more precise mass values.

The next step in the implementation of the optical method will be accessing the quantum regime by further cooling the unbalanced ion crystal to the ground state of motion. The lower motional amplitudes will translate into smaller frequency

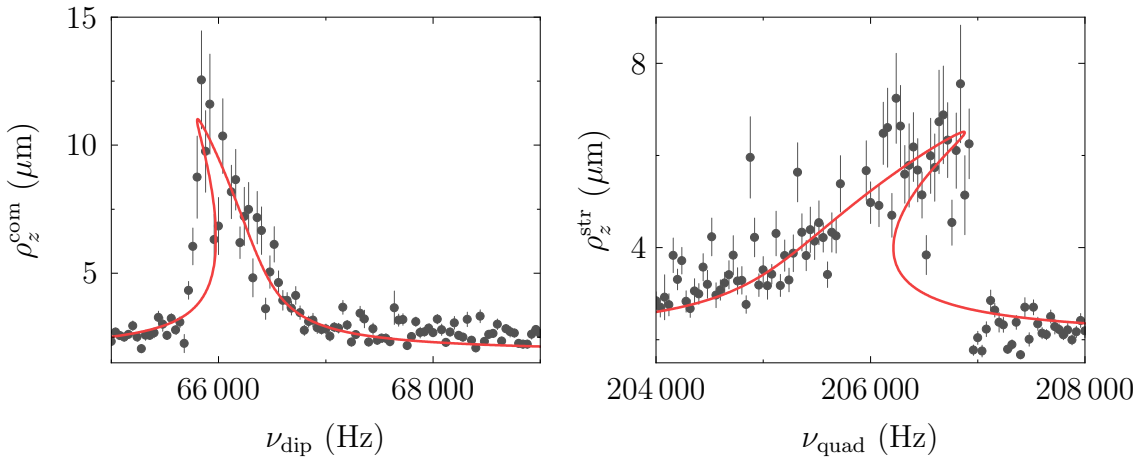

Figure 7.1. Detection of the unbalanced crystal $^{232}ThO_2^+$ - $^{40}Ca^+$. Left: common mode. Right: stretch mode. The frequencies extracted from the fitting procedure are 66 241(30) Hz and 205 600(400) Hz.

shifts. Nonetheless, it will be necessary to measure all the cross-coupling terms and actively correct the frequency shifts at the phonon level. This can be accomplished using well-established procedures in quantum optics experiments in RF traps [38].

Trapping and sympathetic cooling of $^{232}ThO_2^+$ via $^{40}Ca^+$ was demonstrated at the end of this thesis work. Figure 7.1 shows the scan of the axial eigenfrequencies of a $^{232}ThO_2^+$ - $^{40}Ca^+$ crystal in the Penning trap. In this case, anharmonicity is observed, with a softening and hardening behaviour for the common and stretch modes, respectively. $^{232}Th^+$ is an interesting ion to test the optical method due to its high mass compared to calcium, which will allow for a comprehensive evaluation of the technique. Furthermore, the measurements envisaged can be extended to ^{229}Th, which is under study by an international collaboration aiming at implementing a nuclear clock in an RF trap [59]. In our setup, the advantages of the Penning trap can be exploited, i.e., the stability for a broad range of mass-to-charge ratios, the absence of micromotion, and the low heating rates in the ground state of motion.

Appendix A

The new cryogenic trap

A new cryogenic Penning trap has been designed during thesis work. This system is intended to improve the background pressure in the trapping region so that it will not be a limiting factor in long, precise motional frequency measurements. In addition, the operation at cryogenic temperatures will also improve the ion heating rate at the ground state of motion and open the possibility of using quartz crystals at low temperatures.

In the design of the new cryogenic trap, the aim has been to modify the previous structure (see Fig. 3.2) as little as possible. Figure A.1 shows the new system integrated into the Penning-trap tower. It consists of the new Penning trap (upgrade of MT in Fig. 3.2), which conserves the electrode geometry but has been redesigned to improve the mechanical stability, and two surrounding cans thermally connected to the corresponding stages of a cryocooler. The trap is thermally anchored to the inner can, which is connected to the 4-K (second) stage by a 1/2-inch bar. The parts at 4 K are surrounded by a structure at 45 K consisting of the outer can and a piping system around the thermal-connection bar which provides thermal-radiation shielding from the room-temperature components. The lens ToF-1 has been thinned to accommodate a double-bend piece used for the pipe-can junction. The thermal connection to the cryocooler, the trap cans, and the trap electrodes are machined from oxygen-free high conductivity (OFHC) copper (conductivity of 640 W/(m·K) at 4.2 K and 1210 W/(m·K) conductivity at 45 K [206] for $RRR = 100$), and the latter are also silver- and gold-plated to prevent oxidation (silver avoids gold to diffuse). The trap insulators are machined from sapphire (α-Al_2O_3), which features a good thermal conductivity (42 W/(m·K) at 4.2 K [207]). The interfaces between pieces at different temperature (room at 297 K, first stage at 45 K, and second stage at 4.2 K) are machined from G-10 (conductivity of 0.073 W/(m·K) at 4.2 K and 0.29 W/(m·K) conductivity at 45 K [206]). All these materials present sufficiently low values of magnetic susceptibility and magnetization.

The trap can constitute a vacuum subsystem inside which the pressure drops due to cryopumping (see Sec. 3.2.1). The two cans are open on both sides along the beamline so that the ions created at the upstream-located ion sources out-

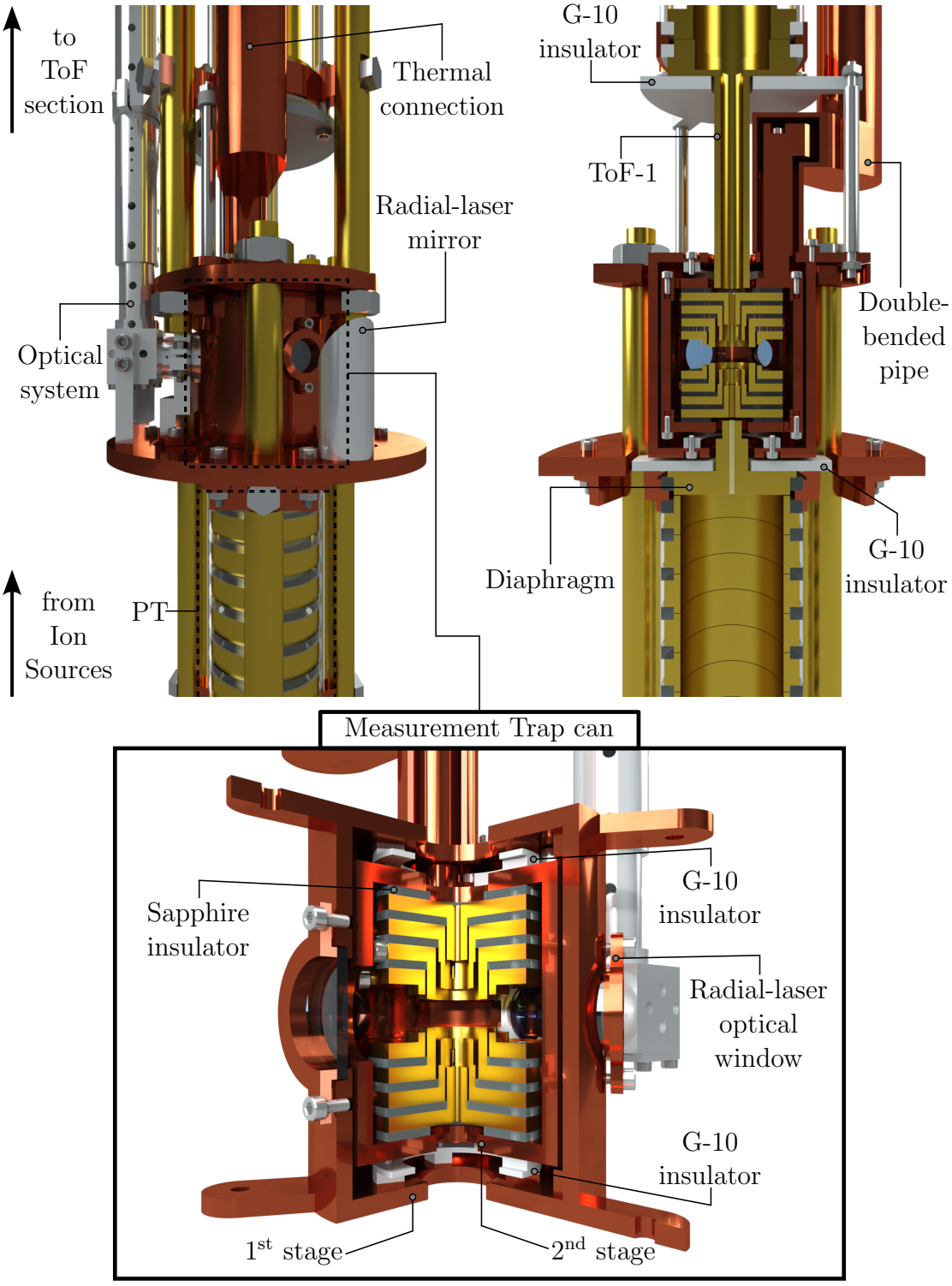

Figure A.1. The new cryogenic Penning trap. Upper left: three-dimensional technical drawing. Upper right: longitudinal cut. Lower: right-angle cut of the Measurement Trap and the radiation shieldings.

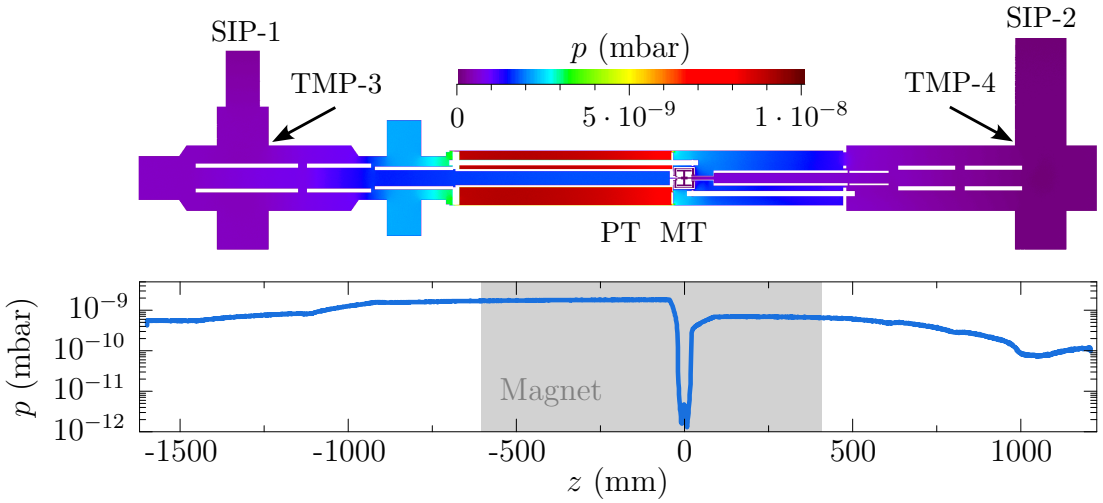

Figure A.2. Vacuum simulations of the new cryogenic trap. The plot arrangement is identical to Fig. 3.5.

side the magnet can be in-flight trapped and time-of-flight measurements can be performed using the MCP downstream. Radial lasers enter the trapping region through a fused-silica optical window, and the optical system's objective (at room temperature) fits into an orifice in the outer can. A drawback of an open cryogenic system is the pumping saturation for the background-gas species that cannot be removed by cryocondensation (see Sec. 3.2.3 for details). In hermetically-sealed systems, the volume is previously evacuated by mechanical pumps and the vacuum chamber is pinched afterwards so that everything but helium and hydrogen is removed by cryocondensation. The number of remaining molecules of these two species is so small that they can be pumped out by cryoadsorption.

Figure A.2 shows the outcome of the vacuum simulations of the new cryogenic system carried out using Molflow+ [103]. The parts thermally anchored to the cryocooler's first and second stages are set to 45 K and 4 K, respectively, and the sticking factor is 0.1 in both cases. The outgassing rate of the room-temperature components was detailed in Sec. 3.2.2. The pressure p in the trapping region is now lower than in the surroundings due to the cryopumping effect. The simulation estimates $p < 10^{-11}$ mbar, which according to the model employed in Sec. 4.2.3 would imply an average time between collisions higher than 300 s.

Appendix B

Brief description of diffraction theory

From Maxwell's equations and assuming a dielectric, non-magnetic, homogeneous, and isotropic medium, any of the components of the electric and magnetic field $u(\vec{r},t)$ obeys the scalar wave equation,

$$\left[\nabla^2 - \frac{1}{c^2}\frac{\varepsilon}{\varepsilon_0}\frac{\partial^2}{\partial t^2}\right] u(\vec{r},t) = 0, \tag{B.1}$$

where ∇^2 is the Laplace operator, c is the speed of light in vacuum, ε_0 is the vacuum permittivity, and ε is the medium (constant) permittivity. For a monochromatic wave $u(\vec{r},t) = u_0(\vec{r})\cos(kc\,t + \theta(\vec{r}))$, the phasor $U(\vec{r}) = u_0(\vec{r})\,e^{-i\theta(\vec{r})}$ follows the Helmholtz equation,

$$\left[\nabla^2 + k^2\right] U = 0, \tag{B.2}$$

where $k = 2\pi/\lambda$ is the wavenumber, with λ the wavelength.

The Green theorem states that, for two complex-valued functions $U(\vec{r})$ and $G(\vec{r})$, and being S_0 a surface surrounding the volume V_0,

$$\iiint_{V_0}\left[U\nabla^2 G - G\nabla^2 U\right] dv = \iint_{S_0}\left[U\frac{\partial G}{\partial r_n} - G\frac{\partial U}{\partial r_n}\right] ds, \tag{B.3}$$

where $\partial/\partial r_n$ is the partial derivative with respect to the outward normal direction $\vec{r}_n$ on S_0. If U fulfils Eq. (B.2) and $G = e^{ikr_{01}}/r_{01}$, with r_{01} the distance from the observation point P_0 within S_0 to the point P_1 on the surface, the scalar field U at P_0 can be calculated as

$$U(P_0) = \frac{1}{4\pi}\iint_{S_0}\left[G\frac{\partial U}{\partial r_n} - U\frac{\partial G}{\partial r_n}\right] ds, \tag{B.4}$$

which is known as the Kirchhoff-Helmholtz integral theorem. This result is of great importance as it allows the scalar field at any point P_0 to be calculated from its boundary values on any closed surface S_0 surrounding that point.

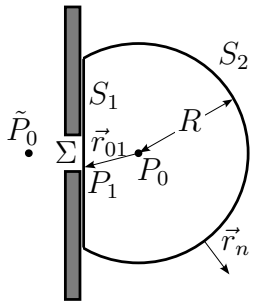

Figure B.1. Kirchhoff diffraction by a finite aperture on a planar screen. P_0 is the observation point and P_1 can be any point on the surface $S_0 = S_1 + S_2 + \Sigma$ surrounding P_0. Σ is the finite-aperture surface, S_2 is the spherical cap of radius R, and S_1 is the surface on the solid screen. $\tilde{P}_0$ and P_0 are symmetric respect to the screen. Adapted from Ref. [109].

The particular case of diffraction by a finite aperture on an infinite opaque screen serves as a basis for modelling the effect an optical system has over a wavefront. Figure B.1 illustrates the situation. S_0 is conveniently divided into three parts, $S_0 = S_1 + S_2 + \Sigma$. The value of the Kirchhoff-Helmholtz integral on S_1 can be made zero if the Green's function G is chosen to be $G_\pm = e^{ikr_{01}}/r_{01} \pm e^{ik\tilde{r}_{01}}/\tilde{r}_{01}$ (if $G = e^{ikr_{01}}/r_{01}$, both U and $\partial U/\partial r_n$ must be zero on S_1 to cancel the integral, which are known as Kirchhoff boundary conditions, inconsistent since they imply U to vanish all around [108]), where $\tilde{r}_{01}$ is the distance from a second reference point $\tilde{P}_0$ which is the mirror image of P_0 respect to the planar screen (see Fig. B.1). The Kirchhoff-Helmholtz integral is also zero on S_2 provided that the wave is travelling from left to right, which is known as the Sommerfeld radiation condition (U vanishes at least as fast as a diverging spherical wave) [109]. Substituting G_- in Eq. (B.3) leads to what is known as the first solution of the Rayleigh-Sommerfeld formulation of diffraction,

$$U(P_0) = \frac{1}{i\lambda} \iint_\Sigma U(P_1) \frac{e^{ikr_{01}}}{r_{01}} \cos(\vec{r}_n, \vec{r}_{01})\, ds, \tag{B.5}$$

where it has been assumed that $r_{01} \gg \lambda$. G_+ leads to equivalent results [109]. Equation (B.5) is identical to the Huygens-Fresnel principle, which states that every point on a wavefront may be regarded as the source of new wavelets.

Appendix C

Method of multiple scales

Equations (6.3) and (6.4) are used to model the anharmonicities arising from the non-negligible amplitude of the frequency-scanning mode. These equations are particular cases of a single-degree-of-freedom non-linear oscillator. Since the ions perform small oscillations around the equilibrium positions, it is reasonable to suppose that the motional equation deviates only slightly from the harmonic solution. Therefore, perturbation theory can be used to resolve the problem. This appendix encloses the mathematical derivation of Eq. (6.6) by means of the method of multiple scales, for which Ref. [200] is followed.

Axial modes

All the measurements presented in Chapter 6 in which frequency shifts are detected have been frequency-scanned maintaining laser cooling activated while the excitation is applied, analogously as it is done in Refs. [159, 160]. The motional equation which describes the system dynamics is that of a driven damped harmonic oscillator. For the ion's amplitudes presented in this chapter, the Doppler broadening is still much lower than the natural linewidth of the cooling transition, so the laser resistive force can be considered to depend linearly on the ion's velocity and is quantified by the parameter γ. Including the dimensionless parameter ϵ as a crutch to obtain the approximate solution, Eq. (6.3) becomes

$$\ddot{u} + \omega_0^2 u = -2\epsilon^2\gamma\dot{u} - \epsilon\alpha_2 u^2 - \epsilon^2\alpha_3 u^3 + \epsilon^2 E\cos(\omega t)\,, \tag{C.1}$$

where E quantifies the external excitation voltage. If perturbation theory to order n is applied in a straightforward way, the solution obtained is invalid when t becomes larger than $\mathcal{O}(\epsilon^{-n})$. The cubic perturbation $\alpha_3 u^3$ already introduces terms that grow rapidly with the time variable, called secular terms. A generalization of the perturbation theory called the method of multiple scales can be used to obtain solutions of Eq. (C.1) that are bounded in time. This method takes into account that the system exhibits characteristic physical behaviours at several time scales through a series of new independent time variables

$$T_n = \epsilon^n t, \qquad \text{for} \quad n = 0, 1, 2, \ldots \tag{C.2}$$

The proposed solution is assumed to depend not only on the time scale $t = T_0$ but also on $T_1, T_2, \ldots$,

$$u(t;\epsilon) = u_0(T_0, T_1, T_2, \ldots) + \epsilon u_1(T_0, T_1, T_2, \ldots) + \epsilon^2 u_2(T_0, T_1, T_2, \ldots) + \ldots \tag{C.3}$$

To solve the second-order perturbation problem of Eq. (C.1), two extra time scales are necessary, so $u(t;\epsilon) \equiv u(T_0, T_1, T_2; \epsilon)$. In general, N independent time scales are necessary to solve a perturbation problem of order $\mathcal{O}(\epsilon^N)$. The time derivatives become now expansions in terms of the partial derivatives with respect to T_n,

$$\frac{d}{dt} = \frac{\partial}{\partial T_0} + \epsilon\frac{\partial}{\partial T_1} + \epsilon^2\frac{\partial}{\partial T_2} + \mathcal{O}(\epsilon^3), \tag{C.4a}$$

$$\frac{d^2}{dt^2} = \frac{\partial^2}{\partial T_0^2} + 2\epsilon\frac{\partial^2}{\partial T_1 \partial T_0} + \epsilon^2\left[\frac{\partial^2}{\partial T_1^2} + 2\frac{\partial^2}{\partial T_2 \partial T_0}\right] + \mathcal{O}(\epsilon^3). \tag{C.4b}$$

Applying Eqs. (C.4) to the proposed solution, Eq. (C.3),

$$\frac{du}{dt} = \frac{\partial u_0}{\partial T_0} + \epsilon\left[\frac{\partial u_0}{\partial T_1} + \frac{\partial u_1}{\partial T_0}\right] + \epsilon^2\left[\frac{\partial u_0}{\partial T_2} + \frac{\partial u_1}{\partial T_1} + \frac{\partial u_2}{\partial T_0}\right] + \mathcal{O}(\epsilon^3), \tag{C.5a}$$

$$\frac{d^2u}{dt^2} = \frac{\partial^2 u_0}{\partial T_0^2} + \epsilon\left[\frac{\partial^2 u_1}{\partial T_0^2} + 2\frac{\partial^2 u_0}{\partial T_1 \partial T_0}\right] + \epsilon^2\left[\frac{\partial^2 u_2}{\partial T_0^2} + \frac{\partial^2 u_0}{\partial T_1^2} + 2\frac{\partial^2 u_0}{\partial T_2 \partial T_0} + 2\frac{\partial^2 u_1}{\partial T_1 \partial T_0}\right] + \mathcal{O}(\epsilon^3). \tag{C.5b}$$

Introducing Eqs. (C.5) in the eigenmode motional Equation (C.1), three relationships are obtained for the different orders in ϵ,

$$\epsilon^0: \quad \frac{\partial^2 u_0}{\partial T_0^2} + \omega_0^2 u_0 = 0, \tag{C.6a}$$

$$\epsilon^1: \quad \frac{\partial^2 u_1}{\partial T_0^2} + \omega_0^2 u_1 = -2\frac{\partial^2 u_0}{\partial T_1 \partial T_0} - \alpha_2 u_0^2, \tag{C.6b}$$

$$\epsilon^2: \quad \frac{\partial^2 u_2}{\partial T_0^2} + \omega_0^2 u_2 = -\frac{\partial^2 u_0}{\partial T_1^2} - 2\frac{\partial^2 u_0}{\partial T_2 \partial T_0} - 2\frac{\partial^2 u_1}{\partial T_1 \partial T_0} - 2\alpha_2 u_0 u_1 - \alpha_3 u_0^3 - 2\gamma\frac{\partial u_0}{\partial T_0} + E\cos(\omega_0 T_0 + \sigma T_2), \tag{C.6c}$$

where the excitation frequency ω has been expressed in terms of the detuning σ respect to the natural frequency ω_0 as $\omega = \omega_0 + \epsilon^2\sigma$. The general solution of Eq. (C.6a) is

$$u_0 = A(T_1, T_2)\, e^{i\omega_0 T_0} + \bar{A}(T_1, T_2)\, e^{-i\omega_0 T_0}. \tag{C.7}$$

Substituting u_0 into Eq. (C.6b) yields

$$\frac{\partial^2 u_1}{\partial T_0^2} + \omega_0^2 u_1 = -2i\omega_0\frac{\partial A}{\partial T_1}e^{i\omega_0 T_0} - \alpha_2\left[A^2 e^{2i\omega_0 T_0} + A\bar{A}\right] + c.c., \tag{C.8}$$

where *c.c.* stands for complex conjugate. The factor $e^{i\omega_0 T_0}$ constitutes a secular term since it represents a resonant excitation that gives rise to a term increasing linearly with t. To eliminate this secular term, $(\partial A)/(\partial T_1) = 0$, so $A = A(T_2)$. The solution of Eq. (C.8) is

$$u_1 = \frac{\alpha_2}{\omega_0^2}\left[-2A\bar{A} + \frac{1}{3}A^2 e^{2i\omega_0 T_0} + \frac{1}{3}\bar{A}^2 e^{-2i\omega_0 T_0}\right]. \tag{C.9}$$

Substituting Eqs. (C.7) and (C.9) into Eq. (C.6c) leads to

$$\begin{aligned}\frac{\partial^2 u_2}{\partial T_0^2} + \omega_0^2 u_2 = -\Big[2i\omega_0\left(\frac{dA}{dT_2} + \gamma A\right) + \left(3\alpha_3 - \frac{10\alpha_2^2}{3\omega_0^2}\right)A^2\bar{A} \\ - \frac{1}{2}Ee^{i\sigma T_2}\Big]e^{i\omega_0 T_0} - \left[\frac{2}{3}\frac{\alpha_2^2}{\omega_0^2} + \alpha_3\right]A^3 e^{3i\omega_0 T_0} + c.c.\,.\end{aligned} \tag{C.10}$$

Secular terms are avoided only if

$$2i\omega_0\left(\frac{dA}{dT_2} + \gamma A\right) + \left(3\alpha_3 - \frac{10\alpha_2^2}{3\omega_0^2}\right)A^2\bar{A} - \frac{1}{2}Ee^{i\sigma T_2} = 0. \tag{C.11}$$

The unknown variable A is expressed in polar coordinates, $A = \frac{1}{2}ae^{i\beta}$ for convenience. A set of two equations, for the real and imaginary parts, are obtained by substituting in Eq. (C.11):

$$a\dot{\delta} = a\sigma - \frac{9\alpha_3\omega_0^2 - 10\alpha_2^2}{24\omega_0^3}a^3 + \frac{E}{2\omega_0}\cos\delta, \tag{C.12a}$$

$$\dot{a} = -\gamma a + \frac{E}{2\omega_0}\sin\delta. \tag{C.12b}$$

The new variable $\delta = \sigma T_2 - \beta$ has been introduced to omit the explicit dependence on T_2. In the steady state, $\dot{a} = \dot{\delta} = 0$. An implicit equation in the amplitude a can be obtained if the trigonometric identity $\sin^2\delta + \cos^2\delta = 0$ is used,

$$\left\{\left[(\omega - \omega_0) - \frac{9\alpha_3\omega_0^2 - 10\alpha_2^2}{24\omega_0^3}a^2\right]^2 + \gamma^2\right\}^2 a^2 = \frac{E^2}{4\omega_0^2}. \tag{C.13}$$

Radial modes

The motional equation for the radial modes including the crutch parameter ϵ and the external-driven and damping terms is

$$\begin{aligned}\ddot{u} - i\omega_c u - \frac{1}{2}\omega_0^2 u = -2\epsilon^2\gamma\dot{u} - \epsilon\left(\alpha_2^1 u^2 + \alpha_2^2 u\bar{u} + \alpha_2^2\bar{u}^2\right) \\ -\epsilon^2\left(\alpha_3^1 u^3 + \alpha_3^2 u^2\bar{u} + \alpha_3^3 u\bar{u}^2 + \alpha_3^4\bar{u}^3\right) + \epsilon^2 E\cos(\omega t)\,,\end{aligned} \tag{C.14}$$

where the constants α_2^i and α_3^i account for the second and third-order non-linearities, respectively. Following the same procedure as for the axial modes, the three differential equations equivalent to Eq. (C.6) obtained for the different orders in the parameter ϵ are

$$\epsilon^0: \quad \frac{\partial^2 u_0}{\partial T_0^2} - i\omega_c \frac{\partial u_0}{\partial T_0} - \frac{1}{2}\omega_0^2 u_0 = 0, \tag{C.15a}$$

$$\epsilon^1: \quad \frac{\partial^2 u_1}{\partial T_0^2} - i\omega_c \frac{\partial u_1}{\partial T_0} - \frac{1}{2}\omega_0^2 u_1 = -2\frac{\partial^2 u_0}{\partial T_1 \partial T_0} + i\omega_c \frac{\partial u_0}{\partial T_1} - \left[\alpha_2^1 u_0^2 + \alpha_2^2 u_0 \bar{u}_0 + \alpha_2^3 \bar{u}_0^2\right], \tag{C.15b}$$

$$\begin{aligned}\epsilon^2: \quad \frac{\partial^2 u_2}{\partial T_0^2} - i\omega_c \frac{\partial u_2}{\partial T_0} - \frac{1}{2}\omega_0^2 u_2 = &-\frac{\partial^2 u_0}{\partial T_1^2} - 2\frac{\partial^2 u_0}{\partial T_2 \partial T_0} - 2\frac{\partial^2 u_1}{\partial T_1 \partial T_0} \\ &+ i\omega_c \left[\frac{\partial u_0}{\partial T_2} + \frac{\partial u_1}{\partial T_1}\right] \\ &- \left[2\alpha_2^1 u_0 u_1 + \alpha_2^2 \left(u_0 \bar{u}_1 + \bar{u}_0 u_1\right) + 2\alpha_2^3 \bar{u}_0 \bar{u}_1\right] \\ &- \left[\alpha_3^1 u_0^3 + \alpha_3^2 \bar{u}_0^2 u_0 + \alpha_3^3 u_0 \bar{u}_0^2 + \alpha_3^4 \bar{u}_0^3\right] \\ &- 2\gamma \frac{\partial u_0}{\partial T_0} + E\cos\left(\omega_0 T_0 + \sigma T_2\right).\end{aligned} \tag{C.15c}$$

The general solution of Eq. (C.15a) is

$$u_0 = A_+\left(T_1, T_2\right) e^{i\omega_+ T_0} + A_-\left(T_1, T_2\right) e^{-i\omega_- T_0}. \tag{C.16}$$

To avoid secular terms in Eq. (C.15b), $\left(\partial A_\pm\right)/\left(\partial T_1\right) = 0$, analogously as it appeared in the axial modes. The general solution of Eq. (C.15b) is

$$\begin{aligned}u_1 = &\, c_0 \alpha_2^2 \left(A_+ \bar{A}_+ + A_- \bar{A}_-\right) + c_1 \alpha_2^1 A_+^2 e^{2i\omega_+ T_0} + c_2 \alpha_2^1 A_-^2 e^{2i\omega_- T_0} \\ &+ c_3 \alpha_2^2 A_+ A_- e^{i(\omega_+ + \omega_-)T_0} + c_4 \alpha_2^2 A_+ \bar{A}_- e^{i(\omega_+ - \omega_-)T_0} + c_5 \alpha_2^3 \bar{A}_+^2 e^{-2i\omega_+ T_0} \\ &+ c_6 \alpha_2^3 \bar{A}_-^2 e^{-2i\omega_- T_0} + c_7 \alpha_2^2 \bar{A}_+ \bar{A}_- e^{-i(\omega_+ + \omega_-)T_0} + c_8 \alpha_2^2 \bar{A}_+ A_- e^{-i(\omega_+ - \omega_-)T_0},\end{aligned} \tag{C.17}$$

where c_i are real numbers depending on the frequencies ω_c, ω_0 and the eigenvalues $\omega_\pm$. Introducing Eqs. (C.16) and (C.17) in Eq. (C.15c) yields again new secular terms. If the external excitation is close to the eigenfrequency ω_+, it can be written as $\omega = \omega_+ + \epsilon^2 \sigma$. The secular term at ω_+ is removed if

$$\begin{aligned}&i\left(2\omega_+ - \omega_c\right)\frac{dA_+}{dT_2} + 2i\omega_+ A_+ \gamma \\ &+2\alpha_2^1 \left[c_0 \alpha_2^2 \left(A_+ \bar{A}_+ + A_- \bar{A}_-\right) A_+ + c_4 \alpha_2^2 A_+ \bar{A}_- A_-\right] \\ &+\alpha_2^2 \left[c_0 \alpha_2^2 \left(A_+ \bar{A}_+ + A_- \bar{A}_-\right) A_+ + c_8 \bar{\alpha_2^2} A_+ \bar{A}_- A_-\right] \\ &+\alpha_2^2 \left[c_1 \alpha_2^1 A_+^2 \bar{A}_+ + c_3 \alpha_2^2 A_+ A_- \bar{A}_-\right] \\ &+2\alpha_2^3 \left[c_5 \bar{\alpha_2^3} A_+^2 \bar{A}_+ + c_7 \bar{\alpha_2^2} A_+ A_- \bar{A}_-\right] \\ &+\alpha_3^2 \left[A_+^2 \bar{A}_+ + 2A_+ A_- \bar{A}_-\right] - E e^{i\sigma T_2} = 0.\end{aligned} \tag{C.18}$$

If the amplitude of the mode oscillating at ω_-, A_-, is considered negligible compared to A_+, Eq. (C.18) becomes a differential equation with terms proportional to A_+ and $A_+^2\bar{A}$ of the same type as Eq. (C.11). Therefore, the mode amplitude follows likewise an implicit equation of the type

$$\left\{\left[(\omega-\omega_0)-F\left(\alpha_2,\alpha_3\right)A^2\right]^2+\gamma^2\right\}^2 A^2=\frac{E^2}{4\omega_0^2}. \tag{C.19}$$

Resumen extenso en español

En esta tesis doctoral se presentan las primeras medidas de ratios de frecuencia ciclotrónica utilizando detección óptica en una trampa Penning. La técnica se ha implementado en iones individuales de isótopos de calcio y en cristales de Coulomb de dos iones. A continuación, se exponen las partes más relevantes del contenido de este manuscrito, incluyendo la motivación y los objetivos de la tesis, los principales progresos técnicos llevados a cabo en el experimento, los resultados obtenidos y las conclusiones que se derivan de este trabajo.

Introducción

Desde que fuera ideada por Hans G. Dehmelt para medir el momento magnético del electrón de forma directa [1], la trampa Penning ha sido ampliamente utilizada para determinar propiedades fundamentales de las partículas confinadas con una alta precisión. Una de estas propiedades es la masa, que en el caso de un átomo está directamente relacionada con la energía de enlace y, por tanto, contiene información sobre su estructura interna y la interacción entre los constituyentes [10]. La masa se extrae de una medida de la frecuencia ciclotrónica, que a su vez está relacionada con las frecuencias de movimiento del ion en la trampa.

Las técnicas existentes en la actualidad se pueden clasificar en dos grupos, dependiendo del método de detección: técnicas destructivas, en las que el propio ion genera un pulso eléctrico al impactar en un detector [11], y técnicas basadas en la detección de la corriente inducida en un electrodo de la trampa [12]. Las técnicas destructivas se han utilizado ampliamente en instalaciones radiactivas para medir la masa de elementos de vida media corta. La técnica PI-ICR (phase-imaging ion-cyclotron-resonance) [14], que determina la fase de movimiento de los iones para extraer su frecuencia, es la más avanzada de este tipo en la actualidad, logrando alcanzar incertidumbres relativas del orden de 10^{-10}. Las técnicas basadas en la detección de corrientes inducidas han sido empleadas mayoritariamente en elementos estables. Aunque existen múltiples variantes, la técnica PnP (pulse-and-phase) [16] ha sido aplicada con éxito en diferentes situaciones llegando a alcanzar incertumbres relativas por debajo de 10^{-11} [20–23].

El principal objetivo del experimento de trampas Penning en la Universidad de Granada es el desarrollo una nueva técnica de medida de masas en la que un ion sensor enfriado por láser [24, 25] se utiliza para recabar información sobre la

amplitud de movimiento del sistema que forma junto con el ion de interés [35]. La primera implementación está siendo desarrollada en el cristal de Coulomb formado por los dos iones cuando estos son enfriados por láser [37]. En comparación con otras técnicas, este planteamiento ofrece universalidad, ya que es aplicable a iones de cualquier relación carga-masa, y basta con un solo ion para alcanzar una precisión arbitraria. Además, el uso del enfriamiento por láser en la etapa preparatoria, idealmente hasta el estado fundamental de movimiento, reduce la amplitud de oscilación requerida, lo que se traduce en incertidumbres sistemáticas más bajas [38].

Una de las motivaciones para el desarrollo de la técnica de detección óptica es la determinación de la masa de elementos súper-pesados (SHE, por sus siglas en inglés). En la actualidad, el experimento SHIPTRAP, en el GSI, es el único espectrómetro de masas basado en trampas Penning acoplado a una instalación capaz de producir este tipo de elementos [42]. La determinación de la energía de enlace de los SHE proporciona información útil sobre su estructura nuclear interna, aportando en ocasiones nuevas pistas sobre los efectos de capa necesarios para explicar su existencia [43]. Las bajas tasas de producción, menores cuanto mayor es la masa, hacen cada vez más difícil la implementación de la técnica PI-ICR [46], y al mismo tiempo las técnicas basadas en corrientes inducidas no han alcanzado hasta la fecha relaciones masa-carga superiores a 65 u/e [18].

El método óptico también también encuentra una importante aplicación en la determinación del valor Q de procesos de desintegración β^- y captura electrónica que son de interés en el campo de la física de neutrinos [50]. La comparación del valor Q y del punto final del espectro en estos procesos proporciona un valor de la masa absoluta del neutrino. En este sentido, ^{163}Ho es una especie de interés, ya que experimentos como ECHo [52] o HOLMES [53] persiguen el estudio de su espectro de desexcitación atómica tras el proceso de captura electrónica. Aparte de los procesos β estándar mencionados anteriormente, también es posible observar doble desintegración beta para algunas especies como ^{48}Ca [55]. La búsqueda de este tipo de proceso, en su versión sin emisión de neutrinos, intenta desentrañar si esta partícula tiene naturaleza de Dirac o Majorana [56].

Finalmente, la combinación de trampa Penning y detección óptica también tiene el potencial de ser utilizada para experimentos de espectroscopía óptica que normalmente se llevan a cabo en trampas Paul. Las principales ventajas de una trampa Penning son la ausencia de micromovimiento en todo el volumen de atrapamiento, una menor tasa de calentamiento en el estado cero de energía y la posibilidad de albergar partículas con relaciones carga-masa muy diferentes. Una aplicación de la espectroscopía en trampas de iones con particular interés es la nueva generación de relojes basados en transiciones nucleares que se encuentran dentro del espectro óptico [59]. La principal ventaja con respecto a las transiciones atómicas es la insensibilidad frente a ruido procedente de campos electromagnéticos externos. El candidato mejor posicionado en la actualidad es ^{229}Th, que tiene un isómero nuclear de baja energía, ^{229m}Th, a sólo 8,338(24) eV (150 nm) [60].

Desarrollos técnicos

La trampa Penning del Laboratorio de Trampas de Iones de la Universidad de Granada [98] se puso en marcha a lo largo de dos tesis anteriores [64,65]. Durante esta tesis doctoral, se han llevado a cabo varias mejoras técnicas que han permitido implementar con éxito el método óptico.

Se han instalado dos nuevas fuentes de iones externas: una trampa Paul de anillos que se utiliza para producir isótopos de calcio y una fuente de ablación láser que permite crear cualquier especie. Ambas han sido caracterizadas en términos de la distribución de energía del pulso de iones que generan. La primera se ha utilizado de forma rutinaria para inyectar iones de calcio que son enfriados por láser en la trampa Penning, mientras que la segunda se ha empleado para producir torio, renio y oro, entre otros elementos. El enfriamiento por láser se ha extendido al plano radial, algo esencial para enfriar iones individuales y pequeñas estructuras cristalinas hasta el límite Doppler [77]. Se han mejorado las condiciones de vacío en la zona de la trampa Penning mediante la instalación de una bomba criogénica a medida, cuyo impacto en la línea se ha simulado utilizando el paquete informático Molflow+ [103].

El diseño e implementación del nuevo sistema óptico ha sido el avance técnico más importante llevado a cabo durante este trabajo. Las simulaciones del sistema óptico anterior utilizando el paquete informático Zemax mostraron que carecía de la suficiente resolución espacial para discernir la posición del ion en un cristal de Coulomb. El nuevo sistema, que opera en su mayor parte en condiciones de vacío, se compone exclusivamente de elementos comerciales, su diseño se ha adaptado a la geometría impuesta por el sistema de trampas Penning, y consigue generar imágenes carentes de aberraciones para objetos situados en el eje óptico. Ha sido caraterizado antes de su instalación en vacío midiendo la función de transferencia de modulación y la función de transferencia de contraste utilizando impulsos cuadrados. En su caracterización en vacío, se ha utilizado un ion como fuente puntual para medir la función de dispersión de punto. El análisis de esta función ha permitido cuantificar el peso de cada tipo de aberración en la base de polinomios de Zernike. En un principio, el sistema presentaba un fuerte astigmatismo, posiblemente por no estar perfectamente alineado con el centro de la trampa, que se ha corregido mediante la inclusión de una lente cilíndrica apropiada.

A lo largo de este trabajo también se han desarrollado los programas necesarios para controlar el experimento y adquirir datos mediante un sistema basado en ARTIQ. La mayoría de los protocolos de medida han sido automatizados: la captura de iones por tiempo de vuelo se ha sincronizado con la fase de extracción de las fuentes de iones para mejorar su reproducibilidad; la frecuencia de emisión de los láseres y los parámetros de los AOM se pueden controlar desde los propios programas; la lectura del PMT (siglas en inglés de tubo fotomultiplicador) se ha implementado directamente a través del hardware de ARTIQ, lo que se suma a la cámara EMCCD (siglas en inglés de dispositivo de carga acoplada con multiplicación de electrones) y los generadores de funciones [65]; y la señal del detector

MCP (siglas en inglés de detector de microcanales) ahora también se puede leer a través del hardware de ARTIQ.

Caracterización del enfriamiento por láser

La implementación de los avances técnicos mencionados anteriormente ha hecho posible el enfriamiento por láser y la detección de iones individuales y cristales de Coulomb en el límite Doppler [77]. En particular, la cristalización de conjuntos de hasta miles de iones implica que se han alcanzado temperaturas por debajo de 5 mK. La distancia relativa entre los dos iones de un cristal de $^{40}Ca^{+}$ se ha utilizado para caracterizar la trampa Penning en términos de su frecuencia axial en un amplio rango de voltajes de atrapamiento. También se ha explorado la sensibilidad de detección del PMT, obteniéndose relaciones señal-ruido superiores a la unidad para tiempos de lectura del orden de milisegundos.

Se ha estudiado en detalle el enfriamiento por láser de los modos radiales de un solo ion y de un cristal de dos iones mediante axialización [140]. Esta técnica utiliza un campo cuadripolar para intercambiar energía entre los modos radiales, de forma que el modo magnetrón se enfría indirectamente por láser a través del modo ciclotrón reducido. Se han encontrado las condiciones óptimas de operación, para lo cual se ha monitorizando la temperatura de los iones a partir de la anchura de la imagen del ion. Se estima un límite superior de 753(36) nm para los modos radiales en el cristal de dos iones de $^{40}Ca^{+}$. También se ha caracterizado el fenómeno de resonancia oscura en los sistemas de cuatro niveles que aparecen en el esquema de bombeo láser del enfriamiento Doppler en el campo magnético de 7 T.

Medida de los ratios de frecuencia de los isótopos de calcio

El método óptico se ha aplicado en primer lugar en iones de calcio individuales. Cada uno de los modos propios de un único ion de $^{40}Ca^{+}$ ha sido excitado por campos eléctricos dipolares externos durante un intervalo de tiempo en el que se desactiva el enfriamiento por láser. La amplitud de oscilación final se ha deducido a partir de la evolución temporal y la distribución espacial de los fotones emitidos mientras el ion se enfriaba de nuevo hasta el límite Doppler, para lo cual se ha utilizado la cámara EMCCD y el PMT. Para las condiciones específicas de enfriamiento de este experimento, la amplitud de los modos radiales ha podido detectarse con una sensibilidad mayor que la del modo axial. Esto se explica por la menor tasa de enfriamiento en el plano radial, con una constante de decaimiento de la amplitud de 80(23) ms, que ha permitido la medida directa de la evolución de la amplitud radial con la cámara EMCCD.

Cada una de las frecuencias propias se ha determinado a través del estudio de la amplitud del ion cuando se realiza un barrido de la frecuencia del campo dipolar externo. En el caso de los modos radiales, el pico resultante está centrado en la frecuencia de movimiento del ion, mientras que para el modo axial se obtiene una disminución en el número de fotones detectados. Se han explorado dos métodos

diferentes para determinar la frecuencia ciclotrónica: el teorema de invariancia y la determinación directa a través de las frecuencias radiales. En este último caso, la frecuencia magnetrón se ha medido indirectamente a partir de las bandas laterales detectadas en torno a la frecuencia del modo ciclotrón reducido cuando se aplica un campo cuadripolar que acopla los modos radiales. Ambo métodos alcanzan incertidumbres relativas del orden de 10^{-8} para tiempos de excitación de 500 ms en los modos ciclotrón reducido y axial. El teorema de invariancia necesita determinar la frecuencia axial pero es más robusto frente a desalineamientos o falta de simetría en los campos de atrapamiento.

El método óptico ha sido utilizado para determinar el ratio de masas de varios isótopos de calcio ($A = 42, 44, 48$) frente a $^{40}Ca^+$ [148]. Los iones indiviuales de cada isótopo se han cargado de forma secuencial en la trampa y se han realizado varios barridos de frecuencia para cada uno de los modos propios. El ion $^{40}Ca^+$ se ha utilizado como referencia, y su frecuencia ciclotrónica en el momento en que se mide el ion de interés se ha calculado mediante interpolación lineal. Los tres ratios de frecuencia ciclotrónica medidos experimentalmente coinciden con la bibliografía dentro de 1σ [149]. Para $^{48}Ca^+$, se obtiene un valor de $1,199\,938\,029(15)$ a partir de 26 medidas, con una incertidumbre relativa de $1,3 \cdot 10^{-8}$ que es un factor 20 superior al valor de la bibliografía medido utilizando PI-ICR [175]. En el caso de $^{44}Ca^+$, los 18 datos recabados dan lugar a un valor de $1,099\,917\,0772(89)$, que coincide con la incertidumbre actual de la bibliografía, $8,1 \cdot 10^{-9}$. Las 11 medidas de $^{42}Ca^+$ arrojan un valor de $1,049\,948\,070(11)$, con una incertidumbre de $1,0 \cdot 10^{-8}$ que es 2,5 veces mayor que el valor de la bibliografía.

La monitorización de la amplitud del ion en todo momento ha permitido estimar de forma directa la incertidumbre sistemática debida a las imperfecciones de los campos de atrapamiento. Para relaciones masa-carga equivalentes, el método óptico presenta incertidumbres sistemáticas más bajos que la detección por corrientes inducidas. Por su parte, la monitorización de las frecuencias propias ha permitido encontrar que fuertes correlaciones en su evolución temporal que apuntan a posibles inestabilidades del campo eléctrico como factor limitante de la precisión en estos momentos. La estabilidad para tiempos largo deducida a partir de los valores de cualquiera de las frecuencias propias es $4,5 \cdot 10^{-5}$.

Primeras medidas con cristales de dos iones

El método óptico se ha implementado en los cristales de Coulomb $^{40}Ca^+$ - $^{40}Ca^+$ y $^{42}Ca^+$ - $^{40}Ca^+$. El protocolo de medida es equivalente al empleado para iones individuales. Sin embargo, en los casos en los que la fuerza de Coulomb da lugar a desplazamientos en frecuencia [37] mucho mayores que la anchura de línea se ha aplicado enfriamiento láser de forma continua. Para estos casos, se ha desarrollado un modelo de oscilador no lineal que contiene los términos de segundo y tercer orden de la fuerza de Coulomb, de cara a realizar ajustes de los datos de amplitud de movimiento del cristal en función de la frecuencia de excitación. Además, el campo eléctrico de excitación debe presentar una geometría cuadripolar para

lograr un acoplamiento efectivo a los modos diferenciales (los dos iones se mueven en oposición de fases).

Se han llevado a cabo tres medidas completas de las seis frecuencias propias del cristal $^{40}Ca^{+}$ - $^{40}Ca^{+}$. En este caso, sólo se ha observado dependencia de la frecuencia con la amplitud para el modo diferencial axial. En el estado estacionario del sistema no lineal forzado (campo dipolar eléctrico) y amortiguado (enfriamiento láser), se observa una región de frecuencia en la que tres valores diferentes de amplitud son solución de la ecuación diferencial, lo cual se puede interpretar como un efecto de histéresis. Estas medidas sirven para validar el teorema de invariancia generalizado [41] a un nivel de $7 \cdot 10^{-6}$.

En el caso del cristal $^{42}Ca^{+}$ - $^{40}Ca^{+}$, se han realizado dos medidas completas. Los desplazamientos de frecuencia son más evidentes que para el cristal simétrico, apareciendo incluso para el modo ciclotrón reducido común. En el caso del modo ciclotrón reducido diferencial, la discrepancia en la masa de los constituyentes implica una amplitud de movimiento 20 veces mayor para el ion más pesado ($^{42}Ca^{+}$). Por lo tanto, la excitación mínima de varios micrómetros necesaria para detectar un cambio en la amplitud de movimiento del ion brillante (más ligero) $^{40}Ca^{+}$ no cumple la aproximación de baja amplitud en la que el cristal se alinea a lo largo del eje axial. En este caso, se ha monitorizado la distancia axial del ion brillante al centro de la trampa, que disminuye para una excitación resonante. La frecuencia ciclotrónica de iones individuales de $^{40}Ca^{+}$ y $^{42}Ca^{+}$ se ha determinado antes y después de cada medida del cristal de cara a la calibración. La frecuencia ciclotrónica de $^{42}Ca^{+}$ calculada mediante el teorema de invariancia generalizado se ha derivado con una incertidumbre relativa de $4 \cdot 10^{-5}$.

Conclusiones

En la primera parte de esta tesis doctoral se han llevado a cabo desarrollos técnicos que han resultado fundamentales para la primera implementación del método óptico. Las nuevas fuentes externas de iones permiten crear cualquier tipo de cristal asimétrico y han contribuido a la mejora del nivel de vacío en comparación con la fuente interna localizada en la propia trampa. Por su parte, la bomba criogénica a medida ha permitido alcanzar un nivel de vacío estimado en $3 \cdot 10^{-10}$ mbar en base a la frecuencia de colisión con el gas residual de un ion enfriado por láser. Como se ha comentado anteriormente, el nuevo sistema óptico ha sido un elemento clave para poder detectar iones individuales y estructuras cristalinas en la trampa Penning. Su resolución, medida utilizando un ion en el límite Doppler, es de 3,69(3) μm y 2,75(3) μm en las direcciones axial y radial, respectivamente. La integración de varios elementos en ARTIQ, como el PMT, el MCP o el control de los láseres, ha permitido automatizar y centralizar de forma completa el experimento en un solo sistema de control y adquisición de datos.

Los valores de ratios de masas de los isótopos de calcio podrían mejorarse fácilmente utilizando una fuente de tensión más estable y, presumiblemente, mediante un mejor aislamiento frente al ruido externo. La precisión puede aumentarse

excitando el ion durante un periodo más largo, siempre que se mantenga la relación señal-ruido. Una ventaja del método óptico respecto a la detección de corrientes inducidas es la posibilidad de detectar amplitudes de movimiento más pequeñas. Por ejemplo, utilizando el protocolo de medida desarrollado en este trabajo, la amplitud mínima detectable se estima en torno a 4 μm, sólo limitada por la resolución del sistema óptico y la tasa de enfriamiento. Las incertidumbres sistemáticas asociadas a las imperfecciones de los campos de atrapamiento se ven atenuadas para menores amplitudes, e incluso podrían minimizarse ajustando adecuadamente las amplitudes relativas en cada modo o tratarse como una corrección a la medida experimental.

La aplicación del método óptico en el cristal de dos iones está limitada actualmente por la dependencia de las frecuencias propias con la amplitud de movimiento. El modelo no lineal desarrollado es capaz de corregir los desplazamientos en frecuencia debidos a la amplitud del modo analizado, pero no tiene en cuenta los desplazamientos sistemáticos consecuencia de los términos cruzados y además proporciona una menor precisión en comparación con el protocolo de medida pulsando el láser. El siguiente paso en la aplicación del método óptico será el acceso al régimen cuántico enfriando el cristal hasta el estado fundamental de movimiento. La menor amplitud de movimiento se traducirá en menores desplazamientos de frecuencia, y será necesario medir todos los términos de acoplamiento cruzado y corregir activamente los desplazamientos de frecuencia al nivel de un solo fonón. [38].

Bibliography

[1] H. Dehmelt, Experiments with an isolated subatomic particle at rest, *Rev. Mod. Phys.* **62**, 525–530 (1990). [Pages 1, 7, and 141].

[2] D. L. Farnham, R. S. Van Dyck Jr., and P. B. Schwinberg, Determination of the electron's atomic mass and the proton/electron mass ratio via Penning trap mass spectroscopy, *Phys. Rev. Lett.* **75**, 3598–3601 (1995). [Page 1].

[3] S. Sturm, F. Köhler, J. Zatorski, A. Wagner, Z. Harman, G. Werth, W. Quint, C. H. Keitel, and K. Blaum, High-precision measurement of the atomic mass of the electron, *Nature* **506**, 467–470 (2014). [Pages 1 and 91].

[4] F. Heiße, F. Köhler-Langes, S. Rau, J. Hou, S. Junck, A. Kracke, A. Mooser, W. Quint, S. Ulmer, G. Werth, K. Blaum, and S. Sturm, High-precision measurement of the proton's atomic mass, *Phys. Rev. Lett.* **119**, 033001 (2017). [Page 1].

[5] M. J. Borchert, J. A. Devlin, S. R. Erlewein, M. Fleck, J. A. Harrington, T. Higuchi, B. M. Latacz, F. Voelksen, E. J. Wursten, F. Abbass, M. A. Bohman amd A. H. Mooser, D. Popper, M. Wiesinger, C. Will, K. Blaum, Y. Matsuda, C. Ospelkaus, W. Quint, J. Walz, Y. Yamazaki, C. Smorra, and S. Ulmer, A 16-parts-per-trillion measurement of the antiproton-to-proton charge–mass ratio, *Nature* **601**, 53–57 (2022). [Pages 1 and 20].

[6] D. Hanneke, S. Fogwell, and G. Gabrielse, New measurement of the electron magnetic moment and the fine structure constant, *Phys. Rev. Lett.* **100**, 120801 (2008). [Page 1].

[7] R. S. Van Dyck Jr., P. B. Schwinberg, and H. G. Dehmelt, New high-precision comparison of electron and positron g factors, *Phys. Rev. Lett.* **59**, 26–29 (1987). [Page 1].

[8] G. Schneider, A. Mooser, M. Bohman, N. Schön, J. Harrington, T. Higuchi, H. Nagahama, S. Sellner, C. Smorra, K. Blaum, Y. Matsuda, W. Quint, J. Walz, and S. Ulmer, Double-trap measurement of the proton magnetic

moment at 0.3 parts per billion precision, *Science* **358**, 1081–1084 (2017). [Page 1].

[9] C. Smorra, S. Sellner, M. J. Borchert, J. A. Harrington, T. Higuchi, H. Nagahama, T. Tanaka, A. Mooser, G. Schneider, M. Bohman, K. Blaum, Y. Matsuda, C. Ospelkaus, W. Quint, J. Walz, Y. Yamazaki, and S. Ulmer, A parts-per-billion measurement of the antiproton magnetic moment, *Nature* **550**, 371–374 (2017). [Page 1].

[10] J. Dilling, K. Blaum, M. Brodeur, and S. Eliseev, Penning-trap mass measurements in atomic and nuclear physics, *Annu. Rev. Nucl. Part. Sci.* **68**, 45–74 (2018). [Pages 1 and 141].

[11] G. Gräff, H. Kalinowsky, and J. Traut, A direct determination of the proton electron mass ratio, *Z. Physik A* **297**, 35–39 (1980). [Pages 1, 17, and 141].

[12] P. B. Schwinberg, R. S. Van Dyck Jr., and H. G. Dehmelt, Trapping and thermalization of positrons for geonium spectroscopy, *Phys. Lett. A* **81**, 119–120 (1981). [Pages 1 and 141].

[13] M. König, G. Bollen, H.-J. Kluge, T. Otto, and J. Szerypo, Quadrupole excitation of stored ion motion at the true cyclotron frequency, *Int. J. Mass Spectrom.* **142**, 95–116 (1995). [Pages 1, 14, 17, 18, and 70].

[14] S. Eliseev, K. Blaum, M. Block, C. Droese, M. Goncharov, E. Minaya Ramírez, D. A. Nesterenko, Yu. N. Novikov, and L. Schweikhard, Phase-imaging ion-cyclotron-resonance measurements for short-lived nuclides, *Phys. Rev. Lett.* **110**, 082501 (2013). [Pages 1, 17, 18, and 141].

[15] R. S. Van Dyck Jr., D. B. Pinegar, S. Van Liew, and S. L. Zafonte, The UW-PTMS: Systematic studies, measurement progress, and future improvements, *Int. J. Mass Spectrom.* **251**, 231–242 (2006). [Page 2].

[16] E. A. Cornell, R. M. Weisskoff, K. R. Boyce, R. W. Flanagan Jr., G. P. Lafyatis, and D. E. Pritchard, Single-ion cyclotron resonance measurement of $m\left(CO^{+}\right)/m\left(N_2^{+}\right)$, *Phys. Rev. Lett.* **63**, 1674–1677 (1989). [Pages 2, 20, and 141].

[17] F. DiFilippo, V. Natarajan, K. R. Boyce, and D. E. Pritchard, Accurate atomic masses for fundamental metrology, *Phys. Rev. Lett.* **73**, 1481–1484 (1994). [Page 2].

[18] M. P. Bradley, J. V. Porto, S. Rainville, J. K. Thompson, and D. E. Pritchard, Penning trap measurements of the masses of ^{133}Cs, ^{87,85}Rb, and ^{23}Na with uncertainties ≤ 0.2 ppb, *Phys. Rev. Lett.* **83**, 4510–4513 (1999). [Pages 2, 3, and 142].

[19] M. Medina Restrepo and E. G. Myers, Mass difference of tritium and Helium-3, *Phys. Rev. Lett.* **131**, 243002 (2023). [Pages 2 and 3].

[20] S. Rainville, J. K. Thompson, and D. E. Pritchard, An ion balance for ultra-high-precision atomic mass measurements, *Science* **303**, 334–338 (2004). [Pages 2, 20, 76, and 141].

[21] D. J. Fink and E. G. Myers, Deuteron-to-proton mass ratio from simultaneous measurement of the cyclotron frequencies of H_2^+ and D^+, *Phys. Rev. Lett.* **127**, 243001 (2021). [Pages 2, 20, and 141].

[22] K. Kromer, C. Lyu, M. Door, P. Filianin, Z. Harman, J. Herkenhoff, P. Indelicato, C. H. Keitel, D. Lange, Y. N. Novikov, C. Schweiger, S. Eliseev, and K. Blaum, Observation of a low-lying metastable electronic state in highly charged lead by penning-trap mass spectrometry, *Phys. Rev. Lett.* **131**, 223002 (2023). [Pages 2, 20, and 141].

[23] S. Rau, F. Heiße, F. Köhler-Langes, S. Sasidharan, R. Haas, D. Renisch, C. E. Düllmann, W. Quint, S. Sturm, and K. Blaum, Penning trap mass measurements of the deuteron and the HD^+ molecular ion, *Nature* **585**, 43–47 (2020). [Pages 2, 20, 76, and 141].

[24] T. W. Hänsch and A. L. Schawlow, Cooling of gases by laser radiation, *Opt. Commun.* **13**, 68–69 (1975). [Pages 2 and 141].

[25] D. J. Wineland and H. G. Dehmelt, Proposed $10^{14}\,\delta\nu < \nu$ laser fluorescence spectroscopy on Tl^+ mono-ion oscillator III, *Bull. Am. Phys. Soc.* **20**, 637 (1975). [Pages 2 and 141].

[26] D. J. Wineland, R. E. Drullinger, and F. L. Walls, Radiation-pressure cooling of bound resonant absorbers, *Phys. Rev. Lett.* **40**, 1639–1642 (1978). [Page 2].

[27] W. Neuhauser, M. Hohenstatt, P. Toschek, and H. Dehmelt, Optical-sideband cooling of visible atom cloud confined in parabolic well, *Phys. Rev. Lett.* **41**, 233–236 (1978). [Page 2].

[28] F. Diedrich, J. C. Bergquist, W. M. Itano, and D. J. Wineland, Laser cooling to the zero-point energy of motion, *Phys. Rev. Lett.* **62**, 403–406 (1989). [Pages 2 and 12].

[29] D. J. Larson, J. C. Bergquist, J. J. Bollinger, W. M. Itano, and D. J. Wineland, Sympathetic cooling of trapped ions: A laser-cooled two-species nonneutral ion plasma, *Phys. Rev. Lett.* **57**, 70–73 (1986). [Pages 2 and 108].

[30] P. O. Schmidt, T. Rosenband, C. Langer, W. M. Itano, J. C. Bergquist, and D. J. Wineland, Spectroscopy using quantum logic, *Science* **309**, 749–752 (2005). [Page 2].

[31] J. W. Britton, B. C. Sawyer, A. C. Keith, C.-C. J. Wang, J. K. Freericks, H. Uys, M. J. Biercuk, and J. J. Bollinger, Engineered two-dimensional Ising interactions in a trapped-ion quantum simulator with hundreds of spins, *Nature* **484**, 489–492 (2012). [Page 2].

[32] K. A. Gilmore, M. Affolter, R. J. Lewis-Swan, D. Barberena, E. Jordan, A. M. Rey, and J. J. Bollinger, Quantum-enhanced sensing of displacements and electric fields with two-dimensional trapped-ion crystals, *Science* **373**, 673–678 (2021). [Pages 2, 75, and 104].

[33] J. F. Goodwin, G. Stutter, R. C. Thompson, and D. M. Segal, Resolved-sideband laser cooling in a Penning trap, *Phys. Rev. Lett.* **116**, 143002 (2016). [Pages 2 and 4].

[34] P. Hrmo, M. K. Joshi, V. Jarlaud, O. Corfield, and R. C. Thompson, Sideband cooling of the radial modes of motion of a single ion in a Penning trap, *Phys. Rev. A* **100**, 043414 (2019). [Page 2].

[35] D. Rodríguez, A quantum sensor for high-performance mass spectrometry, *Appl. Phys. B* **107**, 1031–1042 (2012). [Pages 3, 20, 75, 107, and 142].

[36] D. J. Heinzen and D. J. Wineland, Quantum-limited cooling and detection of radio-frequency oscillations by laser-cooled ions, *Phys. Rev. A* **42**, 2977–2994 (1990). [Page 3].

[37] M. J. Gutiérrez, J. Berrocal, F. Domínguez, I. Arrazola, M. Block, E. Solano, and D. Rodríguez, Dynamics of an unbalanced two-ion crystal in a Penning trap for application in optical mass spectrometry, *Phys. Rev. A* **100**, 063415 (2019). [Pages 3, 11, 12, 20, 21, 75, 107, 109, 113, 114, 116, 118, 120, 142, and 145].

[38] J. Cerrillo and D. Rodríguez, Motional quantum metrology in a Penning trap, *EPL* **134**, 38001 (2021). [Pages 3, 22, 121, 127, 142, and 147].

[39] J. M. Cornejo, R. Lehnert, M. Niemann, J. Mielke, T. Meiners, A. Bautista-Salvador, M. Schulte, D. Nitzschke, M. J. Borchert, K. Hammerer, S. Ulmer, and C. Ospelkaus, Quantum logic inspired techniques for spacetime-symmetry tests with (anti-)protons, *New J. Phys.* **23**, 073045 (2021). [Page 3].

[40] M. Bohman, V. Grunhofer, C. Smorra, M. Wiesinger, C. Will, M. J. Borchert, J. A. Devlin, S. Erlewein, M. Fleck, S. Gavranovic, J. Harrington, B. Latacz, A. Mooser, D. Popper, E. Wursten, K. Blaum, Y. Matsuda, C. Ospelkaus, W. Quint, J. Walz, S. Ulmer, and BASE Collaboration, Sympathetic cooling of a trapped proton mediated by an LC circuit, *Nature* **596**, 514–518 (2021). [Page 3].

[41] S. Jain, J. Alonso, M. Grau, and J. P. Home, Scalable arrays of micro-Penning traps for quantum computing and simulation, *Phys. Rev. X* **10**, 031027 (2020). [Pages 3, 12, 107, 126, and 146].

[42] F. Giacoppo, K. Blaum, M. Block, P. Chhetri, C. Droese, Ch. E. Düllmann, S. Eliseev, P. Filianin, S. Götz, Y. Gusev, F. Herfurth, F. P. Heßberger, O. Kaleja J. Khuyagbaatar, M. Laatiaoui, F. Lautenschläger, C. Lorenz, G. Marx, E. Minaya-Ramírez, A. Mistry, Yu. N. Novikov, W. R. Plaß, S. Raeder, D. Rodríguez, D. Rudolph, L. G. Sarmiento, C. Scheidenberger, L. Schweikhard, P. G. Thirolf, and A. Yakushev, Recent upgrades of the SHIPTRAP setup: On the finish line towards direct mass spectroscopy of Superheavy elements, *Acta Physica Polonica B* **48**, 423–429 (2017). [Pages 3 and 142].

[43] M. Block, Direct mass measurements of the heaviest elements with Penning traps, *Nuc. Phys. A* **944**, 471–491 (2015). [Pages 3 and 142].

[44] M. Block, D. Ackermann, K. Blaum, C. Droese, M. Dworschak, S. Eliseev, T. Fleckenstein, E. Haettner, F. Herfurth, F. P. Heßberger, S. Hofmann, J. Ketelaer, J. Ketter, H.-J. Kluge, G. Marx, M. Mazzocco, Yu. N. Novikov, W. R. Plaß, A. Popeko, S. Rahaman, D. Rodríguez, C. Scheidenberger, L. Schweikhard, P. G. Thirolf, G. K. Vorobyev, and C. Weber, Direct mass measurements above uranium bridge the gap to the island of stability, *Nature* **463**, 785–788 (2010). [Page 3].

[45] E. Minaya-Ramírez, D. Ackermann, K. Blaum, M. Block, C. Droese, Ch. E. Düllmann, M. Dworschak, M. Eibach, S. Eliseev, E. Haettner, F. Herfurth, F. P. Heßberger, S. Hofmann, J. Ketelaer, G. Marx, M. Mazzocco, D. Nesterenko, Yu. N. Novikov, W. R. Plaß, D. Rodríguez, C. Scheidenberger, L. Schweikhard, P. G. Thirolf, and C. Weber, Direct mapping of nuclear shell effects in the heaviest elements, *Science* **337**, 1207–1210 (2012). [Page 3].

[46] O. Kaleja, B. Anđelić, O. Bezrodnova, K. Blaum, M. Block, S. Chenmarev, P. Chhetri, C. Droese, Ch. E. Düllmann, M. Eibach, S. Eliseev, J. Even, P. Filianin, F. Giacoppo, S. Götz, Yu. Gusev, M. J. Gutiérrez, F. P. Heßberger, N. Kalantar-Nayestanaki, J. J. W. van de Laar, M. Laatiaoui, S. Lohse, N. Martynova, E. Minaya Ramírez, A. K. Mistry, T. Murböck, Yu. Novikov S. Raeder, D. Rodríguez, F. Schneider, L. Schweikhard, P. G. Thirolf, and A. Yakushev, Direct high-precision mass spectrometry of superheavy elements with SHIPTRAP, *Phys. Rev. Lett.* **106**, 054325 (2022). [Pages 3 and 142].

[47] S. Lohse, J. Berrocal, M. Block, S. Chenmarev, J. M. Cornejo, J. G. Ramírez, and D. Rodríguez, A quartz amplifier for high-sensitivity Fourier-transform

ion-cyclotron-resonance measurements with trapped ions, *Rev. Sci. Instrum.* **90**, 063202 (2019). [Pages 3 and 19].

[48] S. Lohse, J. Berrocal, S. Böhland, J. van de Laar, M. Block, S. Chenmarev, Ch. E. Düllmann, Sz. Nagy, J. G. Ramírez, and D. Rodríguez, Quartz resonators for penning traps toward mass spectrometry on the heaviest ions, *Rev. Sci. Instrum.* **91**, 093202 (2020). [Pages 3 and 19].

[49] J. Berrocal, S. Lohse, F. Domínguez, M. J. Gutiérrez, F. J. Fernández, M. Block, J. J. García-Ripoll, and D. Rodríguez, Non-equilibrium coupling of a quartz resonator to ions for Penning-trap fast resonant detection, *Quantum Sci. Technol.* **6**, 044002 (2021). [Pages 3 and 20].

[50] J. M. Cornejo and D. Rodríguez, A quantum sensor for neutrino mass measurements, *Adv. High Energy Phys.* **2012**, 849497 (2012). [Pages 3, 61, 89, and 142].

[51] The KATRIN collaboration, Direct neutrino-mass measurement with sub-electronvolt sensitivity, *Nature Physics* **18**, 160–166 (2022). [Page 3].

[52] L. Gastaldo, K. Blaum, K. Chrysalidis, et al., The electron capture in ^{163}Ho experiment - ECHo, *Eur. Phys. J. Spec. Top.* **226**, 1623–1694 (2017). [Pages 3 and 142].

[53] B. Alpert, M. Balata, M. Bennet, et al., The electron capture decay of ^{163}Ho to measure the electron neutrino mass with sub-eV sensitivity, *Eur. Phys. J. C* **75**, 112 (2015). [Pages 3 and 142].

[54] S. Eliseev, K. Blaum, M. Block, S. Chenmarev, H. Dorrer, Ch. E. Düllmann, C. Enss, P. E. Filianin, L. Gastaldo, M. Goncharov, U. Köster, F. Lautenschläger, Yu. N. Novikov, A. Rischka, R. X. Schüssler, L. Schweikhard, and A. Türler, Direct measurement of the mass difference of ^{163}Ho and ^{163}Dy solves the Q-value puzzle for the neutrino mass determination, *Phys. Rev. Lett.* **115**, 062501 (2015). [Page 3].

[55] A. Balysh, A. De Silva, V. I. Lebedev, K. Lou, M. K. Moe, M. A. Nelson, A. Piepke, A. Pronskiy, M. A. Vient, and P. Vogel, Double beta decay of ^{48}Ca, *Phys. Rev. Lett.* **77**, 5186–5189 (1996). [Pages 4, 89, and 142].

[56] K. Blaum, S. Eliseev, F. A. Danevich, V. I. Tretyak, S. Kovalenko, M. I. Krivoruchenko, Yu. N. Novikov, and J. Suhonen, Neutrinoless double-electron capture, *Rev. Mod. Phys.* **92**, 045007 (2020). [Pages 4 and 142].

[57] A. D. Ludlow, M. M. Boyd, J. Ye, E. Peik, and P. O. Schmidt, Optical atomic clocks, *Rev. Mod. Phys.* **87**, 637–701 (2015). [Page 4].

[58] S. M. Brewer, J.-S. Chen, A. M. Hankin, E. R. Clements, C. W. Chou, D. J. Wineland, D. B. Hume, and D. R. Leibrandt, $^{27}Al^{+}$ quantum-logic clock with a systematic uncertainty below 10^{-18}, *Phys. Rev. Lett.* **123**, 033201 (2019). [Page 4].

[59] E. Peik, T. Schumm, M. S. Safronova, A. Pálffy, J. Weitenberg, and P. G. Thirolf, Nuclear clocks for testing fundamental physics, *Quantum Sci. Technol.* **6**, 034002 (2021). [Pages 4, 61, 127, and 142].

[60] S. Kraemer, J. Moens, M. Athanasakis-Kaklamanakis, S Bara, K. Beeks, P. Chhetri, K. Chrysalidis, A. Claessens, T. E. Cocolios, J. G. M. Correia, H. De Witte, R. Ferrer, S. Geldhof, R. Heinke, N. Hosseini, M. Huyse, U. Köster, Y. Kudryavtsev, M. Laatiaoui, R. Lica, G. Magchiels, V. Manea, C. Merckling, L. M. C. Pereira, S. Raeder, T. Schumm, S. Sels, P. G. Thirolf, S. Malven Tunhuma, P. Van Den Bergh, P. Van Duppen, A. Vantomme, M. Verlinde, R. Villarreal, and U. Wahl, Observation of the radiative decay of the ^{229}Th nuclear clock isomer, *Nature* **617**, 706–710 (2023). [Pages 4 and 142].

[61] Fouad G. Major, Viorica N. Gheorghe, and Günther Werth, *Charged Particle Traps*, Springer (2005). [Pages 7, 9, and 28].

[62] Günther Werth, Viorica N. Gheorghe, and Fouad G. Major, *Charged Particle Traps II*, Springer (2009). [Pages 7, 9, 28, and 56].

[63] W. Paul, Electromagnetic traps for charged and neutral particles, *Rev. Mod. Phys.* **62**, 531–540 (1990). [Page 7].

[64] J. M. Cornejo, *The preparation Penning trap and recent developments on high-performance ion detection for the project TRAPSENSOR*, PhD thesis, Universidad de Granada (2016). [Pages 7, 23, 25, 123, and 143].

[65] M. J. Gutiérrez, *Studying an unbalanced two-ion crystal in a Penning trap: towards the quantum regime in a high magnetic fields*, PhD thesis, Universidad de Granada (2021). [Pages 7, 11, 12, 15, 16, 23, 25, 34, 52, 57, 64, 109, 113, 123, 124, and 143].

[66] J. M. Cornejo, M. Colombano, J. Doménech, M. Block, P. Delahaye, and D. Rodríguez, Extending the applicability of an open-ring trap to perform experiments with a single laser-cooled ion, *Rev. Sci. Instrum.* **86**, 103104 (2015). [Pages 7 and 28].

[67] L. S. Brown and G. Gabrielse, Geonium theory: Physics of a single electron or ion in a Penning trap, *Rev. Mod. Phys.* **58**, 233–311 (1986). [Page 10].

[68] J. Ketter, T. Eronen, M. Höcker, S. Streubel, and K. Blaum, First-order perturbative calculation of the frequency-shifts caused by static cylindrically-symmetric electric and magnetic imperfections of a Penning trap, *Int. J. Mass Spectrom.* **358**, 1–16 (2014). [Pages 10, 97, 99, and 100].

[69] David J. Griffiths, *Introduction to electrodynamics*, Pearson Education, Inc. 4$^{\text{th}}$ edition (2013). [Page 10].

[70] E. A. Cornell, R. M. Weisskoff, K. R. Boyce, and D. E. Pritchard, Mode coupling in a Penning trap: π pulses and a classical avoided crossing, *Phys. Rev. A* **41**, 312–315 (1990). [Pages 11 and 86].

[71] D. J. Wineland and W. M. Itano, Laser cooling of atoms, *Phys. Rev. A* **20**, 1521–1540 (1979). [Pages 12 and 13].

[72] D. Leibfried, R. Blatt, C. Monroe, and D. Wineland, Quantum dynamics of single trapped ions, *Rev. Mod. Phys.* **75**, 281–324 (2003). [Page 12].

[73] W. M. Itano and D. J. Wineland, Laser cooling of ions stored in harmonic and Penning traps, *Phys. Rev. A* **25**, 35–54 (1982). [Pages 13 and 14].

[74] S. Stenholm, The semiclassical theory of laser cooling, *Rev. Mod. Phys.* **58**, 699–739 (1986). [Page 13].

[75] R. C. Thompson and J. Papadimitriou, Simple model for the laser cooling of an ion in a Penning trap, *J. Phys. B: At. Mol. Opt. Phys.* **33**, 3393–3405 (2000). [Page 14].

[76] R. J. Hendricks, E. S. Phillips, D. M. Segal, and R. C. Thompson, Laser cooling in the Penning trap: an analytical model for cooling rates in the presence of an axializing field, *J. Phys. B: At. Mol. Opt. Phys.* **41**, 035301 (2008). [Page 14].

[77] J. Berrocal, E. Altozano, F. Domínguez, M. J. Gutiérrez, J. Cerrillo, F. J. Fernández, M. Block, C. Ospelkaus, and D. Rodríguez, Formation of two-ion crystals by injection from a Paul-trap source into a high-magnetic-field Penning trap, *Phys. Rev. A* **105**, 052603 (2022). [Pages 15, 55, 69, 112, 124, 143, and 144].

[78] M. Ramm, T. Pruttivarasin, M. Kokish, I. Talukdar, and H. Häffner, Precision measurement method for branching fractions of excited $P_{1/2}$ states applied to $^{40}Ca^{+}$, *Phys. Rev. Lett.* **111**, 023004 (2013). [Page 16].

[79] D. R. Crick, S. Donnellan, D. M. Segal, and R. C. Thompson, Magnetically induced electron shelving in a trapped Ca^{+} ion, *Phys. Rev. A* **81**, 052503 (2010). [Page 16].

[80] M. Hettrich, T. Ruster, H. Kaufmann, C. F. Roos, C. T. Schmiegelow, F. Schmidt-Kaler, and U. G. Poschinger, Measurement of dipole matrix elements with a single trapped ion, *Phys. Rev. Lett.* **115**, 143003 (2015). [Page 16].

[81] Z. Meir, M. Sinhal, M. S. Safronova, and S. Willitsch, Combining experiments and relativistic theory for establishing accurate radiative quantities in atoms: The lifetime of the $^2P_{3/2}$ state in $^{40}Ca^+$, *Phys. Rev. A* **101**, 012509 (2020). [Page 16].

[82] A. Kreuter, C. Becher, G. P. T. Lancaster, A. B. Mundt, C. Russo, H. Häffner, C. Roos, W. Hänsel, F. Schmidt-Kaler, R. Blatt, and M. S. Safronova, Experimental and theoretical study of the $3d^2D$–level lifetimes of $^{40}Ca^+$, *Phys. Rev. A* **71**, 032504 (2005). [Page 16].

[83] F. Gebert, Y. Wan, F. Wolf, C. N. Angstmann, J. C. Berengut, and P. O. Schmidt, Precision isotope shift measurements in calcium ions using quantum logic detection schemes, *Phys. Rev. Lett.* **115**, 053003 (2015). [Pages 16, 75, and 103].

[84] W. Nörtershäuser, K. Blaum, K. Icker, P. Müller, A. Schmitt, K. Wendt, and B. Wiche, Isotope shifts and hyperfine structure in the transitions in calcium II, *Eur. Phys. J. D* **2**, 33–39 (1998). [Page 16].

[85] A. Kramida, Isotope shifts in neutral and singly-ionized calcium, *At. Data Nucl. Data Tables* **133–134**, 101322 (2020). [Page 16].

[86] Y. Wan, F. Gebert, J. B. Wübbena, N. Scharnhorst, S. Amairi, I. D. Leroux, B. Hemmerling, N. Lörch, K. Hammerer, and P. O. Schmidt, Precision spectroscopy by photon-recoil signal amplification, *Nat. Commun.* **5**, 3096 (2014). [Page 16].

[87] Y. Huang, H. Guan, P. Liu, W. Bian, L. Ma, K. Liang, T. Li, and K. Gao, Frequency comparison of two $^{40}Ca^+$ optical clocks with an uncertainty at the 10^{-17} level, *Phys. Rev. Lett.* **116**, 013001 (2016). [Page 16].

[88] R. Gerritsma, G. Kirchmair, F. Zähringer, J. Benhelm, R. Blatt, and C. F. Roos, Precision measurement of the branching fractions of the 4p $^2P_{3/2}$ decay of Ca II, *Eur. Phys. J. D* **50**, 13–19 (2008). [Page 16].

[89] S. George, S. Baruah, B. Blank, K. Blaum, M. Breitenfeldt, U. Hager, F. Herfurth, A. Herlert, A. Kellerbauer, H.-J. Kluge, M. Kretzschmar, D. Lunney, R. Savreux, S. Schwarz, L. Schweikhard, and C. Yazidjian, Ramsey method of separated oscillatory fields for high-precision Penning trap mass spectrometry, *Phys. Rev. Lett.* **98**, 162501 (2007). [Page 18].

[90] D. A. Nesterenko, S. Eliseev, K. Blaum, M. Block, S. Chenmarev, A. Dörr, C. Droese, P. E. Filianin, M. Goncharov, E. Minaya Ramírez, Yu. N. Novikov, L. Schweikhard, and V. V. Simon, Direct determination of the atomic mass difference of ^{187}Re and ^{187}Os for neutrino physics and cosmochronology, *Phys. Rev. C* **90**, 042501(R) (2014). [Page 18].

[91] D. J. Wineland and H. G. Dehmelt, Principles of the stored ion calorimeter, *J. Appl. Phys.* **46**, 919—930 (1975). [Pages 18 and 76].

[92] S. Ulmer, H. Kracke, K. Blaum, S. Kreim, A. Mooser, W. Quint, C. C. Rodegheri, and J. Walz, The quality factor of a superconducting rf resonator in a magnetic field, *Rev. Sci. Instrum.* **80**, 123302 (2009). [Page 19].

[93] E. Altozano, J. Berrocal, S. Lohse, F. Domínguez, M. Block, J. J. García-Ripoll, and D. Rodríguez, Coupled-oscillator model to analyze the interaction between a quartz resonator and trapped ions, *Phys. Rev. A* **107**, 053116 (2023). [Page 20].

[94] S. Sturm, A. Wagner, B. Schabinger, and K. Blaum, Phase-sensitive cyclotron frequency measurements at ultralow energies, *Phys. Rev. Lett.* **107**, 143003 (2011). [Page 20].

[95] R. S. Van Dyck Jr., S. L. Zafonte, S. Van Liew, D. B. Pinegar, and P. B. Schwinberg, Ultraprecise atomic mass measurement of the α particle and ^{4}He, *Phys. Rev. Lett.* **92**, 220802 (2004). [Page 20].

[96] S. Eliseev, K. Blaum, M. Block, A. Dörr, C. Droese, T. Eronen, M. Goncharov, M. Höcker, J. Ketter, E. Minaya Ramírez, D. A. Nesterenko, Yu. N. Novikov, and L. Schweikhard, A phase-imaging technique for cyclotron-frequency measurements, *Appl. Phys. B* **114**, 107–128 (2014). [Page 21].

[97] H. G. Dehmelt, Proposed $10^{14}\,\delta\nu < \nu$ laser fluorescence spectroscopy on Tl^+ mono-ion oscillator II, *Bull. Am. Phys. Soc.* **20**, 60 (1975). [Page 22].

[98] M. J. Gutiérrez, J. Berrocal, J. M. Cornejo, F. Domínguez, J. J. Del Pozo, I. Arrazola, J. Bañuelos, P. Escobedo, O. Kaleja, L. Lamata, R. A. Rica, S. Schmidt, M. Block, E. Solano, and D. Rodríguez, The TRAPSENSOR facility: an open-ring 7 tesla Penning trap for laser-based precision experiments, *New J. Phys.* **21**, 023023 (2019). [Pages 23, 64, 123, and 143].

[99] J. M. Cornejo and D. Rodríguez, A preparation Penning trap for the TRAPSENSOR project with prospects for MATS at FAIR, *Nucl. Instrum. Methods Phys. Res. B* **376**, 288–291 (2016). [Page 25].

[100] D. Rodríguez et al., MATS and LaSpec: High-precision experiments using ion traps and lasers at FAIR, *Eur. Phys. J. Spec. Top.* **183**, 1–123 (2010). [Page 25].

[101] J. Doménech, *Implementación y puesta a punto de un modulador electro-óptico y mejora de las prestaciones del sistema de detección en el proyecto TRAPSENSOR*, Master's thesis, Universidad de Granada (2015). [Pages 27 and 56].

[102] B. Anđelić, M. Block, P. Chhetri, J. Even, F. Giacoppo, N. Kalantar-Nayestanaki, O. Kaleja, T. Murböck, F. Schneider, and S. Raeder, Simulation studies of the laser ablation ion source at the SHIPTRAP setup, *Hyperfine Interact.* **241**, 46 (2020). [Page 29].

[103] R. Kersevan and M. Ady, Recent developments of Monte-Carlo codes MOLFLOW+ and SYNRAD+, In *Proc. 10th Int. Particle Accelerator Conf. (IPAC'19)* pages 1327–1330 Melbourne, Australia (2019). ANTO's Australian Synchrotron JACoW Publishing. [Pages 30, 123, 131, and 143].

[104] Karl Jousten (Ed.), *Handbook of Vacuum Technology*, Wiley-VCH (2016). [Pages 30, 31, and 32].

[105] R. Kersevan and J.-L. Pons, Introduction to MOLFLOW+: New graphical processing unit-based Monte Carlo code for simulating molecular flows and for calculating angular coefficients in the compute unified device architecture environment, *J. Vac. Sci. Technol. A* **27**, 1017–1023 (2009). [Page 30].

[106] M. Ady, *Monte Carlo simulations of ultra high vacuum and synchrotron radiation for particle accelerators*, PhD thesis, Ecole Polytechnique, Lausanne (2016). [Page 31].

[107] P. Chiggiato, Outgassing properties of vacuum materials for particle accelerators, In *Proceedings of the 2017 CERN–Accelerator–School course on Vacuum for Particle Accelerators* pages 143–189 Glumslöv, Sweden (2017). CERN CERN Document Server. [Page 32].

[108] Max Born and Emil Wolf, *Principles of Optics*, Cambridge University Press 7nd edition (1999). [Pages 37, 38, 39, and 134].

[109] Joseph W. Goodman, *Introduction to Fourier Optics*, McGraw-Hill 2nd edition (1996). [Pages 38, 39, 40, and 134].

[110] W. Alt, An objective lens for efficient fluorescence detection of single atoms, *Optik* **113**, 142–144 (2002). [Page 41].

[111] M. W. Gempel, T. Hartman, T. A. Schulze, K. K. Voges, A. Zenesini, and S. Ospelkaus, An adaptable two-lens high-resolution objective for single-site resolved imaging of atoms in optical lattices, *Rev. Sci. Instrum.* **90**, 053201 (2019). [Page 41].

[112] H. Ball, Ch. D. Marciniak, R. N. Wolf, A. T.-H. Hung, K. Pyka, and M. J. Biercuk, Site-resolved imaging of beryllium ion crystals in a high-optical-access Penning trap with inbore optomechanics, *Rev. Sci. Instrum.* **90**, 053103 (2019). [Page 41].

[113] C. Robens, S. Brakhane, W. Alt, F. Kleißler, D. Meschede, G. Moon, G. Ramola, and A. Alberti, High numerical aperture (NA = 0.92) objective lens for imaging and addressing of cold atoms, *Opt. Lett.* **42**, 1043–1046 (2017). [Page 41].

[114] Robert E. Fisher, Biljana Tadic-Galeb, and Paul R. Yoder, *Optical System Design*, McGraw-Hill 2nd edition (2008). [Page 41].

[115] Daniel Malacara and Zacarias Malacara, *Handbook of Optical Design*, Marcel Dekker 2nd edition (2004). [Page 42].

[116] Glenn D. Boreman, *Modulation transfer function in optical and electro-optical systems*, SPIE—The International Society for Optical Engineering 2nd edition (2021). [Page 47].

[117] I. Iglesias, Parametric wave-aberration retrieval from point-spread function data by use of a pyramidal recursive algorithm, *Appl. Opt.* **37**, 5427–5430 (1998). [Page 47].

[118] R. Barakat and B. H. Sandler, Determination of the wave-front aberration function from measured values of the point-spread function: a two-dimensional phase retrieval problem, *J. Opt. Soc. Am. A* **9**, 1715–1723 (1992). [Page 47].

[119] J. D. Wong-Campos, K. G. Johnson, B. Neyenhuis, J. Mizrahi, and C. Monroe, High-resolution adaptive imaging of a single atom, *Nat. Photon.* **10**, 606–610 (2016). [Page 47].

[120] D. F. V. James, Quantum dynamics of cold trapped ions with application to quantum computation, *Appl. Phys. B* **66**, 181–190 (1998). [Page 51].

[121] S. Bourdeauducq, whitequark, R. Jördens, D. Nadlinger, Y. Sionneau, F. Kermarrec, C. Ballance, T. Harty, pca006132, E. Wodey, H. Ho, D. Ridinger, S. Maka, C. Baynham, J. Britton, L. Riesebos, M. Weber, D. Slichter, Garrett, mntng, occheung, P. Kulik, N. Krackow, T. Ballance, A. R. Kamat, S. Chen, S. Mackenzie, apatura iris, charlesbaynham, and raghu, ARTIQ: A leading-edge control system for quantum information experiments (2021). [Page 52].

[122] LEBIT software repository. [Page 54].

[123] N. Kjaergaard, L. Hornekaer, A. M. Thommesen, Z. Videsen, and M. Drewsen, Isotope selective loading of an ion trap using resonance-enhanced two-photon ionization, *Appl. Phys. B* **71**, 207–210 (2000). [Page 55].

[124] S. Gulde, D. Rotter, P. Barton, F. Schmidt-Kaler, R. Blatt, and W. Hogervorst, Simple and efficient photo-ionization loading of ions for precision ion-trapping experiments, *Appl. Phys. B* **73**, 861–863 (2001). [Page 55].

[125] Ing. Gert Hofstätter, Alfavakuo e.u. [Page 55].

[126] D. M. Lucas, A. Ramos, J. P. Home, M. J. McDonnell, S. Nakayama, J.-P. Stacey, S. C. Webster, D. N. Stacey, and A. M. Steane, Isotope-selective photoionization for calcium ion trapping, *Phys. Rev. A* **69**, 012711 (2004). [Page 56].

[127] V. Salas, *Estudio experimental de la producción de iones moleculares para experimentos con trampas Penning*, Master's thesis, Universidad de Granada (2022). [Page 59].

[128] J. H. Wesenberg, R. J. Epstein, D. Leibfried, R. B. Blakestad, J. Britton, J. P. Home, W. M. Itano, J. D. Jost, E. Knill, C. Langer, R. Ozeri, S. Seidelin, and D. J. Wineland, Fluorescence during Doppler cooling of a single trapped atom, *Phys. Rev. A* **76**, 053416 (2007). [Page 63].

[129] J. J. Bollinger and D. J. Wineland, Strongly coupled nonneutral ion plasma, *Phys. Rev. Lett.* **53**, 348–351 (1984). [Page 65].

[130] S. L. Gilbert, J. J. Bollinger, and D. J. Wineland, Shell-structure phase of magnetically confined strongly coupled plasmas, *Phys. Rev. Lett.* **60**, 2022–2026 (1988). [Page 65].

[131] W. M. Itano, J. J. Bollinger, J. N. Tan, B. Jelenković, X.-P. Huang, and D. J. Wineland, Bragg diffraction from crystallized ion plasmas, *Science* **279**, 686–689 (1998). [Page 65].

[132] L. R. Brewer, J. D. Prestage, J. J. Bollinger, W. M. Itano, D. J. Larson, and D. J. Wineland, Static properties of a non-neutral $^{9}Be^{+}$-ion plasma, *Phys. Rev. A* **38**, 859–873 (1988). [Page 65].

[133] R. C. Thompson, Ion coulomb crystals, *Contemp. Phys.* **56**, 63–79 (2015). [Page 65].

[134] J. P. Hansen, Statistical mechanics of dense ionized matter. I. Equilibrium properties of the classical one-component plasma, *Phys. Rev. A* **8**, 3096–3109 (1973). [Page 65].

[135] E. L. Pollock and J. P. Hansen, Statistical mechanics of dense ionized matter. II. Equilibrium properties and melting transition of the crystallized one-component plasma, *Phys. Rev. A* **8**, 3110–3122 (1973). [Page 65].

[136] W. L. Slattery, G. D. Doolen, and H. E. DeWitt, Improved equation of state for the classical one-component plasma, *Phys. Rev. A* **21**, 2087–2095 (1980). [Page 65].

[137] S. Mavadia, J. F. Goodwin, G. Stutter, S. Bharadia, D. R. Crick, D. M. Segal, and R. C. Thompson, Control of the conformations of ion Coulomb crystals in a Penning trap, *Nat. Commun.* **4**, 2571 (2013). [Page 65].

[138] R. D. Johnson III (1999), Computational Chemistry Comparison and Benchmark Database, CCCBDBD, [Online], Available: http://cccbdb.nist.gov/ (Accessed September 14, 2023) (2022), National Institute of Standards and Technology, Gaithersburg, MD. [Page 67].

[139] D. J. Wineland, C. Monroe, W. M. Itano, D. Leibfried, B. E. King, and D. M. Meekhof, Experimental issues in coherent quantum-state manipulation of trapped atomic ions, *J. Res. Natl. Inst. Stand. Technol.* **103**, 259–328 (1998). [Pages 67 and 68].

[140] H. F. Powell, D. M. Segal, and R. C. Thompson, Axialization of laser cooled magnesium ions in a Penning trap, *Phys. Rev. Lett.* **89**, 093003 (2002). [Pages 69, 124, and 144].

[141] G. Janik, W. Nagourney, and H. Dehmelt, Doppler-free optical spectroscopy on the Ba^+ mono-ion oscillator, *J. Opt. Soc. Am. B* **2**, 1251–1257 (1985). [Page 71].

[142] Y. Stalgies, I. Siemers, B. Appasamy, T. Altevogt, and P. E. Toschek, The spectrum of single-atom resonance fluorescence, *EPL* **35**, 259–264 (1996). [Page 71].

[143] Rodney Loudon, *The Quantum Theory of Light*, Oxford University Press 2nd edition (1995). [Pages 71 and 73].

[144] M. Fleischhauer, A. Imamoglu, and J. P. Marangos, Electromagnetically induced transparency: Optics in coherent media, *Rev. Mod. Phys.* **77**, 633–673 (2005). [Page 72].

[145] D. Manzano, A short introduction to the Lindblad master equation, *AIP Advances* **10**, 025106 (2020). [Pages 72 and 73].

[146] H. Oberst, *Resonance fluorescence of single barium ions*, Master's thesis, Leopold-Franzens-Universität Innsbruck (1999). [Page 73].

[147] J. Roßnagel, K. N. Tolazzi, F. Schmidt-Kaler, and K. Singer, Fast thermometry for trapped ions using dark resonances, *New J. Phys.* **17**, 045004 (2015). [Page 73].

[148] J. Berrocal, A. Hernández, I. Arrazola, F. Domínguez, A. Carrasco-Sanz, F. J. Fernández, M. Block, and D. Rodríguez, Penning-trap eigenfrequency measurements with optical radiofrequency detectors, *Phys. Rev. Res.* **6**, L012001 (2024). [Pages 75, 125, and 145].

[149] M. Wang, W. J. Huang, F. G. Kondev, G. Audi, and S. Naimi, The AME 2020 atomic mass evaluation (II). Tables, graphs and references, *Chinese Phys. C* **45**, 030003 (2021). [Pages 75, 90, 91, 95, 96, 102, 125, and 145].

[150] M. J. Biercuk, H. Uys, J. W. Britton, A. P. VanDevender, and J. J. Bollinger, Ultrasensitive detection of force and displacement using trapped ions, *Nature Nanotech.* **5**, 646–650 (2010). [Pages 75 and 104].

[151] C. Solaro, S. Meyer, K. Fisher, J. C. Berengut, E. Fuchs, and M. Drewsen, Improved isotope-shift-based bounds on bosons beyond the standard model through measurements of the $^2D_{3/2}$–$^2D_{5/2}$ interval in Ca^+, *Phys. Rev. Lett.* **125**, 123003 (2020). [Pages 75, 103, 104, and 126].

[152] D. J. Wineland, J. J. Bollinger, and W. M. Itano, Laser-fluorescence mass spectroscopy, *Phys. Rev. Lett.* **50**, 628–631 (1983). [Pages 76 and 78].

[153] K. Okada, M. Wada, L. Boesten, T. Nakamura, I. Katayama, and S. Ohtani, Acceleration of the chemical reaction of trapped Ca^+ ions with H_2O molecules by laser excitation, *J. Phys. B: At. Mol. Opt. Phys.* **36**, 33–46 (2003). [Page 76].

[154] M. Drewsen, A. Mortensen, R. Martinussen, P. Staanum, and J. L. Sørensen, Nondestructive identification of cold and extremely localized single molecular ions, *Phys. Rev. Lett.* **93**, 243201 (2004). [Page 76].

[155] B. Roth, P. Blythe, and S. Schiller, Motional resonance coupling in cold multispecies Coulomb crystals, *Phys. Rev. A* **75**, 023402 (2007). [Page 76].

[156] P. F. Staanum, K. Højbjerre, R. Wester, and M. Drewsen, Probing isotope effects in chemical reactions using single ions, *Phys. Rev. Lett.* **100**, 243003 (2008). [Page 76].

[157] A. D. Gingell, M. T. Bell, J. M. Oldham, T. P. Softley, and J. N. Harvey, Cold chemistry with electronically excited Ca^+ Coulomb crystals, *J. Chem. Phys.* **133**, 194302 (2010). [Page 76].

[158] M. V. DePalatis and M. S. Chapman, Production of translationally cold barium monohalide ions, *Phys. Rev. A* **88**, 023403 (2013). [Page 76].

[159] F. Domínguez, I. Arrazola, J. Doménech, J. S. Pedernales, L. Lamata, E. Solano, and D. Rodríguez, A single-ion reservoir as a high-sensitive sensor of electric signals, *Sci. Rep.* **7**, 8336 (2017). [Pages 76, 78, and 135].

[160] F. Domínguez, M. J. Gutiérrez, I. Arrazola, J. Berrocal, J. M. Cornejo, J. J. Del Pozo, R. A. Rica, S. Schmidt, E. Solano, and D. Rodríguez, Motional studies of one and two laser-cooled trapped ions for electric-field sensing applications, *J. Mod. Opt.* **65**, 613–621 (2018). [Pages 76, 78, and 135].

[161] H. Imajo, S. Urabe, K. Hayasaka, and M. Watanabe, Measurements of motional frequencies for laser-cooled ions in a Penning trap, *J. Mod. Opt.* **39**, 317–324 (1992). [Pages 76 and 78].

[162] B. J. McMahon, C. Volin, W. G. Rellergert, and B. C. Sawyer, Doppler-cooled ions in a compact reconfigurable Penning trap, *Phys. Rev. A* **101**, 013408 (2020). [Pages 76 and 78].

[163] A. Rischka, H. Cakir, M. Door, P. Filianin, Z. Harman, W. J. Huang, P. Indelicato, C. H. Keitel, C. M. König, K. Kromer, M. Müller, Y. N. Novikov, R. X. Schüssler, C. Schweiger, S. Eliseev, and K. Blaum, Mass-difference measurements on heavy nuclides with an eV/c^2 accuracy in the PENTATRAP spectrometer, *Phys. Rev. Lett.* **124**, 113001 (2020). [Page 76].

[164] R. T. Birge, The calculation of errors by the method of least squares, *Phys. Rev.* **40**, 207–227 (1932). [Page 82].

[165] Student, The probable error of a mean, *Biometrika* **6**, 1–25 (1908). [Page 83].

[166] Philip R. Bevington and D. Keith Robinson, *Data Reduction and Error Analysis*, McGraw-Hill 3$^{\text{rd}}$ edition (2003). [Page 83].

[167] L. S. Brown and G. Gabrielse, Precision spectroscopy of a charged particle in an imperfect Penning trap, *Phys. Rev. A* **25**, 2423–2425(R) (1982). [Page 85].

[168] G. Gabrielse, Why is sideband mass spectrometry possible with ions in a Penning trap?, *Phys. Rev. Lett.* **102**, 172501 (2009). [Page 87].

[169] R. Arnold et al., Measurement of the double-beta decay half-life and search for the neutrinoless double-beta decay of ^{48}Ca with the NEMO-3 detector, *Phys. Rev. D* **93**, 112008 (2016). [Page 89].

[170] E. Majorana, Teoria simmetrica dell'elettrone e del positrone, *Nuovo Cim* **14**, 171–184 (1937). [Page 89].

[171] G. Racah, Sulla simmetria tra particelle e antiparticelle, *Nuovo Cim* **14**, 322–328 (1937). [Page 89].

[172] W. H. Furry, On transition probabilities in double beta-disintegration, *Phys. Rev.* **56**, 1184–1193 (1939). [Page 89].

[173] A. A. Kwiatkowski, T. Brunner, J. D. Holt, A. Chaudhuri, U. Chowdhury, M. Eibach, J. Engel, A. T. Gallant, A. Grossheim, M. Horoi, A. Lennarz, T. D. Macdonald, M. R. Pearson, B. E. Schultz, M. C. Simon, R. A. Senkov, V. V. Simon, K. Zuber, and J. Dilling, New determination of double-β-decay properties in ^{48}Ca: High-precision $Q_{\beta\beta}$-value measurement and improved nuclear matrix element calculations, *Phys. Rev. C* **89**, 045502 (2014). [Page 89].

[174] M. Miyabe, C. Geppert, M. Kato, M. Oba, I. Wakaida, K. Watanabe, and K. D. A. Wendt, Determination of ionization potential of calcium by high-resolution resonance ionization spectroscopy, *J. Phys. Soc. Jpn.* **75**, 034302 (2006). [Page 91].

[175] F. Köhler, K. Blaum, M. Block, S. Chenmarev, S. Eliseev, D. A. Glazov, M. Goncharov, J. Hou, A. Kracke, D. A. Nesterenko, Y. N. Novikov, W. Quint, E. Minaya-Ramirez, V. M. Shabaev, S. Sturm, A. V. Volotka, and G. Werth, Isotope dependence of the Zeeman effect in lithium-like calcium, *Nat. Commun.* **7**, 10246 (2016). [Pages 91, 125, and 145].

[176] Sz. Nagy, T. Fritioff, A. Solders, R. Schuch, M. Björkhage, and I. Bergström, Precision mass measurements of ^{40}Ca^{17+} and ^{40}Ca^{19+} ions in a Penning trap, *Eur. Phys. J. D* **39**, 1–4 (2006). [Page 91].

[177] P. Martin, M. Buenerd, Y. Dupont, and M. Chabre, Proton-deuteron reactions at 40 MeV on the calcium isotopes, *Nuc. Phys. A* **185**, 465–487 (1972). [Page 94].

[178] P. Doll, G. J. Wagner, K. T. Knöpfle, and G. Mairle, The quasihole aspect of hole strength distributions in odd potassium and calcium isotopes, *Nuc. Phys. A* **263**, 210–236 (1976). [Page 94].

[179] S. W. Kikstra, C. Van Der Leun, S. Raman, E. T. Jurney, and I. S. Tourner, Superallowed ^{42}Sc(β^+)^{42}Ca decay, *Nuc. Phys. A* **496**, 429–445 (1989). [Page 96].

[180] R. X. Schüssler, *First High-Precision Mass Measurements at PENTATRAP on highly charged Xe and Re ions*, PhD thesis, Ruprecht-Karls-Universität Heidelberg (2019). [Page 99].

[181] M. Redshaw, *Precise Measurements of the Atomic Masses of ^{28}Si, ^{31}P, ^{32}S, ^{84,86}Kr, ^{129,132,136}Xe, and the Dipole Moment of PbF$^+$ Using Single-Ion and Two-Ion Penning Trap Techniques*, PhD thesis, Florida State University (2007). [Page 99].

[182] A. Kellerbauer, K. Blaum, G. Bollen, F. Herfurth, H.-J. Kluge, M. Kuckein, E. Sauvan, C. Scheidenberger, and L. Schweikhard, From direct to absolute mass measurements: A study of the accuracy of ISOLTRAP, *Eur. Phys. J. D* **22**, 53–64 (2003). [Page 100].

[183] H. Häffner, *Präzisionsmessung des magnetischen Moments des Elektrons in wasserstoffähnlichem Kohlenstoff*, PhD thesis, Johannes Gutenberg-Universität Mainz (2000). [Page 101].

[184] J. C. Berengut, D. Budker, C. Delaunay, V. V. Flambaum, C. Frugiuele, E. Fuchs, C. Grojean, R. Harnik, R. Ozeri, G. Perez, and Y. Soreq, Probing new long-range interactions by isotope shift spectroscopy, *Phys. Rev. Lett.* **120**, 091801 (2018). [Pages 102 and 126].

[185] C. Frugiuele, E. Fuchs, G. Perez, and M. Schlaffer, Constraining new physics models with isotope shift spectroscopy, *Phys. Rev. D* **96**, 015011 (2017). [Page 102].

[186] A. Kramida, Y. Ralchenko, J. Reader, and NIST ASD Team (2022), NIST Atomic Spectra Database (version 5.10), [Online], Available: https://physics.nist.gov/asd (Accessed September 14, 2023) (2023), National Institute of Standards and Technology, Gaithersburg, MD. [Page 103].

[187] H. D. Wohlfahrt, E. B. Shera, M. V. Hoehn, Y. Yamazaki, G. Fricke, and R. M. Steffen, Muonic isotope shifts in the stable Ca nuclei, *Phys. Lett. B* **73**, 131–134 (1978). [Page 103].

[188] W. H. King, Comments on the Article "Peculiarities of the isotope shift in the samarium spectrum", *J. Opt. Soc. Am.* **53**, 638–639 (1963). [Page 103].

[189] F. W. Knollmann, A. N. Patel, and S. C. Doret, Part-per-billion measurement of the $4^2S_{1/2} \rightarrow 3^2D_{5/2}$ electric-quadrupole-transition isotope shifts between $^{42,44,48}Ca^+$ and $^{40}Ca^+$, *Phys. Rev. A* **100**, 022514 (2019). [Pages 104 and 126].

[190] W. Nagourney, J. Sandberg, and H. Dehmelt, Shelved optical electron amplifier: Observation of quantum jumps, *Phys. Rev. Lett.* **56**, 2797 (1986). [Page 104].

[191] C. Solaro, S. Meyer, K. Fisher, M. V. DePalatis, and M. Drewsen, Direct frequency-comb-driven Raman transitions in the terahertz range, *Phys. Rev. Lett.* **120**, 253601 (2018). [Page 104].

[192] X. Fan, T. G. Myers, B. A. D. Sukra, and G. Gabrielse, Measurement of the electron magnetic moment, *Phys. Rev. Lett.* **130**, 071801 (2023). [Page 105].

[193] P. Bowe, L. Hornekær, C. Brodersen, M. Drewsen, J. S. Hangst, and J. P. Schiffer, Sympathetic crystallization of trapped ions, *Phys. Rev. Lett.* **82**, 2071–2074 (1999). [Page 108].

[194] P. Blythe, B. Roth, U. Fröhlich, H. Wenz, and S. Schiller, Production of ultracold trapped molecular hydrogen ions, *Phys. Rev. Lett.* **95**, 183002 (2005). [Page 108].

[195] L. Schmöger, O. Versolato, M. Schwarz, M. Kohnen, A. Windberger, B. Piest, S. Feuchtenbeiner, J. Pedregosa-Gutiérrez, T. Leopold, P. Micke, A. K. Hansen, T. M. Baumann, M. Drewsen, J. Ullrich, P. O. Schmidt, and J. R. Crespo López-Urrutia, Coulomb crystallization of highly charged ions, *Science* **347**, 1233–1236 (2015). [Page 108].

[196] M. D. Barrett, B. DeMarco, T. Schaetz, V. Meyer, D. Leibfried, J. Britton, J. Chiaverini, W. M. Itano, B. Jelenković, J. D. Jost, C. Langer, T. Rosenband, and D. J. Wineland, Sympathetic cooling of $^{9}Be^{+}$ and $^{24}Mg^{+}$ for quantum logic, *Phys. Rev. A* **68**, 042302 (2003). [Page 108].

[197] H. Imajo, K. Hayasaka, R. Ohmukai, U. Tanaka, M. Watanabe, and S. Urabe, High-resolution ultraviolet spectra of sympathetically-laser-cooled Cd^{+} ions, *Phys. Rev. A* **53**, 122–125 (1996). [Page 108].

[198] T. Murböck, S. Schmidt, G. Birkl, W. Nörtershäuser, R. C. Thompson, and M. Vogel, Rapid crystallization of externally produced ions in a Penning trap, *Phys. Rev. A* **94**, 043410 (2016). [Page 108].

[199] M. Guggemos, D. Heinrich, O. A. Herrera-Sancho, R. Blatt, and C. F. Roos, Sympathetic cooling and detection of a hot trapped ion by a cold one, *New J. Phys.* **17**, 103001 (2015). [Page 108].

[200] Ali Hasan Nayfeh and Dean T. Mook, *Nonlinear Oscillators*, John Wiley & Sons (1979). [Pages 112 and 135].

[201] N. Akerman, S. Kotler, Y. Glickman, Y. Dallal, A. Keselman, and R. Ozeri, Single-ion nonlinear mechanical oscillator, *Phys. Rev. A* **82**, 061402(R) (2010). [Page 112].

[202] H.-Y. Wu, Y. Xie, W. Wan, L. Chen, F. Zhou, and M. Feng, A complicated Duffing oscillator in the surface-electrode ion trap, *Appl. Phys. B* **114**, 81–88 (2014). [Page 112].

[203] J. P. Home, D. Hanneke, J. D. Jost, D. Leibfried, and D. J. Wineland, Normal modes of trapped ions in the presence of anharmonic trap potentials, *New J. Phys.* **13**, 073026 (2011). [Pages 114, 116, and 120].

[204] F. Wolf, C. Shi, J. C. Heip, M. Gessner, L. Pezzè, A. Smerzi, M. Schulte, K. Hammerer, and P. O. Schmidt, Motional Fock states for quantum-enhanced amplitude and phase measurements with trapped ions, *Nat. Commun.* **10**, 2929 (2019). [Page 121].

[205] R. X. Schüssler, H. Bekker, M. Braß, H. Cakir, J. R. Crespo López-Urrutia, M. Door, P. Filianin, Z. Harman, M. W. Haverkort, W. J. Huang, P. Indelicato, C. H. Keitel, C. M. König, K. Kromer, M. Müller, Y. N. Novikov, A. Rischka, C. Schweiger, S. Sturm, S. Ulmer, S. Eliseev, and K. Blaum, Detection of metastable electronic states by Penning trap mass spectrometry, *Nature* **581**, 42–46 (2020). [Page 125].

[206] P. E. Bradley, R. Radebaugh, and M. A. Lewis, Cryogenic material properties database, update 2006, In *Proceedings of ICMC '06 Twenty First International Cryogenic Engineering Conference and 9th Cryogenics* pages 13–21 Prague, Czech Republic (206). Icaris Ltd Icaris Ltd. [Page 129].

[207] Valerian Pishchik, Leonid A. Lytvynov, and Elena R. Dobrovinskaya, *Sapphire. Material, Manufacturing, Applications*, Springer (2009). [Page 129].